UNIVERSITÉ DE GRENOBLE

THÈSE

Pour obtenir le grade de

DOCTEUR DE L'UNIVERSITÉ DE GRENOBLE

Spécialité : **Physique des Particules**

Arrêté ministériel : 7 août 2006

Présentée par

Thi Kieu Oanh Doan

Thèse dirigée par **Lucia Di Ciaccio**
codirigée par **Theodore Todorov**

préparée au sein du **LAPP**
dans **l'École Doctorale de Physique, Grenoble**

Mesure de la section efficace différentielle de production du boson Z se désintégrant en paires électron-positon, dans l'expérience ATLAS

Thèse soutenue publiquement le **« 28 Novembre 2012 »**,
devant le jury composé de :

M. Daniel Froidevaux
European Organiz. for Nuclear Res. (CH), Rapporteur
M. Maarten Boonekamp
CEA - Centre d'Etudes de Saclay (FR), Rapporteur
M. Terence Richard Wyatt
University of Manchester (UK), Examinateur
M. Yannis Karyotakis
Centre National de la Recherche Scientifique (FR), Examinateur
Mme. Lucia Di Ciaccio
Centre National de la Recherche Scientifique (FR), Directeur de thèse
M. Theodore Todorov
Centre National de la Recherche Scientifique (FR), CoDirecteur de thèse

Membre invité:

M. Vincenzo Lombardo
Centre National de la Recherche Scientifique (FR)

Université Joseph Fourier / Université Pierre Mendès France /
Université Stendhal / Université de Savoie / Grenoble INP

Acknowledgements

I would like to use the first sentence in my thesis to say my gratefulness to my supervisors Lucia Di Ciaccio and Theodore Todorov for their supervising of my thesis and their patience to teach me in the first days of my PhD. I was lucky to have a chance to work with Isabelle Wingerter-Seez. I am grateful to her advices during my technical study which was a good starting of my thesis. I would like to thank Corinne Goy and Michel Lefebvre for their discussions of our analysis, and especially Emmanuel Sauvan and Vincenzo Lombardo who have followed my work up to the date of my thesis defense.

A very special thanks is to Patrick Aurenche, Sandrine Laplace, Nguyen Anh Ky and Vu Anh Tuan. They encouraged me to continue my study career. Patrick Aurenche is like my father in France. With Bui Thi Thu Thuy and Nguyen Nam Anh they are like my big family in France. I could not get these happy days without their help.

I am thankful all people at Lapp, especially Yannis Karyotakis and Jean-Pierre Lees for their help to find the financial support for my study here as well as for the good work conditions I could have to finish my PhD. I thank also the Lapp secretaries, especially Chantal Vallee for her help with all official papers for my life in France.

I would like to thank all members of the jury, Daniel Froidevaux, Maarten Boonekamp and Terence Richard Wyatt for their valuable comments and discussions during the finalization of my thesis. I am thankful Zbigniew Andrzej Was for his kindly discussions of our analysis.

An acknowledgement is to CERN, the LHC and the ATLAS experiment which are the biggest collaborations I have known in my life. I did have an opportunity to work and discuss with many people from all of the world. My knowledge is improved by learning from them.

I will never forget everybody in my group at Lapp, the ATLAS group: Stephane Jezequel, Nicolas Berger, Tetiana Berger-Hryn'Ova, Jessica Leveque, Marco Delmastro, Remi Lafaye, Helenka Przysiezniak, Sabine Elles and others. They are so warm and so nice. From each of them I always could find

somethings interesting to learn. A special thanks to all of them. I would like to thank also all my friends at Lapp: Mayuko Kataoka, Ludovica Aperio-Bella, Maud Schwoerer, Elisabeth Petit, Dimitra Tsionov, Louis Helary, Olivier Arnaez, Mathieu Aurousseau and other students. They helped me pass many difficult days.

A special thanks is to my Vietnamese friends including Nguyen Thi Hong Van, Nguyen Chi Linh and Nguyen Ngoc Quynh Mai. They make me feel that my country is always in my heart.

I am grateful to my family in Vietnam. Even if they have never been with me in France, I feel their love every day. A special love is for my mother who I admire all my life. I could cry with her hours when I felt so lonely.

Finally is my love for my small family: my husband and my baby. From the time I knew him, from the time I had her, they are beside me each second. Their love is the biggest encouragement for me.

Contents

Introduction

There are several reasons to study the Z and W bosons at LHC. The understanding of weak vector boson production tests the Standard Model predictions and is necessary to maximize the sensitivity to new physics at hadron colliders. Moreover, the W and Z boson productions play an important role in the calibration of the ATLAS (A Toroidal LHC ApparatuS) detector.

The focus of my thesis work is on the study of a new variable which addresses the same physics issues as the Z transverse momentum (p_T^Z). The relatively large cross section at LHC of the Z production decaying into lepton pairs and its very low background enable a precise measurement of p_T^Z which gives a very sensitive way of studying dynamical effects of the strong interaction, complementary to measurements of the associated production of the bosons with jets. At large p_T^Z (greater than approximately 30 GeV), the radiation of a single parton with large transverse momentum dominates the cross section, and fixed-order perturbative Quantum chromodynamics (pQCD) calculations yield reliable predictions. So this measurement provides an ideal testing of pQCD. At lower p_T^Z, pQCD no longer gives accurate results due to the emission of multiple soft gluons. This fact has been solved in two ways: by using resummation to all orders up to next-to-next-to-leading logarithms (NNLL) in α_s, or by modeling with parton showers. For such reasons, this measurement is important in tuning Monte Carlo generators.

Many studies showed that there is an optimized variable which is less sensitive to the experiment resolution, and probes the same physics as p_T^Z. The precise measurement using this optimized variable will allow to test a very small effect like the small-x broadening of the p_T^Z distribution which takes into account the parton momentum fraction dependence in the resummation form factor. My thesis will show the result for the differential cross section of the Z boson as a function of the new variable ϕ_η^* in comparison with different theoretical predictions and with different Monte Carlo generators.

The thesis is organized in 6 chapters. Chapter 1 is devoted to a theoretical review. The predictions from QCD calculations and from different Monte Carlo generators of the p_T^Z spectrum and the ϕ_η^*

spectrum of the Z boson are presented. The general structure of the LHC and the ATLAS detector is introduced in Chapter 2. Their operation parameters at 7 TeV collisions are shown. Chapter 3 introduces the event reconstruction in the ATLAS experiment. A technical study performed by the author is presented here. Chapter 4 is dedicated to the event reconstruction of the Z boson decaying into a pair of electron and positron. The treatments for the different effects such as the multiple interactions in proton-proton collisions, the mis-modeling of the p_T^Z spectrum in data by the Monte Carlo generators are discussed. Most of the work in this chapter concentrates on the QCD background estimation. The differential cross section measurement of the Z boson as a function of ϕ_η^* is presented in Chapter 6. The result of this measurement is precise at the per mil level. The unfolded ϕ_η^* spectrum in data is compared with many predictions that will help for the future tuning of Monte Carlo generators. In order to express the complementarity of the ϕ_η^* measurement with respect to the p_T^Z measurement, the p_T^Z measurement is also done in my thesis and is presented in Chapter 5.

Il y a plusieurs raisons d'étudier les bosons Z et W au LHC. La compréhension de la production des bosons vecteurs faibles teste les prédictions du Modèle Standard et elle est nécessaire pour maximiser la sensibilité à la nouvelle physique. En outre, la production des bosons Z et W joue un rôle important dans l'étalonnage d'ATLAS (A Toroidal LHC ApparatuS).

Mon travail de thèse porte sur l'étude d'une nouvelle variable qui caractérise la même physique que la distribution en impulsion transverse du boson Z (p_T^Z*). Le section efficace relativement importante de production du Z se désintégrant en paire de leptons et son fond très faible mène à une mesure précise de* p_T^Z *ce qui permet de faire une étude très sensible de la dynamique des interactions fortes, complémentaire de la mesure de la production de bosons avec des jets. En général pour* $p_T^Z \gtrsim 30$ *GeV, le mécanisme de production est dominé le rayonnement d'un parton unique avec grande impulsion transverse et les calculs de QCD perturbatif à ordre fixé (pQCD) donnent des prédictions fiables. Cette mesure fournit donc un test idéal de pQCD. Pour les petits* p_T^Z*, inférieurs à 30 GeV, QCD perturbatif à ordre fixé ne s'applique pas en raison de l'émission multiple de gluons mous. Ce problème a été résolu de deux manières: d'une part en resommant à tous les ordres, l'émission de gluons mous à l'approximation "next-to-next-to leading logarithms" (NNLL), d'autre part par la modélisation des "parton showers" à l'aide de codes Monte Carlo qui seront fortement contraints par la mesure du spectre en impulsion transverse du Z.*

De nombreuses études ont montré qu'il existe une variable optimisée qui est moins sensible à la résolution expérimentale que la variable p_T^Z *mais qui sonde la même physique qu'elle. La mesure précise de la distribution en cette variable optimisée permettra de tester un effet très faible comme celui de l'élargissement à petit x de la distribution en* p_T^Z *qui prend en compte la dépendance en impulsion des partons initiaux dans le facteur de forme de la resommation. Dans cette thèse, je présente la mesure de la section efficace diférentielle du boson Z en fonction de cette nouvelle variable* ϕ_η^* *ainsi que la comparaison à diférentes prédictions théoriques et différents générateurs Monte Carlo.*

La thèse est organisée en 6 chapitres. Le chapitre 1 est consacré à l'examen théorique des différentes prédictions des calculs QCD et des générateurs Monte Carlo: on y présente les prdictions pour le spectre en p_T^Z *et* ϕ_η^* *de cette différentes approches. La structure générale du LHC et du détecteur ATLAS est introduite dans le chapitre 2 et les paramètres de fonctionnement à 7 TeV sont également donnés. Dans le chapitre 3 on s'intéresse à la reconstruction des évènements dans l'expérience ATLAS. Une étude technique réalisée par l'auteur est présentée ici. Le chapitre 4 est consacré à la reconstruction* *des évènements Z où le boson se désintègre en une paire electron-positon. Le traitement de différents effets tels que les interations multiples dans les collisions proton-proton ou la mauvaise modélisation du spectre en* p_T^Z *donnée par les générateurs Monte Carlo sont discutés. La plupart des travaux dans ce chapitre se concentre sur l'estimation du fond QCD. La mesure de la section efficace différentielle du boson Z en fonction de* ϕ_η^* *est présentée dans le chapitre 6. Le résultat de cette mesure atteint la précision du pour mille. Les données du spectre en* ϕ_η^* *sont comparées à de nombreuses prédictions ce qui aidera à l'ajustement futur des générateurs Monte Carlo. Pour montrer la complémentarité des mesures en* ϕ_η^* *et* p_T^Z*, je présente dans la chapitre 5 la mesure du spectre en* p_T^Z*.*

Chapter 1

Theoretical review

The theoretical knowledge of the Z boson properties and its transverse momentum, p_T^Z, presented in this chapter will be the guideline for the experimental measurements concerning p_T^Z. In this chapter, Section 1.1 will introduce the Standard Model as a unified theory of electroweak and strong interactions. The Z boson properties and its interactions with the other particles in the context of the Standard Model are reviewed as well. Section 1.2 will be devoted to the presentation of p_T^Z predictions in different approximations of Quantum Chromodynamics. Section 1.3 will introduce the optimization of new variables which address the same physics issues as p_T^Z.

1.1 Standard Model

The Standard Model (SM) of particle physics describes the properties and interactions of the fundamental particles. These are classified as bosons, which transmit the forces, or fermions, which form the matter.

The fundamental fermions are divided into two main groups: the quarks and the leptons. The quarks interact among each other with the strong and electroweak force. The strong interaction makes them non observable in nature as isolated particles, but combined to form hadrons, a phenomenon called confinement. Hadrons may be mesons ($q\bar{q}$, where q represents a quark and $\bar{q}$ an anti-quark), or baryons (qqq, or $\overline{qqq}$). The charged leptons interact among each other with the electromagnetic and weak forces. Finally, the neutral leptons, the neutrinos, interact only via the weak force.

There are twelve gauge bosons which correspond to the three forces in the SM: eight gluons mediate the strong force, the massive $W^{\pm}$ and Z bosons mediate the weak force while the electromagnetic force is mediated by the photon (γ). In oder to explain the fundamental forces, the SM structure is described by the gauge symmetry group $SU(3) \otimes SU(2)_L \otimes U(1)_Y$. $SU(3)$ is the symmetry of the strong force. The weak force is described by the group $SU(2)_L$, where L indicates that it only acts on chirally left-handed particles. $U(1)_Y$ is similar to the $U(1)$ symmetry of Quantum electrodynamics (QED), but acts on particles with the weak hypercharge Y.

The complete particle content of the Standard Model is listed in Table 1.1 where the fermions come in three generations. The charged leptons and quarks in the second and third generations are more massive than those in the first, and are unstable. Conventional matter is thus made entirely of fermions from the first generation.

Fundamental particles		Generation		
		1	2	3
Fermions (f)	Leptons(l, ν)	e	μ	τ
		ν_e	ν_μ	ν_τ
	Quarks(q)	u	c	t
		d	s	b
Bosons (V)	Electroweak	W, Z, γ		
	Strong	g		

Table 1.1: Fundamental particles in the SM.

1.1.1 Electroweak theory

1.1.1.1 Gauge invariance and origin of gauge boson masses

The Lagrangian describing the electroweak interactions of fermions in the SM is required to be invariant under the local gauge transformation (a unitary transformation in the $SU(2)_L \otimes U(1)_Y$ space):

$$\begin{aligned} \psi_L &\rightarrow \exp\Big[-i\Big(\frac{g'}{2}Y\theta'(x) + g\boldsymbol{I}.\boldsymbol{\theta}(x)\Big)\Big]\psi_L, \\ \psi_R &\rightarrow \exp\Big[-i\Big(\frac{g'}{2}Y\theta'(x)\Big)\Big]\psi_R, \end{aligned} \tag{1.1}$$

where $\theta'(x)$ and $\boldsymbol{\theta}(x)$ are abitrary functions of space-time, g and g' are coupling constants, Y is the hypercharge and $\boldsymbol{I}$ are the Pauli matrices. The matrices $\boldsymbol{I}$ satisfy the commutation relations $[I_i, I_j] = i\varepsilon_{ijk}I_k$, making this a non-Abelian theory. The left-handed fermions are organized in $SU(2)_L$ doublets. The right-handed fermions are singlets of $SU(2)_L$.

The fermions are supposed to be massless and the Lagrangian for free fermions is written as

$$\mathscr{L}_{free} = i\overline{\psi}_L\gamma^\mu\partial_\mu\psi_L + i\overline{\psi}_R\gamma^\mu\partial_\mu\psi_R, \tag{1.2}$$

where $\overline{\psi} = \psi^\dagger\gamma_0$. The Lagrangian in 1.2 is invariant under the gauge transformation 1.1 if the derivative ∂_μ is replaced by a covariant derivative introducing new degrees of freedom interpreted as boson fields:

$$\begin{aligned}\mathscr{D}_{L\mu} &= \partial_\mu + i\frac{g'}{2}YB_\mu + ig\boldsymbol{I}.\boldsymbol{W}_\mu,\\ \mathscr{D}_{R\mu} &= \partial_\mu + i\frac{g'}{2}YB_\mu.\end{aligned} \tag{1.3}$$

To satisfy the gauge invariance, the new fields (the gauge fields) $\boldsymbol{W}_\mu$ and B_μ must transform as:

$$\begin{aligned}\boldsymbol{W}_\mu &\rightarrow \boldsymbol{W}_\mu + \partial_\mu\boldsymbol{\theta}(x) + g\boldsymbol{\theta}(x)\wedge\boldsymbol{W}_\mu,\\ B_\mu &\rightarrow B_\mu + \partial_\mu\theta'(x),\end{aligned} \tag{1.4}$$

The electroweak Lagrangian including kinetic terms of the gauge fields now is:

$$\mathscr{L}_{EW} = i\overline{\psi}_L\gamma^\mu\mathscr{D}_\mu\psi_L + i\overline{\psi}_R\gamma^\mu\mathscr{D}_\mu\psi_R - \frac{1}{4}\boldsymbol{W}_{\mu\nu}.\boldsymbol{W}^{\mu\nu} - \frac{1}{4}B_{\mu\nu}B^{\mu\nu}, \tag{1.5}$$

where

$$\begin{aligned}\boldsymbol{W}_{\mu\nu} &= \partial_\mu\boldsymbol{W}_\nu - \partial_\nu\boldsymbol{W}_\mu - g\boldsymbol{W}_\mu\wedge\boldsymbol{W}_\nu,\\ B_\mu &= \partial_\mu B_\nu - \partial_\nu B_\mu.\end{aligned} \tag{1.6}$$

The B_μ field could represent the electromagnetic field but $\boldsymbol{W}_\mu$ can not directly describe the weak force, a short-range force which requires massive bosons, since the appearance of a mass term would destroy the gauge invariance of the Lagrangian. This problem was solved by introducing the Higgs mechanism. This mechanism spontaneously breaks the $SU(2)_L \otimes U(1)_Y$ symmetry through the action of an $SU(2)_L$ doublet of complex scalar fields:

$$\phi(x) = \frac{1}{\sqrt{2}}\begin{pmatrix}\phi_1(x) + i\phi_2(x)\\ \phi_3(x) + i\phi_4(x)\end{pmatrix} \tag{1.7}$$

The Lagrangian of this field includes a potential term:

$$\mathscr{L}_{Higgs} = \mathscr{D}_{L\mu}\phi^\dagger\mathscr{D}_L^\mu\phi - V(\phi), \tag{1.8}$$

where

$$V(\phi) = -\mu^2\phi^\dagger\phi + \lambda(\phi^\dagger\phi)^2. \tag{1.9}$$

If $\mu^2 > 0$ and $\lambda > 0$, the potential $V(\phi)$ has a minimum at $| < 0|\phi|0 > | = v/\sqrt{2}$ where $v = \sqrt{\mu^2/\lambda}$. This ground state is highly degenerate, with an infinite number of solutions which differ by a phase. Choosing a phase (ϕ real for example) gives rise to three massless Goldstone bosons, which can be eliminated through a suitable choice of gauge. A fourth massive scalar boson, the Higgs boson, $H(x)$, arises from a vacuum excitation. The field ϕ may now be written as

$$\phi(x) = \frac{1}{\sqrt{2}} \begin{pmatrix} 0 \\ v + H(x) \end{pmatrix}. \tag{1.10}$$

Inserting this expression into Equation 1.8 gives mass terms involving the $\boldsymbol{W}_\mu$ and B_μ fields, through a mechanism which respects the local gauge invariance of the Lagrangian:

$$\mathscr{D}_{L\mu}\phi^\dagger \mathscr{D}_L^\mu \phi \supset \frac{g^2 v^2}{4} W_\mu^+ W^{-\mu} + \frac{1}{2}\frac{(g^2 + g'^2)v^2}{4} Z_\mu Z^\mu \tag{1.11}$$

where the physical electroweak bosons (the mass and charge eigenstates) can be written as:

$$\begin{aligned} W^{+\mu} &= \frac{W_1^\mu + iW_2^\mu}{\sqrt{2}} \\ W^{-\mu} &= \frac{W_1^\mu - iW_2^\mu}{\sqrt{2}} \\ Z^\mu &= \cos\theta_W W_3^\mu - \sin\theta_W B^\mu \\ A^\mu &= \sin\theta_W W_3^\mu + \cos\theta_W B^\mu. \end{aligned} \tag{1.12}$$

The angle $\theta_W = \tan^{-1}(g'/g)$ is a parameter of the theory, and describes the mixing between the weak bosons W_3^μ and B^μ. The W and Z boson masses are given by

$$\begin{aligned} M_W &= \frac{gv}{2} \\ M_Z &= \frac{\sqrt{g^2 + g'^2}}{2} v. \end{aligned} \tag{1.13}$$

The masses of fermions can also be generated by the Higgs boson, if it couples to each of them with a strength proportional to its mass.

1.1.1.2 The Z couplings

The couplings of the physical bosons can be obtained by combining Equation 1.12 with Equation 1.5. The W couples only to left-handed fermions. Its coupling constant, g, is related to the Fermi constant for low energy weak interactions (G_F) by

$$\frac{G_F}{\sqrt{2}} = \frac{g^2}{8M_W^2}. \tag{1.14}$$

The photon couples equally to left and right-handed fermions. The charged fermion-photon coupling strength (e) is known from QED. In terms of electroweak parameters, this is given by

$$e = g\sin\theta_W = g'\cos\theta_W. \tag{1.15}$$

The Z, like the photon, couples to both left and right-handed fermions, but with a different strength to each:

$$\begin{aligned} g_L &= I_3 - Q\sin^2\theta_W \\ g_R &= -Q\sin^2\theta_W, \end{aligned} \tag{1.16}$$

where Q is the fermion charge and I_3 is the third component of weak isospin. This is sometimes expressed in terms of a vector coupling (c_V) and an axial coupling (c_A):

$$\begin{aligned} c_V &= g_L + g_R \\ c_A &= g_L - g_R. \end{aligned} \tag{1.17}$$

The Z couplings are summarised in Table 1.2.

Fermions	Q	I_3	g_L	g_R
ν_e, ν_μ, ν_τ	0	$\frac{1}{2}$	$\frac{1}{2}$	0
e^-, μ^-, τ^-	-1	$-\frac{1}{2}$	$-\frac{1}{2}+\sin^2\theta_W$	$\sin^2\theta_W$
u, c, t	$\frac{2}{3}$	$\frac{1}{2}$	$\frac{1}{2}-\frac{2}{3}\sin^2\theta_W$	$-\frac{2}{3}\sin^2\theta_W$
d, s, b	$-\frac{1}{3}$	$-\frac{1}{2}$	$-\frac{1}{2}+\frac{1}{3}\sin^2\theta_W$	$\frac{1}{3}\sin^2\theta_W$

Table 1.2: The Z couplings in the electroweak theory [65].

1.1.1.3 The branching ratios

The interaction between matter and gauge fields in the electroweak theory are described by the vertices shown in Figure 1.1. In the Standard Model, there are 3 generations of leptons and 3 generations of quarks (see Table 1.1), and each quark flavor carries 3 colors. The W boson couples with the same strength to all fermion pairs of an SU(2) doublet. However, because the top quark is heavier than the W and Z bosons, these bosons do not decay to top quarks. Therefore neglecting fermion masses each leptonic decay mode of the W boson will have a branching ratio $1/9$. For Z boson, the branching fractions are proportional to $(c_V^2 + c_A^2)$ in which c_V and c_A are obtained from formulas in 1.17 and Table 1.2. The predicted branching ratios of various W and Z decay modes are summarised in Table 1.3 [72].

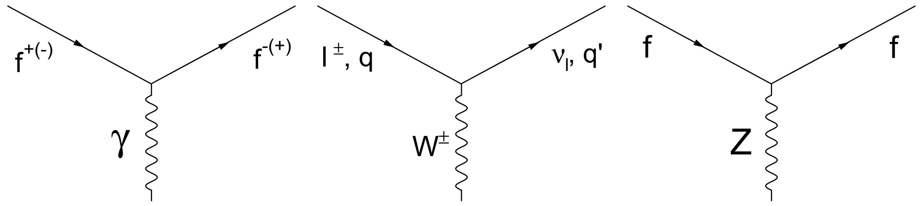

(a) $-iQ\gamma^{\mu}$ (b) $-i\frac{g}{\sqrt{2}}\gamma^{\mu}\frac{1-\gamma^5}{2}$ (c) $-i\frac{g}{\cos\theta_W}\gamma^{\mu}\frac{c_V - c_A\gamma^5}{2}$

Figure 1.1: The gauge boson-fermion vertex factors in the electroweak theory. The factors with (γ^{μ}) are vector couplings (V) and the factors with ($\gamma^{\mu}\gamma^5$) are axial-vector (A) couplings.

Decay mode	Branching ratio (%)
$W^+ \to \ell^+\nu_\ell, (l = e, \mu, \tau)$	11.1
$W^+ \to \bar{d}u(\bar{s}c)$	33.3
$Z \to \ell^+\ell^-, (l = e, \mu, \tau)$	3.4
$Z \to \nu_\ell\nu_\ell, (l =\text{e}, \mu, \tau)$	6.8
$Z \to q\bar{q}, (q = d, s, b)$	15.2
$Z \to q\bar{q}, (q = u, c)$	11.8

Table 1.3: Expected branching ratios of W and Z bosons decays [72].

Table 1.3 shows that the charged lepton decay modes of the W and Z bosons have the smallest branching ratios. Nevertheless they are used as signatures of the production of weak bosons in experiments due to low backgrounds coming from Quantum Chromodynamics processes.

1.1.2 The theory of strong interactions

The strong nuclear force is described in the Standard Model by the theory of Quantum Chromodynamics (QCD) [72].

1.1.2.1 The Lagrangian of QCD

The basic symmetry group of QCD is SU(3). This symmetry remains unbroken in nature, meaning that gluons are massless, like the photon. The symmetry group SU(3) has eight generators, referred to as $\boldsymbol{T}$, corresponding to the eight gluons of the theory. The three dimensions involve three charges, called colour. Therefore, the elements of $\boldsymbol{T}$, denoted T_a, $a = \{1-8\}$, are represented as 3×3 matrices in the colour space. As with the elements of $\boldsymbol{I}$ in SU(2), these elements do not commute:

$$[T_a, T_b] = i f_{abc} T_c, \tag{1.18}$$

where f_{abc} denotes one element of a $8 \times 8 \times 8$ array of structure constants. The quark fields ψ_q are SU(3) triplets, which transform under a rotation in colour space:

$$\psi_q \rightarrow \exp[-i g_s \boldsymbol{T}.\boldsymbol{\theta}(x)] \psi_q, \tag{1.19}$$

where g_s is the strong coupling. The transformation in Equation 1.19 modifies the free-fermion Lagrangian. Invariance of the Lagrangian under the local SU(3) gauge transformation can be achieved by the introduction of an eight-component vector boson field $\boldsymbol{G}$. These fields transform as follows:

$$G_{a\mu} \rightarrow G_{a\mu} + \partial_\mu \theta_a(x) + g_s f_{abc} \theta_b(x) G_{c\mu}, \tag{1.20}$$

with an appropriate covariant derivative:

$$\mathscr{D}_\mu = \partial_\mu + i g_s \boldsymbol{T}.\boldsymbol{G}_\mu. \tag{1.21}$$

The QCD Lagrangian can then be written:

$$\mathscr{L}_{QCD} = i\overline{\psi}_q \gamma^\mu \mathscr{D}_\mu \psi_q - m_q \overline{\psi}_q \psi_q - \frac{1}{4} \boldsymbol{G}_{\mu\nu}.\boldsymbol{G}^{\mu\nu}, \tag{1.22}$$

where the first two terms are to be summed over all quark flavours, The gluon kinetic tensor $\boldsymbol{G}_{\mu\nu}$ has the form below:

$$G_{a\mu\nu} = \partial_\mu G_{a\nu} - \partial_\nu G_{a\mu} - g_s f_{abc} G_{b\mu} G_{c\nu}. \tag{1.23}$$

Again, the non-Abelian nature of this interaction gives rise to self-coupling terms, meaning that gluons will couple to gluons. This has some important consequences for the QCD phenomenology.

1.1.2.2 Running coupling constant

We consider as an example a dimensionless physical observable R which depends on a single energy scale Q. In a renormalizable quantum field theory, when we calculate R as a perturbation series in the coupling $\alpha_s = g_s^2/4\pi$, (defined in analogy with the fine structure constant of QED), the perturbation series requires a renormalization procedure to remove ultraviolet divergences. This procedure requires introducing a second mass scale, μ, and R depends in general on the ratio Q^2/μ^2 and is therefore not constant. It follows that the renormalized coupling α_s depends on the choice made for the subtraction point μ. However μ is an arbitrary parameter and physical quantities such as R cannot depend on the choice made for μ and can only depend on the ratio Q^2/μ^2 and the renormalized coupling α_s following a Callan-Symanzik equation [97]. The solution of this equation shows that all of the scale dependence in R enters through the running of the coupling constant $\alpha_s(Q^2)$. The running of the coupling constant α_s is determined by the renormalization group equation:

$$Q^2 \frac{\partial \alpha_s}{\partial Q^2} = \beta(\alpha_s). \tag{1.24}$$

In QCD, the β function has the perturbative expansion (at the first order):

$$\beta(\alpha_s) = -b\alpha_s^2, \tag{1.25}$$

where

$$b = \frac{33 - 2n_f}{12\pi}, \tag{1.26}$$

and $n_f = 6$ is the number of quark flavours. These equations give the solution:

$$\alpha_s(Q^2) = \frac{\alpha_s(\mu^2)}{1 + \alpha_s(\mu^2) b \ln(Q^2/\mu^2)}. \tag{1.27}$$

Because the renormalized coupling $\alpha_s(\mu^2)$ depends on the choice of the renormalization scale μ, the equation 1.27 can be written in a simpler way by choosing $\mu = \Lambda_{QCD}$ with $\Lambda_{QCD} \sim 200$ MeV [97]:

$$\alpha_s(Q^2) = \frac{12\pi}{(33 - 2n_f) \ln(Q^2/\Lambda_{QCD}^2)}. \tag{1.28}$$

The equation 1.28 shows two consequences of the running coupling constant:

Asymptotic freedom: $\alpha_s(Q^2) \to 0$ as $Q^2 \to \infty$ which implies that at very high energy regimes or at short distances, quarks and gluons appear like almost free particles. The prediction of this QCD property was made in 1973 by D. Politzer, D. Gross and F. Wilczek and brought them the 2004 Nobel prize in physics.

Confinement: $\alpha_s(Q^2) \to \infty$ as $Q^2 \to \Lambda^2_{QCD}$, which implies that quarks are always confined inside hadrons and they can never be found as free (unbounded) states.

1.2 The transverse momentum predictions of the Z boson at hadron colliders

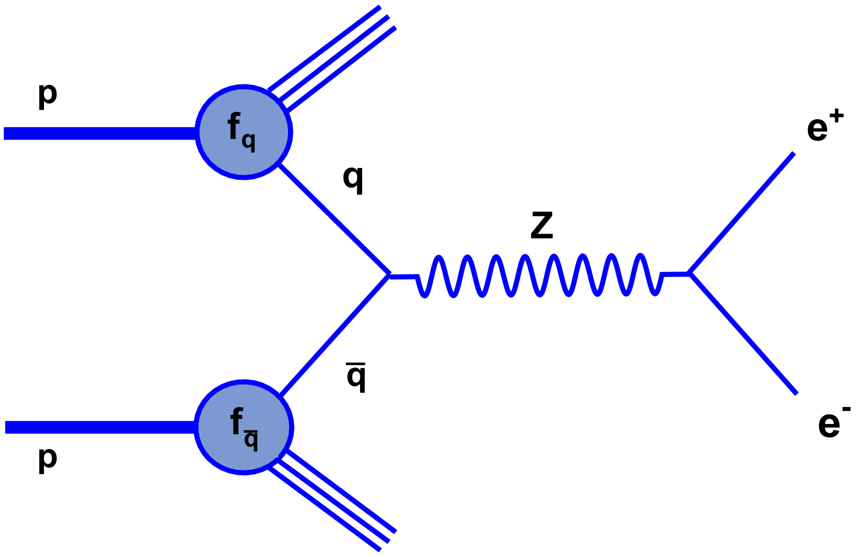

Figure 1.2: The Z boson decaying to electron and positron at proton-proton collisions.

In high energy proton-proton collisions at the tree level, the Z boson is produced in the Drell-Yan process [71] in which a quark and an antiquark annihilate into a weak boson which decays into a lepton pair as in Figure 1.2. The hadronic cross section $\sigma(AB \to X)$ of the process can be obtained by weighting the subprocess cross section $\hat{\sigma}$ for $q\bar{q} \to X$ with the parton distribution functions (pdfs) f_q extracted from deep inelastic scattering:

$$\sigma_{AB} = \sum_{ab} \int dx_a dx_b f_a(x_a, Q^2) f_b(x_b, Q^2) \hat{\sigma}_{ab\to X}, \tag{1.29}$$

where in this case $A, B = proton$, $ab = q\bar{q}$, $\bar{q}q$, $X = Z(\ell^+\ell^-)$ and Q^2 is the virtuality of the Z boson. $\hat{\sigma}$ describes the hard parton-parton cross section with a partonic center-of-mass energy squared $\hat{s} = x_a x_b s$ (s is the center-of-mass energy squared of the collider, x_a, x_b are parton momentum fractions) and has the complete form in the perturbative expansion as below:

$$\hat{\sigma}_{ab\to X} = [\hat{\sigma}_0 + \alpha_s(\mu_R^2)\hat{\sigma}_1 + ...]_{ab\to X}, \tag{1.30}$$

where μ_R is the renormalization scale for the QCD running coupling constant α_s. At the lowest order (Leading Order - LO), the subprocess cross section for on-shell Z boson production can be expressed as below [59]:

$$\hat{\sigma}^{q\bar{q}\to Z} = \frac{\pi}{3}\sqrt{2} G_F M_Z^2 (c_{Vq}^2 + c_{Aq}^2)\delta(\hat{s} - M_Z^2), \tag{1.31}$$

where G_F is the Fermi constant, and c_{Vq}, c_{Aq} is the vector and axial couplings (see 1.17) of the Z to the quarks. This formula is valid in the narrow width production in which the decay width of the gauge boson is neglected. The resulting cross section can then be multiplied by the branching ratio for any particular hadronic or leptonic final state of interest.

1.2.1 The high p_T^Z predictions

At the leading order of the cross section the colliding partons are assumed to be exactly collinear with respect to the colliding beam particles, therefore the gauge bosons are produced with zero transverse momentum. At higher orders, the transverse momentum of Z generated is balanced by a recoiling hadronic system mainly arising from initial state QCD radiation of quarks and gluons. The differential cross section has the form [38]:

$$\frac{d\sigma}{dp_T^2} = \alpha_w \alpha_s (u_1 + u_2 \alpha_s + u_3 \alpha_s^2 + ...), \tag{1.32}$$

where $\alpha_w = \sqrt{2} G_F M_Z^2/\pi$ and the $u_i (i = 1, 2, ...)$ are calculable expressions in perturbation theory. Examples of processes that are in the 1st-order in α_s are shown in Figures 1.3(a) 1.3(b). At the 2nd-order, one may either produce an extra jet, such as in Figure 1.3(c), or consider the interference of the 1st-order in α_s process of Figure 1.3(a) with one-loop corrections such as Figure 1.3(d) [38].

The form of Equation 1.32 depends on the range of p_T^Z. In the high p_T^Z region ($p_T^Z > M_Z/2$), the contribution of higher α_s orders in 1.32 decreases quickly and a fixed order calculation is thus valid to

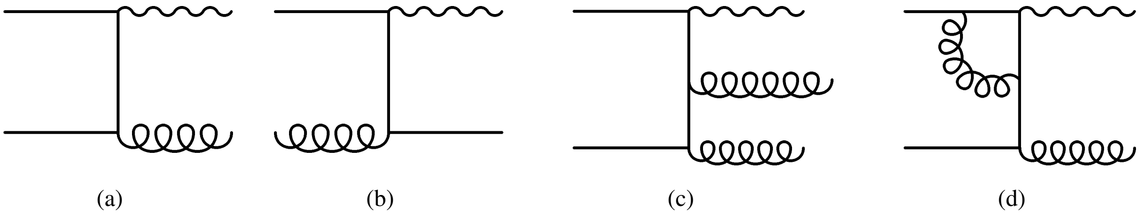

Figure 1.3: Examples of processes at the 1st-order (a,b) and 2nd-order (c,d) of α_s.

describe the p_T^Z distribution. At the 1st order in α_s, which is the next-to-leading order (NLO) of the cross section, the differential cross section has the form ($Q = M_Z$) [72]

$$\frac{d\sigma}{dp_T^2} = \alpha_s\Big(A\frac{\ln(Q^2/p_T^2)}{p_T^2} + B\frac{1}{p_T^2} + C(p_T^2)\Big). \tag{1.33}$$

Currently, the highest available order of the total cross section predictions is the next-to-next-to-leading order (NNLO) which corresponds to a NLO prediction for p_T^Z. The complete calculations to NNLO perturbative corrections for W and Z boson production at high p_T can be found in [37, 79]. Results from NLO and NNLO corrections for the total cross section showed that NLO corrections provide a large increase to the cross section but do not reduce the scale dependence relative to leading order (LO). NNLO corrections, although they are small, significantly reduce the scale dependence thus providing a more stable theoretical prediction.

The predicted cross sections of different processes at NLO, including W and Z boson productions, are shown in Figure 1.4 as a function of $\sqrt{s}$.

NLO and NNLO calculations are included in several programs as FEWZ [75, 76, 91], RESBOS [40, 103], MCFM [58], DYNNLO [60]. In this analysis, we use FEWZ and RESBOS programs to produce the theoretical predictions for the p_T^Z spectrum in this region, details will be discussed in Section 1.2.3. These predictions will be compared with our measurement of the p_T^Z spectrum using the large amount of data collected by the ATLAS detector in 2011.

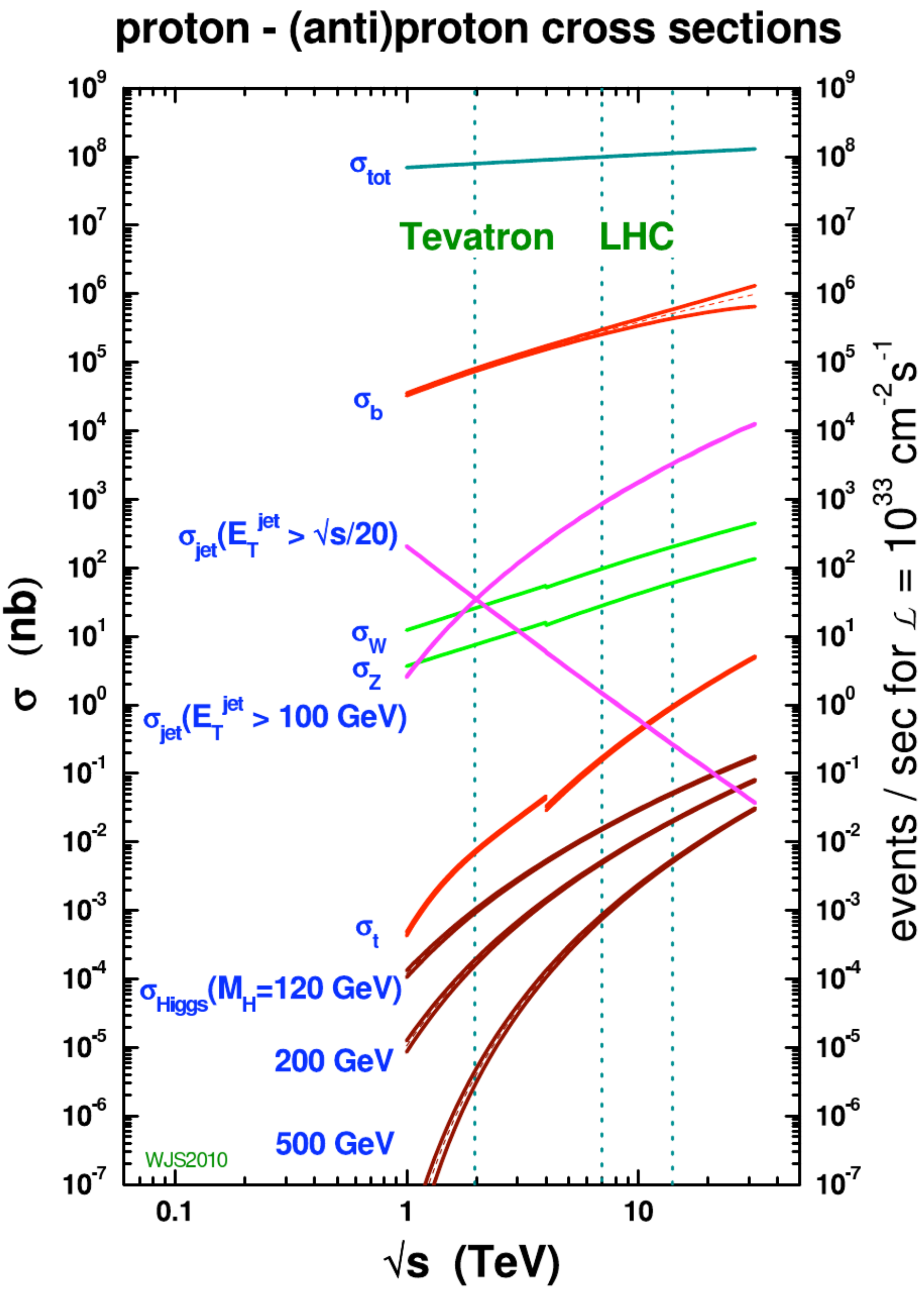

Figure 1.4: Cross sections for different processes in hadron colliders as a function of centre-of-mass energy. The centre-of-mass energy of the Tevatron and the current as well as the foreseen energy of the LHC are presented with dotted lines. The break points in the curves correspond to the difference in the estimated cross sections between proton-proton (LHC) and proton-antiproton (Tevatron) production [51].

1.2.2 The low p_T^Z predictions

1.2.2.1 The transverse momentum resummation

At low p_T, the convergence of the perturbation series deteriorates due to multiple soft gluon emissions. The dominant contributions to Equation 1.32 have the form ($Q = M_Z$) [38]

$$\frac{d\sigma}{dp_T^2} \sim \frac{\alpha_w \alpha_s}{p_T^2} \ln\left(\frac{Q^2}{p_T^2}\right)\left[v_1 + v_2 \alpha_s \ln^2\left(\frac{Q^2}{p_T^2}\right) + v_3 \alpha_s^2 \ln^4\left(\frac{Q^2}{p_T^2}\right) + \ldots\right], \tag{1.34}$$

where the $v_i[i = 1,2,\ldots]$ are calculable coefficients. This is known as the leading-logarithm approximation to $d\sigma/dp_T^2$. At sufficiently low p_T, $\alpha_s \ln^2(Q^2/p_T^2)$ will be large even when α_s is small. By placing an arbitrarily small cut on p_T, one can still obtain an arbitrarily large cross section. Because of this unphysical result, the cross section can not be calculated accurately in any fixed perturbative order of perturbation theory. However the coefficients v_i of Equation 1.34 are not independent and it is possible to sum the series exactly even when $\alpha_s \ln^2(Q^2/p_T^2)$ is large. The result of summing at the leading-logarithm approximation can be performed in b-space which is the Fourier conjugate of p_T-space [38]:

$$\frac{d\sigma}{dp_T^2 dy} = \frac{4\pi^3 \alpha_w}{3s} e^2 \int \frac{d^2b}{(2\pi)^2} e^{ib.p_T} exp\left[-\frac{1}{2}\left(\frac{\alpha_s}{2\pi}\right) A^{(1)} \ln^2(b^2 Q^2)\right] f_a(x_a) f_b(x_b), \tag{1.35}$$

where y is the Z rapidity, e is the electron charge, $A^{(1)}$ is a numerical coefficient calculable from perturbation theory. This technique can be generalized to resum all terms of the perturbation series. It is called resummation and was carried out by Collins, Soper and Sterman (CSS) [64], who express the result in the form

$$\frac{d\sigma}{dp_T^2 dy} = \frac{4\pi^3 \alpha_w}{3s} e^2 \int \frac{d^2b}{(2\pi)^2} e^{ib.p_T} W(b), \tag{1.36}$$

$$W(b) = e^{-S(b)} (C \otimes f_a)(x_a; C_3^2/b^2)(C \otimes f_b)(x_b; C_3^2/b^2), \tag{1.37}$$

where $S(b)$ is the Sudakov form factor and has the form

$$S(b) = \int_{C_1^2/b^2}^{C_2^2 Q^2} \frac{dq^2}{q^2}\left[\ln\left(\frac{C_2^2 Q^2}{q^2}\right) A(\alpha_s(q^2)) + B(\alpha_s(q^2))\right]. \tag{1.38}$$

The parameters C_1, C_2, and C_3, are unphysical and arbitrary and can be chosen for convenient calculations, $S(b)$ and $C = C(x; \alpha_s(C_3^2/b^2))$ can be calculated order-by-order in perturbative QCD. Up to now, the highest available approximation of resummation is the next-to-next-to-leading logarithmic accuracy (NNLL) which is included in several programs as [55], RESBOS [40, 103]. In this analysis, we use the RESBOS program to produce the theoretical predictions for the p_T^Z spectrum in the low p_T^Z region. More details will be discussed in Section 1.2.3.

1.2.2.2 The non-perturbative function

In Equation 1.36 the variable b is integrated from 0 to ∞. When $b \gtrsim 1$ GeV^{-1}, the perturbative calculation for $W(b)$ is no longer reliable and complicated long distance physics comes in. Non-perturbative contributions to $W(b)$ can be approximated by some phenomenological model with measurable and universal parameters for Drell-Yan like processes. Collins, Soper and Sterman [64] suggested the introduction of the non-perturbative terms in the form of an additional factor $W_{NP}(b) = e^{-S_{NP}(b)}$, where $S_{NP}(b)$ is called the "non-perturbative Sudakov function" and satisfies $S_{NP} \to 0$ as $b \to 0$ and $S_{NP} \to \infty$ as $b \to \infty$. So $W(b)$ can be expressed in the new form

$$W(b) = W_{pert}(b_*)W_{NP}(b), \tag{1.39}$$

with

$$b_* = \frac{b}{\sqrt{1+(b/b_{max})^2}}. \tag{1.40}$$

In numerical calculations, b_{max} is typically set to be of order of 1 GeV^{-1}. The variable b_* never exceeds b_{max}, so that $W_{pert}(b_*)$ can be reliably calculated in perturbation theory for all values of b. In reference [64] it was found that the non-perturbative function can be generally written as

$$S_{NP}(b) = h_1(x_a,b) + h_1(x_b,b) + h_2(b)\ln Q^2, \tag{1.41}$$

The non-perturbative contribution is due to the long-distance effects that are incalculable at the present time so the parameters h_1 and h_2 must be extracted from the data with the constraint that

$$S_{NP}(b=0) = 0. \tag{1.42}$$

In reference [85] it is suggested to consider three different functional forms for $S_{NP}(b)$: the Davies-Webber-Stirling (DWS) form ($Q_0 = 1/b_{max}$)

$$\left[g_1 + g_2\ln\left(\frac{Q}{2Q_0}\right)\right]b^2; \tag{1.43}$$

the Ladinsky-Yuan (LY) form

$$\left[g_1 + g_2\ln\left(\frac{Q}{2Q_0}\right)\right]b^2 + [g_1 g_3\ln(100x_a x_b)]b; \tag{1.44}$$

and the Brock-Landry-Nadolsky-Yuan (BLNY) form

$$\left[g_1 + g_2\ln\left(\frac{Q}{2Q_0}\right) + g_1 g_3\ln(100x_a x_b)\right]b^2. \tag{1.45}$$

1.2.2.3 The small-x broadening effect

The resummation presented here is possible due to the collinear factorization of hadronic cross sections, valid when Q is not small compared to the total energy $\sqrt{s}$ of the hadronic collision. The CSS approach describes well the p_T distribution of the Z boson at the Tevatron [86]. In the range of energies accessible to the Large Hadron Collider (LHC) at the 7 TeV pp collisions, the typical fraction of the collision energy going into the production of moderately heavy bosons decreases leading to new effects. Transverse momentum distributions of W and Z bosons can be changed at small Born level parton momentum fractions x ($x \sim Q/\sqrt{s} \to 0$) by increased contributions from qg and gg hard scattering, which tends to produce electroweak bosons with larger transverse momenta as compared to the dominant process of $q\bar{q}$ scattering. The logarithms $\ln(1/x)$ in the matrix elements of order α_s^2 and beyond may be increased by a larger QCD coupling strength α_s at p_T less than a few GeV. Consequently, the non-perturbative contribution at $b \gtrsim 1$ GeV^{-1} may also depend on x. The magnitude of the x-dependent corrections to W and Z boson production at the LHC energy is unknown and expected to be tested using data collected at LHC.

Refs. [94, 96] have compared predictions of p_T resummation of semi-inclusive deep inelastic scattering (SIDIS) to the data for the transverse energy flow in the Hera experiment [24, 32]. The experimentally observed p_T distribution at x below 10^{-2} becomes wider as x decreases, so it is called the small-x broadening effect. The phenomenological parametrization for the small p_T cross section found in SIDIS was employed to predict the x dependence of p_T distributions at $x \lesssim 10^{-2}$ at hadron-hadron colliders by [50]. The proposed new form of the Drell-Yan resummed form factor at $x \lesssim 10^{-2}$ is given by

$$W(b) = W_{BLNY}(b) e^{-\rho(x_a)b^2 - \rho(x_b)b^2}, \tag{1.46}$$

where $W_{BLNY}(b)$ is the quantity in Equation 1.36 with the non-perturbative form of Equation 1.45 and with the parametrization found in the global fit [86] to the Drell-Yan data at larger x. The exponential $e^{-\rho(x_a)b^2 - \rho(x_b)b^2}$ parametrizes the small-x broadening. A smooth trial function $\rho(x)$ was chosen as

$$\rho(x) = c_0 \left(\sqrt{\frac{1}{x^2} + \frac{1}{x_0^2}} - \frac{1}{x_0} \right), \tag{1.47}$$

where c_0 controls the magnitude of the broadening for a given x, and x_0 is a characteristic value of x below which $\rho(x)$ becomes non-negligible. The p_T distribution of Z boson with the small-x broadening effect at the LHC 7 TeV is shown in Figure 1.5.

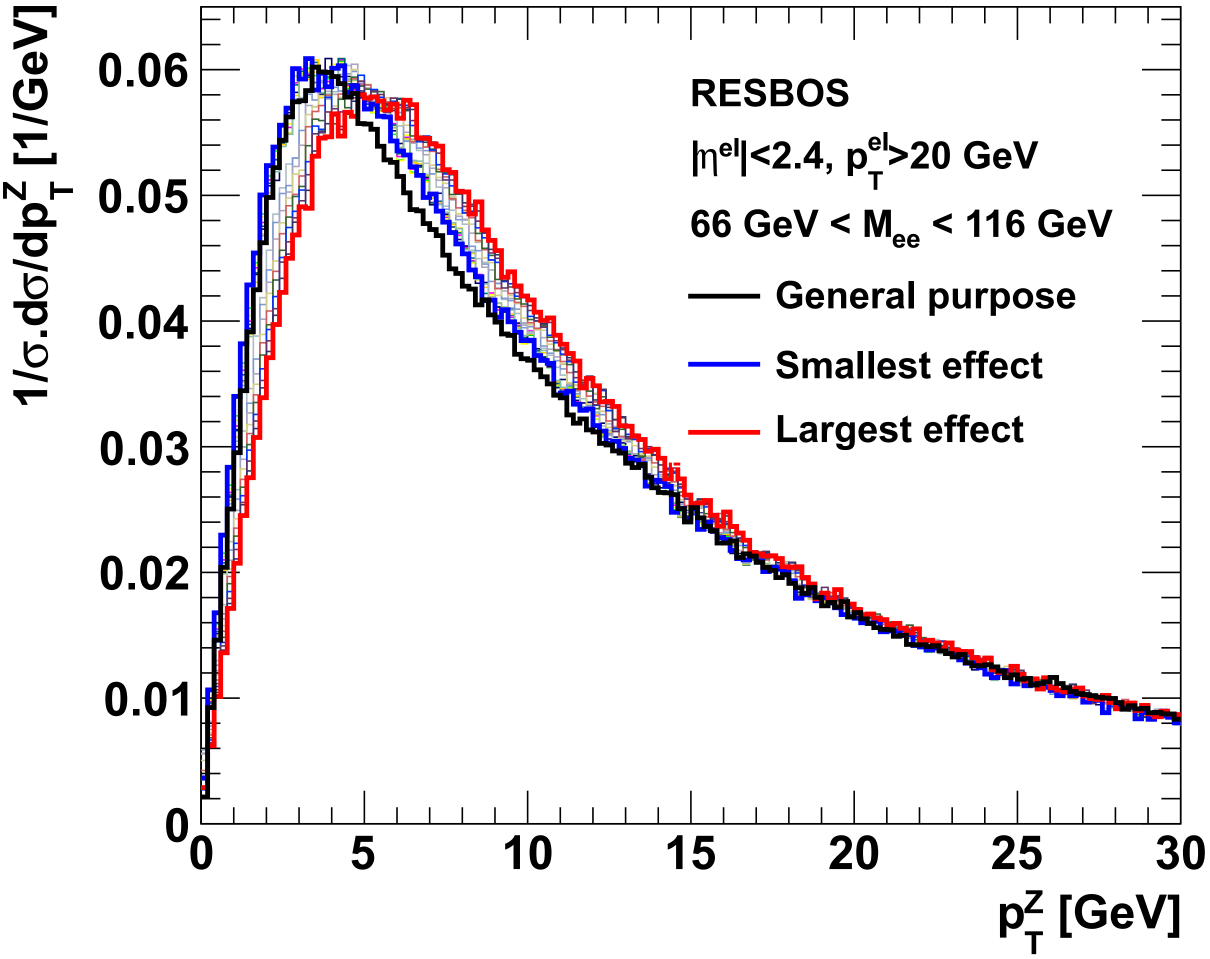

Figure 1.5: Transverse momentum distributions of Z bosons produced at the LHC operating at 7 TeV collider. These curves are obtained using the RESBOS *package in [102] and input grid files in [39] for a general purpose case (black) and input grid files in [49] for the small-x broadening distributions (different colors) with different numerical parametrizations of c_0 and x_0 from small to large effects. The events are selected by requiring $|\eta^{el}| < 2.4$, $p_T^{el} > 20$ GeV for both decay electrons, and 66 GeV $< M_{ee} < 116$ GeV.*

1.2.3 NNLL and (N)NLO QCD predictions of the p_T^Z spectrum of the Z boson

As already mentioned, the comparison of the p_T^Z measurement with different theoretical predictions is a good test of pQCD calculations and helps for tuning MC models. In order to study the theoretical predictions, I investigated the FEWZ [75,76,91] and RESBOS [40,103] programs. Here is a brief summary of this work.

FEWZ includes the fixed order perturbative QCD calculations up to NNLO. RESBOS matches the prediction of soft gluon resummation including a non-perturbative form factor [86] at low p_T^Z (see Section 1.2.2) with the fixed order pQCD calculation at $\mathscr{O}(\alpha_s)$ at high p_T^Z, which is corrected to $\mathscr{O}(\alpha_s^2)$ using a K-factor.

FEWZ2.1 and RESBOS041511 versions are compared. The RESBOS program uses the PDFs CT10. The FEWZ program uses the new PDFs CT10NNLO [84, 93] issued in May 2012. The p_T^Z spectrum for FEWZ and RESBOS is presented in Table 1.4. Only the PDF uncertainty is considered when dealing with RESBOS predictions. This PDF uncertainty results from variations within the 90% C.L. CT10NNLO (CT10 in the case of RESBOS) eigenvectors [84,93]. The theoretical uncertainties on the FEWZ prediction include the PDF uncertainty, the renormalization and factorization scale uncertainties. To determine the scale uncertainty, the factorization (μ_F) and renormalization (μ_R) scales were varied between $1/2m_Z$ and $2m_Z$ with the constraint $1/2 \leq \mu_R/\mu_F \leq 2$ (as recommended and explained in [82]) and the largest deviation among the various scale choices is used as the final scale uncertainty.

The typical shape of the p_T^Z spectrum from the RESBOS prediction is shown in Figure 1.6. The comparison between RESBOS and FEWZ predictions are shown in Figure 1.7. In the analysis of this thesis, the RESBOS prediction with CT10 PDFs is used as a reference prediction.

The RESBOS calculation using CT10 PDFs is also compared to another RESBOS calculation using CTEQ6.6 PDFs which is shown in Figure 1.8. We can observe that the prediction using CTEQ6.6 differs by $\sim 2\%$ from the prediction using CT10. This difference stays within the CT10 error band.

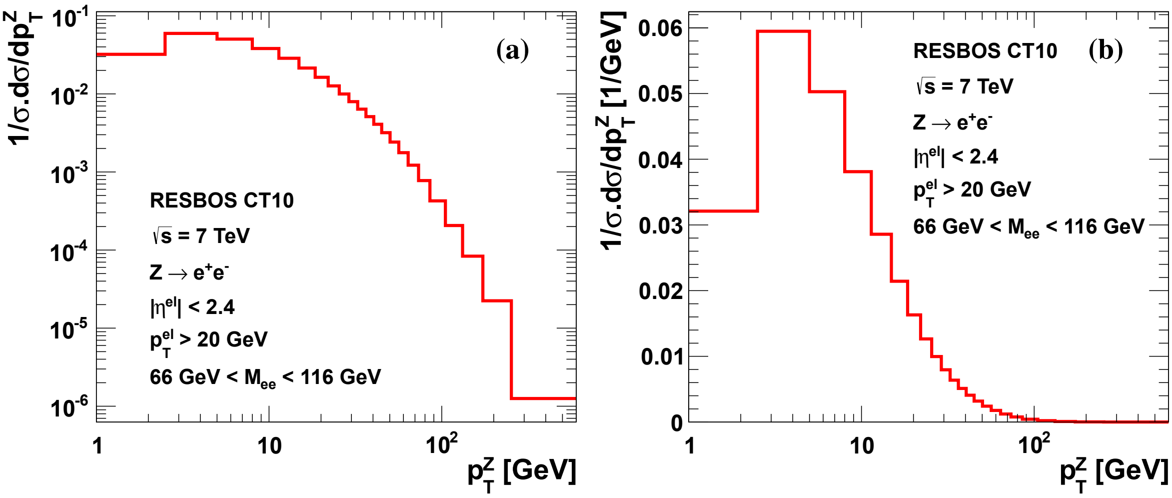

Figure 1.6: The p_T^Z spectrum from RESBOS *predictions in log10-x,y scale (a), with the typical peak arround* $3-5$ *GeV in log10-x scale (b). The events are selected by requiring* $|\eta^{el}| < 2.4$*,* $p_T^{el} > 20$ *GeV for both decay electrons, and* 66 *GeV* $< M_{ee} <$ 116 *GeV.*

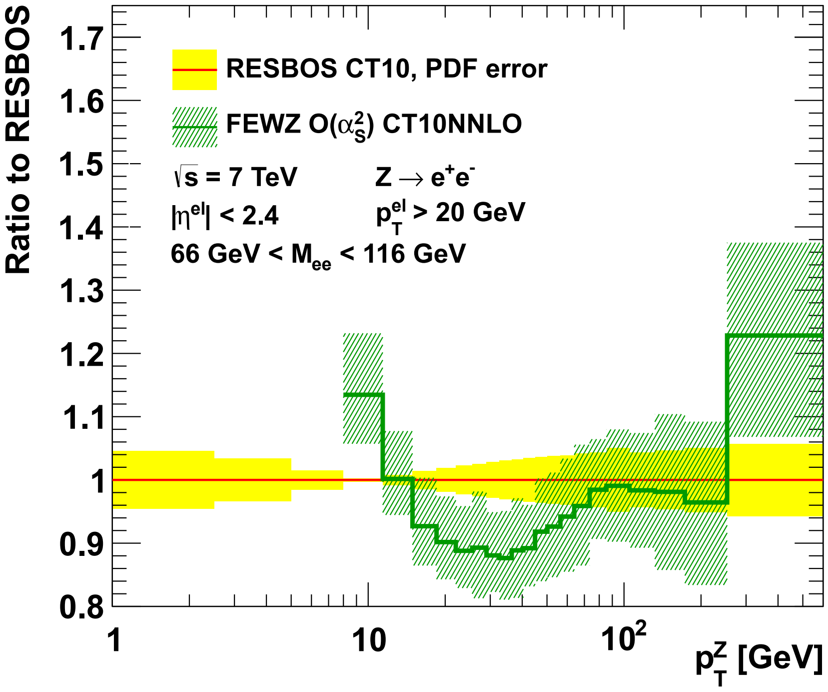

Figure 1.7: The ratio of the p_T^Z predictions provided by FEWZ *and* RESBOS*. The theoretical uncertainties on the* FEWZ *prediction and the PDF uncertainty on the* RESBOS *prediction are shown. The events are selected by requiring* $|\eta^{el}| < 2.4$*,* $p_T^{el} > 20$ *GeV for both decay electrons, and* 66 *GeV* $< M_{ee} <$ 116 *GeV.*

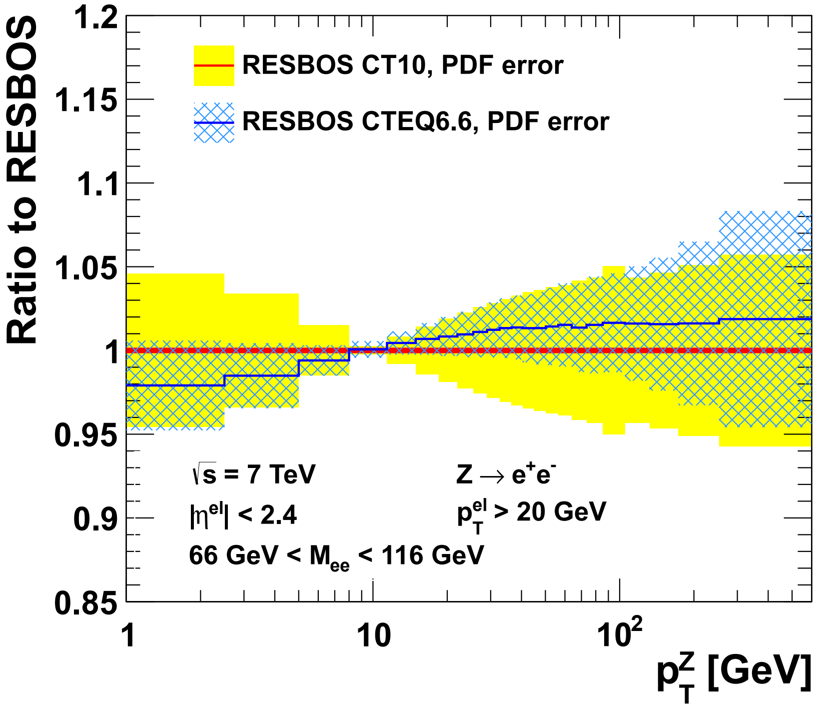

Figure 1.8: The comparison between two RESBOS *predictions for the fiducial cross section, using CTEQ6.6 or CT10 PDFs. The events are selected by requiring* $|\eta^{el}| < 2.4$, $p_T^{el} > 20$ *GeV for both decay electrons, and* 66 *GeV* $< M_{ee} < 116$ *GeV.*

	Resbos			Fewz			
p_T^Z (GeV)	$\frac{1}{\sigma}\frac{d\sigma}{dp_T^Z}$ (1/GeV)	stat. (%)	PDF unc. (%)	$\frac{1}{\sigma}\frac{d\sigma}{dp_T^Z}$ (1/GeV)	stat. (%)	$+$sys. (%)	$-$sys. (%)
0.0 - 2.5	0.0321	0.01	4.58	–	–	–	–
2.5 - 5.0	0.0595	0.01	3.39	–	–	–	–
5.0 - 8.0	0.0503	0.01	1.50	–	–	–	–
8.0 - 11.4	0.0381	0.01	0.25	0.0432	0.29	8.56	6.82
11.4 - 14.9	0.0286	0.01	0.82	0.0286	0.28	7.54	5.69
14.9 - 18.5	0.0214	0.01	1.43	0.0199	0.28	8.27	6.70
18.5 - 22.0	0.0163	0.01	1.89	0.0147	0.30	8.00	6.51
22.0 - 25.5	0.0127	0.02	2.27	0.0112	0.31	7.95	6.63
25.5 - 29.0	0.0100	0.02	2.57	0.0089	0.34	9.94	8.95
29.0 - 32.6	0.0080	0.02	2.83	0.0070	0.36	7.76	6.55
32.6 - 36.4	0.0064	0.02	3.06	0.0056	0.37	8.49	7.48
36.4 - 40.4	0.0051	0.02	3.28	0.0045	0.39	9.27	8.45
40.4 - 44.9	0.0041	0.03	3.47	0.0036	0.38	7.67	6.75
44.9 - 50.2	0.0032	0.03	3.61	0.0029	0.36	9.17	8.53
50.2 - 56.4	0.0024	0.03	3.77	0.0022	0.35	9.22	8.64
56.4 - 63.9	0.0018	0.03	3.88	0.0017	0.33	9.72	9.25
63.9 - 73.4	0.0012	0.04	4.16	0.0012	0.32	10.11	9.81
73.4 - 85.4	$7.8 \cdot 10^{-4}$	0.05	4.33	$7.6 \cdot 10^{-4}$	0.32	8.12	7.89
85.4 - 105.0	$4.3 \cdot 10^{-4}$	0.04	5.03	$4.2 \cdot 10^{-4}$	0.29	9.00	8.90
105.0 - 132.0	$2.1 \cdot 10^{-4}$	0.05	4.34	$2.0 \cdot 10^{-4}$	0.35	9.21	9.22
132.0 - 173.0	$8.4 \cdot 10^{-5}$	0.04	4.65	$8.2 \cdot 10^{-5}$	0.46	12.52	12.58
173.0 - 253.0	$2.2 \cdot 10^{-5}$	0.03	5.10	$2.2 \cdot 10^{-5}$	0.89	13.20	13.51
253.0 - 600.0	$1.3 \cdot 10^{-6}$	0.05	5.73	$1.5 \cdot 10^{-6}$	3.07	11.55	12.67

Table 1.4: Predictions from Resbos *(NNLL+NLO) and* Fewz *(NNLO). The events are selected by requiring* $|\eta^{el}| < 2.4$, $p_T^{el} > 20$ *GeV for both decay electrons, and* 66 *GeV* $< M_{ee} < 116$ *GeV.*

1.2.4 The Monte Carlo event generators

At high energy hadron colliders, the structure of the hadrons, the hadronization and the hard scattering process give rise to complex final states that may contain many particles produced by a variety of physics processes. The event simulations using different Monte Carlo (MC) event generators based on the most recent theoretical knowledge are crucial. The comparison between the data and the MC allows, on one hand, to understand the measured data and the physics behind and on the other hand to tune the MC itself for future physics analyses.

There are many MC event generator programs using different approximate calculations for the hard scattering (LO or NLO) and different methods to deal with multiple soft gluon emissions at low p_T^Z.

1.2.4.1 The parton showering MC generators

While the resummation is the best choice for the transverse momentum predictions, the parton shower is a common tool used in many current physics analyses since it is possible to simulate events as expected in experiments. The merging of parton showers and fixed order calculations also allows to perform approximately all range of the transverse momentum predictions.

In the parton showering model, in order to solve the problem of multiple soft and collinear gluon emissions, a few partons produced in a hard interaction at a high energy scale can be related to partons at an energy scale close to Λ_{QCD}. At this lower energy scale, a universal non-perturbative model can then be used to provide the transition from partons to the hadrons that are observed experimentally. This is possible because the parton showering allows for the evolution, using the DGLAP QCD evolution formalism [34, 70, 80, 89], of the parton fragmentation function. The solution of this DGLAP evolution equation can be rewritten with the help of the Sudakov form factor, which indicates the probability of evolving from a higher scale to a lower scale without the emission of a gluon greater than a given value. For the case of parton showers from the initial state, the evolution proceeds backwards from the hard scale of the process to the cutoff scale, with the Sudakov form factors being weighted by the parton distribution functions at the relevant scales.

In the parton showering process, successive values of an evolution variable t, a momentum fraction z and an azimuthal angle ϕ are generated, along with the flavours of the partons emitted during the showering. The evolution variable t can be the virtuality of the parent parton, $E^2(1-\cos\theta)$, where E is the energy of the parent parton and θ is the opening angle between the two partons, or the square of the relative transverse momentum of the two partons in the splitting depending on MC generators. The evolution variable must have angular ordering to simulate more precisely the higher order contributions that are enhanced due to soft gluon emissions (colour coherence). Fixed order calculations explicitly account for colour coherence, while parton showers that include colour flow information model it only approximately.

The Sudakov exponential form factor of an initial state parton can be written as below [59]

$$\Delta(t) \equiv \exp\left[-\int_{t_0}^{t}\frac{dt'}{t'}\int\frac{dz}{z}\frac{\alpha_s}{2\pi}P(z)\frac{f(x/z,t)}{f(x,t)}\right], \tag{1.48}$$

where t is the hard scale, t_0 is the cutoff scale, $P(z)$ is the splitting function for the branching under consideration and f is the parton distribution function. The Sudakov form factor has a similar form for the final state but without the pdf weighting. The introduction of the Sudakov form factor resums all the effects of soft and collinear gluon emission, which leads to well-defined predictions even in these regions.

At high p_T, parton showers can not give an accurate event rate while matrix element calculations provide a good description of processes where the partons are energetic and widely separated. In order to obtain a reliable prediction in the full range of the transverse momentum, parton showers must be merged with fixed order calculation. The merging should be done carefully to avoid double-counting in kinematic regions where the two calculations overlap. There are some general techniques that allow matrix element calculations and parton showers to be used in kinematic regions where they provide the best description of the event properties. CKKW [61] is one of such techniques. The matrix element description is used to describe parton branchings at large angle and/or energy, while the parton shower description is used for the smaller angle, lower energy emissions. The phase space for parton emission is thus divided into two regions, matrix element dominated and parton shower dominated. The example of CKKW scheme for the case of $W+$ jets production at a hadron-hadron collider is shown in Figure 1.9.

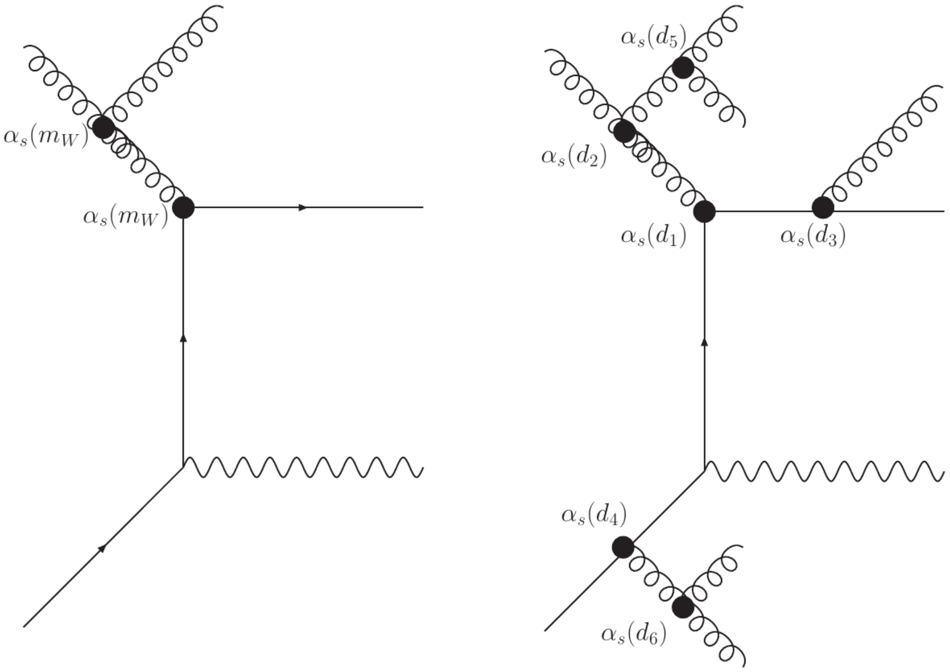

Figure 1.9: In the NLO formalism, the same scale, proportional to the hardness of the process, is used for each QCD vertex. For the case of the $W+2$ jet diagram shown above to the left, a scale related to the mass of the W boson, or to the average transverse momentum of the produced jets, is typically used. The figure to the right shows the results of a simulation using the CKKW formalism. Branchings occur at the vertices with resolution parameters d_i, where $d_1 > d_2 \gg d_{ini} > d_3 > d_4 > d_5 > d_6$. Branchings at the vertices with d_1, d_2 are produced with matrix element information while the branchings at vertices $d_3, ..., d_6$ are produced by the parton shower [59].

Parton showering MC generator programs. There are basically two kinds of event generators. The first one is so called the LO event generator such as PYTHIA [98], HERWIG [66], ALPGEN [90], SHERPA [77]. The second one is so called the NLO event generator such as MC@NLO [74], POWHEG [73].

- PYTHIA [98] is a general purpose event generator, which is commonly used in high energy physics due to its easy handling. The hard scattering process is calculated in leading order approximation and the higher order corrections are approximated with a parton shower approach, which has limited accuracy for predicting events with higher jet multiplicity.
- HERWIG [66] is different with respect to PYTHIA in the modeling of the parton shower and the hadronization process.
- ALPGEN [90] is dedicated to the study of multiparton hard processes in hadronic collisions. The code performs, at the leading order in QCD and EW interactions, the calculation of the exact matrix elements for a large set of parton-level processes of interest in the study of the Tevatron and LHC data. ALPGEN is thus useful for analyses including jets. The hard matrix element calculation process is interfaced with HERWIG for hadronization simulation.
- SHERPA [77] accounts for multijet production through multi-parton tree-level matrix elements merged with the parton shower.
- MC@NLO [74] includes full NLO calculations of rates for QCD processes during the hard scattering. MC@NLO is thus useful for precision measurement where LO calculations are not sufficient. The output of the simulation is further handled by HERWIG event generator, which adds higher order approximations of the parton shower and simulates the hadronization step.
- POWHEG [73] is a prescription for interfacing the NLO QCD calculation with parton shower generators. Unlike MC@NLO, POWHEG produces events with positive (constant) weight and furthermore, does not depend on the subsequent shower Monte Carlo program. POWHEG can be interfaced with any modern shower generator such as HERWIG and PYTHIA.

QED final state radiation interface. The QED corrections for the leading order subprocess includes photon radiation off the final state lepton. The multiple photon emissions off the final state lepton can be generated by the PHOTOS Monte Carlo program [78] which is often used in conjunction with other generators.

1.2.4.2 The predictions of the p_T^Z spectrum of the Z boson in Monte Carlo generators

The MC generator samples used to produce the predictions of the p_T^Z spectrum of the Z boson in this analysis are listed in Table 1.5. The ratios between MC generator predictions and RESBOS prediction are shown in Figure 1.10.

Comparing predictions from many MC generators allows to understand the effect of parton shower models and the QCD calculations on different regions of p_T^Z. Using the same method (POWHEG) for interfacing with the NLO QCD calculation, parton shower models PYTHIA and HERWIG introduce different shape of p_T^Z. Including multiple jets in the cross section calculation programs such as ALPGEN and SHERPA increases the contribution at high p_T^Z and shows a different behaviour compared to other programs. The difference at low p_T^Z can be up to 40% between POWHEG+PYTHIA6 and POWHEG+HERWIG programs and at $p_T^Z > 253$ GeV can be up to 70% between ALPGEN and MC@NLO programs. These predictions will be studied by comparing with the measurement on data.

Generator	Dataset	PDF	$\mathscr{L}$(fb^{-1})	$\sigma \times BR$ (nb)
SHERPA	mc11_7TeV.147770.Sherpa_CT10_Zee.evgen.EVNT.e1238	CT10	4.78	1.05
MC@NLO	mc11_7TeV.106087.McAtNloZee_no_filter.evgen.EVNT.e1096	CT10	5.25	0.95
POWHEG+PYTHIA6	mc11_7TeV.108303.PowHegZePythia.evgen.EVNT.e825	CT10	20.67	0.97
POWHEG+PYTHIA8	mc12_7TeV.147806.PowhegPythia8_AU2CT10_Zee.evgen.EVNT.e1312	CT10	5.24	0.95
POWHEG+HERWIG	mc11_7TeV.126006.PowHegZeJimmy.evgen.EVNT.e995	CTEQ6L1	20	1.00
ALPGEN	mc11_7TeV.107650.AlpgenJimmyZeeNp0_pt20.evgen.EVNT.e835	CTEQ6L1	9.88	0.67
ALPGEN	mc11_7TeV.107651.AlpgenJimmyZeeNp1_pt20.evgen.EVNT.e835	CTEQ6L1	14.2	0.14
ALPGEN	mc11_7TeV.107652.AlpgenJimmyZeeNp2_pt20.evgen.EVNT.e835	CTEQ6L1	60.68	0.04
ALPGEN	mc11_7TeV.107653.AlpgenJimmyZeeNp3_pt20.evgen.EVNT.e835	CTEQ6L1	70.15	0.01
ALPGEN	mc11_7TeV.107654.AlpgenJimmyZeeNp4_pt20.evgen.EVNT.e835	CTEQ6L1	93.16	0.0028
ALPGEN	mc11_7TeV.107655.AlpgenJimmyZeeNp5_pt20.evgen.EVNT.e835	CTEQ6L1	99.09	0.00076

Table 1.5: MC generator prediction samples used in this analysis. Each ALPGEN *sample corresponds with a number of jets varying from 0 to 5.*

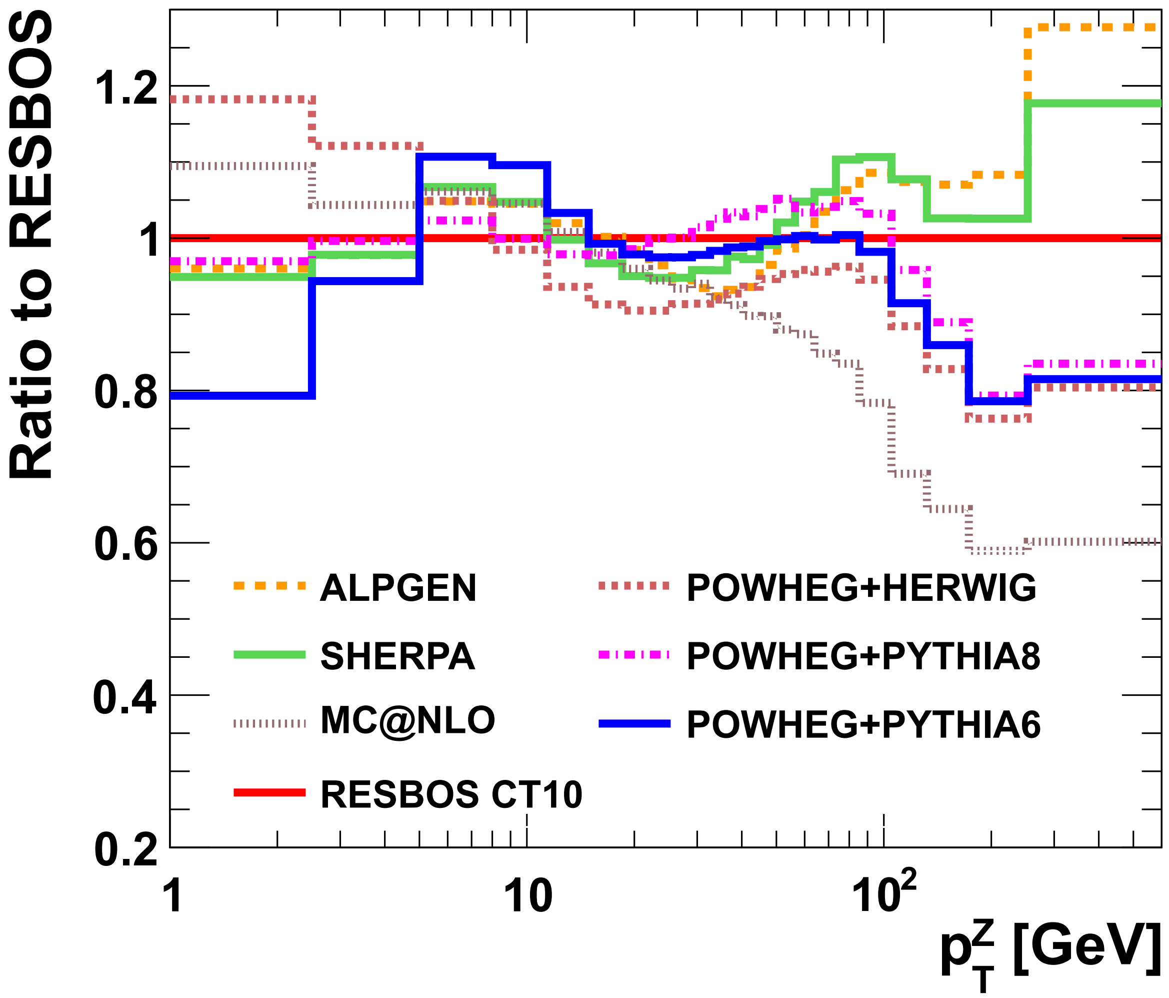

Figure 1.10: The ratio between different MC generator prections and RESBOS *prediction of the* p_T^Z *spectrum of the Z boson. The events are selected by requiring* $|\eta^{el}| < 2.4$, $p_T^{el} > 20$ *GeV for both decay electrons, and* 66 *GeV* $< M_{ee} <$ 116 *GeV.*

1.3 Optimization of new variables to study the Z boson transverse momentum

1.3.1 Motivation of the optimization

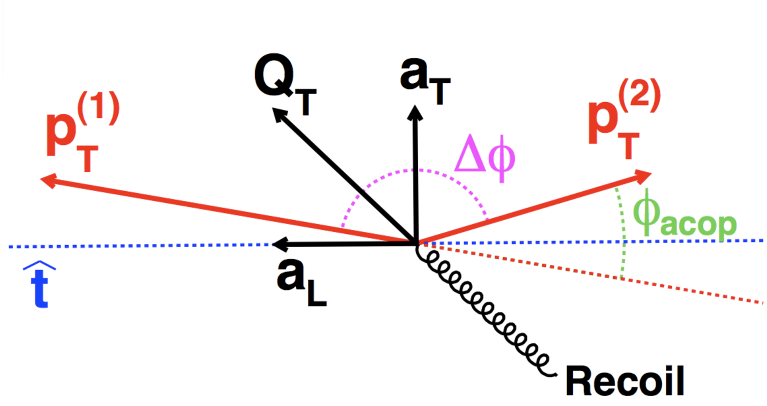

Figure 1.11: Graphical illustration in the plane transverse to the beam direction of the variables defined in the text and used to analyze dilepton transverse momentum distribution at hadron colliders [45].

The ATLAS and CMS Collaborations have recently published the measurement of the transverse-momentum distribution of Drell-Yan muon and electron pairs with an integrated luminosity of ~ 40 pb^{-1} [16, 62]. In Chapter 5 of my thesis, I will present the measurement of the di-electron transverse momentum at LHC using the full ATLAS 2011 data sample corresponding to an integrated luminosity of ~ 4.7 fb^{-1}. The precision of this measurement is limited by the experimental resolution rather than by the available event statistics. Additional analyzing variables with better experimental resolution have been proposed and studied in the last few years [45, 54, 100]. The variable, a_T, which corresponds to the component of p_T^Z ($\equiv Q_T$) that is transverse to the dilepton thrust axis [1], $\hat{t}$, has been proposed in Ref. [100] as an alternative analyzing variable that allows to study the issues discussed above but is less sensitive than p_T^Z to detector resolution effects. The a_T distribution was subsequently calculated to next-to-next-to-leading-log (NNLL) accuracy using resummation techniques [42]. The variable a_L [100] corresponds to the component of Q_T that is longitudianl to $\hat{t}$. For a graphical illustration of Q_T, a_T, a_L and other variables defined below we refer to Fig. 1.11.

---

[1] The thrust axis is defined as $\hat{t} = (p_T^{(1)} - p_T^{(2)})/|p_T^{(1)} - p_T^{(2)}|$, where $p_T^{(1)}$ and $p_T^{(2)}$ are the lepton momentum vectors in the plane transverse to the beam direction.

A recent paper [54] has discussed the idea of using the azimutal opening angle, $\Delta\phi$, as an analysing variable that is sensitive to the physics of p_T^Z, and insensitive to lepton momentum uncertainties. Whilst $\Delta\phi$ is primarily sensitive to the same component of p_T^Z as a_T, the translation from a_T to $\Delta\phi$ depends on the scattering angle θ^* of the leptons relative to the beam direction in the dilepton rest frame. Thus, $\Delta\phi$ is less directly related to p_T^Z than a_T. The idea is to correct $\Delta\phi$ on event-by-event basis for the scattering angle θ^* in order to improve the sensitivity to p_T^Z. For convenience, the acoplanarity angle is defined as $\phi_{acop} \equiv \pi$ - $\Delta\phi$. For $p_T^{(1)} \approx p_T^{(2)}$ where $p_T^{(1,2)}$ are the two lepton momenta it can be shown that [45]:

$$a_T/m_Z \approx \tan(\phi_{acop}/2)\sin(\theta^*) \tag{1.49}$$

The angle θ^* is commonly evaluated in the Collins-Soper frame [63] and requires the knowledge of the lepton momenta and is thus sensitive to the effects of the lepton momentum resolution. An alternative way to measure the scattering angle is based entirely on the measured track directions, It is expected to give the best experimental resolution. This scattering angle is approximated by the angle θ_η^* where [45]:

$$\cos(\theta_\eta^*) \equiv \tanh[(\eta^- - \eta^+)/2] \tag{1.50}$$

where η^- and η^+ are the pseudo-rapiditities of the negatively and positively charged lepton, respectively.

The optimal variable to probe the transverse momentum domain of Z production was found to be ϕ_η^* which is defined as [45]:

$$\phi_\eta^* \equiv \tan(\phi_{acop}/2)\sin(\theta_\eta^*) \tag{1.51}$$

Since ϕ_η^* depends exclusively on ϕ_{acop} and θ_η^* which themselves depend exclusively on the directions of the two leptons, ϕ_η^* is experimentally well measured compared to any quantity that relies on the momenta of the leptons. As a concrete example of the utility and discriminating power of the ϕ_η^* variable one can consider the issue of the small-x broadening which is neglected by conventional resummation techniques but may become important at values of x relevant for LHC [50]. The reduced experimental systematic uncertainties achievable with the ϕ_η^* variable in the low-p_T domain and the large statistics of inclusive Z bosons collected in 2011 will allow ATLAS to further investigate this effect.

The ϕ_η^* variable has recently been measured by the D0 Collaboration using 7.3 fb^{-1} of $p\bar{p}$ collisions at the Tevatron [22]. Predictions from RESBOS are unable to describe the detailed shape of the corrected D0 data even if the overall agreement is reasonably good. The effect of the small-x broadening is strongly disfavored in the D0 data. Another prediction at the Tevatron of the ϕ^*_η spectrum at low ϕ^*_η was calculated at NNLL accuracy in Ref. [44] and showed an agreement with the D0 data within theoretical errors.

In next sections, the interest in the use of the ϕ^*_η variable will be discussed in detail. The predictions from QCD calculations as well as from MC generators for the ϕ^*_η spectrum are also presented.

1.3.2 Dependence on the detector resolution

To ilustrate the interest in using the new variables, the experimental resolution of these new variables and of p_T^Z are compared. In particular, I compare the variation of the experimental resolution for each variable as a function of that variable. The variables considered are p_T^Z, a_T, a_T/m_Z, ϕ^*_η. This comparison can be done after having ensured that all distributions have approximately the same scale. Compared to p_T^Z, all other variables are on average a factor $\sqrt{2}$ smaller. A simple multiplication by $M_Z = 91.19$ GeV [52] corrects the a_T/m_Z and the angular variable ϕ^*_η and conveniently ensures that all variables have the same units (GeV). These factors are summarised in Table 1.6. This method was proposed and used in [45].

Variable	Scaling factor
p_T^Z	1
a_T	$\sqrt{2}$
a_T/m_Z	$\sqrt{2}M_Z$
ϕ^*_η	$\sqrt{2}M_Z$

Table 1.6: Scaling factors for the different variables [45].

Figure 1.12 compares the mean and the RMS of the resolution, Δx, of various candidate variables, x, as a function of generated level x_{Truth} using $Z \to ee$ PYTHIA MC sample [2]. The x_{Truth} uses the ”Dressed“ electron momenta. More details of the ”Dressed“ electron can be found in Section 5.2. All variables are scaled by the factors in Table 1.6. Figure 1.12 shows that ϕ^*_η has the best resolution in comparison with other variables to study p_T^Z.

---

[2] mc10_7TeV.106046.PythiaZee_no_filter.merge.NTUP_SMWZ.e574_s933_s946_r2302_r2300_p591.

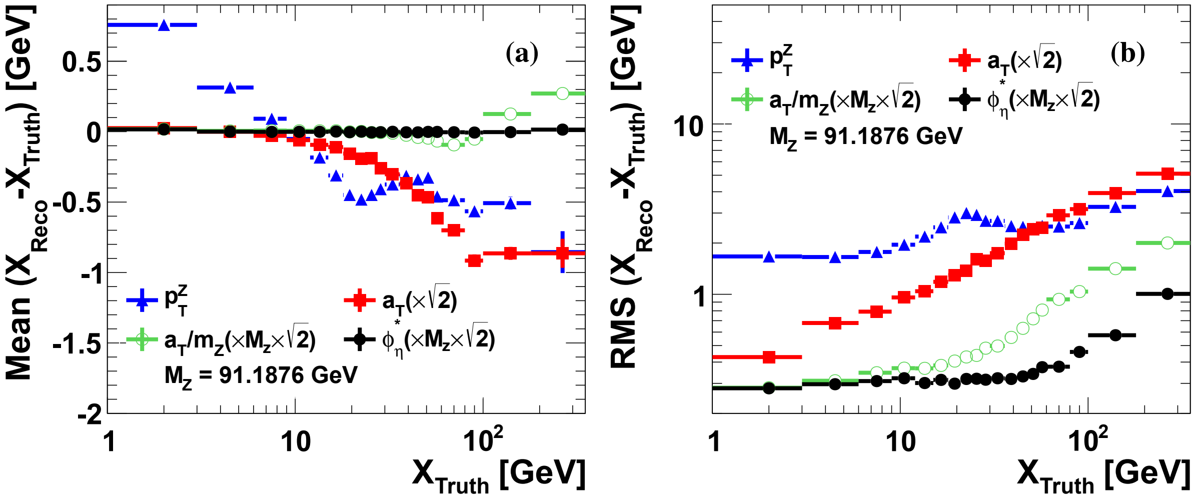

Figure 1.12: The mean (a) and the RMS (b) of the resolution of various candiate variables, x, as a function of generated level x_{Truth}.

1.3.3 Sensitivity to physics

Figure 1.13 shows the correlation between the new variable ϕ_η^* and p_T^Z. This plot indicates that ϕ_η^* is sensitive to the same physics as p_T^Z.

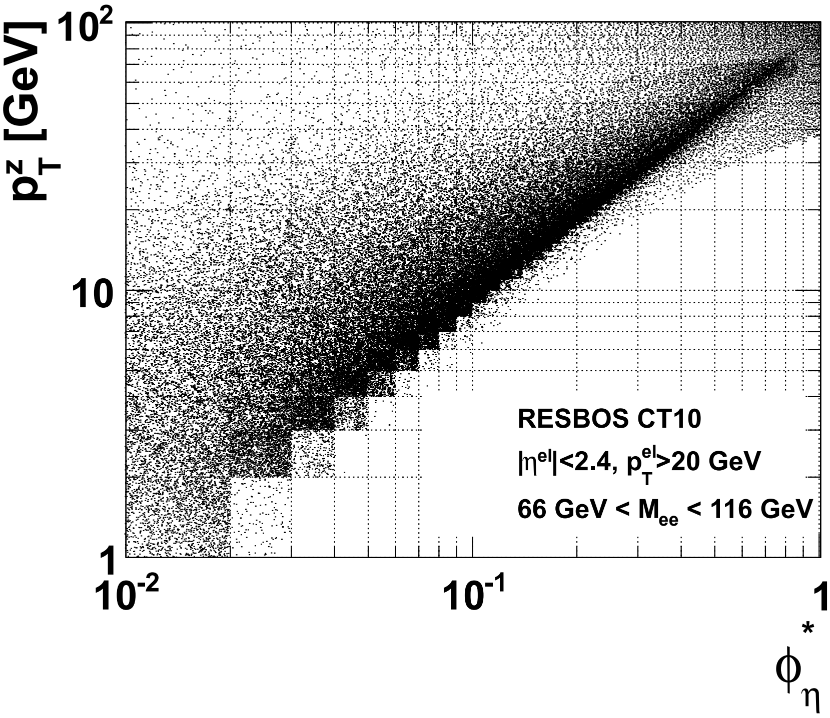

Figure 1.13: The correlation between the new variable ϕ_η^* and p_T^Z in RESBOS *prediction.*

1.3.4 NNLL and (N)NLO QCD predictions of the ϕ^*_η spectrum of the Z boson

The details of this work using FEWZ and RESBOS programs was introduced in Section 1.2.3. The shape of the ϕ^*_η spectrum from RESBOS prediction is shown in Figure 1.14. The difference between the ϕ^*_η spectrum and the p_T^Z spectrum (in Figure 1.6) in the low p_T^Z region is one of the main interest of this new variable. The ϕ^*_η measurement is mostly not affected by the MC shape dependence in the unfolding procedure, details will be discussed in Section 5.6.5 and Section 6.2.5.

The comparison between RESBOS and FEWZ predictions of the ϕ^*_η spectrum is shown in Figure 1.15. The ϕ^*_η spectrum from RESBOS and FEWZ predictions is listed in Table 1.7.

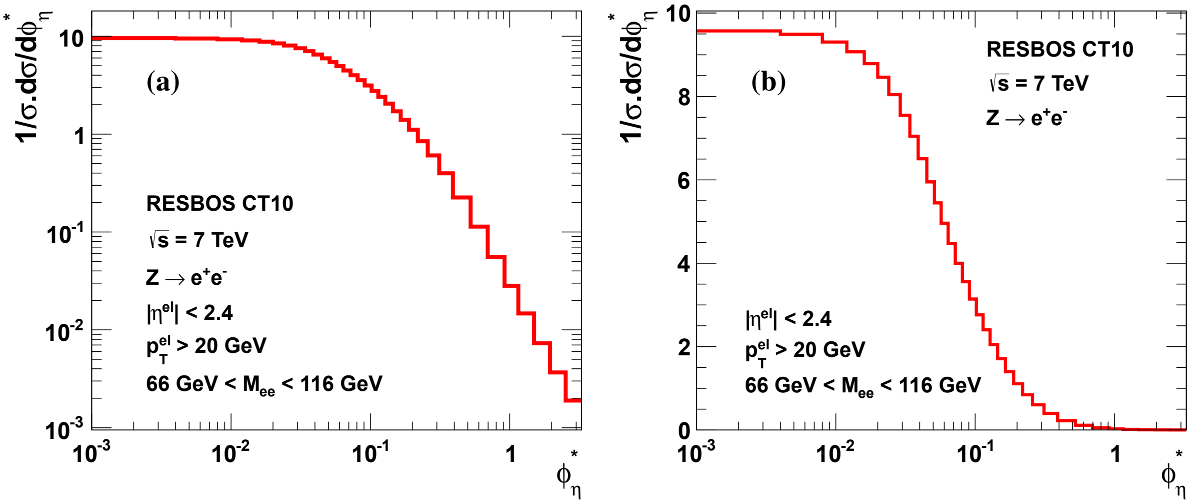

Figure 1.14: The ϕ^*_η spectrum from RESBOS *predictions in log10-x,y scale (b), in log10-x scale (b). The events are selected by requiring $|\eta^{el}| < 2.4$, $p_T^{el} > 20$ GeV for both decay electrons, and 66 GeV $< M_{ee} <$ 116 GeV.*

The RESBOS calculation using CT10 PDFs is also compared to another RESBOS calculation using CTEQ6.6 PDFs in Figure 1.16. We can observe that the prediction using CTEQ6.6 differs by $\sim 1\%$ from the prediction using CT10. This difference stays within the CT10 error band.

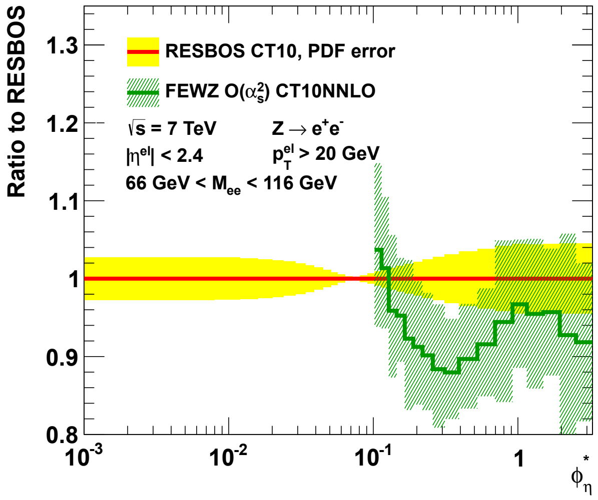

Figure 1.15: The comparison between two predictions RESBOS *and* FEWZ *including their systematic uncertainties for the fiducial cross section. The events are selected by requiring* $|\eta^{el}| < 2.4$, $p_T^{el} > 20$ *GeV for both decay electrons, and* 66 *GeV* $< M_{ee} <$ 116 *GeV.*

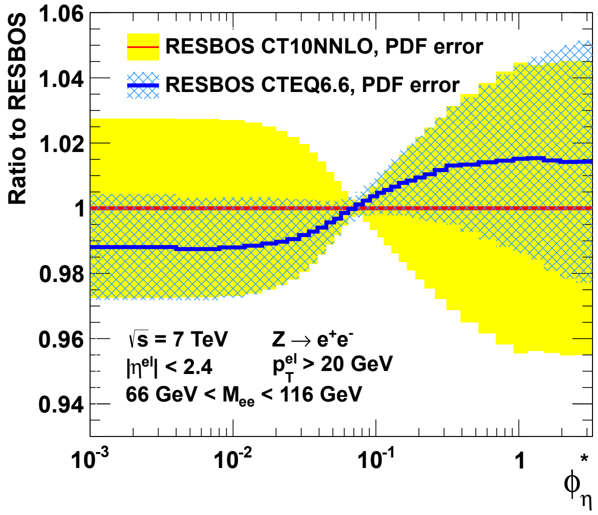

Figure 1.16: The comparison between two RESBOS *predictions for the fiducial cross section, using CTEQ6.6 or CT10 PDFs. The events are selected by requiring* $|\eta^{el}| < 2.4$, $p_T^{el} > 20$ *GeV for both decay electrons, and* 66 *GeV* $< M_{ee} <$ 116 *GeV.*

ϕ^*_η	RESBOS			FEWZ			
	$\frac{1}{\sigma}\frac{d\sigma}{d\phi^*_\eta}$	stat. (%)	PDF unc. (%)	$\frac{1}{\sigma}\frac{d\sigma}{d\phi^*_\eta}$	stat. (%)	+sys. (%)	−sys. (%)
0.000 - 0.004	9.5728	0.02	2.75	–	–	–	–
0.004 - 0.008	9.4909	0.02	2.74	–	–	–	–
0.008 - 0.012	9.3055	0.02	2.70	–	–	–	–
0.012 - 0.016	9.0730	0.02	2.62	–	–	–	–
0.016 - 0.020	8.7885	0.02	2.50	–	–	–	–
0.020 - 0.024	8.4611	0.02	2.36	–	–	–	–
0.024 - 0.029	8.0454	0.02	2.18	–	–	–	–
0.029 - 0.034	7.5490	0.02	1.96	–	–	–	–
0.034 - 0.039	7.0461	0.02	1.71	–	–	–	–
0.039 - 0.045	6.5072	0.02	1.42	–	–	–	–
0.045 - 0.051	5.9524	0.02	1.11	–	–	–	–
0.051 - 0.057	5.4481	0.02	0.82	–	–	–	–
0.057 - 0.064	4.9605	0.02	0.53	6.5199	0.99	8.96	7.29
0.064 - 0.072	4.4711	0.02	0.26	5.3636	0.93	7.85	5.84
0.072 - 0.081	3.9995	0.02	0.20	4.6307	0.85	12.01	10.87
0.081 - 0.091	3.5570	0.02	0.42	3.9991	0.77	10.68	9.39
0.091 - 0.102	3.1418	0.02	0.67	3.3855	0.73	9.14	7.61
0.102 - 0.114	2.7620	0.02	0.90	2.8797	0.71	10.16	8.89
0.114 - 0.128	2.4033	0.02	1.14	2.4241	0.63	9.18	7.87
0.128 - 0.145	2.0496	0.02	1.39	1.9682	0.59	9.69	8.46
0.145 - 0.165	1.7118	0.02	1.65	1.6224	0.52	7.98	6.45
0.165 - 0.189	1.3986	0.02	1.91	1.2959	0.45	10.32	9.24
0.189 - 0.219	1.1103	0.02	2.18	1.0038	0.39	9.78	8.74
0.219 - 0.258	0.8456	0.02	2.47	0.7619	0.35	8.69	7.61
0.258 - 0.312	0.6059	0.02	2.78	0.5355	0.30	9.13	8.14
0.312 - 0.391	0.3979	0.02	3.12	0.3506	0.25	7.52	6.46
0.391 - 0.524	0.2254	0.02	3.50	0.2017	0.20	7.76	6.96
0.524 - 0.695	0.1135	0.03	3.84	0.1041	0.22	7.47	6.89
0.695 - 0.918	0.0553	0.04	4.18	0.0525	0.25	10.35	10.06
0.918 - 1.153	0.0282	0.05	4.46	0.0273	0.35	8.35	8.19
1.153 - 1.496	0.0147	0.05	4.38	0.0140	0.41	9.91	9.86
1.496 - 1.947	0.0073	0.05	4.45	0.0070	0.54	7.48	7.47
1.947 - 2.522	0.0037	0.06	4.51	0.0034	0.83	13.75	13.77
2.522 - 3.277	0.0019	0.08	4.50	0.0017	1.08	9.27	9.30

Table 1.7: Predictions from RESBOS *(NNLL+NLO) and* FEWZ *(NNLO). The events are selected by requiring* $|\eta^{el}| < 2.4$, $p_T^{el} > 20$ *GeV for both decay electrons, and* 66 *GeV* $< M_{ee} < 116$ *GeV.*

1.3.5 The predictions of the ϕ_η^* spectrum of the Z boson in Monte Carlo generators

The comparison between different MC predictions (listed in Table 1.5) and RESBOS prediction of the ϕ_η^* spectrum of the Z boson is shown in Figure 1.17. As shown in this figure the ϕ_η^* variable is less sensitive to the fragmentation of parton shower models. The difference between POWHEG+PYTHIA6 and POWHEG+HERWIG predictions at low ϕ_η^* is $\sim 20\%$ which is 40% at low p_T^Z in Figure 1.10.

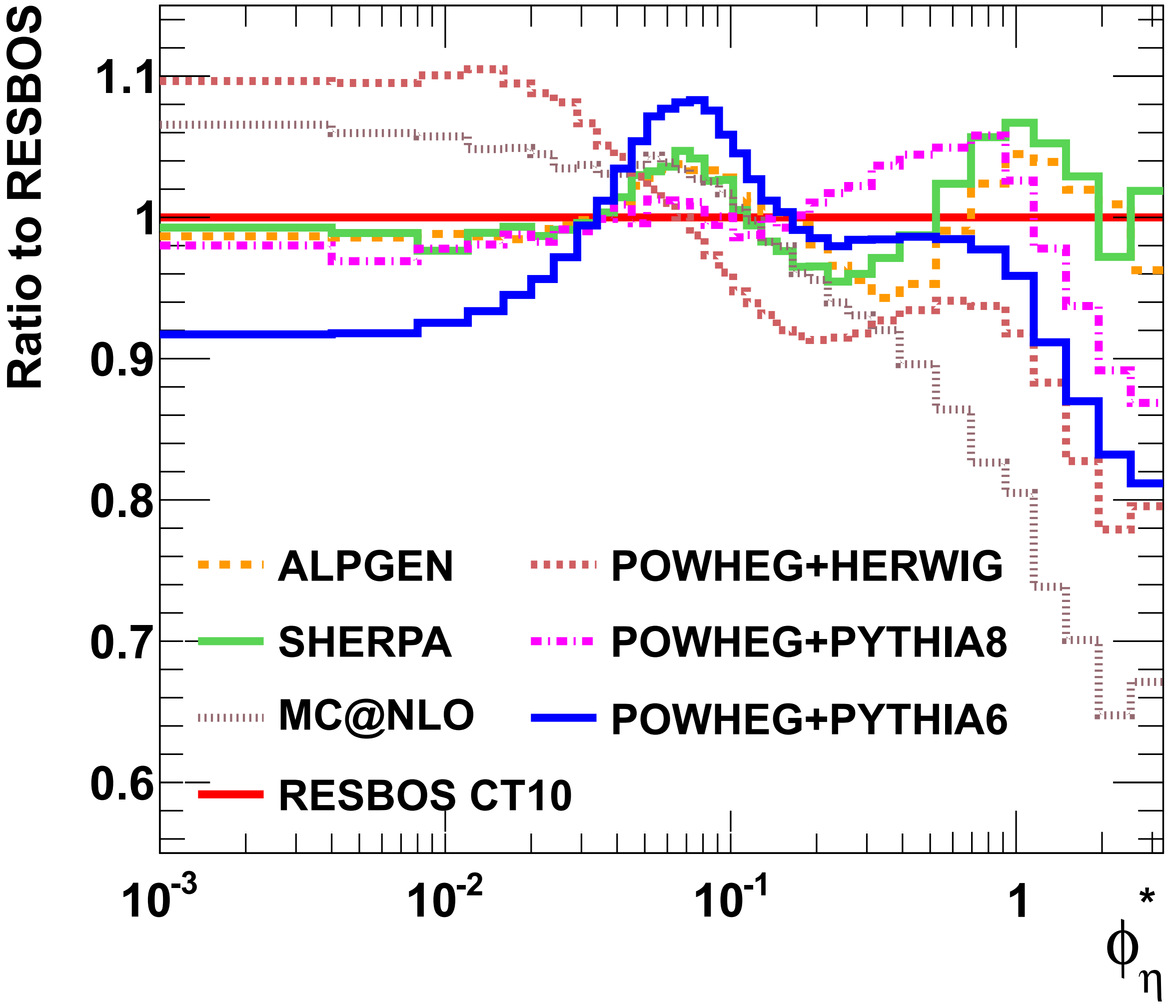

Figure 1.17: The ratio between different MC generator prections and RESBOS *prediction of the* ϕ_η^* *spectrum of the Z boson. The events are selected by requiring* $|\eta^{el}| < 2.4$, $p_T^{el} > 20$ *GeV for both decay electrons, and* 66 *GeV* $< M_{ee} <$ 116 *GeV [69].*

Chapter 2

The ATLAS Detector at the LHC

The Large Hadron Collider (LHC) is a new particle collider located at CERN near Geneva in Switzerland (see Figure 2.1). The accelerator is designed to collide two beams of protons at a centre-of-mass energy of 14 TeV. The centre-of-mass energy was 7 TeV during the 2010-2011 data taking and is 8 TeV at present. The machine is installed at 50-175m underground in the former LEP tunnel which has a circumference of about 27 km. After over 10 years of preparation and construction the LHC released the first beam on 10 September 2008 and made the first collision in November 2009. Among the six detectors of the LHC (ALICE, ATLAS, CMS, TOTEM, LHCb, and LHCf), ATLAS (A Toroidal LHC ApparatuS) and CMS (Compact Muon Solenoid) are the two largest and general purpose experiments located at two interaction points of the LHC. This chapter will introduce briefly the LHC and the ATLAS delector as well as their functions and current status.

2.1 The LHC

Before being accelerated by the LHC, the proton beams travel through other accelerators at CERN to increase their energy in several stages [48]. Figure 2.2 illustrates the path traveled by the protons through the accelerator complex at CERN. In the LHC, the particle beams are accelerated in an ultrahigh vacuum (10^{-10} Torr). To circulate in the tunnel they are bent by 1232 powerful superconducting dipole magnets and focused by quadrupole magnets. To ensure their normal operation the superconducting magnets with niobium-titanium coils (NbTi) must be kept at a temperature of 1.9K. In order to bend 7 TeV beams around the LHC ring the dipole magnets should have a field of about 8.33 Tesla.

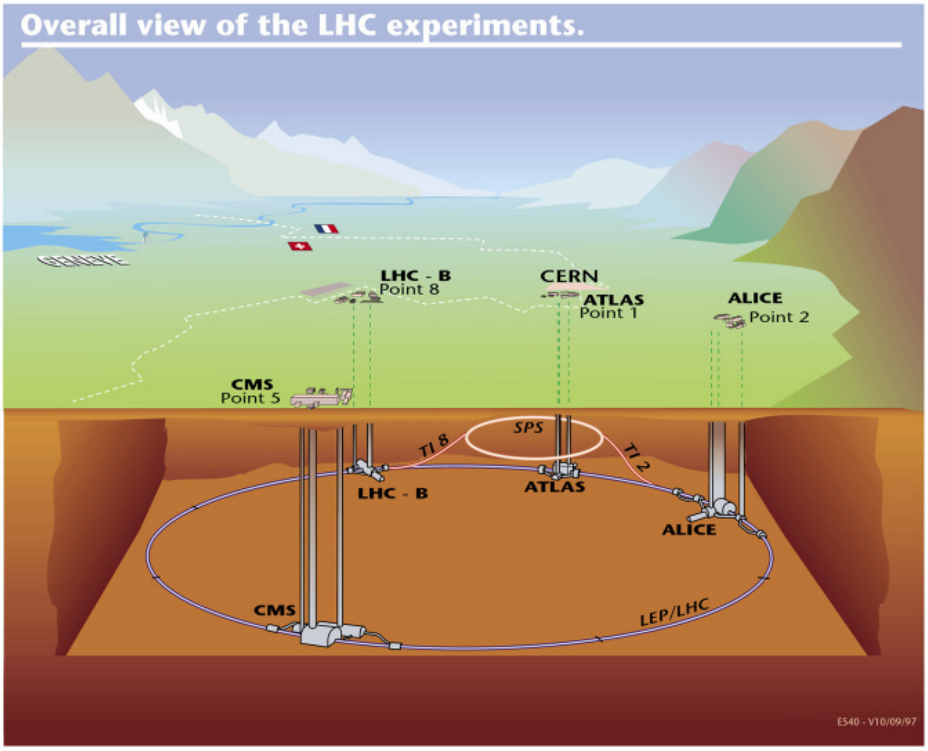

Figure 2.1: The LHC general scheme

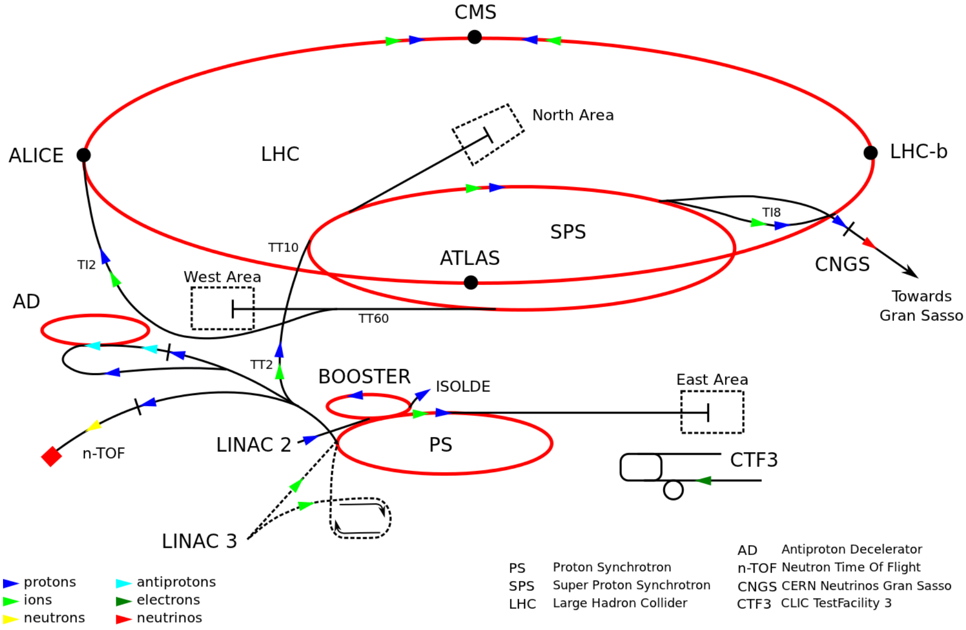

Figure 2.2: The CERN accelerator complex

The number of events per second produced in the LHC collisions is given by:

$$N_{event} = L\sigma_{event}, \tag{2.1}$$

where σ_{event} is the cross section for the process under study and L is the machine luminosity. The machine luminosity depends only on the beam parameters and for a Gaussian beam distribution can be written as:

$$L = \frac{N_b^2 n_b f_{rev} \gamma_r}{4\pi \varepsilon_n \beta^*} F, \tag{2.2}$$

where N_b is the number of particles per bunch, n_b the number of bunches per beam, f_{rev} the revolution frequency, γ_r the relativistic gamma factor, ε_n the normalized transverse beam emittance, β^* the beta function at the collision point and F the geometric luminosity reduction factor due to the crossing angle at the interaction point (IP):

$$F = 1/\sqrt{1 + \left(\frac{\theta_c \sigma_z}{2\sigma^*}\right)^2}, \tag{2.3}$$

where θ_c is the full crossing angle at the IP, σ_z the RMS bunch length and σ^* the transverse RMS beam size at the IP. The above expression assumes equal beam parameters for both circulating beams. The exploration of rare events in the LHC collisions requires both high beam energies and high beam intensities.

A summary of some of the LHC design beam parameters together with the parameters reached during the 2011 run used for the analysis performed in this thesis can be found in Table 2.1. The delivered and recorded integrated luminosity in 2011 are displayed in Figure 2.3.

2.2 Coordinates for LHC

Two coordinate systems are used in the LHC. The Cartesian system has an origin at the nominal collision point, the positive direction of the x-axis points to the center of the LHC ring, the positive direction of the y-axis is upward and the z-axis along the beam line has a direction to form with the x- and y- axes a right-handed Cartesian coordinate system. The polar coordinate system is defined by choosing the polar angle θ with respect to the z-axis, the azimuthal angle ϕ around this axis, and the radial coordinate $\rho = \sqrt{x^2 + y^2}$.

Since the boost of the parton centre-of-mass along the beam line is unknown, to characterize a particle in hadron colliders the transverse momentum p_T is used. This is defined as the momentum projected in

Beam parameter	Nominal	October 2011
Proton energy [TeV]	7	3.5
β^* [m]	0.55	1.0
Transverse normalized emittance ε_n [μm rad]	3.75	2.5
RMS beam size σ^* [μm]	16.7	24
Number of particles per bunch N_b	1.15×10^{11}	1.5×10^{11}
Number of bunches n_b	2808	1331
Bunch spacing [ns]	25	50
RMS bunch length [cm]	7.55	9
Peak luminosity [$cm^{-2}s^{-1}$]	10^{34}	3.6×10^{33}
Average peak pile-up	25	18

Table 2.1: Nominal design values of the LHC beam parameters together with the numbers reached during 2011 data-taking [13, 56].

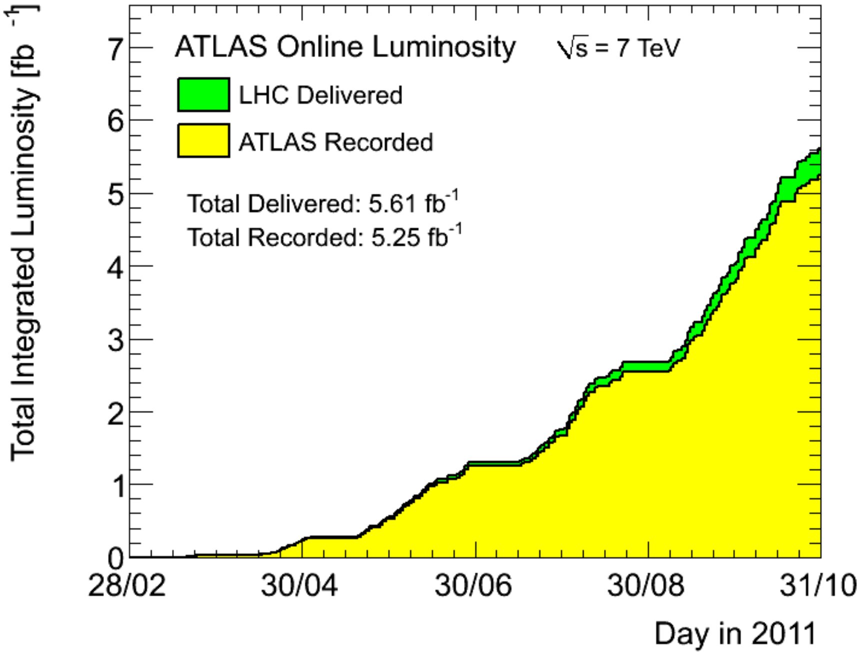

Figure 2.3: Integrated luminosity delivered by the LHC and recorded by the ATLAS detector in 2011.

the plane orthogonal to the beam axis. A particle is also characterized by its rapidity. The rapidity of a particle relative to the beam axis is defined as below:

$$y = \frac{1}{2} \ln \frac{E + p_z}{E - p_z}, \tag{2.4}$$

where $E = \sqrt{\overrightarrow{p}^2 + m^2}$ is the energy, $\overrightarrow{p}$ the momentum, m the mass of a particle and p_z is the component of the particle momentum along the z-axis. In the approximation that the mass of the particle is nearly zero $E \simeq |\overrightarrow{p}|$:

$$y \rightarrow \frac{1}{2} \ln \frac{1 + \cos\theta}{1 - \cos\theta} = -\ln\left[\tan\left(\frac{\theta}{2}\right)\right] \equiv \eta, \tag{2.5}$$

where η is the pseudo-rapidity, which has an one-to-one correspondence with the polar angle θ. So in the massless limit the rapidity is equivalent to the pseudo-rapidity.

For a charged particle track, there are two more parameters, d_0 and z_0: d_0 is the transverse distance to the beam axis at the point of closest approach of the track, while z_0 is the distance from the origin along the z-axis at the point of closest approach.

2.3 The ATLAS detector

The ATLAS experiment is a general-purpose detector and it consists of many components designed to detect different types of particles produced in the collisions. The ATLAS detector is a massive device with a weight of 7000 tons, a length of 42 meters and a diameter of 25 meters. Therefore it is the largest experiment at the LHC. The technical specification of ATLAS is published in detail in the Technical Design Report (TDR) [3,4] and, after installation at collision point 1, in the ATLAS technical paper [15]. The ATLAS detector has three major parts (counted from the center outwards): the Inner Detector, the Calorimetry and the Muon Spectrometer. Two magnet systems are designed to bend charged particles in the Inner Detector and the Muon Spectrometer. Data from the ATLAS detector are selected through the trigger system. An overall ATLAS layout is shown in Figure 2.4 and its main performance goals are listed in table 2.2.

The Inner Detector tracks the charged particle trajectories precisely, the calorimeters measure the energy of the particles and the muon spectrometer identifies the muons. If the strength of the magnetic field is known, the particle momenta can be measured by the Inner Detector and the Muon Spectrometer. Particles like neutrinos which do not interact with the detector can be inferred via an estimation of

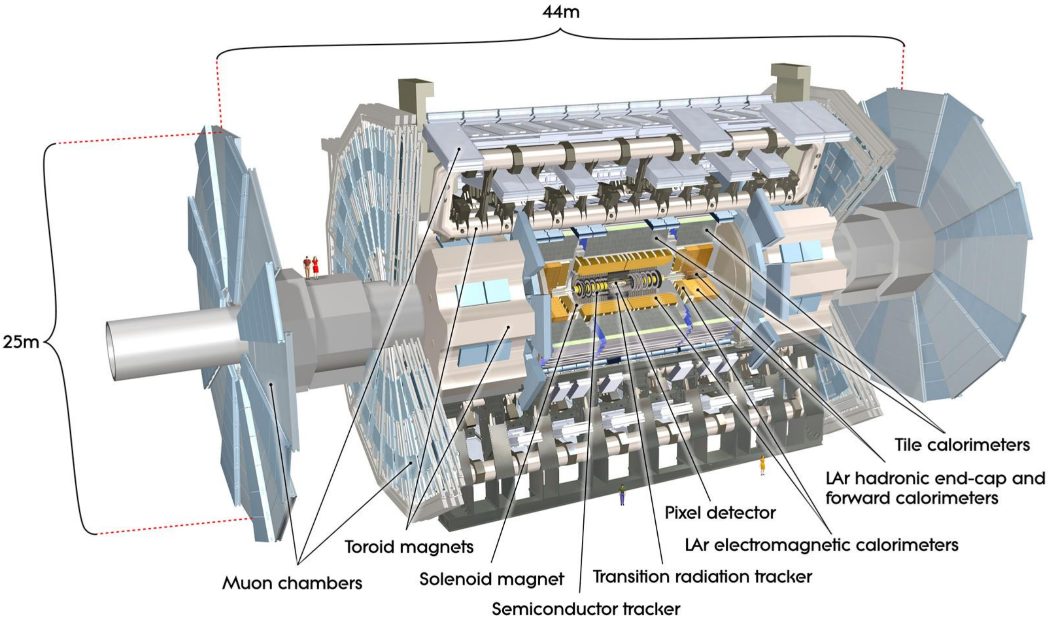

Figure 2.4: The ATLAS detector layout [15].

Detector component	Required resolution	η coverage	
		Measurement	Trigger
Inner Detector	$\sigma_{p_T}/p_T = 0.05\% p_T \oplus 1\%$	± 2.5	
EM calorimetry	$\sigma_E/E = 10\%/\sqrt{E} \oplus 0.7\%$	± 3.2	± 2.5
Hadronic calorimetry			
barrel and end-cap	$\sigma_E/E = 50\%/\sqrt{E} \oplus 3\%$	± 3.2	± 3.2
forward	$\sigma_E/E = 100\%/\sqrt{E} \oplus 10\%$	$3.1 < \lvert\eta\rvert < 4.9$	$3.1 < \lvert\eta\rvert < 4.9$
Muon spectrometer	$\sigma_{p_T}/p_T = 10\%$ at $p_T = 1 TeV$	± 2.7	± 2.4

Table 2.2: General performance goals of the ATLAS detector [15].

missing transverse energy E_T^{miss}: $E_T^{miss} = |\overrightarrow{p}_T^{miss}|$, $\overrightarrow{p}_T^{miss} = -\sum_{i=1}^{N} \overrightarrow{p}_{T,i}^{vis}$, where $\overrightarrow{p}_{T,i}^{vis}$ is the momentum of a detected particle and N is the total number of detected particles.

2.3.1 Inner detector

The high bunch-crossing rate of 40 MHz imposes rigorous requirements on the ATLAS detectors. The Inner Detector (ID), which is closest to the collision point and responsible for the tracking of charged particles in ATLAS, is designed to withstand such high rate of collisions and to provide pattern recognition, primary and secondary vertex measurements as well as momentum measurement for charged particles within $|\eta| < 2.5$. The ID consists of three sub-detectors: the Pixel detector, the Semiconductor Tracker (SCT) and the Transition Radiation Tracker (TRT). The structure and components of the Inner Detector can be seen in Figures 2.5 and 2.6.

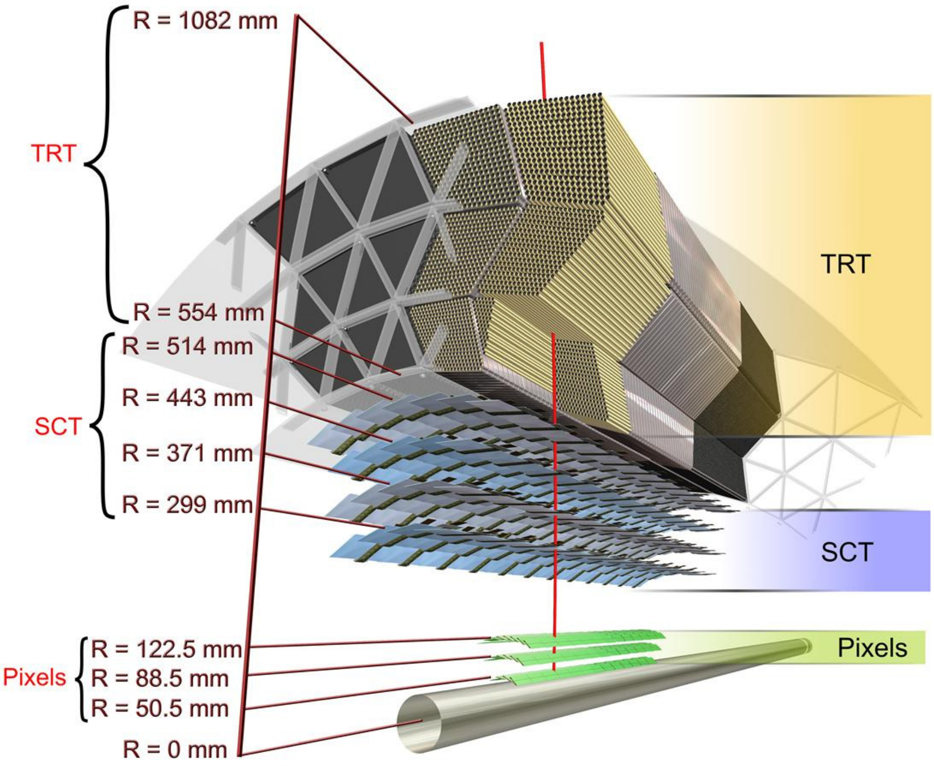

Figure 2.5: The barrel region of the ID is traversed by a charged track of $p_T = 10$ *GeV at* $\eta = 0.3$ *[15].*

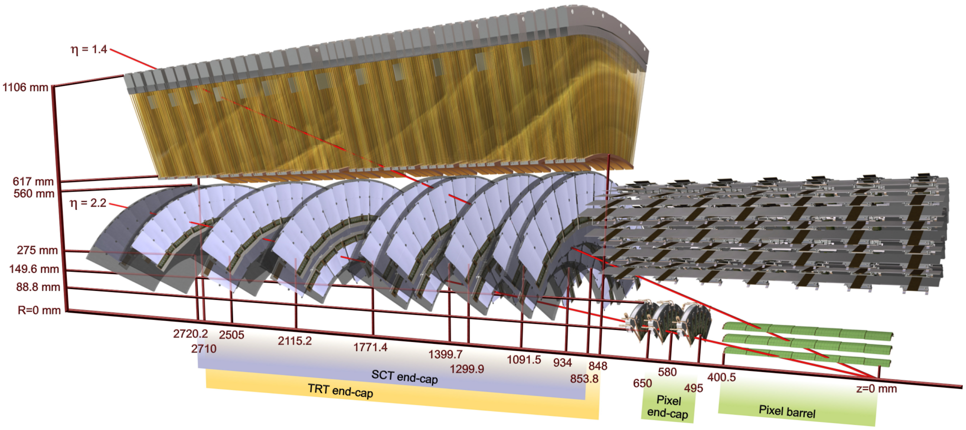

Figure 2.6: The end-cap region of the ID is traversed by two charged tracks of transverse momentum of $p_T = 10$ *GeV at* $\eta = 1.4$ *and 2.2 [15].*

The Pixel, SCT and TRT are immersed inside a 2 T solenoidal field in order to measure the charged particle momentum. A more detailed overview of the design resolution and technical performance of the Inner Detector can be found in [14, 15]. The main characteristics of the three ATLAS ID subdetectors are summarized in Table 2.3

Subdetector	Radius [cm]	Element size	Resolution	Hits/track in the barrel	Readout channels
Pixel	5 - 12	$50\mu m \times 400\mu m$	$10\mu m \times 115\mu m$	3	80×10^6
SCT	30 - 52	$80\mu m$	$17\mu m \times 580\mu m$	8	6×10^6
TRT	56 - 107	4 mm	$130\mu m$	30	3.5×10^5

Table 2.3: Summary of the main characteristics of the three ATLAS ID subdetectors [1].

The Pixel detector

The Pixel detector is a very high-granular and high-precision semiconductor based tracker. It is the closest detector to the beam pipe and is used to reconstruct the primary vertex and the displaced vertices such as those from *B* hadron decay in the environment of the very high particle multiplicity of the LHC collisions. It contains three layers and three disks on each end-cap. The detecting material is made of silicon with a thickness of 250 μm. In total, the pixel detector has 1744 modules. Each module contains 16 readout chips and other electronic components. The smallest unit that can be read out is a pixel, (50 in each 400 μm); there are roughly 47000 pixels per module. The intrinsic barrel spatial resolution is 10 μm and 115 μm in rϕ and z respectively.

The Pixel detector is currently fully operational and performing close to design specifications. The hit efficiency (the probability to register a hit given an incident particle) is above 98%. The noise occupancy is at a low level of 10^{-9} hits/pixel/bunch-crossing, well below the 10^{-7} requirement [88].

The Semiconductor Tracker

The Semi-Conductor Tracker (SCT) is the middle component of the Inner Detector arranged in four double layers of silicon strips. It is the most critical part of the Inner Detector for basic tracking in the plane perpendicular to the beam. It consists of 4088 modules of silicon strip detectors. The intrinsic accuracies per module in the barrel are 17 μm and 580 μm in $r\phi$ and z [15]. The total number of readout channels in the SCT is approximately 6.3 million.

The SCT is currently fully operational and meeting the design requirements. The noise occupancy is in good agreement with simulation. The hit efficiency for the barrel layers is 99.8% above the design goal of 99% [88].

The Transition Radiation Tracker

The Transition Radiation Tracker (TRT) is a gaseous drift (straw) tube detector. The main goals of the TRT are to enhance the tracking capability of the ID and to provide particle identification, in particular by identifying electrons from pions and other charged particles. The TRT uses 351 000 straw detectors, which are about 150 cm long, located axially in the barrel and radially in the end-caps. It provides $R-\phi$ information, but has no or little spatial resolution in the z-direction. A large number of position measurements are acquired for each track: on average 36 in the barrel and over 40 in the end-caps. This is due to the small diameter of the straw as well as to the fact that the sense wires are isolated within separate gas volumes. An important functionality of the TRT is based on detection of transition radiation photons which are created in the gas by traversing charged particles. This is made possible by using a gas containing 70% xenon to detect the transition-radiation photons which are created in between the straws. Electrons can thus be distinguished from pions through their transition radiation emissions. For momenta above a few GeV, electrons have a much higher probability of depositing an energy greater than a certain threshold in comparisons with pions with the equivalent momentum. The TRT, in addition to the Pixel detector, uses the Time-over-Threshold technique to measure dE/dx to carry out particle identification for heavily ionizing particles. The TRT hit reconstruction efficiency is about 94% for data and 95% for simulation [88].

In order to fully exploit the excellent spatial resolution of each subdetectors in the Inner Detector, an alignment procedure has to be applied to accurately determine their position and orientation. Alignment of the Inner Detector geometry is implemented using a track-based approach, where alignment and track parameters are derived from the minimisation of a global chi-square, which consists of track-to-hit distances known as residuals. An example of the benefit from the updated alignment of the Inner Detector is shown in Figure 2.7 with the better agreement between data and MC of the invariant mass distribution of $Z \to \mu\mu$ decays. In this figure the mass is reconstructed using track parameters from the Inner Detector track of the muons.

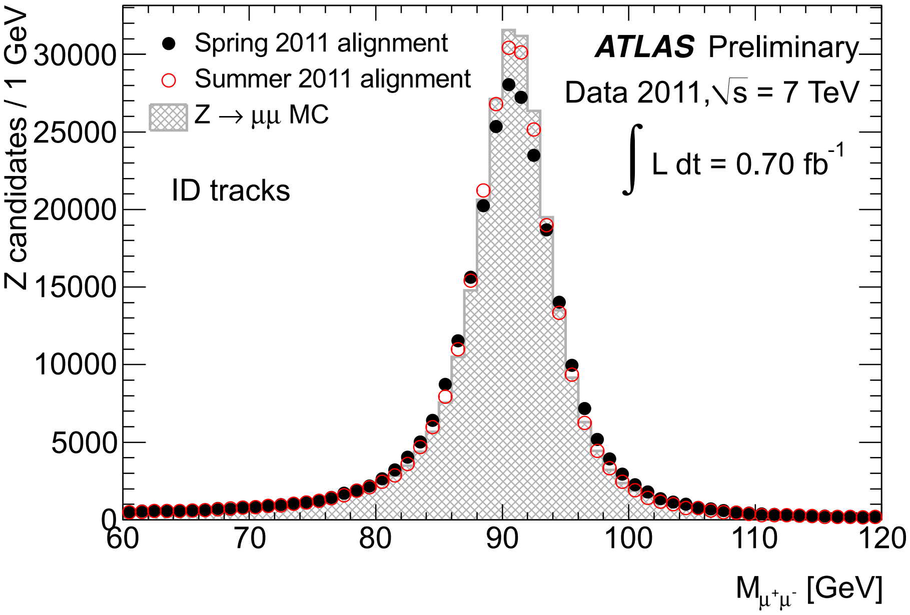

Figure 2.7: Invariant mass distribution of $Z \to \mu\mu$ decays, where the mass is reconstructed using track parameters from the Inner Detector track of the muons, using about 702 pb-1 of data collected during spring 2011. Ideal alignment performance based on Monte Carlo is compared to observed performance of data processed with spring 2011 alignment (full circles) and data processed with updated alignment constants in summer 2011 (open circles) [99].

The tracking performance of the Inner Detector was assessed via the observation of well measured particle decays, like K_s^0, ϕ, D mesons and Ω, Ξ, Λ baryons and Z boson. Clear signals of all these resonances were obtained in data. Figure 2.8 shows two examples of such particles namely the reconstruction of K_s^0 decaying into a pair of pions and the J/ψ decaying into a pair of muons. Those studies allowed the momentum scale to be determined at the per mill level for the low transverse momentum region, and for higher momentum at the percent level (for momentum up to 100 GeV). In the low transverse momentum region the resolution was found as expected to be dominated by multiple scattering.

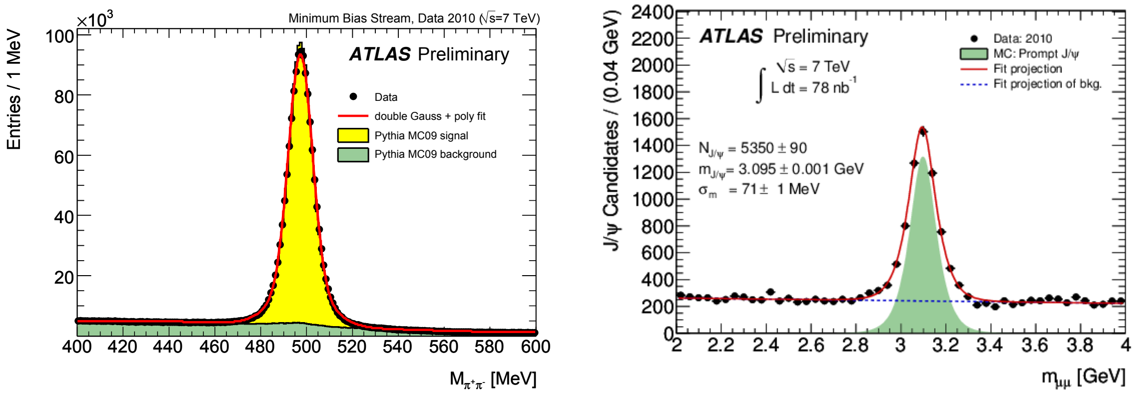

(a) (b)

Figure 2.8: a) Reconstruction of K_s^0 invariant mass in the barrel region (both tracks are in $|\eta| < 1.2$). The black circles are the data, while the histograms show the Monte Carlo simulation (normalized to the data). The red line is the line-shape function fitted to data [9]. b) Di-muon invariant mass spectrum at the J/ψ mass range [8].

2.3.2 Calorimeters

In the highly granular ATLAS calorimetry system, electrons, photons and hadrons (often forming a jet) shower and deposit their energy, which can then be measured. Since electromagnetic and hadronic objects interact differently with matter, they need to be treated by two different systems: the electromagnetic and the hadronic calorimeters. The electromagnetic (EM) calorimeter is used to identify and measure the energy of electrons and photons, while the hadronic calorimeter is used for the identification and the energy measurement of hadrons. The EM calorimeter, the end-cap and the forward components of the hadronic calorimeters use a highly granular liquid argon technique (LAr). The barrel of the hadronic calorimeter consists of a Tile Calorimeter. The overall pseudorapidity coverage is $|\eta| < 4.9$. An illustrative overview of the different components of the ATLAS calorimetry system is shown in Figure 2.9.

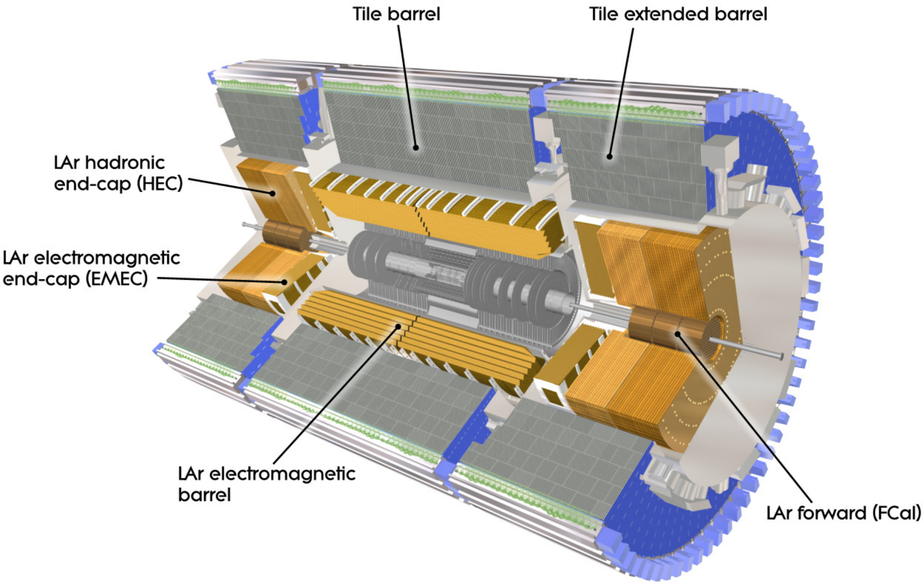

Figure 2.9: The ATLAS calorimeter layout [15].

In order to have precise measurements of electrons, photons, jets and E_T^{miss}, calorimeters must contain all final state particles (except muons). The calorimeter depth is therefore an important quality. Approximately 9.7 interaction lengths (λ) of active calorimeter in the barrel (10 λ in the end-caps) ensures good E_T^{miss} resolution, which is particularly important for beyond SM searches, such as searches for SUSY particles. The total thickness, including 1.3 λ from the outer support, is 11 λ at $\eta = 0$ which is sufficient to provide good resolution and punch-through reduction for high energy jets.

LAr electromagnetic calorimeter

The EM calorimeter [15] consists of a barrel ($|\eta| < 1.475$) and two end-cap components ($1.375 < |\eta| < 3.2$), with a transition region at $1.37 < |\eta| < 1.52$. The barrel is divided into two identical parts of length 3.2 m with a 4 mm gap separating them at $z = 0$. The calorimeter uses liquid argon as detector medium with lead plates as absorbing medium. Liquid argon has been chosen for its intrinsic linear behaviour, its stability of response over time and its intrinsic radiation-hardness . An accordion geometry has been chosen for the absorbers since such a geometry naturally provides full azimuthal coverage without any gap together with a fast signal extraction at the rear or at the front of the electrodes. In the barrel, the accordion waves are axial and run in ϕ (see Figure 2.10(a)). In the end-caps, the waves are parallel to the radial direction and run axially (see Figure 2.10(b)).

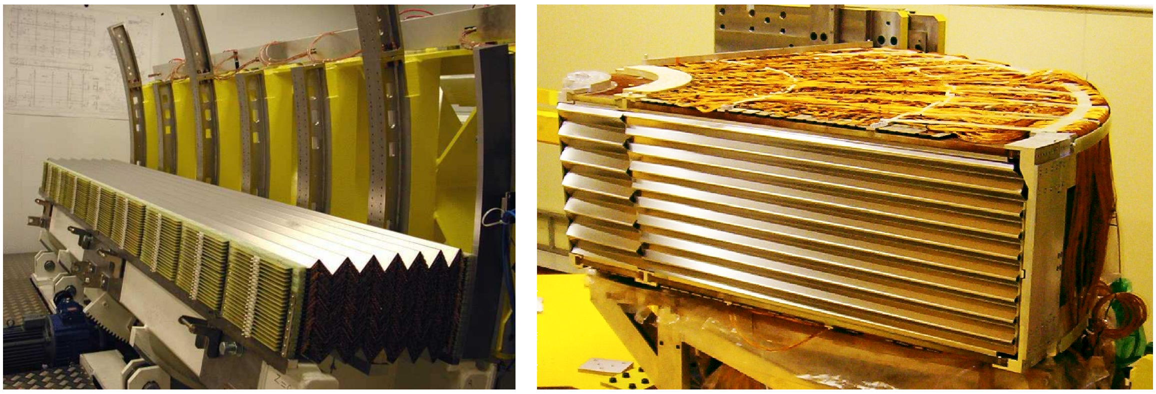

(a) The Barrel

(b) The End-Cap

Figure 2.10: The accordion shape in the Barrel and End-Cap of the EM calorimeter.

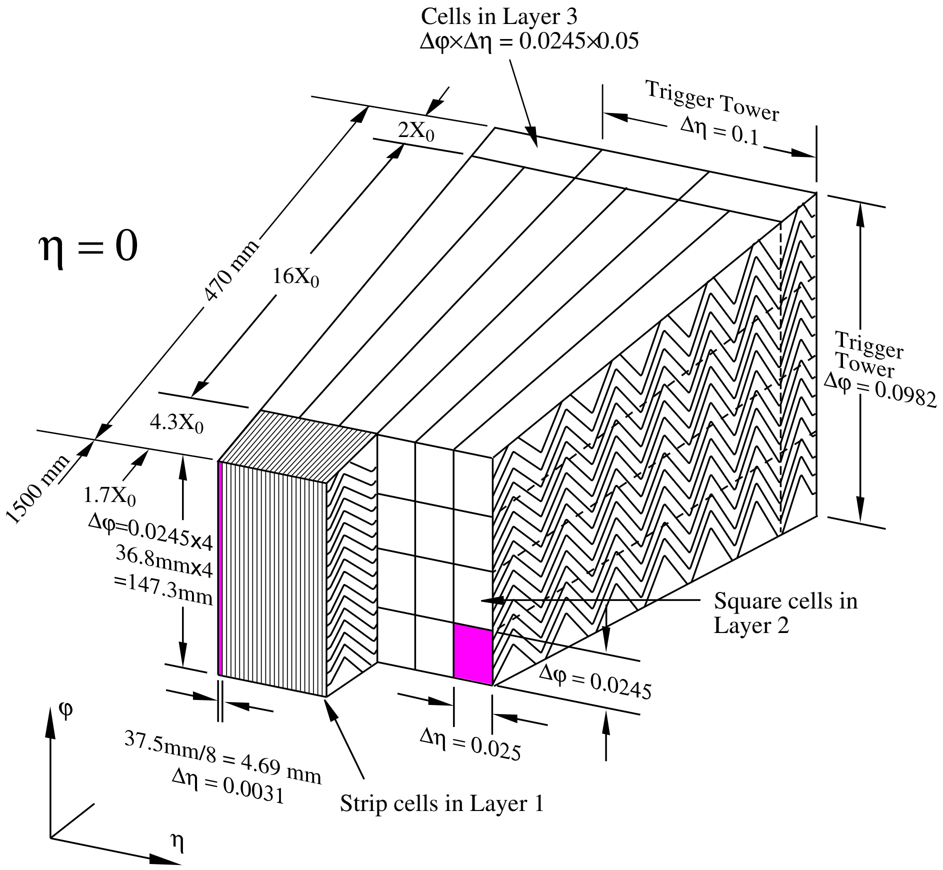

Figure 2.11: The granularity in η and ϕ of the cells in three layers of the EM Barrel Calorimeter [15].

	Barrel		End-cap	
Pre-sample	0.025×0.1	$\|\eta\| < 1.52$	0.025×0.1	$1.5 < \|\eta\| < 1.8$
Calorimeter				
1st layer	$0.025/8 \times 0.1$	$\|\eta\| < 1.40$	0.050×0.1	$1.375 < \|\eta\| < 1.425$
	0.025×0.025	$1.4 < \|\eta\| < 1.475$	0.025×0.1	$1.425 < \|\eta\| < 1.5$
			$0.025/8 \times 0.1$	$1.5 < \|\eta\| < 1.8$
			$0.025/6 \times 0.1$	$1.8 < \|\eta\| < 2.0$
			$0.025/4 \times 0.1$	$2.0 < \|\eta\| < 2.4$
			0.025×0.1	$2.4 < \|\eta\| < 2.5$
			0.1×0.1	$2.5 < \|\eta\| < 3.2$
2nd layer	0.025×0.025	$\|\eta\| < 1.40$	0.050×0.025	$1.375 < \|\eta\| < 1.425$
	0.075×0.025	$1.4 < \|\eta\| < 1.475$	0.025×0.025	$1.425 < \|\eta\| < 2.5$
			0.1×0.1	$2.5 < \|\eta\| < 3.2$
3rd layer	0.050×0.025	$\|\eta\| < 1.35$	0.050×0.025	$1.5 < \|\eta\| < 2.5$
TileCal				
First two layers	0.1×0.1	$\|\eta\| < 1.0$	0.1×0.1	$0.8 < \|\eta\| < 1.7$
Last layer	0.2×0.1	$\|\eta\| < 1.0$	0.2×0.1	$0.8 < \|\eta\| < 1.7$
Hadronic end-cap				
First two layers			0.1×0.1	$1.5 < \|\eta\| < 2.5$
Last layer			0.2×0.2	$2.5 < \|\eta\| < 3.2$

Table 2.4: Granularity of the EM and hadronic calorimeters for $\Delta\eta \times \Delta\phi$ versus $|\eta|$ [15].

The calorimeter modules are divided longitudinally into three layers (strip, middle and back layers). The typical granularity of a barrel module is shown in Figure 2.11. The strip layer is finely segmented in η in order to measure the direction with higher precision. The middle layer contains most of the energy in the shower and the back layer is designed to contain the electromagnetic shower. Due to the large amount of material between the Inner Detector and the Calorimeters, a presampler is installed at $|\eta| < 1.8$ to determine the energy loss. The different setup in the different regions of the detector leads to a uniform performance in terms of linearity and resolution as a function of ϕ. The granularity of the entire calorimeter system for different $|\eta|$ is summarized in Table 2.4.

The LAr calorimeters are read out via a system of custom electronics. An overview of the ATLAS LAr readout electronics is shown in Figure 2.12. The electronic readout is divided into a Front End (FE) system of circuit boards mounted in custom crates directly on the detector cryostats, and a Back End (BE) system of VME-based boards located off the detector, outside the detector hall. The FE system includes Front End Boards (FEBs), (which perform the readout and digitization of the calorimeter signals), calibration boards (which inject precision calibration signals), layer sum boards (which produce analog sums for the Level 1 (L1) trigger system), and control boards which receive and distribute the 40 MHz LHC clock (in the designed performance) as well as other configuration and control signals. The BE electronics are made up primarily of Read Out Driver (ROD) boards which receive the digitized signals from the FEBs over 1.6 Gbps optical links. The RODs perform digital filtering, formatting, and monitoring of the calorimeter signals before transmitting the processed data to the ATLAS data acquisition system (DAQ).

The ATLAS LAr calorimeters are finely segmented, with a total of 182,468 channels to be read out. With each FEB handling up to 128 channels, a total of 1524 FEBs are required. The on-detector FE electronics have been built to withstand the high levels of radiation which result from the collisions of the intense LHC beams. They are fully operational and meet the design requirements.

An example of the ATLAS LAr readout electronic performance during 2011 collision is represented by the noise level. Figure 2.13(a) shows the noise measurement for a run with the mean number of inelastic collisions per crossing of $<\mu>\sim 14$. The ratio between the data and the MC results is shown in Figure 2.13(b).

The design resolution for the LAr EM calorimeter, obtained from test beam studies, is shown in Table 2.2. The EM energy scale and resolution of the electromagnetic calorimeter can be determined by

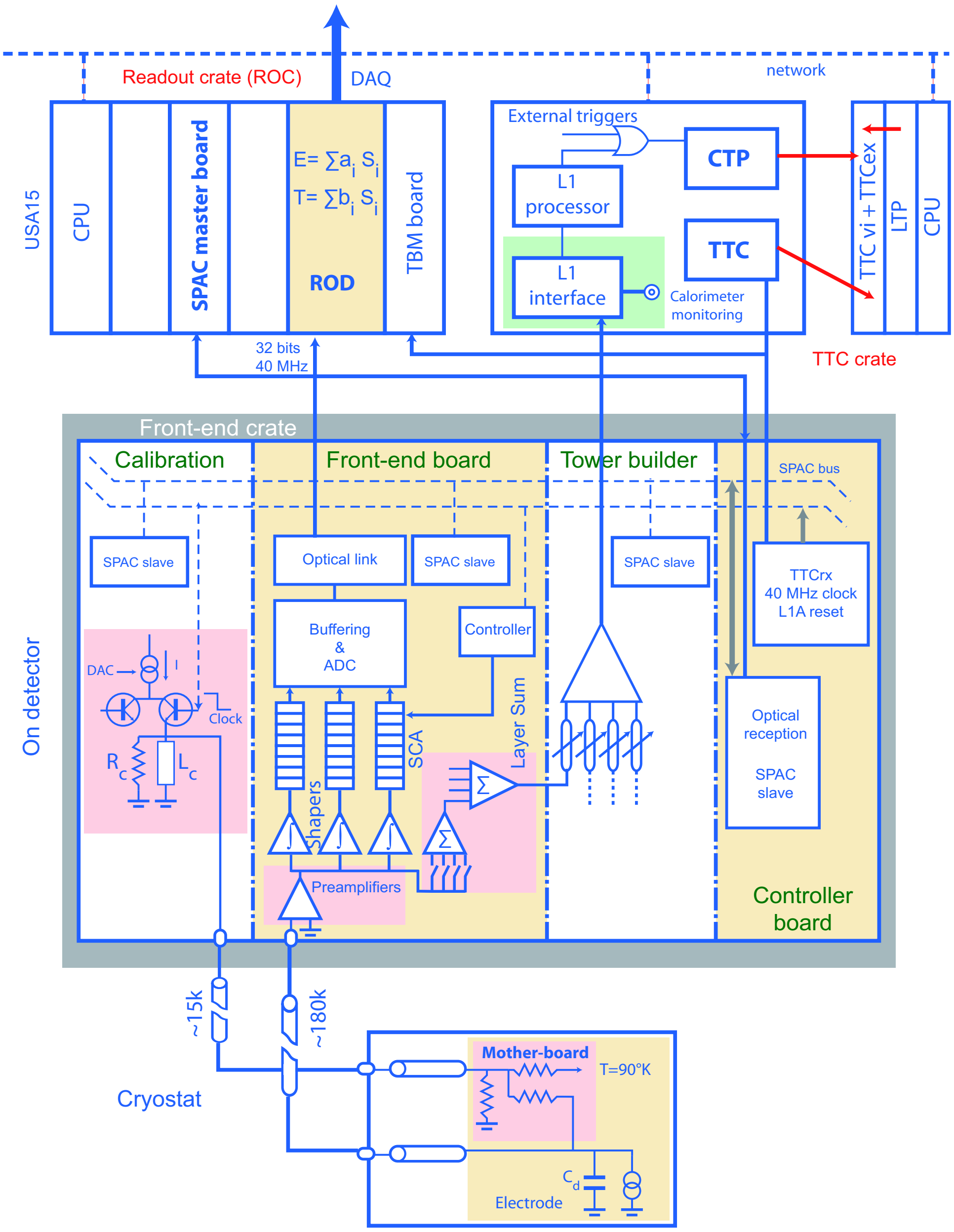

Figure 2.12: In this schematic drawing depicting the overall architecture of the ATLAS LAr readout electronics, the LAr detectors are located at the bottom. The LAr ionization signal proceed upwards, through the FE crates mounted on the detector to an off-detector processing center. central trigger processor (CTP) [15].

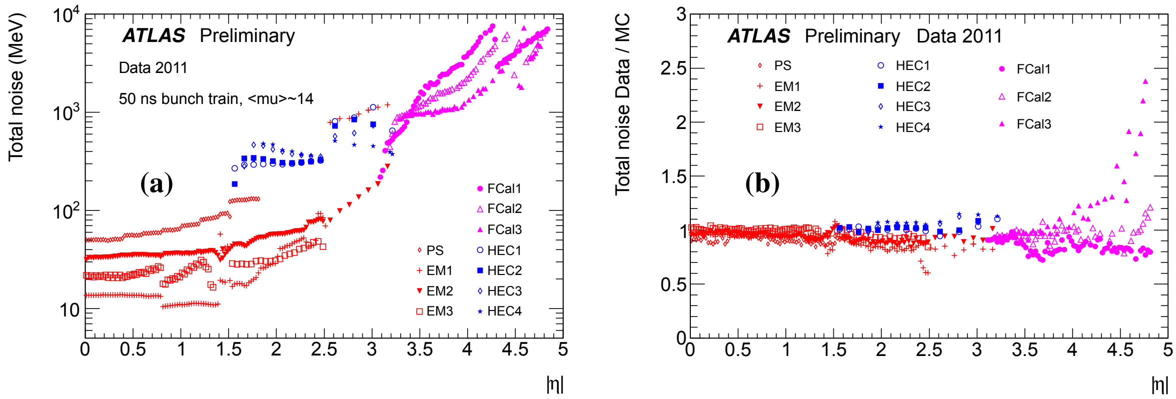

Figure 2.13: Total noise (electronics and pileup) in data for a run with $<\mu>\sim 14$ at the electron scale (a) and the ratio between data and MC (b) [5].

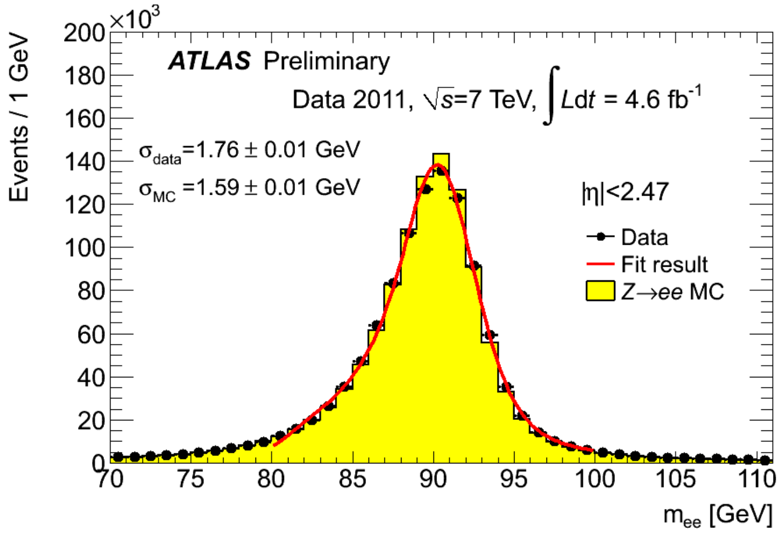

Figure 2.14: Calibrated $Z \to e^+e^-$ invariant mass: all pairs [31].

reconstructing the invariant mass of di-photon or di-electron from π_0 and Z decays respectively. Using 4.6 fb-1 of 2011 data, the Z boson decaying into a pair of electrons was used to determine the EM energy scale and resolution [31]. Events with two opposite-sign reconstructed electrons with $E_T > 25 GeV$, $|\eta| < 2.47$ (the transition region $1.37 < |\eta| < 1.52$ excluded) and passing medium identification criteria are selected. Over a million Z candidates are used within the di-electron mass window [80,100] GeV. The method [17] constrains the observed di-electron invariant mass distribution to follow the Z lineshape obtained from Monte Carlo where the resolution constant term was set to zero. The method has been applied to 26 electromagnetic calorimeter pseudo-rapidity regions. The energy corrections applied to the electrons are within 0.5% in the barrel region, and within 1% in the endcaps. The mass peak resolution has been determined by fitting the distributions with a Breit-Wigner function convoluted with a Crystal Ball function. A good agreement of the $Z \rightarrow ee$ reconstruction in the data and the MC after correcting the electron energy is shown in Figure 2.14. The corrections of the electron energy scale and resolution are required for any analysis using electron objects. More details on electron energy scale and resolution, measured with Z boson decays in data, can be found in Chapter 3.

Hadronic calorimeters

The main goal of the hadronic calorimeters is to provide accurate energy measurements of jets and of the missing transverse energy. They must therefore be sufficiently thick and have a large coverage in $|\eta|$ in order to contain the hadronic shower. The hadronic calorimeter system consists of a barrel Tile Calorimeter (TileCal) and LAr hadronic end-cap and forward calorimeters for higher pseudorapidity where the radiation is more intense. The hadronic end-caps (HECs) and the forward calorimeter system (FCal) use the same LAr technology as the EM calorimeter and share the cryostat. The FCal extends the pseudorapidity coverage up to $|\eta| = 4.9$. It consists of three layers: one for EM particle detection using copper plates as the absorber and an additional two layers for hadronic particle detection using tungsten plates as the absorber. The Tile Calorimeter, which is placed directly outside the EM and HEC calorimeters, consists of one central barrel ($|\eta| < 1.0$) and two extended barrels ($0.8 < |\eta| < 1.7$). The TileCal is a sampling calorimeter with steel as the absorber and plastic scintillating tiles as the active material. The tiles are placed in a periodic pattern, and every tile is connected via fiber optics to a photomultiplier on each side. The granularity of the hadronic calorimeters are shown in Table 2.4.

2.3.3 Muon spectrometer

The Muon Spectrometer (Figure 2.15) is a huge tracking system which defines the large dimensions of the ATLAS detector. It identifies muons, the only known final state charged particles emerging from the interaction point and traversing all other sub-dectectors. The Muon Spectrometer measures accurately the momenta of muons using the magnetic deflection of muon tracks in a large superconducting air-core toroid magnets, instrumented with separate trigger and high-precision tracking chambers. Over the range $|\eta| < 1.4$, the magnetic bending is provided by the large barrel toroid. For $1.6 < |\eta| < 2.7$, the muon tracks are bent by two smaller end-cap magnets inserted into both ends of the barrel toroid. Over the region $1.4 < |\eta| < 1.6$, usually referred to as the transition region, magnetic deflection is provided by a combination of barrel and end-cap fields. This magnet configuration provides a field which is mostly orthogonal to the muon trajectories, while minimising the degradation of resolution due to multiple scattering. In the barrel region, tracks are measured in chambers arranged in three cylindrical layers around the beam axis; in the transition and end-cap regions, the chambers are installed in planes perpendicular to the beam, also in three layers.

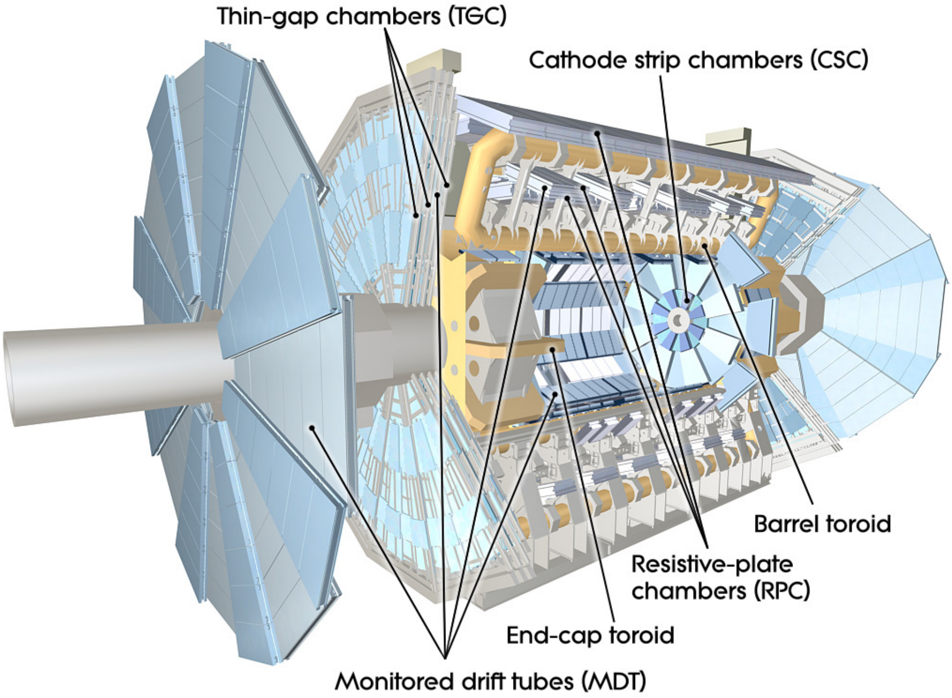

Figure 2.15: The muon spectrometer layout [15].

2.3.4 The magnet system

The magnet system (Figure 2.16) is used to bend charged particles so that their momenta can be measured. It contains two parts: the inner solenoid and the outer toroidal. The inner solenoid produces a 2 Tesla magnetic field surrounding the Inner Detector. The outer toroidal magnetic field is produced by eight very large air-core super-conducting barrel loops and two end-caps, all situated outside the calorimeters and within the muon system. This magnetic field is 26 metres long and 20 metres in diameter.

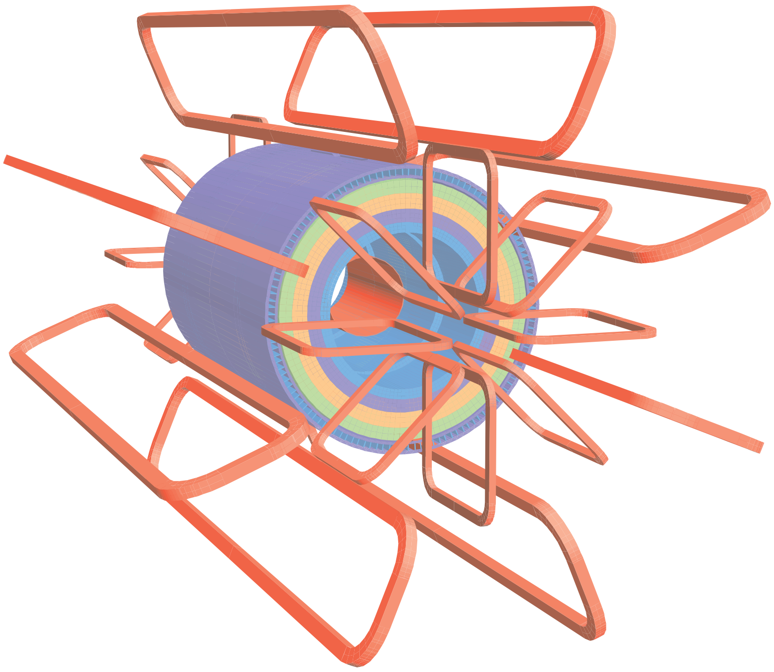

Figure 2.16: Geometry of magnet windings and tile calorimeter steel. The eight barrel toroid coils, with the end-cap coils interleaved are visible. The solenoid winding lies inside the calorimeter volume [15].

2.3.5 Trigger system and data acquisition

An efficient trigger system is of fundamental importance for the LHC detectors due to two main reason: first, each collision produces a huge background with almost particles of low energy, the physics (signals) with higher energy need to be extracted; second, the hardware recording the data has intrinsic limitations in bandwidth and is not able to store all the collision events.

In the ATLAS experiment, the trigger system filters the data recorded by selecting events of interest from the different subdetectors. The trigger system has three distinct levels: L1, L2, and the event filter. Each trigger level refines the decisions made at the previous level and, where necessary, applies additional selection criteria. The data acquisition system receives and buffers the event data from the detector-specific readout electronics, at the L1 trigger accepted rate, over 1600 point-to-point readout links. The first level uses a limited amount of the total detector information to make a decision in less than 2.5 μs, reducing the rate to about 75 kHz. The two higher levels access more detector information for a final rate of up to 200 Hz with an event size of approximately 1.3 Mbyte [3]. An overview of the Trigger-DAQ (TDAQ) system in ATLAS is shown in Figure 2.17, more details in [3, 15].

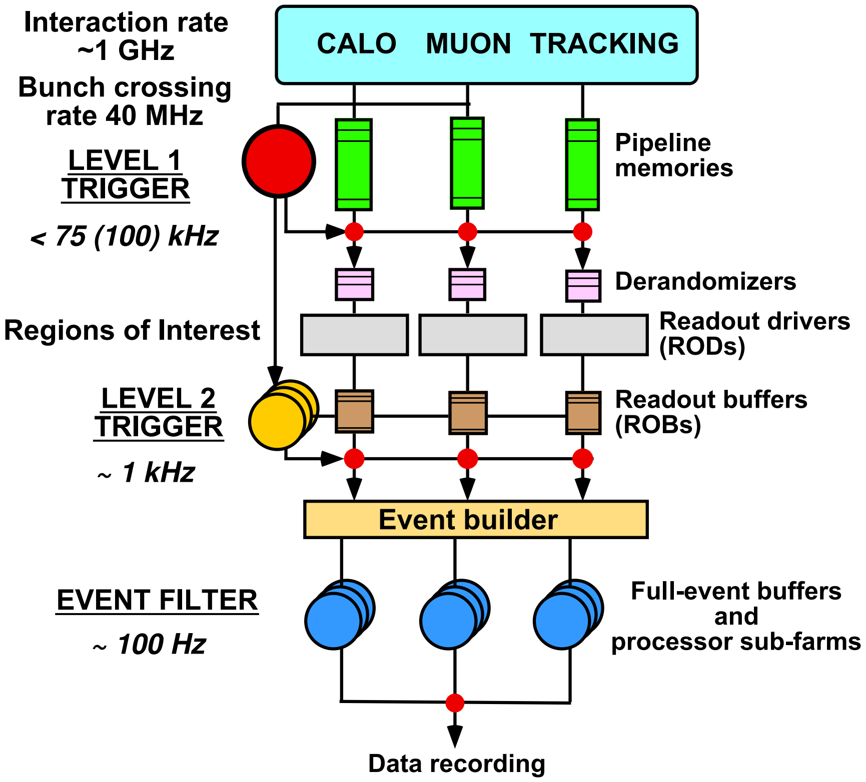

Figure 2.17: Block diagram of the Trigger/DAQ system [3].

First level trigger

The Level 1 (L1) trigger makes the initial decision whether or not to pass on the data to the next trigger level, for each of the individual collision events. The data that passes the L1 trigger is initially stored in so-called pipeline memories. Because of the limited size of the memories together with the relatively long time-of-flight until the muon spectrometers are reached, the decision has to be made in a very limited time-scale 2.5 μs. The L1 selection of events is therefore only based on reduced resolution information from the trigger systems in the muon spectrometer and the calorimeters. The L1 trigger searches for objects like high transverse-momentum muons, electrons, photons, jets, and τ- leptons decaying into hadrons, as well as large missing and total transverse energy. The location where one of these objects is registered is then defined as a region of interest (RoI) for a potentially interesting event. The RoIs extend as a cone from the interaction point to the outer parts of the ATLAS detector. They include information on the type of feature identified and the criteria passed such as a threshold. This information is subsequently used by the high-level trigger.

In the case of electron analyses in 2011, a L1 electromagnetic trigger used a E_T threshold of 30 GeV for e/γ objects (electrons/photons). This trigger has a high rate so that the statistical uncertainty per luminosity block is low.

Second level trigger

Events selected by L1 are read out from electronic systems at the front-end of the detector into readout drivers (RODs) and further on into readout buffers (ROBs). The fragments of Read Out System (ROS), including multiple ROBs, are then joined and the full event is built for a Level 2 (L2). The Level 2 trigger scans the events from the ROBs, now reading the data with full-resolution using all subsystems within the RoI. The aim of the L2 trigger is then to reduce the event rate from L1 by two orders of magnitude. This can be obtained by applying restrictions on the information available within the RoIs. The decision time for this step of the trigger system is on average about 40 ms, which is a significantly longer time scale than the one for the L1 trigger. The L2 trigger menus are designed to reduce the data rate to 3.5 kHz, which is made possible due to the buffering of events in a multiprocess system [3].

Event filter

The data accepted by the L2 trigger system is further passed on to the Event Builder (EB), which performs a full reconstruction of the event and sends it to the final stage of the ATLAS trigger system, the Event Filter (EF). The EF reduces the event rate to approximately 200 Hz with an event size of approximately 1.3 Mbyte [3]. The data passed by the EF is then to be used in the offline analysis. This level of the trigger is commonly denoted as the high level trigger (HLT). The total rejection factor of the whole ATLAS trigger system reaches a factor of about 5.10^6.

Event processing

The events recorded by the Event Filter need to be processed in order to reduce their memory size before being used in an offline physics analysis. The data from the HLT is first stored as object based RAW format, which undergoes event reconstruction by the offline software used in ATLAS known as Athena [2]. A similar chain applies to the simulated data, where the events first pass through a GEANT4 [26] simulation of the ATLAS detector before physics objects can be reconstructed.

Chapter 3

The event reconstruction in the ATLAS experiment

The analysis of this thesis uses electrons as final state particles, therefore this chapter reviews the ATLAS electron reconstruction and identification algorithms and their performance. A study of the calibration for the reconstruction of the Liquid Argon cell energy performed by the author will be described in Section 3.1.2.

In the ATLAS detector, electrons first cross the ID producing tracks, then the EM calorimeter where they deposit their energy. Therefore an electron is reconstructed requiring a track matched to an electromagnetic cluster. Sets of identification requirements need to be applied to select good electron candidates since jets can fake electrons. The multi-jet cross section is much higher ($\sim 10^5$ times) than the cross section of events with high transverse momentum electrons and a huge background from jets is then expected. These identification cuts are optimized by comparing the gain in background rejection and the loss in signal efficiency.

The electron selection efficiency, energy scale and energy resolution need to be taken into account in the analysis. These quantities are measured with data driven methods and compared with MC predictions. Corrections are derived and applied to the MC. The uncertainties on these corrections contribute to the systematic uncertainties of the final measurement. The measurements of electron selection efficiency, energy scale and resolution in the central region of the EM calorimeter corresponding to $|\eta| < 2.47$ are briefly described in Section 3.5, 3.6.1, 3.6.2 [17].

3.1 Energy reconstruction in Calorimeters

3.1.1 Cell energy reconstruction

After passing the ID, an electron emerging from the collision point meets the EM Calorimeters and produces an electromagnetic shower. The ionisation of the liquid argon in the high-voltage potential happens in the gap between two absorber plates and a triangular current pulse is produced (see Figure 3.1). In the Front End Boards, the raw signals are splitted in three overlapping linear gain scales in order to match the detector capacitances and dynamic ranges of the calorimeter sections: 1 for low gain ($200-2000$ GeV in physics), 9,9 for medium gain ($20-200$ GeV), 93 for high gain ($0-20$ GeV) in the second layer of the barrel electromagnetic calorimeter. Each signal is then amplified, shaped, sampled, stored on a capacitor and waiting for the trigger decision. For triggered events, a number of samples N_{sample} per channel is read out. The typical choice of five samples represents a compromise between the noise reduction achieved using an optimal filtering coefficient method and the amount of data that must be digitized and processed in real time.

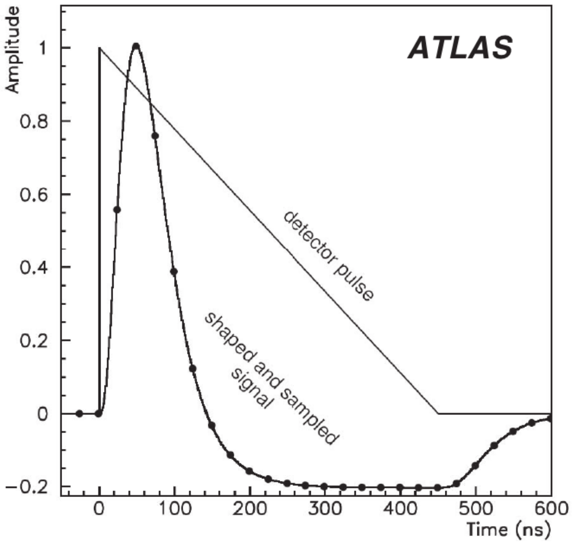

Figure 3.1: Shapes of the LAr calorimeter current pulse in the detector and of the signal output from the shaper chip. The dots indicate an ideal position of samples separated by 25 ns [23].

The ROD reconstructs the amplitude (A) of the signal pulse in ADC (Analog-to-Digital Converter) counts, as well as the time offset of the deposition. Then the reconstructed pulse amplitude A is converted to the deposited energy (E) in MeV using the formula below [23]:

$$E = F_{\mu A \to MeV} \times F_{DAC \to \mu A} \times \frac{1}{\frac{M_{phys}}{M_{cali}}} \times \sum_{j=(0,1)}^{N_{ramps}} G_j A^j. \tag{3.1}$$

The factor $F_{\mu A \to MeV}$ relates the ionization current to the energy deposited in the calorimeter, the value for each channel determined from test beam data using production calorimeter modules and a detailed detector simulation has been validated using high-statistics samples of $Z \to ee$ decays in collisions. The factor $F_{DAC \to \mu A}$ converts the Digital-to-Analog Converter (DAC) setting of the calibration board to the injected current, and is determined from known parameters of the calibration boards and injection resistors. The factor $\frac{M_{phys}}{M_{cali}}$ quantifies the ratio of response to a calibration pulse and an ionization pulse corresponding to the same input current. The factor G_j is the electronic gain of the channel, which is determined from electronic calibration runs. The sum over j starts from $j = 0$ in medium and low gain only, while in high gain, $j = 1$ is the first term used. N_{ramps} is the order of the polynomial function used in the "ramp fits". The ramp fits determining the electronic gains G_j are explained in the following section.

3.1.2 Ramp fit study

To perform the electronic calibration, each cell of the LAr Electromagnetic Calorimeter is pulsed N times ($N = 100$) with a set of given input currents. The signal produced by the calibration board is an exponential pulse with a decay time chosen to match the physics signal triangular shape for the nominal high voltage as shown in Figure 3.1. The amplitude of the signal is controlled by a 16 bit DAC, providing a voltage between 0 and 1 V by a step of $15.26\mu V$. It means the DAC value is chosen between 0 and 65535. The signal is passed through a pre-amplifier and a shaper, and is sampled by 12 bit ADC. The ADC value is in the range $\sim 0-4095$ and has a pedestal of about 1000 ADC counts to accommodate the undershoot of the shaper. This procedure is called "ramp runs".

In normal operation each pulse (signal) is sampled $N_{samples} = 5$ times by the electronic read out of the calorimeter and each time the ADC value is read. One then computes the mean of these ADC values over the N triggers for each sample. In this way one obtains an averaged calibration shape for each DAC value and computes the peak of this average signal ADC_{peak} using a weighted sum over the $N_{samples}$ samples. The ramps will be extracted from the curves expressing the ADC_{peak} versus DAC by using a polynomial function. This is the so called "ramp fits":

$$DAC = G_0 + G_1 ADC_{peak}, \tag{3.2}$$

where G_0 and G_1 are the ramp coefficients (electronic gains) which are indicated as G_j in Formula 3.1. Normally a linear function is used to do ramp fits and the electronic gains are determined as the slope and the offset of the linear fit. An example of a ramp fit using a linear function for one channel is shown in Figure 3.2.

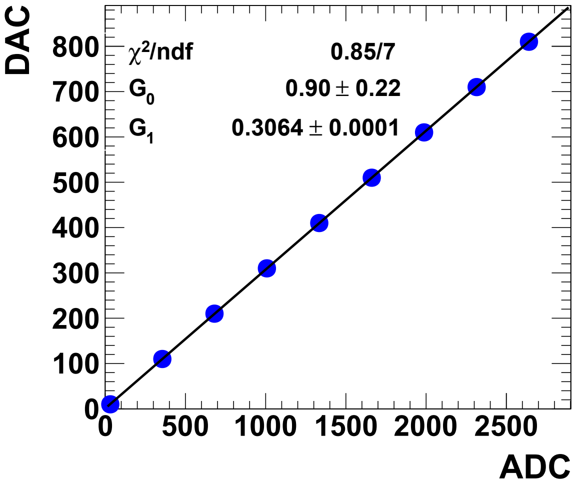

Figure 3.2: The ramp fit using a linear function for channel 65 in slot 11, feedthrough 0, side A of the second layer of the barrel of the electromagnetic calorimeter (EMB). The blue points are the injected DAC versus the output ADC (which is ADC_{peak} in Equation 3.2). The black line is the linear fit. The slope and the offset of the fit are shown.

At the beginning of data taking in $\sim 2009-2010$, some errors occured during data recording where one set of ADC values was lost (one of DAC values was not recorded). This has been then corrected but at that time it led to the question of the stability of the ramp fit depending upon the number of points used. The study presented here is to answer this question.

As a guideline to quantify the amplitude of the effect of lost DAC values on ramp fits, the calibration system requires this effect is below $\sim 0.1\%$. In order to study this effect, we redo the linear fit as in Figure 3.2 each time without one of DAC values. The slope of the new fit is compared with the original one with all DAC values. The variable $\Delta_{G_1} = (G_1^{lost\_DAC} - G_1^{full\_DAC})/G_1^{full\_DAC}$ quantifies this difference and is shown in Figure 3.3(a) for the same channel used in 3.2. The biggest effect is obtained by the point at $DAC_{lost} = 0$ with $\Delta_{G_1} \sim 0.07\%$. The same plot for all channels of side A of the barrel of the electromagnetic calorimeter is shown in Figure 3.3(b). The effect is large for $DAC_{lost} = 0$ and $DAC_{lost} = 500$. The projected distributions of Δ_{G_1} for these two DAC_{lost} values are shown in Figure 3.4.

There are two peaks in these distributions: one with a small effect ($|\Delta_{G_1}| < 0.1\%$ in Figure 3.4(a) , $|\Delta_{G_1}| < 0.05\%$ in Figure 3.4(b)) and one with a larger effect.

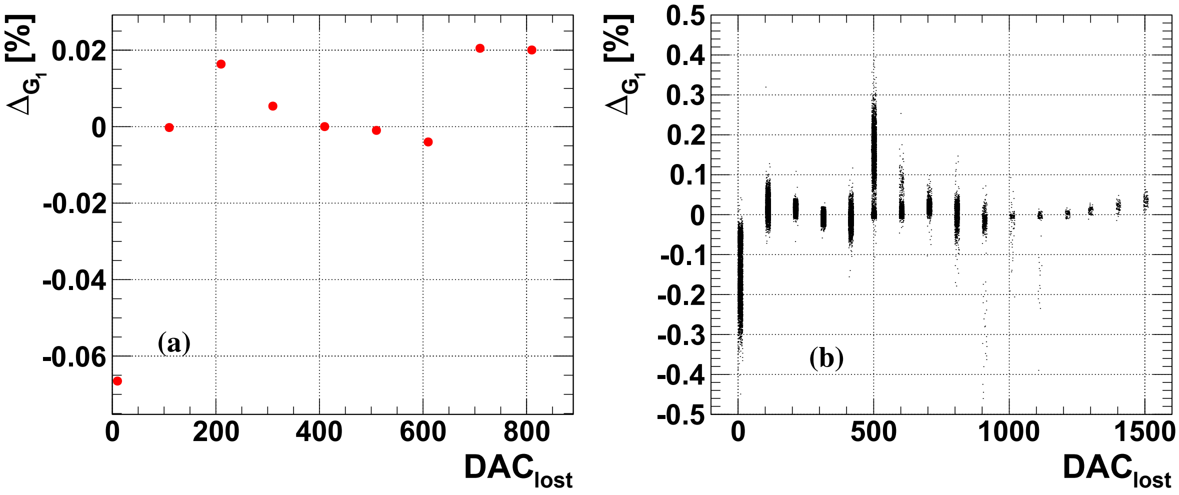

Figure 3.3: The variable Δ_{G_1} as a function of the lost DAC value DAC_{lost}, (a) for one channel, (b) for all channels of side A of the barrel electromagnetic calorimeter (EMBA) in high gain.

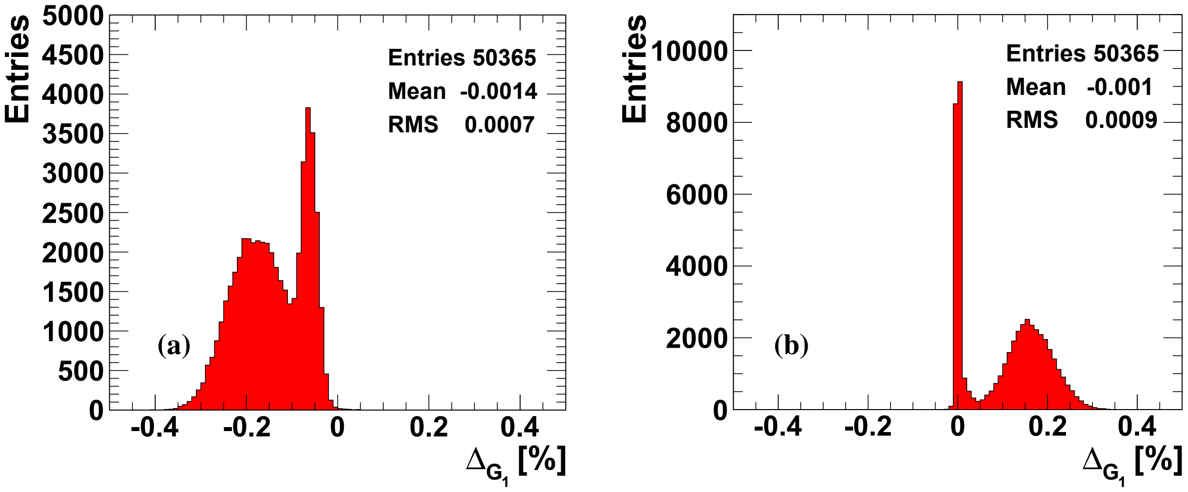

Figure 3.4: The projected distributions of Δ_{G_1} at $DAC_{lost} = 0$ (a) and at $DAC_{lost} = 500$ (b).

We recall that all channels of the barrel electromagnetic calorimeter are grouped in slots as following: the first layer corresponding to slots from 2 to 8; the second layer to slots from 11 to 14; the third layer to slot 9 and slot 10. We found that the larger effect comes from channels in slots from 2 to 8 which correspond to the first layer of EMB. The slot number of the channels with small and large effect at $DAC_{lost} = 0$ is shown in Figure 3.5.

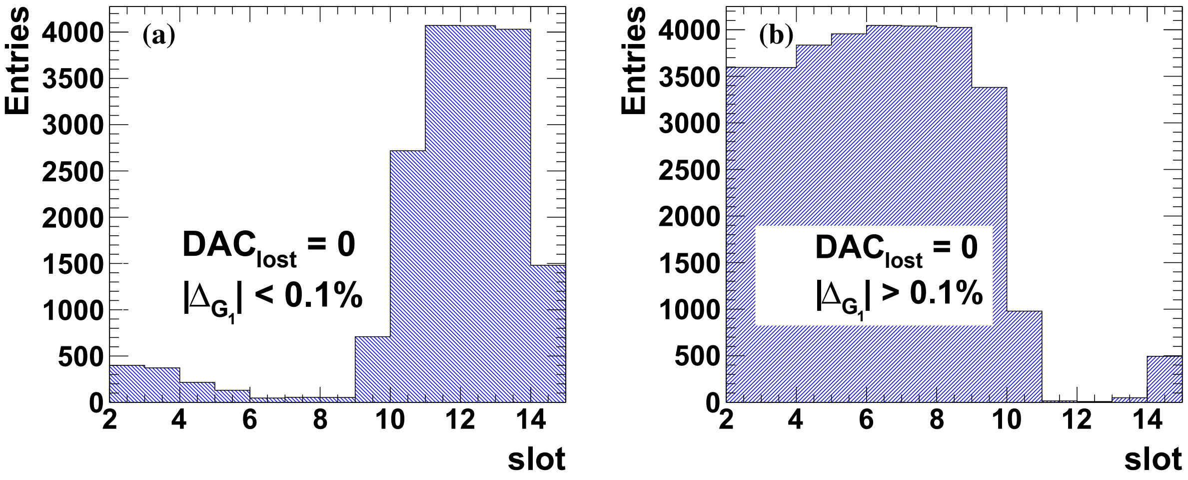

Figure 3.5: The position named slot of the channels with smaller (a) and larger (b) effect for $DAC_{lost} = 0$.

We also found that for channels in slots from 2 to 8 only 6 of 16 injected DAC values are not saturated and are used for ramp fits. That is the reason why the fit is more sensitive when the lost DAC value is the first or the last points in DAC range. The number of DAC values used for ramp fits versus the channel position is shown in Figure 3.6.

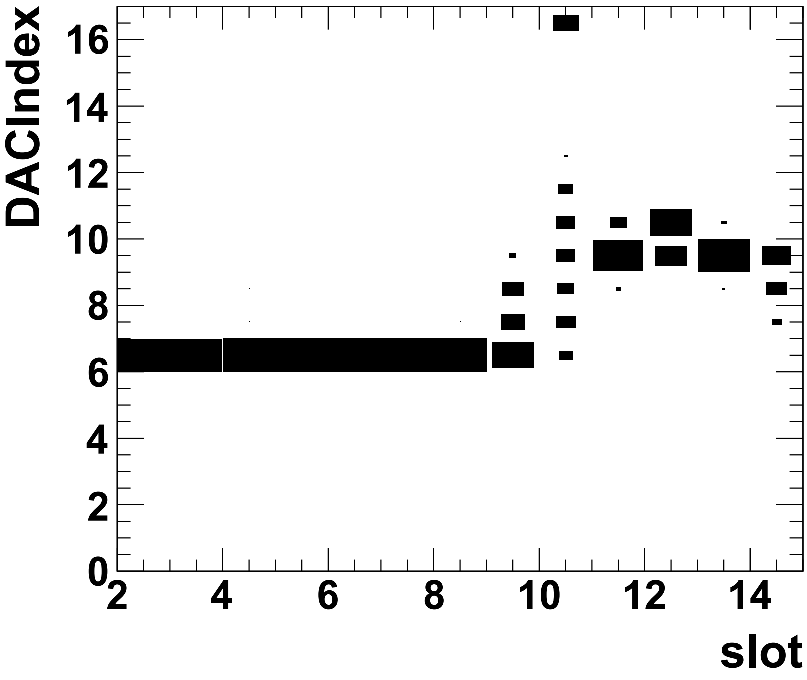

Figure 3.6: The number of DAC values used for ramp fits DACIndex versus the channel position slot.

The first conclusion of this study on EMB in high gain and medium gain is that the effect of the lost DAC values is significant 0.2% when the lost value corresponds to the first or to the last point of the fits especially if the fit is done for 6 (or less than 6) DAC values. This is the case for most channels of the first layer of EMB. This study suggests to increase the number of DAC values for channels in this layer to have more stable fits. This procedure is now applied by the electromagnetic calibration team.

The same study was done on EMB in low gain. The effect of the lost DAC values for channels in three layers of EMB in low gain is shown in Figure 3.7. This effect is dominated when the lost DAC value is the last one in the fit range and is at the level of 0.2% for the second layer, less than 0.15% for the first and the third layers.

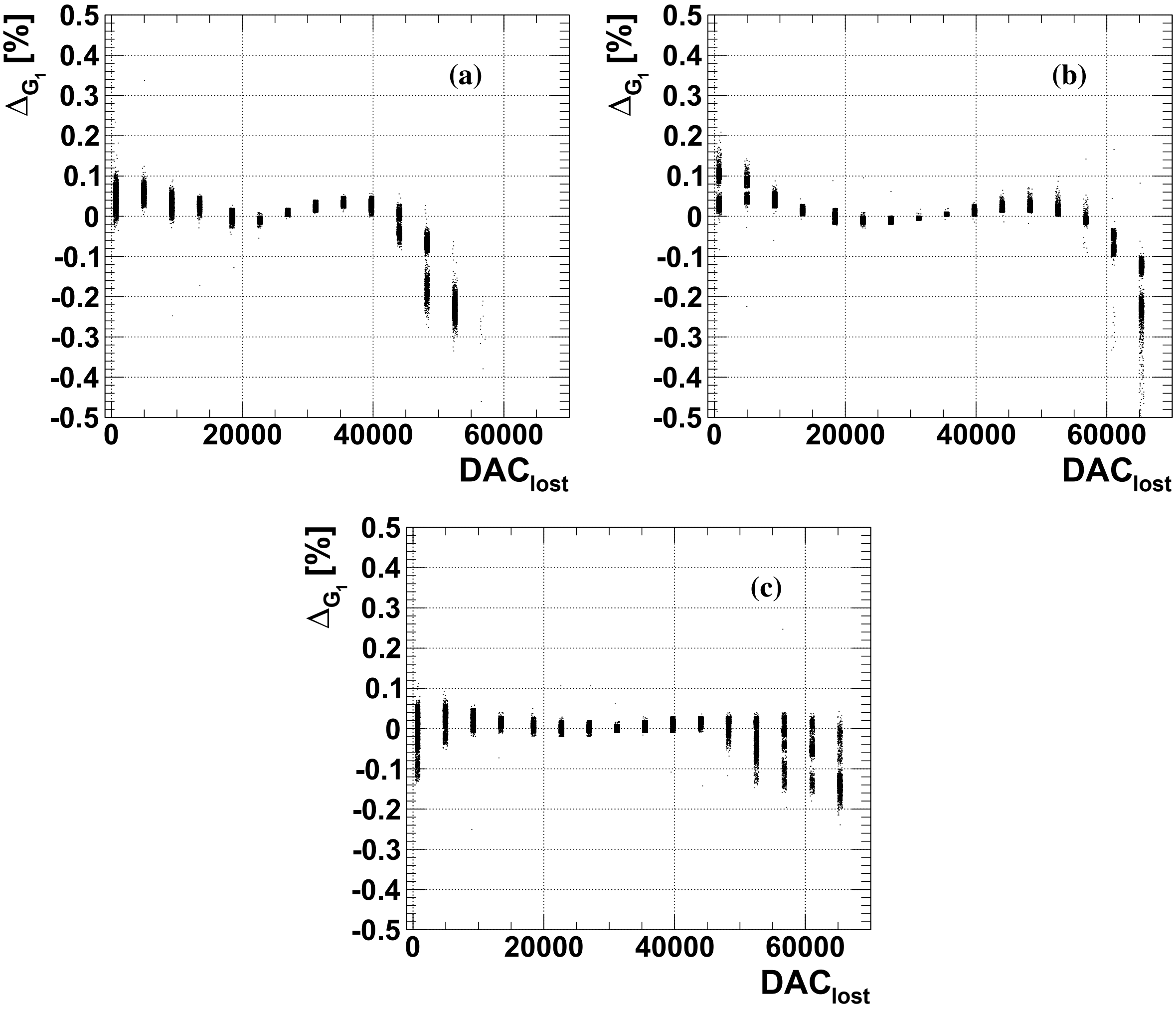

Figure 3.7: The variable Δ_{G_1} as a function of the lost DAC value (DAC_{lost}) for all channels in the first layer (a), the second layer (b), the third layer (c) of EMBA in low gain.

Here we will discuss in detail the study for the effect on the second layer of EMB (EMB2) but the full study was done for all three layers. We concentrate on the effect of the last DAC value. The projected distribution of Δ_{G_1} for the last DAC value is shown in Figure 3.8. This distribution shows that there are two groups of channels: one with a small effect (slot 11, 12) and another with a large effect (slot 13, 14). These two groups of channels correspond to two different electrodes of EMB2. The position of these channels and the two electrodes of EMB2 are shown in Figure 3.9. This is probably due to that the saturation at the level of the preamplifier and shaper occurs for the last DAC value in the region with $|\eta| > 0.8$.

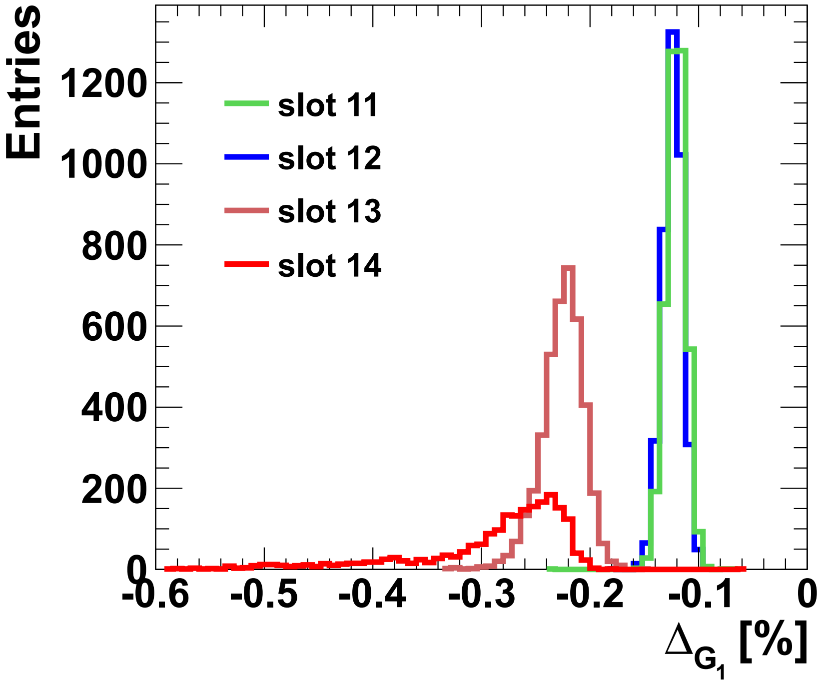

Figure 3.8: The projected distributions of Δ_{G_1} for the last DAC value for channels in different slots of EMB2 in low gain.

The larger spread in the last DAC value suggested also to check for these channels the quality of the linear fit used. Figure 3.10 shows the residual of the fits for all channels in different slots of EMB2, $Residual = (ADC - ADC_{fit})/ADC_{max}$, where ADC is the ADC value recorded, $ADC_{fit} = (DAC - G_0)/G_1$ is the ADC value estimated from the fit and ADC_{max} is the ADC value corresponding to the maximum DAC value (65535 in low gain) [33]. A non-linearity of the linear fit for high DAC values in low gain was observed. The largest deviation happens for the last DAC value of channels in slot 13 and slot 14.

The observed non-linearity suggested to check whether there was an effect coming from the calibra-

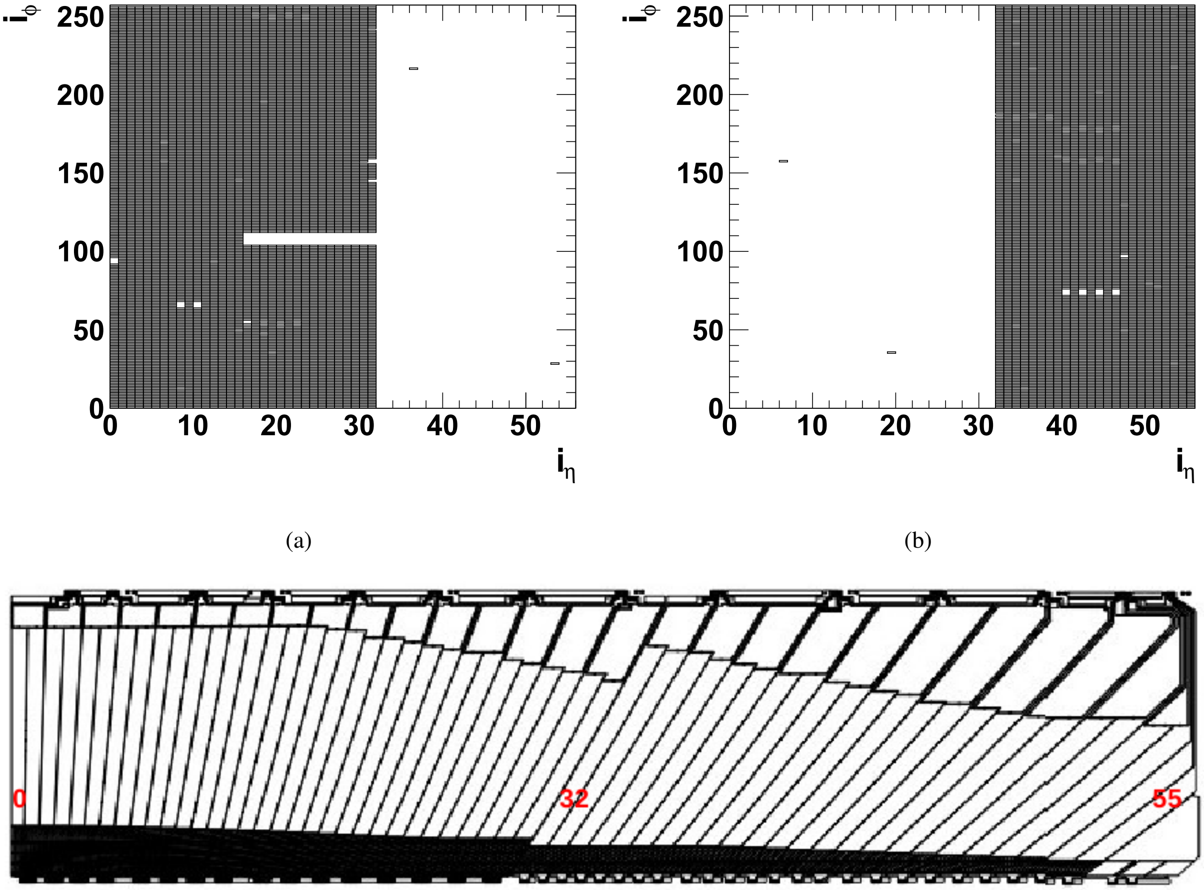

(a)

(b)

(c)

Figure 3.9: The position of channels with smaller effect (a), larger effect (b). The subfigure (c) shows the electrode design [15].

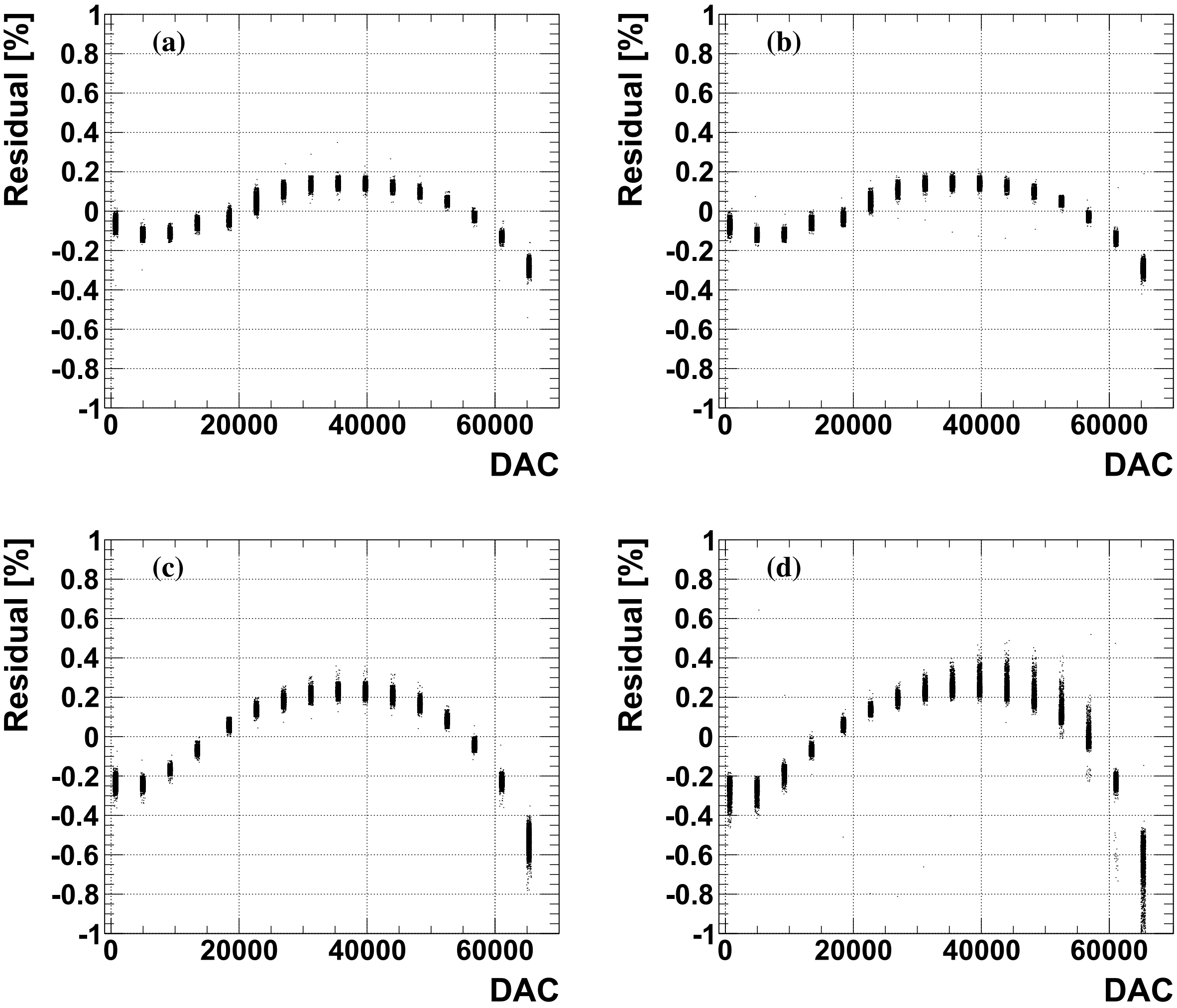

Figure 3.10: The residual of the fits as a function of the DAC values for all channels in different slots of EMB2, slot 11 (a), slot 12 (b), slot 13 (c), slot 14 (d).

tion board in low gain for high DAC values. Special data with high DAC values was taken and no effect was observed. The conclusion is that the non-linearity comes from the linear fit itself. Using a parabolic function, the residual is improved from $\sim 0.2\%$ to $\sim 0.1\%$. The comparison between the residual of a linear fit and the one of a parabolic fit is shown in Figure 3.11 for all channels in slot 14. Moreover the parabolic fit is more stable than the linear fit. The effect of the lost DAC value is smaller than 0.1% when using a parabolic function while it was larger than 0.2% when using a linear function.

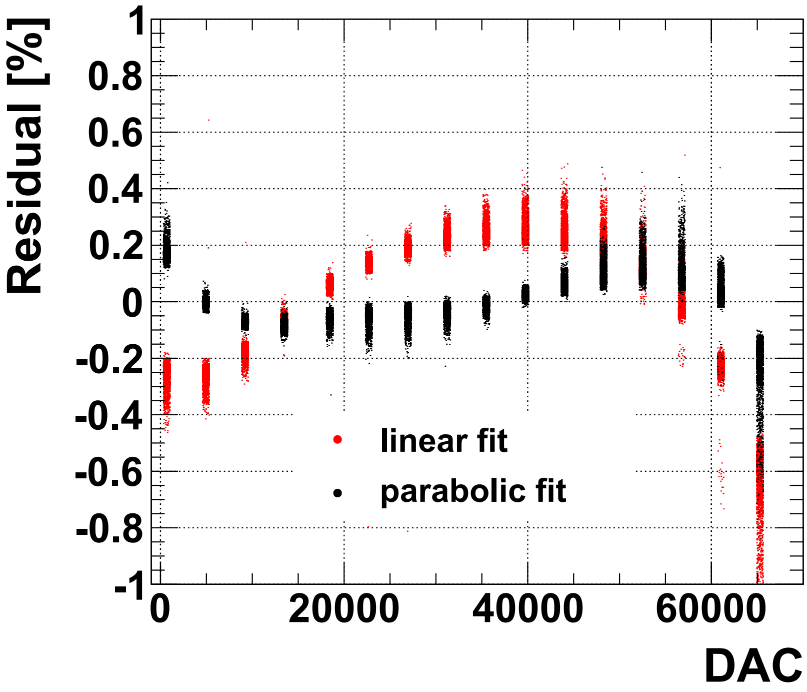

Figure 3.11: The residual of the fits as a function of the DAC values in red for the linear fit and in black for the parabolic fit.

Comparing the gain from the improvement at per mil level using a parabolic function with the convenience of a linear fit, a linear function is still chosen for the ramp fits in the EMB calibration.

3.1.3 Cluster energy reconstruction

The energies deposited in the cells of each individual layer of a cluster are summed. The cluster energy is then determined to include four different contributions: (1) the estimated energy deposited in the material in front of the EM calorimeter, (2) the measured energy deposited in the cluster, (3) the estimated energy deposited outside the cluster (lateral leakage), and (4) the estimated energy deposited beyond the EM calorimeter (longitudinal leakage). The four terms are parametrised as a function of the measured cluster energies in the presampler detector E_{PS} (where it is present) and in the three EM calorimeter longitudinal layers E_{strips}, E_{middle}, E_{back} based on a detailed simulation of the energy deposition in both active and inactive material [15]. A schematic view of an electromagnetic shower developing in the ATLAS LAr EMB is shown in Figure 3.12.

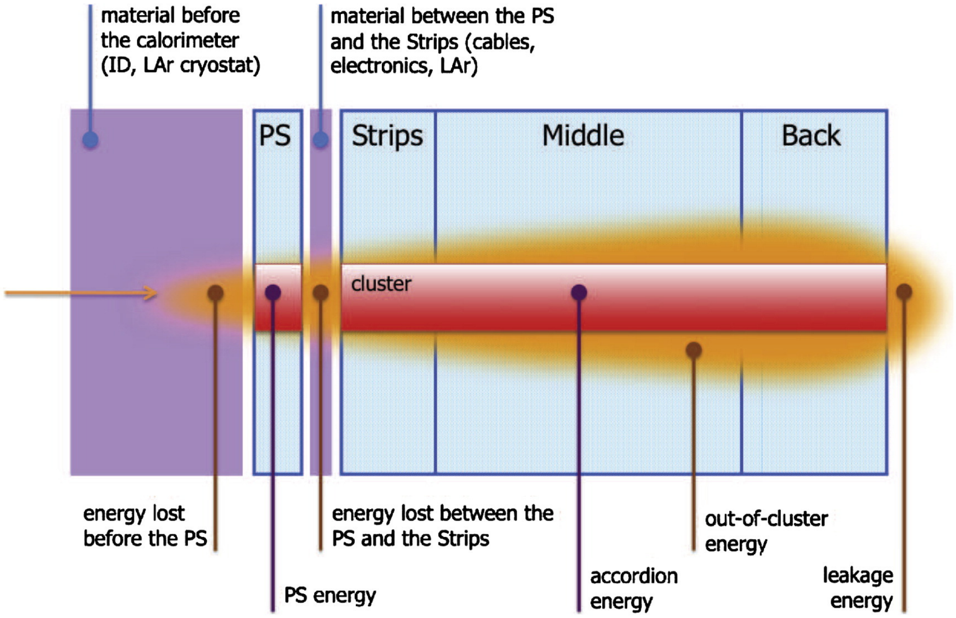

Figure 3.12: Schematic view of an electromagnetic shower developing in the ATLAS LAr EMB [30].

3.2 Track reconstruction in the Inner Detector

As mention in the introduction of this chapter, an electron is reconstructed as a track matched to a cluster in the EM calorimeter. The electron track reconstruction will be reviewed in this section.

The track reconstruction in the Inner Detector is the combination of signals from the Pixels, SCT and TRT using optimised tracking filter and fitting models as described in [15]. Vertices are then recontructed at the final step. Figure 3.13 shows an example of multiple vertex reconstruction in a Higgs candidate event with four final state electrons at 8 TeV proton-proton collisions.

The reconstruction of an electron track is more challenging than the reconstruction of other charged particles, since in addition to ionisation energy loss and multiple Coulomb scattering, electrons suffer from larger energy losses due to bremsstrahlung. Bremsstrahlung can occur when the electrons traverse the Inner Detector. Although most of the limited radiation will be collected by the electromagnetic calorimeter, the track direction can be seriously affected, resulting in a poorly reconstructed momentum

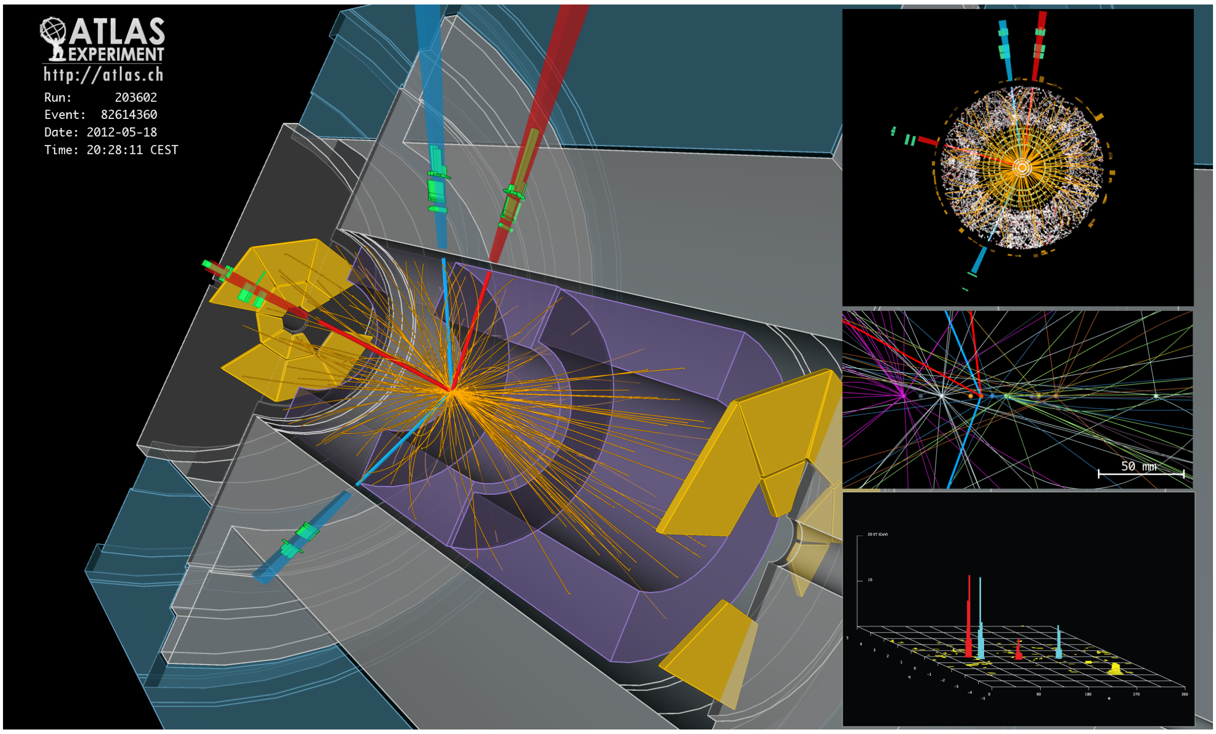

Figure 3.13: Multiple vertex reconstruction in Higgs candiate event with four final state electrons at 8 TeV proton-proton collisions in data [12].

or even in a failure to reconstruct the track altogether. There are three available algorithms in the ATLAS track reconstruction to fit electron tracks in such a way as to account for bremsstrahlung: the dynamic noise adjustment (DNA), the Gaussian-sum filter (GSF) and CaloBrem [92].

The DNA method extrapolates track segments to the next silicon detector layer. If there is a significant χ^2 contribution, compatible with a hard bremsstrahlung, the energy loss is estimated and an additional noise term is included in the Kalman filter otherwise the standard Kalman filter is used.

The Gaussian-sum filter (GSF) is a non-linear generalisation of the Kalman filter, which takes into account non-Gaussian noise by modelling it as a weighted sum of Gaussian components and therefore acts as a weighted sum of Kalman filters operating in parallel. At each layer the track parameters are convoluted with a probability density function describing the material effects (see Figure 3.14).

The CaloBrem algorithm serves to reduce the bias of the track fits caused by the increased track curvature. In order to have a stable fit, the position of the cluster is included in the fit if all energy of the original electron is located in the cluster and the track model is modified to include a single loss of energy at a certain radius (see Figure 3.15).

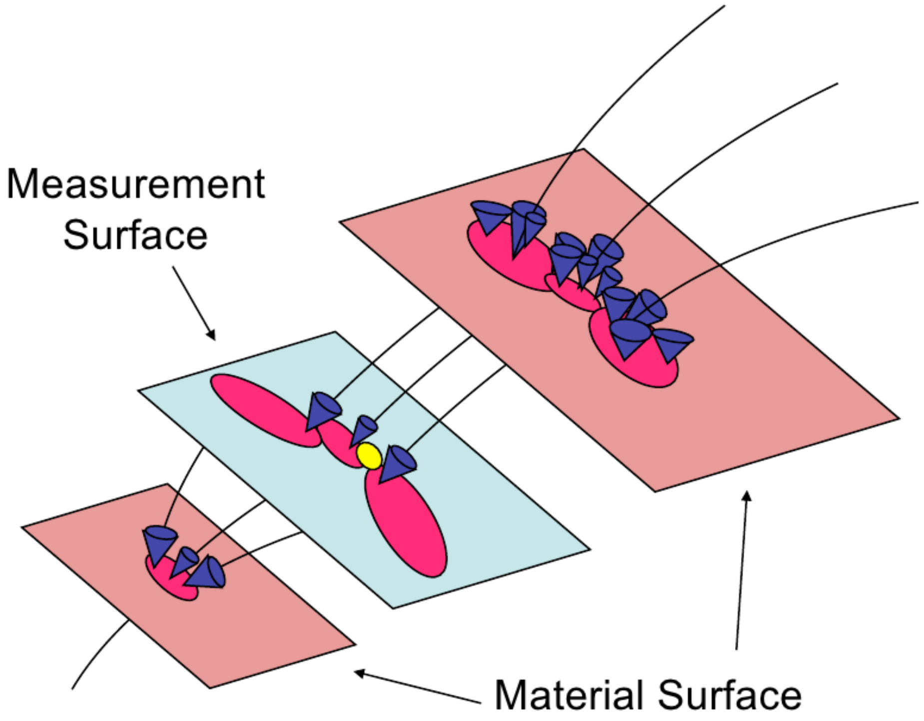

Figure 3.14: Tracking in the GSF algorithm [92]

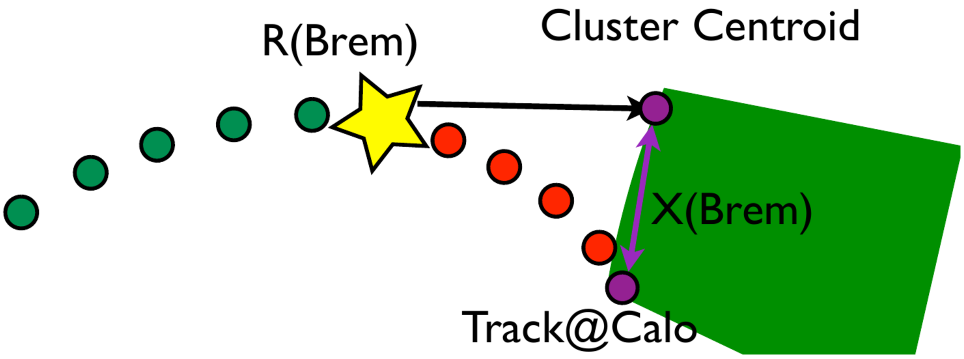

Figure 3.15: Tracking in the CaloBrem algorithm [92]

The analysis of this thesis is the ϕ^*_η measurement which is based entirely on the measured track directions of electrons. Therefore the bremsstrahlung recovery algorithms are important to improve the precision of this measurement. GSF electrons will be used for this analysis. By allowing for changes in the curvature of the track, the bremsstrahlung recovery algorithms follow the tracks better and correctly associate hits in the track, leading to improvements in the reconstruction efficiencies. The GSF algorithm has 2-3% greater efficiency than the default reconstruction algorithm [92]. The impovement on the measured track direction of electrons using the GSF algorithm is shown in Figure 3.16.

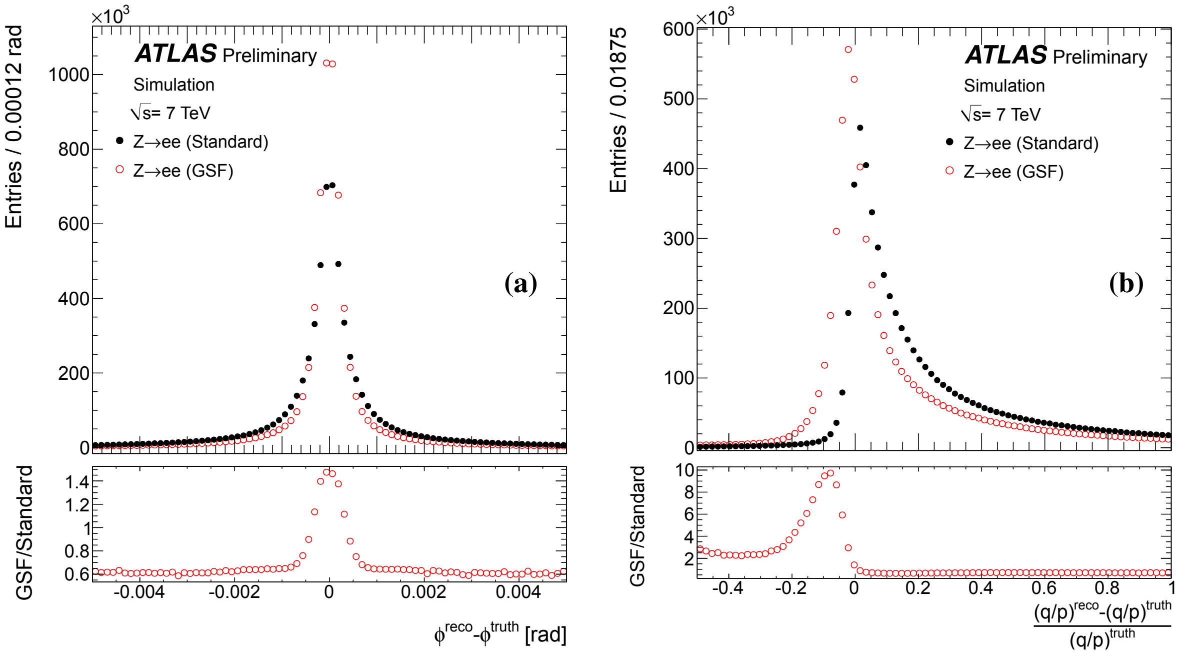

Figure 3.16: The distribution of the resolution of the track direction ϕ at the perigee (a) and of the relative bias on the track inverse momentum multiplied by the charge q/p (b), for both GSF (open red) and standard (solid black) truth-matched Monte-Carlo electrons from Z-boson decays. The bottom plots show the ratio of the entries of the GSF and standard electrons per bin [7].

3.3 Electron reconstruction

There are two algorithms for electron reconstruction in the ATLAS experiment. The standard one is used for the electron reconstruction in this analysis and will be explained in detail in this section. It is seeded from the electromagnetic (EM) calorimeters, starts from clusters reconstructed in the calorimeters and then builds the identification variables based on information from the Inner Detector and the EM calorimeters. A second algorithm is used for the soft electron reconstruction. It is seeded from the Inner Detector tracks and is optimized for electrons with energies as low as a few GeV. It selects good-quality tracks matching a relatively isolated deposition of energy in the EM calorimeters. The identification variables are then calculated in the same way as for the standard algorithm.

In the standard electron reconstruction, seed clusters of longitudinal towers with a total transverse energy above 2.5 GeV are searched for by a sliding-window algorithm. The window size is 3×5 in units of 0.025×0.025 in $\eta \times \phi$ space. In the tracking volume of $|\eta| < 2.5$, reconstructed tracks extrapolated from their last measurement point to the middle layer of the calorimeter are matched to the seed clusters. The distance between the track impact point and the cluster position is required to satisfy $\Delta\eta < 0.05$. An electron is reconstructed if at least one track is matched to the seed cluster. In the case where several tracks are matched to the same cluster, tracks with silicon hits are preferred, and the one with the smallest distance to the seed cluster $\Delta R = \sqrt{\Delta\eta^2 + \Delta\phi^2}$ is chosen.

The electron cluster is then rebuilt using 3×7 (5×5) longitudinal towers of cells in the barrel (endcaps). The four-momentum of central electrons is computed using information from both the final cluster and the best track matched to the original seed cluster. The energy is given by the cluster energy. The ϕ and η directions are taken from the corresponding track parameters at the vertex.

3.4 Electron identification

The electron identification in the central region with $|\eta| < 2.47$ relies on a cut-based selection using calorimeter and tracking variables that provide good separation between isolated or non-isolated signal electrons, background electrons and jets faking electrons. Three reference sets of cuts have been defined with increasing background rejection power. They are loose, medium and tight electron selections and have an expected jet rejection of about 500, 5000 and 50000, respectively, according to MC simulation [14].

The loose electron selection performs a simple identification based only on limited information from the calorimeters. Cuts are applied on the hadronic leakage and on shower-shape variables, derived only from the middle layer of the EM calorimeter. This set of cuts provides excellent identification efficiency, but low background rejection.

The medium electron selection adds cuts on variables computed using the EM calorimeter strip layer, track quality requirements and track-cluster matching.

The tight electron selection tightens the track-matching criteria and the cut on the energy-to-momentum ratio, adds particle identification using the TRT, and discrimination against photon conversions via a b-layer hit requirement and information about reconstructed conversion vertices.

All variables used in the loose, medium and tight selections are listed in Table 3.1. The cuts are optimised in 10 bins of cluster η and 11 bins of cluster E_T from 5 GeV to above 80 GeV. In this analysis which uses all data selected in 2011, the electron identification selection is named "medium++". It is based on the standard medium selection. The "medium++" menu was created to provide a low energy and high efficiency electron sample which met the trigger bandwith restrictions for high luminosity. It offers efficiencies a around $\sim$85% for Z electrons with a small dependence on the number of interactions.

3.5 Efficiency measurement

A measured electron spectrum needs to be corrected for the efficiencies of the electron selection in order to derive cross sections of observed physics processes.

The correction factor for efficiency effects on the measured spectrum is obtained using MC simulation. However, the electron selection efficiencies simulated in MC do not agree perfectly with the ones measured in data using data driven methods. Therefore, small corrections need to be applied on MC in the form of scale factors as explained in the following. The efficiency correction can be expressed as a function of efficiency terms. For the case of a $Z \to ee$ process the correction factor has the form below:

$$C_Z = \varepsilon_{event}.\varepsilon_{reco}.(\varepsilon_{ID})^2.[1-(1-\varepsilon_{trig})^2], \tag{3.3}$$

where ε_{event} denotes the efficiency of event preselection cuts, such as primary vertex requirements and event cleaning. ε_{reco} accounts for the reconstruction efficiency to find an electromagnetic cluster and to match it loosely to a reconstructed charged particle track in the fiducial region of the detector and also for any kinematic and geometrical cuts on the reconstructed object itself. ε_{ID} denotes the efficiency of the identification cuts relative to reconstructed electron objects. ε_{trig} stands for the the trigger efficiency with respect to all reconstructed and identified electron candidates.

The tag and probe technique is chosen for the electron selection efficiency measurement in the ATLAS reconstruction. Then the MC predicted values of the above efficiencies in bins (of E_T and η) are corrected by the measured ratios of the data to MC efficiencies, called scale factor corrections.

Type	Description	Name
Loose selection		
Acceptance	$\|\eta\| < 2.47$	
Hadronic leakage	Ratio of E_T in the first layer of the hadronic calorimeter to E_T of the EM cluster (used over the range $\|\eta\| < 0.8$ and $\|\eta\| > 1.37$)	R_{had1}
	Ratio of E_T in the hadronic calorimeter to E_T of the EM cluster (used over the range $\|\eta\| > 0.8$ and $\|\eta\| < 1.37$)	R_{had}
Middle layer of EM calorimeter	Ratio of the energy in 3×7 cells over the energy in 7×7 cells centred at the electron cluster position	R_η
	Lateral width of the shower	$\omega_{\eta 2}$
Medium selection (includes loose)		
Strip layer of EM calorimeter	Total shower width	ω_{stot}
	Ratio of the energy difference between the largest and second largest energy deposits in the cluster over the sum of these energies	E_{ratio}
Track quality	Number of hits in the pixel detector (≥ 1)	n_{pixel}
	Number of total hits in the pixel and SCT detectors (≥ 7)	n_{Si}
	Transverse impact parameter ($\|d_0\| < 5mm$)	d_0
Track - cluster matching	$\Delta\eta$ between the cluster position in the strip layer and the extrapolated track ($\|\Delta\eta\| < 0.01$)	$\Delta\eta$
Tight selection (includes medium)		
Track - cluster matching	$\Delta\phi$ between the cluster position in the middle layer and the extrapolated track ($\|\Delta\phi\| < 0.02$)	$\Delta\phi$
	Ratio of the cluster energy to the track momentum Tighter $\Delta\eta$ requirement ($\|\Delta\eta\| < 0.005$)	E/p $\Delta\eta$
Track quality	Tighter transverse impact parameter requirement ($\|d_0\| < 1mm$)	d_0
TRT	Total number of hits in the TRT	n_{TRT}
	Ratio of the number of high-threshold hits to the total number of hits in the TRT	f_{HT}
Conversions	Number of hits in the b-layer (≥ 1)	n_{BL}
	Veto electron candidates matched to reconstructed photon conversions	

Table 3.1: Definition of variables used for loose, medium and tight electron identification cuts for the central region of the detector with $|\eta| < 2.47$ *[17].*

The tag and probe method aims to select a clean and unbiased sample of electrons, called probe electrons, using tightened selection cuts, called tag requirements, primarily on other objects in the event. In the $Z \to ee$ process, a well-identified electron is used as the tag. The efficiency of any selection cut can then be measured by applying it to the sample of probe electrons:

$$\varepsilon_{cut} = \frac{N_{probes\_passing\_cut}}{N_{probes}}. \tag{3.4}$$

This section is used to review the measurements of the electron trigger, reconstruction and identification efficiencies which were done first in 2010 [36] and the update information for 2011 analysis is included.

3.5.1 Electron trigger efficiency

The analysis in this thesis uses single electron triggers called e20_medium, e22_medium and e22vh_medium1 depending on the instantaneous luminosity delivered by the LHC as listed in Table 3.2. The EF thresholds for these triggers are 20 GeV to 22 GeV. The letters "vh" were added to the names for the triggers seeded by L1 items with η-dependent thresholds and a hadronic leakage requirement. The "medium1" selection is the re-optimised electron identification criteria of the "medium" selection when luminosities $\geq 3 \times 10^{33}\text{cm}^{-2}\text{s}^{-1}$ in order to avoid raising the EF threshold further [11].

Trigger selection	Luminosity range ($\text{cm}^{-2}\text{s}^{-1}$)
e20_medium	up to 2×10^{33}
e22_medium	$2 - 2.3 \times 10^{33}$
e22vh_medium1	from 2.3×10^{33}

Table 3.2: Single electron triggers and corresponding luminosity ranges [11].

The efficiencies of these trigger selections were measured using the tag and probe method with respect to electrons in $Z \to ee$ events reconstructed and identified by the offline reconstruction program, details of this measurement can be found in [11].

Figure 3.17 shows the efficiencies of the e20_medium, e22_medium and e22vh_medium1 triggers measured in data relative to medium++ offline electrons. The efficiency of e20_medium is computed

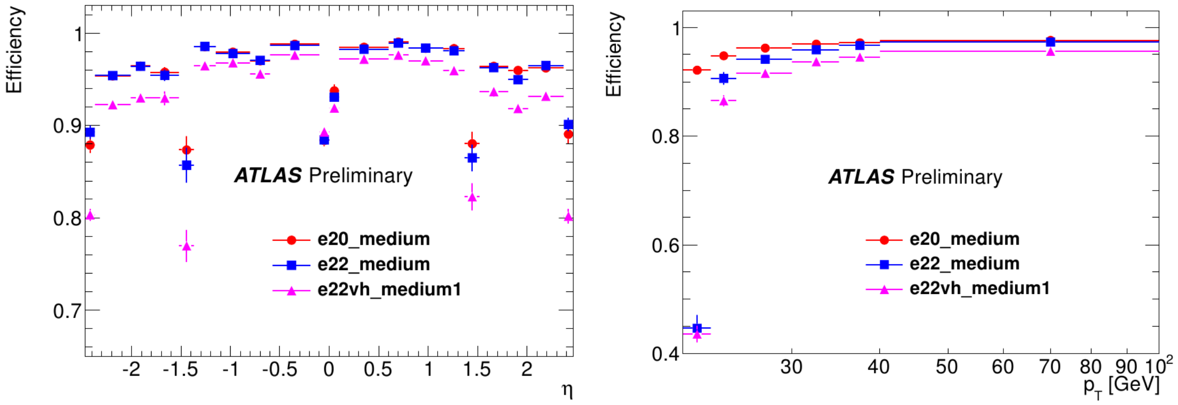

(a)

(b)

Figure 3.17: Efficiencies as functions of the offline medium++ electron η (a) and p_T (b) for the e20_medium, e22_medium and e22vh_medium1 triggers. The vertical bars represent statistical and total systematic uncertainties [11].

relative to offline electrons with $p_T > 21$ GeV and the efficiencies e22_medium and e22vh_medium1 are computed relative to offline electrons with $p_T > 23$ GeV.

Efficiencies measured on data are compared to efficiencies obtained from MC simulations of $Z \rightarrow ee$ events and data/MC ratios (scale factors) are derived. These scale factors are used in physics analyses to correct the MC to describe the data efficiency. The efficiencies and scale factors are summarised in [11]. These scale factors are applied to the MC samples used in my analysis.

3.5.2 Electron reconstruction efficiency

The electron reconstruction efficiencies are studied with respect to sliding-window clusters in the EM calorimeter using $Z \rightarrow ee$ decays and the tag and probe method. The combined electron track reconstruction and track cluster matching efficiency is measured. Details of this measurement can be found in [36]. The electron reconstruction efficiency as a function of η and as a function $E_{T,Cluster}$ is shown in Figure 3.18. Scale factor corrections are extracted from the ratio between electron identification efficiencies in data and in MC ($\varepsilon_{Data}/\varepsilon_{MC}$). These scale factors are applied to the MC samples used in my analysis.

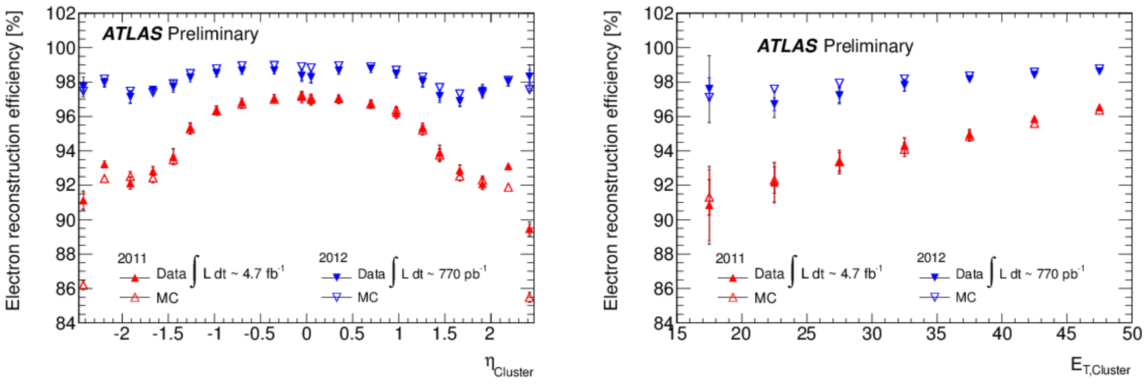

(a) (b)

Figure 3.18: The reconstruction efficiency (including the requirements on the track quality) is shown as a function of the pseudorapidity η for electrons with transverse energy between 30 and 50 GeV (a), as a function of the electron transverse energy (b), for data (filled markers) and MC (open markers) from 2011 (red up triangles) and 2012 (blue down triangles). The total (statistical and systematic) uncertainty is displayed [81].

3.5.3 Electron identification efficiency

The tag and probe method is used to measure the electron identification efficiency. Details of this measurement can be found in [36]. The tag electron was required to have $E_T > 20$ GeV, to match the corresponding trigger object, and to pass the “tight++” (based on “tight” selection in Table 3.1) electron identification requirements. The probe electron was required to have $E_T > 15$ GeV and to be of opposite charge to the tag electron. All tag-probe pairs passing the cuts were considered. The same procedure is applied to the MC simulation, with in addition a reweighting of the MC to reproduce the pile-up observed in data as well as the proper mixture of the various triggers.

Background substraction is needed to have the final efficiency results. There are multiple methods used for this measurement. The reconstructed di-electron mass is a commonly used variable to estimate the signal and background contributions in the selected sample of electron probes from $Z \rightarrow ee$ decays,

$$M = \sqrt{2E_1E_2(1 - \cos\theta_{12})}, \tag{3.5}$$

where E_1 and E_2 are the energies of the two electrons measured by the calorimeter and θ_{12} is the angle in space between the electrons measured by the tracker. The signal region is chosen typically $80 < M_{ee} < 100$ GeV. The efficiencies of the “medium++” electron identification cut as a function of the number of reconstructed vertices is shown in Figure 3.19. The dominant systematic uncertainties on the efficiency measurements come from the background estimation. Other sources of uncertainty were also checked but lead to negligible contributions.

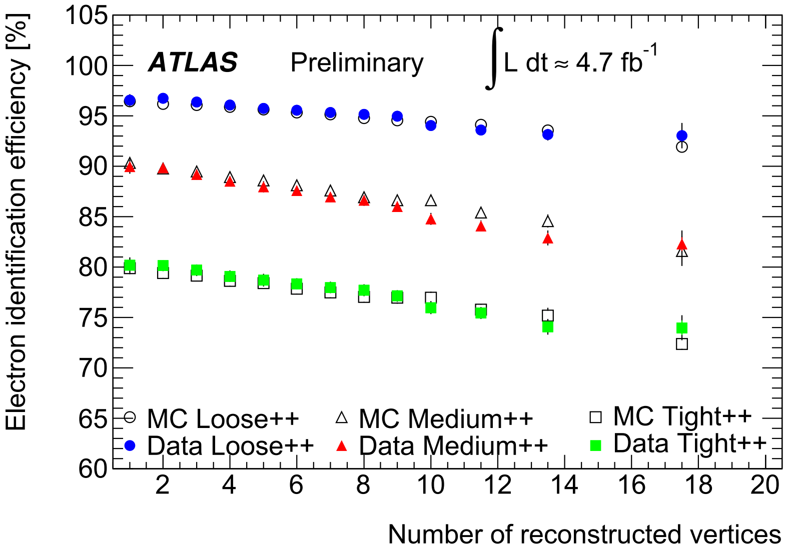

Figure 3.19: Efficiencies are shown for different number of reconstructed primary vertices, going from 1 to 10 in bins of unit size and then wider bins 11-12, 13-14 and 15-20 [53].

The scale factor corrections are extracted from the ratio between electron identification efficiencies in data and in MC ($\varepsilon_{Data}/\varepsilon_{MC}$). These scale factors are applied to the MC samples used in my analysis.

3.6 Energy scale and energy resolution measurement

3.6.1 Energy scale

Details of this measurement can be found in [17]. The electromagnetic calorimeter energy scale was derived from test-beam measurements with a total uncertainty of 3% in the region covering $|\eta| < 2.47$, and 5% in the region covering $2.5 < |\eta| < 4.9$ [28–30]. The knowledge of the electron energy scale was refined using samples of $Z \to ee$, $J/\psi \to ee$ and $W \to e\nu$ events from collision data. This section presents a short description of the measurement of the electron energy scale using $Z \to ee$ samples.

The event selection is similar to the one used in the analysis of this thesis which is described later in Section 4.2. The measured energy E^{meas} is expressed as a function of the true energy, E^{true},:

$$E^{meas} = E^{true}(1 + \alpha_i), \tag{3.6}$$

and α_i is a factor which takes into account possible miscalibration for a given region i. The α energy scale correction factors are determined by a fit minimizing the negative unbinned log-likelihood ([27]) using the Z lineshape obtained from PYTHIA MC simulation.

This procedure was applied to the 2011 (2010) dataset in 26 (58) η bins over the full calorimeter coverage of $|\eta| < 4.9$ and is considered as the baseline calibration method. The resulting α values in 2010 are shown in Figures 3.20. They are within 2% in 2010 measurement and 0.5% in 2011 measurement ([31]) in the barrel region. The rapid variations with η occur at the transitions between the different EM calorimeter systems. The variations within a given calorimeter system are due to several effects related to electronic calibration, high-voltage corrections (in particular in the Endcaps), additional material in front of the calorimeter, differences in the calorimeter and presampler energy scales, and differences in lateral leakage between data and MC.

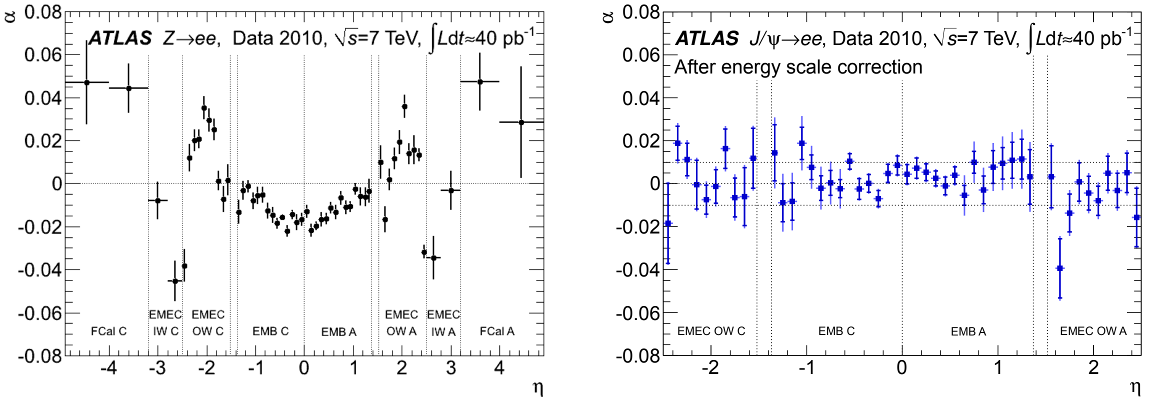

(a) (b)

Figure 3.20: The energy scale correction factor α as a function of the pseudorapidity of the electron cluster derived from fits (left) to $Z \to ee$ data and (right) to $J/\psi \to ee$ data. The uncertainties of the $Z \to ee$ measurement are statistical only. The $J/\psi \to ee$ measurement was made after the $Z \to ee$ calibration had been applied. Its results are given with statistical (inner error bars) and total (outer error bars) uncertainties. The boundaries of the different detector parts defined in Section 2 are indicated by dotted lines [17].

The overall systematic uncertainties on the electron energy scale as function of E_T are shown in Figures 3.21 in two η regions using data in 2010. For central electrons with $|\eta| < 2.47$, the uncertainty varies from 0.3% to 1.6%. The systematic uncertainties are smallest for $E_T = 40$ GeV (corresponding to the average electron E_T in the $Z \to ee$ sample), below 0.4%. Below $E_T = 20$ GeV, the uncertainty grows linearly with decreasing E_T. For forward electrons with $2.5 < |\eta| < 4.9$, the uncertainties are larger and vary between 2% and 3%. For data in 2011, there are several differences such as Calorimeter operating conditions, pileup, signal and background ratio but their contributions are small and the total systematic uncertainty is only slightly different in comparison with 2010.

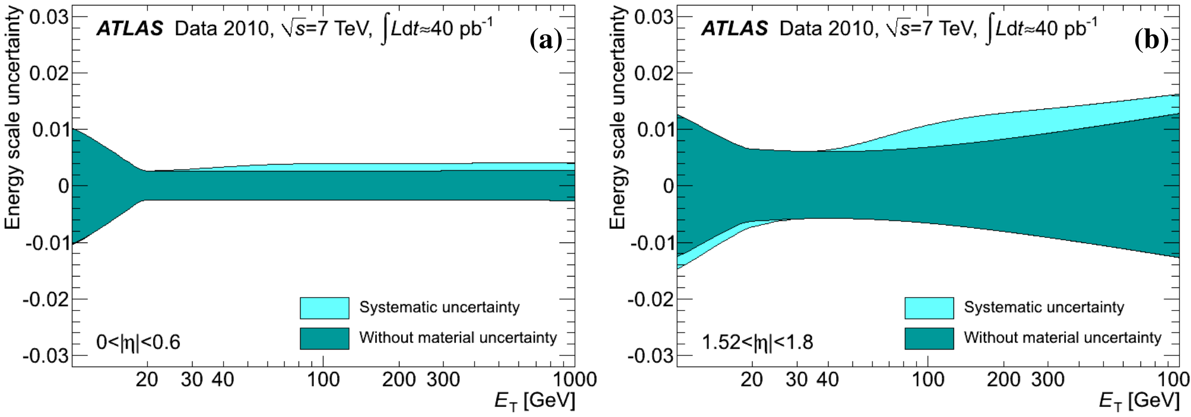

Figure 3.21: Total systematic uncertainty on the electron energy scale (a) for the region $|\eta| < 0.6$ *and (b) for* $1.52 < |\eta| < 1.8$ *[17].*

3.6.2 Energy resolution

Details of this measurement can be found in [17]. The electron energy resolution function is described by the formula:

$$\frac{\sigma_E}{E} = \frac{a}{\sqrt{E}} \oplus \frac{b}{E} \oplus c, \tag{3.7}$$

where a is the sampling term, b is the noise term which has a significant contribution only at low energy, and c is the constant term. The energy resolution and the corresponding parameters can be extracted by measuring the mass resolution for well known resonances like Z and J/ψ in data. The constant term is determined as formula below:

$$c_{data} = \sqrt{2.\left(\left(\frac{\sigma}{m_Z}\right)^2_{data} - \left(\frac{\sigma}{m_Z}\right)^2_{MC}\right) + c^2_{MC}}, \tag{3.8}$$

where c_{MC} is the constant term of about 0.5% in the MC simulation. The parameter c_{data} is an effective constant term which includes both the calorimeter constant term and the effect of additional material, m_Z denotes the Z mass, and σ is the Gaussian component of the experimental resolution.

The resolution parameters extraction is based on fits to the invariant mass distributions of $Z \rightarrow ee$ decays using Breit-Wigner (BW) convoluted with a Crystal-Ball in the mass range 80-100 GeV for central events and in the mass range 75-105 GeV for forward events. The BW width is fixed to the Z width PDG value (2.49 GeV), and the resolution is the sigma of the Crystal Ball function. The invariant mass distributions for Z candidates and corresponding mass peak resolutions are shown in Figures 3.22. The effective constant term and its systematic uncertainties measured with 2011 data are close to the 2010 estimation [27].

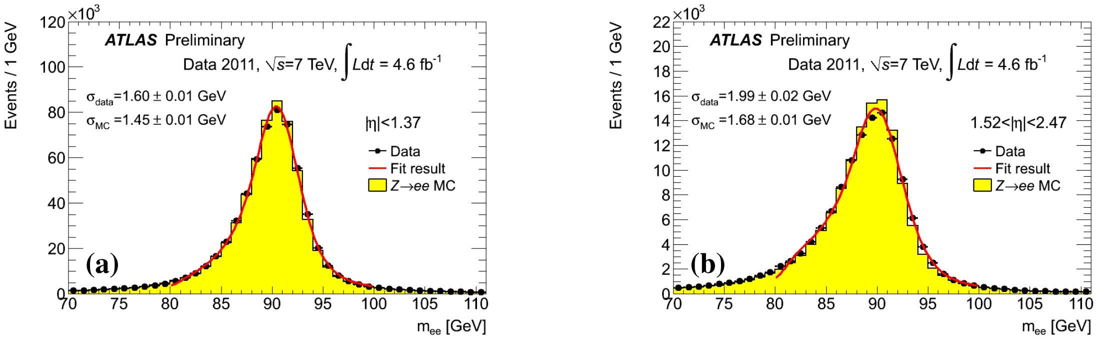

Figure 3.22: Calibrated $Z \rightarrow ee$ invariant mass: (a) all pairs with $|\eta| < 1.37$, (b) all pairs with $1.52 < |\eta| < 2.47$ [31].

3.7 Summary

The general reconstruction of electrons in the ATLAS experiment was introduced. The energy reconstruction in the LAr Calorimeters was presented in detail. The ramp coefficients extracted from ramp fits are used to compute the cell energy. The study on the stability of ramp fits showed that the number of injected signal points (DAC) should be increased for the first layer of EMB to have more stable fits. The non-linearity of ramp fits in low gain was found at the level of 0.5%. The conclusion from this study is that the non-linearity comes from the fit itself which uses a linear function. The non-linearity is impoved from 0.5% to 0.2% by using a parabolic function. The stability of ramp fits is improved from 0.2% to 0.1%.

The results of electron efficiency measurements were introduced. The good agreement between data and MC was observed, only small scale factors were extracted to be applied on MC in order to describe better data. The systematic uncertainties on our measurements due to this correction are very small, at the level of per mil, and will be studied in Chapter 5 and Chapter 6.

The results of electron energy scale and energy resolution measurements were summarised. The knowledge of the electron energy scale and resolution has been improved from test-beam measurements to the measurements using data collected in 2010 and 2011. The systematic uncertainties on the p_T^Z measurements due to the energy scale and resolution corrections applied will be studied in Chapter 5.

Chapter 4

The event reconstruction of the Z boson decaying into a pair of electron and positron

This chapter describes the selection of events with a Z boson decaying into a pair of electron and positron ($Z \to ee$) using the 2011 dataset recorded by the ATLAS detector in proton-proton collisions at the LHC at $\sqrt{s} = 7$ TeV. An example of $Z \to ee$ candidates in 7 TeV collision data is shown in Figure 4.1. The selected candidates will be used for the differential cross section measurements of p_T^Z and ϕ_η^* described in the next two chapters. The work from this chapter is reported partially in Ref. [69]. This chapter is organized in several sections: Section 4.1 presents the data and the MC samples used and the global corrections applied on MC samples to match the data. Section 4.2 presents the criteria to select $Z \to ee$ candidates. Section 4.3 presents all corrections which are applied on data or MC in order to account for remaining mis-calibrations of the electron energy in the data or mis-modeling of the data by the MC. Section 4.4 presents the background estimation using MC predictions for the electroweak (EW) background and data driven methods for the QCD multi-jet background. The final section 4.5 presents selection results and control distributions for kinematic variables of electrons and Z boson candidates. This analysis uses a data skimming and a data selection framework developed by J.B. Sauvan (Universite de Paris-Sud 11) and J.E. Sauvan (Laboratoire d'Annecy-le-Vieux de Physique des Particules).

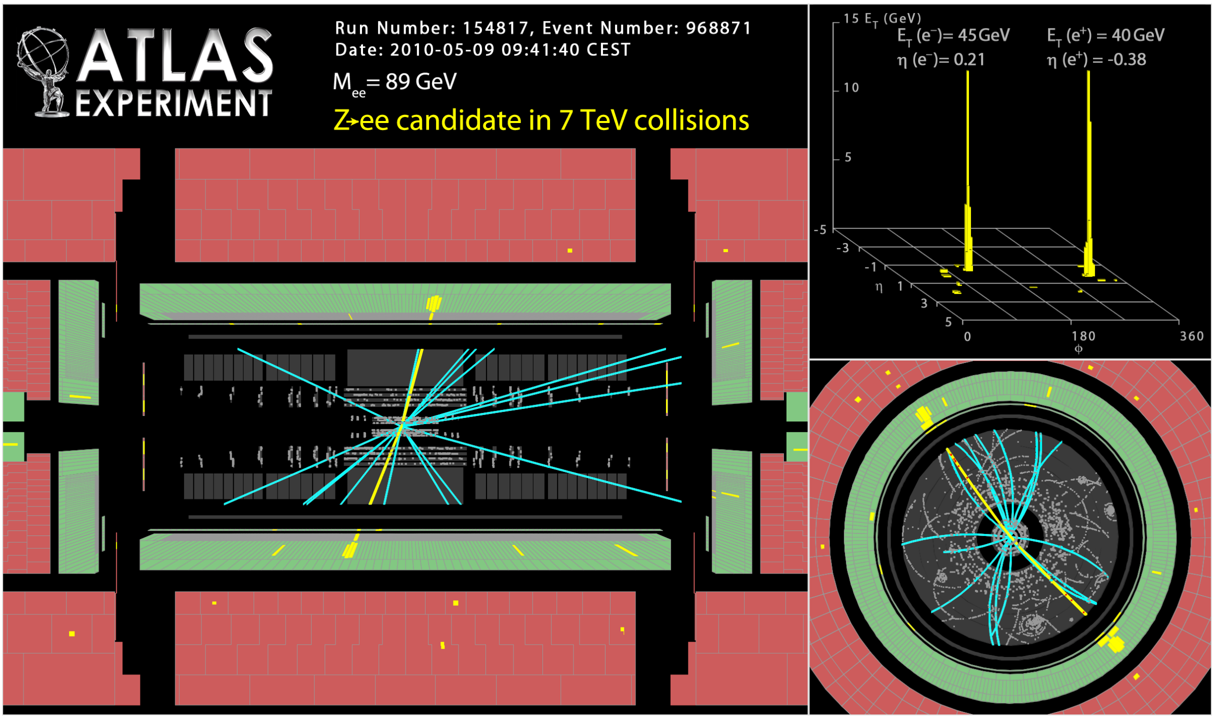

Figure 4.1: First candidate for an event with a Z boson decaying into a pair of electron and positron seen in 7 *TeV collision data in 2010* [12].

4.1 Data and Monte Carlo samples

The total integrated luminosity of 2011 ATLAS data recorded is 5.25 fb^{-1} as shown in Figure 2.3 but the sample used for this analysis is about 4.7 fb^{-1}. This section explains the choice of the dataset for this analysis, the signal MC samples used to correct for efficiency and acceptance effects on the differential cross section measurements, the background MC samples used to estimate the EW background and the global corrections applied on the MC samples.

4.1.1 Data quality requirement and integrated luminosity

The choice of the dataset was determined as a compromise between maximizing the available luminosity while maintaining stable trigger and reconstruction conditions throughout the sample. All selected events must pass certain requirements for the proper functioning of the detector, as described by a Good Runs List (GRL). It requires stable beam conditions at $\sqrt{s} = 7$ TeV as well as good working conditions for all parts of the detector and trigger used including solenoid, toroid, calorimeters, inner detector, L1 trigger hardware, and luminosity monitors. This sample corresponds to 4.7 fb^{-1} with an uncertainty of

3.4% [10] as measured using van der Meer scans.

4.1.2 Monte Carlo samples

Simulated ATLAS Monte Carlo samples are used to calculate acceptances and to model the properties of our signal and backgrounds. The main signal event samples for Z production are generated using POWHEG event generator where parton showers are provided by PYTHIA. For the POWHEG calculations the CT10 NLO PDF set is used. In addition we use LO PYTHIA generator for signal as further cross check where MRST LO* PDFs have been used. All generators are interfaced to PHOTOS to simulate the effect of final state QED radiation. The passage of particles through the ATLAS detector is modelled using GEANT4. The effect of multiple interactions per bunch crossing ("pileup") is modelled by overlaying simulated minimum bias events over the original hard-scattering event. Tables 4.1 summarises the MC datasets. For the electroweak processes, i.e. $W \to \ell\nu$, $Z \to \ell\ell(\ell = e, \mu, \tau)$, the samples are normalized to the NNLO cross sections as provided by FEWZ program [75, 91] with MSTW 2008 NNLO PDFs. The uncertainties on these cross sections arise from the choice of PDFs (3%), from factorization and renormalization scale dependence (4%). The total is about 5%, which we take as an uncertainty on any event count predictions normalized using these cross sections. The $t\bar{t}$ cross section, calculated at m_t = 172.5 GeV is 161 pb, taken from [87]. The uncertainty is 6% plus the PDF uncertainty quoted above. The inclusive diboson samples are normalized to their respective NLO cross sections with 7% uncertainty [57].

4.1.3 Global corrections for Monte Carlo samples

4.1.3.1 Pileup reweighting

The variations in pile-up conditions in 2011 are addressed by dividing the MC into four subsets with different conditions in order to match the observed distribution on data. Residual differences in the pileup between data and Monte Carlo simulation have been corrected by reweighting the Monte Carlo events to reproduce the average number of interactions per bunch-crossing, $< \mu >$, observed in data. The $< \mu >$ distribution and the distribution of the number of primary vertices in data and MC after the pileup reweighting are shown in Figure 4.2.

Generator	Dataset ID	Process	$\mathscr{L}(\mathrm{fb}^{-1})$	$\sigma \times BR$ (nb)	note
Signal					
Pythia	106046	$Z \to ee$	10.1	0.99 ± 0.05	NNLO (wide zvtx)
Powheg+Pythia	108303	$Z \to ee$	5.0	1.02 ± 0.05	NNLO (wide zvtx)
Powheg+Pythia	108303	$Z \to ee$	20.0	1.02 ± 0.05	NNLO (narrow zvtx)
Backgrounds					
Pythia	106043	$W \to e\nu$	4.0	10.46 ± 0.52	NNLO
Pythia	106052	$Z \to \tau\tau$	1.0	0.99 ± 0.05	NNLO
MC@NLO	105200	$t\bar{t}$	12.9	0.16 ± 0.01	NLO
Herwig	105985	WW	142.6	44.9×10^{-3}	NLO
Herwig	105986	ZZ	198.3	6.0×10^{-3}	NLO
Herwig	105987	WZ	174.9	18.5×10^{-3}	NLO

Table 4.1: MC samples used in this analysis.

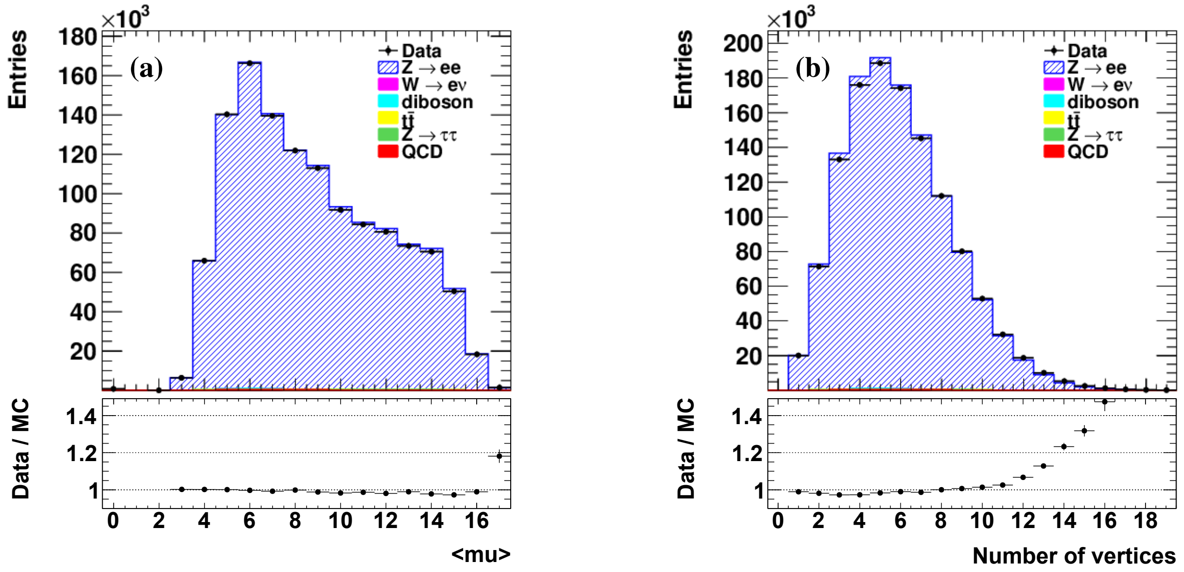

Figure 4.2: Distributions of $< \mu >$ (a) and of the number of primary vertices (b) after the application of the Extended Pileup reweighting tool. Data (black dots) are compared to the $Z \to ee$ POWHEG MC simulation (hatched histograms) [69].

4.1.3.2 Z boson p_T and mass width reweighting

The measured p_T^Z distribution (Chapter 5) and the measured ϕ_η^* distribution (Chapter 6) have to be unfolded due to the effect of detector resolution. The $Z \to ee$ POWHEG+PYTHIA MC sample will be employed for the unfolding procedure. It has been found that the description of the p_T^Z spectrum provided by the $Z \to ee$ POWHEG+PYTHIA MC is not good especially in the low p_T^Z region. Therefore, a reweighting needs to be applied on the p_T^Z spectrum in this MC sample to better describe data before it is employed. More details of this work for the p_T^Z measurement and the ϕ_η^* measurement will be discussed in Section 5.5.4 and Section 6.1.2.

It has been also found that the lineshape of the Z resonance simulated in the $Z \to ee$ POWHEG+PYTHIA MC is different with respect to the one generated in the RESBOS program. The ratio of the generated M_Z distributions from PYTHIA or POWHEG+PYTHIA to RESBOS prediction are shown in Figure 4.3. We decided to reweight the shape of the Z resonance of POWHEG+PYTHIA to the RESBOS prediction. The maximum correction of 2% at the Z peak has no visible effect on the predicted p_T^Z and ϕ_η^* spectra.

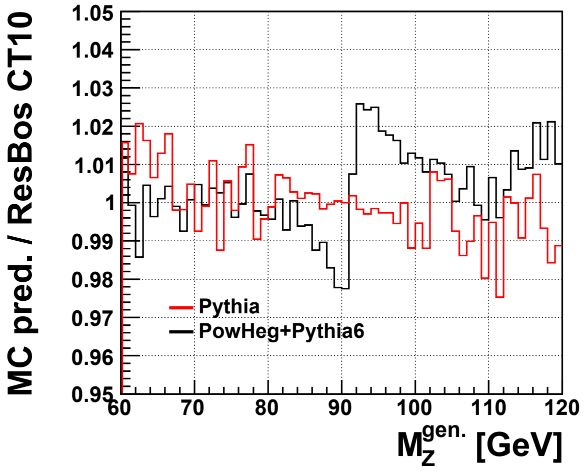

Figure 4.3: Ratio of the generated M_Z distributions from PYTHIA *or* POWHEG+PYTHIA *to* RESBOS *[69].*

4.1.3.3 Reweighting of the z-vertex shape

The distribution of the z coordinate of the primary vertex has a quite large difference between data and some MC simulations used in the analysis. For those MC events we reweighted the z vertex shape to match data. The z vertex shape in MC simulation before and after reweighting is shown in Fig. 4.4 and compared to the shape observed in data.

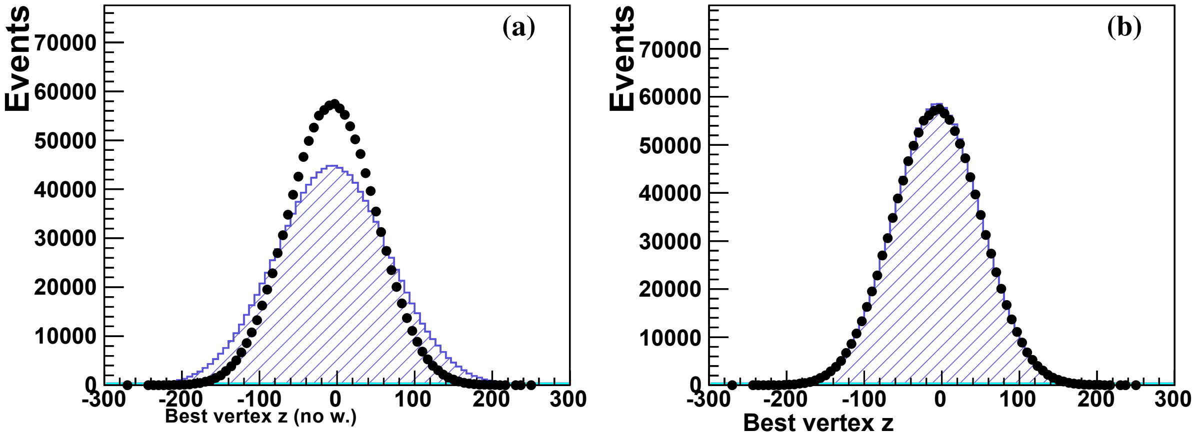

Figure 4.4: Distributions of the z position of the reconstructed primary vertex for $Z \rightarrow ee$ candidates. Data (black dots) are compared to the $Z \rightarrow ee$ POWHEG *MC simulation (hatched histograms), before (a) and after (b) applying the reweighting procedure [69].*

4.2 Event selection

The selection criteria of $Z \rightarrow ee$ events are listed in Table 4.2. Events are selected using single electron triggers. Different triggers are required depending on the data period as detailed in Table 4.3.

The four-momentum of electrons is computed using information from both the cluster and the track matched to the cluster. The energy is given by the cluster energy. The ϕ and η directions are taken from the corresponding track parameters at the vertex. Gaussian-sum filter (GSF - see Section 3.2) electrons are used for this analysis. This allows to take into account the effect of bremsstrahlung in the electron reconstruction. The full analysis chain is run in parallel using either standard or GSF electrons in order to compare the two reconstructions. The ratio of selected events using both electron reconstructions are presented in Figure 4.5, for kinematic variables of the reconstructed Z boson. We observe that the difference in efficiency of the two electron reconstructions is of the order of 0.2 % and is reproduced by the MC. The transverse momentum of the leading electron is required to be larger than 25 GeV in order to avoid the effect from the trigger threshold cuts (20 or 22 GeV). Electrons reconstructed in the LAr transition region are excluded based on the η variable reconstructed from the electron cluster (η_{cl}).

Collision event selection	
GRL: stable colliding beams [6]	
At least 1 good vertex with $N_{\text{tracks}} \geq 3$	
Trigger requirement (period dependent, see Table 4.3)	
Good-electron selection	
Phase space	$p_{\mathrm{T}}^{el1} > 25$ GeV and $p_{\mathrm{T}}^{el2} > 20$ GeV
	$\lvert\eta_{trk}\rvert < 2.4$
Electron ID	Medium++
	GSF Electron author 1 or 3
LAr transition removal	$1.37 < \lvert\eta_{cl}\rvert < 1.52$
$Z \rightarrow ee$ event selection	
	2 highest p_{T} electrons
Charge	Opposite sign
Invariant mass	66 GeV $< M_{ee} <$ 116 GeV

Table 4.2: Event selection for the $Z \rightarrow ee$ channel.

Trigger	Data period	Integrated luminosity [fb^{-1}]
EF_e20_medium	D-J	1.68
EF_e22_medium	K	0.59
EF_e22vh_medium1	L-M	2.43

Table 4.3: Trigger used in the different data taking periods.

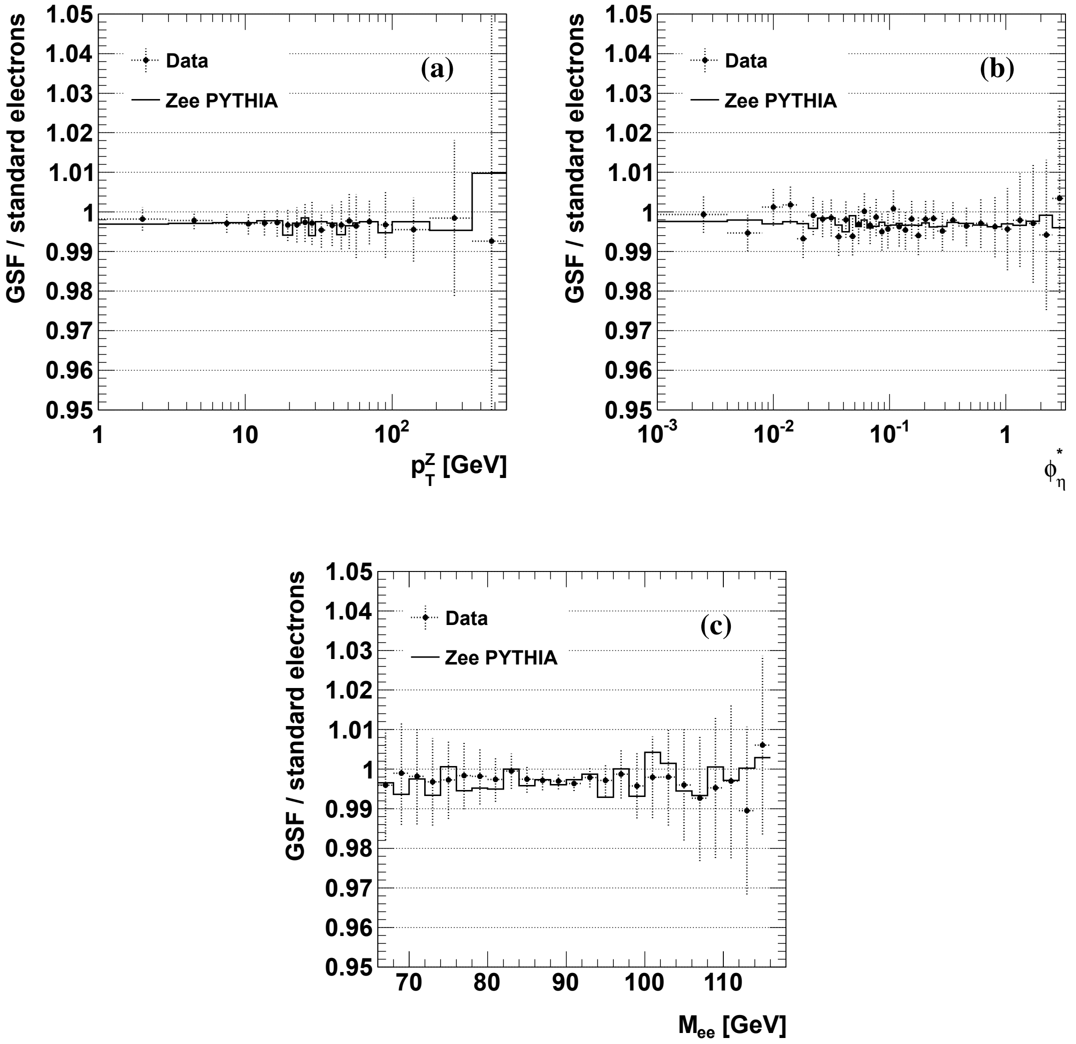

Figure 4.5: Ratio between the number of selected events using GSF or standard electrons in data and in $Z \to ee$ MC samples, as a function of the p_T^Z (a), ϕ^*_η (b) and M_{ee} (c) variables.

4.3 Analysis level corrections

Various corrections are applied to correct for remaining mis-calibrations in data or mis-modeling of the data by the MC. Reweighting corrections applied to the MC samples are detailed in Section 4.1.3. The $Z \to ee$ reconstruction has to take into account all corrections for electrons including trigger efficiency correction, reconstruction and identification efficiency correction, energy scale and resolution corrections (see Sections 3.5, 3.6.1 and 3.6.2). While the energy scale correction is applied on data, all other corrections are applied on MC. Details of these corrections can be found in [69].

4.4 Background estimation

Backgrounds for the $Z \to ee$ selection can be divided in two categories: electroweak background and QCD multi-jet background (QCD background).

4.4.1 Electroweak background

Electroweak (EW) background contains real high transverse momentum electrons from electroweak boson decays. Significant contributions are $W \to \ell\nu$ and $Z \to \tau\tau$ processes, as well as $t\bar{t}$ pairs where W bosons decay into electron-neutrino pairs. In addition the di-bosons decays WW, WZ, ZZ are considered. The contribution of these background processes to the final selection is estimated from MC samples (see Table 4.1).

4.4.2 QCD background

QCD background arises mostly from mis-identification of jets as isolated electrons. The cross sections are huge and suffer significant uncertainties therefore the estimation of this background requires to use data-driven methods.

4.4.2.1 Template fit method

The idea is to select a sample of data events which models the QCD background so that its shape can be extracted for any observable considered in this analysis. The QCD sample is then rescaled to the size of the QCD background in the standard $Z \to ee$ selection and is used to model the distributions of the real QCD background for all observables of interest. In this analysis the observables of interest are p_T^Z and ϕ_η^*. This method assumes that the shape of the observable in the QCD template sample reproduces the shape of the one in the standard selection. The validity of this assumption will be tested by comparing QCD samples selected in different ways. The normalization factor (and equivalently the fraction of QCD background events in the standard selection) is estimated using a maximum likelihood fit to the di-electron mass distribution in the inclusive standard selection with two template distributions: the invariant mass distribution taken from MC predictions for $Z \rightarrow ee$ signal plus EW backgrounds and the invariant mass distribution obtained from the QCD template sample. Since the signal MC does not describe perfectly the mass distribution in the peak region and the contribution of QCD background is very small, the range of the fit is extended with respect to the nominal mass range. The signal MC in POWHEG or PYTHIA is merged with the Drell-Yan (DY) low mass sample to improve the stability of the fit. The mass distributions of this sample at the generated level and at reconstructed level are shown in Figure 4.6.

In order to select a QCD template sample, the standard event selection is modified to enhance the QCD background. There are two QCD samples selected for the template fit. One is used to perform the nominal fit and to study the global systematic uncertainties in the mass fit range, the other one is used to study the systematic uncertainty of the QCD background estimation as a function of p_T^Z or ϕ_η^*.

- **Loosened ID template.** The trigger requirement is relaxed to the lowest un-prescaled di-photon loose trigger EF_2g20_loose. Only electrons passing the loose ID cut and failing the medium one are considered. At least two of these electrons passing other standard cuts (except charge and invariant mass cuts) will contribute to the QCD sample. A small contamination of signal events and events from EW processes is still present in this sample. The contamination is estimated by applying the exact same QCD selection on the signal and EW MC samples and is subtracted to obtain the real QCD sample. The contamination in this QCD sample is 1.7%. The template fit using this QCD sample in the mass range [50 GeV, 200 GeV] has the best χ^2. It is chosen for the nominal result which is $3256.42 \pm 0.17\%$ (stat) $\pm 6.6\%$ (fit) events corresponding to 0.27% the total number of $Z \rightarrow ee$ candidates selected in data. The fit is shown in Figure 4.7.

- **Non-isolated template.** In this selection, we use the same trigger requirement as in the signal selection but only events with two electrons failing "medium++" or one of two electrons failing "medium++" are considered. These events are required to pass other standard cuts as for the signal (except charge and invariant mass cuts). The variable "Etcone40/Et" is used to study the isolation of electrons in this sample, where "Etcone40" indicates the transverse energy in a cone with a radius of 0.4 from the center of an electron cluster subtracting the transverse energy of this electron cluster, "Et" is the transverse energy of this electron. The distributions of this variable for the first and the second electrons are shown in Figure 4.8. The isolation of the first electron versus the isolation of the second electron of QCD candidates in data and in the contamination from $Z \rightarrow ee$ signal MC and EW background is shown in Figure 4.9(a). Before the isolation cut, there is strong contamination from $Z \rightarrow ee$ signal MC and EW background in this QCD sample, the ratio in the isolation window between the number of QCD candidates in data and in the contamination is shown in Figure 4.9(b). In order to reduce the contamination in this QCD sample, we apply the isolation cut to select only candidates in the non-isolated region. This cut is based on the relation between the isolation of the first electron and the second electron as can be seen in Figure 4.9(b). The contamination after this cut is 2% compatible with the first QCD sample 1.7%. The template fit using this QCD sample is also performed in the mass range [50 GeV, 200 GeV].

The final QCD background using the template fit for the two QCD samples is shown in Figure 4.10.

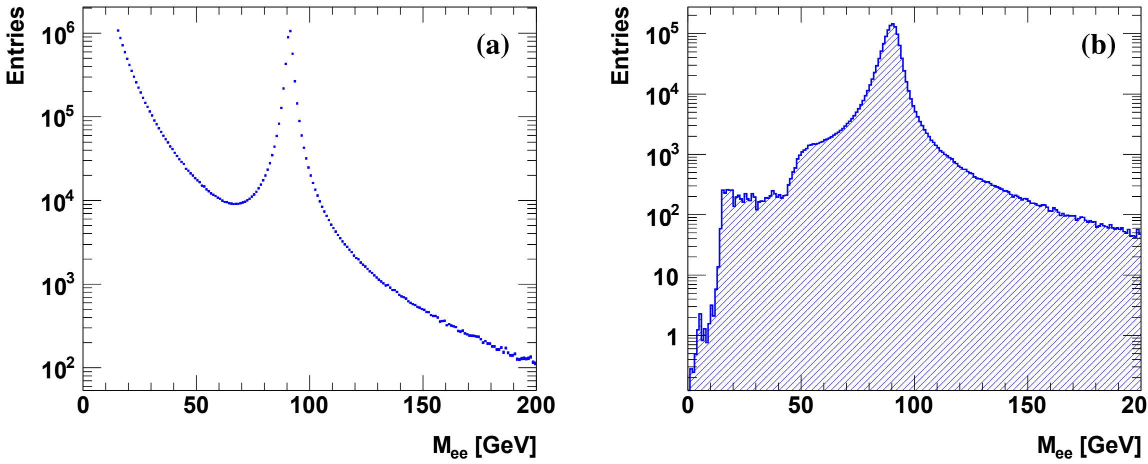

Figure 4.6: The mass distributions of the merged signal sample using POWHEG *and DY samples in the generation (a) and in the reconstruction (b) [69].*

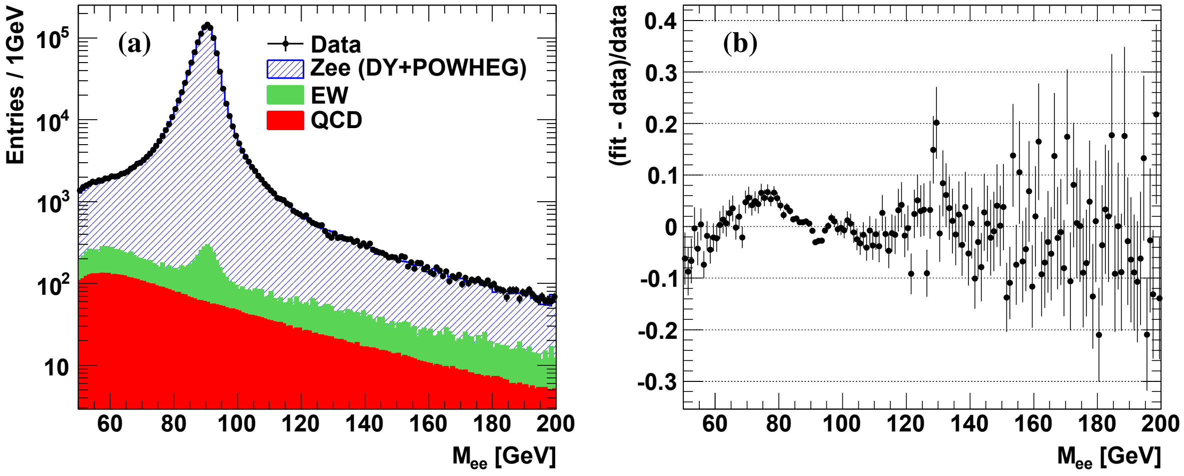

Figure 4.7: Data compared with the signal MC, EW background and fitted QCD background (a), the difference between the fit function and data (b). The signal MC and EW background are normalized by the parameter of the fit (0.99)*. Only statistic uncertainty is displayed [69].*

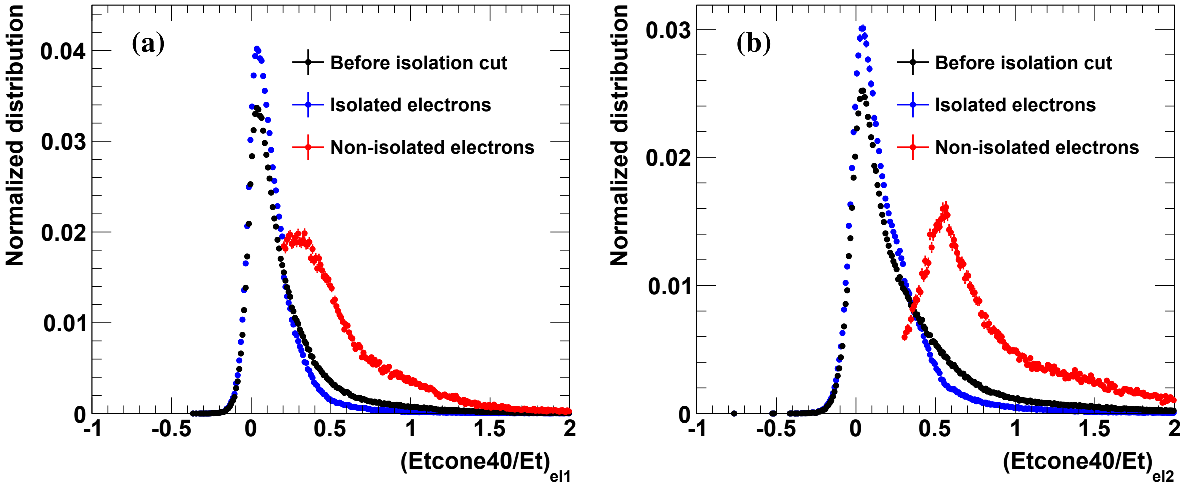

Figure 4.8: The isolation distributions in data of the first electron (a) and of the second electron (b) before the isolation cut and after the isolation cut for isolated electrons and non-isolated electrons [69].

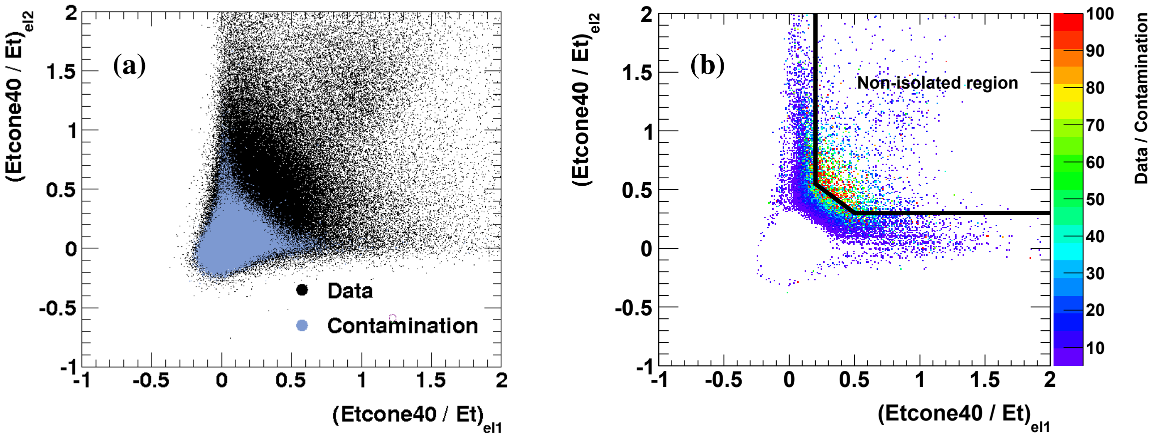

Figure 4.9: The isolation variable "Etcone40/Et" of two electrons of QCD candidates in data and in the contamination from $Z \to ee$ signal MC and EW background (a). The ratio in the isolation window between the number of QCD candidates in data and in the contamination (b) [69].

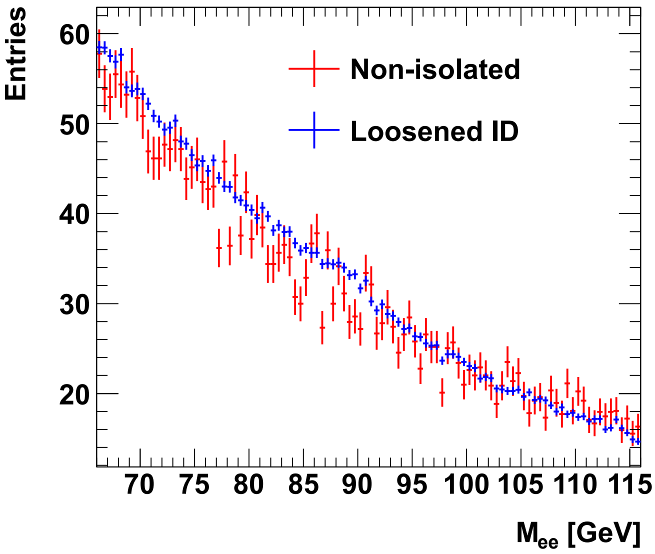

Figure 4.10: The final QCD background using the template fit for the two QCD samples [69].

4.4.2.2 Systematic uncertainties

The systematic uncertainties on the QCD background estimation come from the template fit method and from the fluctuations of the QCD template samples.

- **The uncertainty from the template fit method.** It is estimated using the default QCD template and varying the choice of signal MC samples and the choice of fit ranges and bin widths.

  The choice of signal MC shapes. The normalization of the MC template is constrained in the Z peak region and the normalization of the QCD template is constrained in the side-bands. The MC normalization may be sensitive to the signal MC samples if the predicted shapes in the region of the Z peak are different. The QCD normalization also depends on the shape of the MC template in the side-bands. These effects are studied by using two different signal MC templates: DY+POWHEG (for the nominal result) and DY+PYTHIA. As seen in Section 4.1.3.2 the two POWHEG and PYTHIA MC have two different mass shapes. For this study, the reweighting of the generated M_Z distribution is not applied to POWHEG MC events, in order to maximise the difference with PYTHIA.

  The choice of fit ranges and bin widths. This effect is studied by performing the fit in different mass ranges and with different bin widths. The mass range [50 GeV, 200 GeV] is chosen for the nominal result where the QCD sample in high mass range is enough to constrain the fit and other ranges [55 GeV, 200 GeV], [60 GeV, 200 GeV] and [66 GeV, 200 GeV] are used to study the uncertainty. The bin width of 1 GeV is chosen for the nominal result while 2 and 4 GeV bins are used to determine the uncertainty associated to the binning.

  The fraction of QCD background obtained in the nominal fit and these variations is shown in Table 4.4. Each systematic uncertainty is chosen as the largest variation from the nominal value. The uncertainties in these two different categories are considered as uncorrelated. All systematic uncertainties from the template fit method and the error of the nominal fit (6.6%) are added in the quadratic sum. The total systematic uncertainty from the template fit method is 47%.

Procedure	QCD Fraction [%]	Fit Error [%]
DY+POWHEG 1 GeV bin [50, 200] (nominal value)	0.27	6.60
DY+POWHEG 1 GeV bin [40, 200]	0.26	6.42
DY+POWHEG 1 GeV bin [55, 200]	0.22	8.78
DY+POWHEG 1 GeV bin [60, 200]	0.17	11.66
DY+POWHEG 1 GeV bin [66, 200]	0.15	17.24
DY+POWHEG 2 GeV bin [50, 200]	0.26	6.66
DY+POWHEG 4 GeV bin [50, 200]	0.24	7.58
DY+PYTHIA 1 GeV bin [40, 200]	0.23	7.54
DY+PYTHIA 1 GeV bin [50, 200]	0.22	6.69

Table 4.4: QCD background fractions obtained in each variation of the fitting procedure.

- **The fluctuations of the QCD template samples.** The use of two different QCD background templates allows to access the systematic uncertainty on the shapes of QCD background as a function of p_T^Z or as a function of ϕ_η^*. The ratio between the two results using these two QCD background templates as a function of p_T^Z or as a function of ϕ_η^* is shown in Figure 4.11. The ratio drops at very high ϕ_η^* values and we consider this as a source of systematic uncertainty.

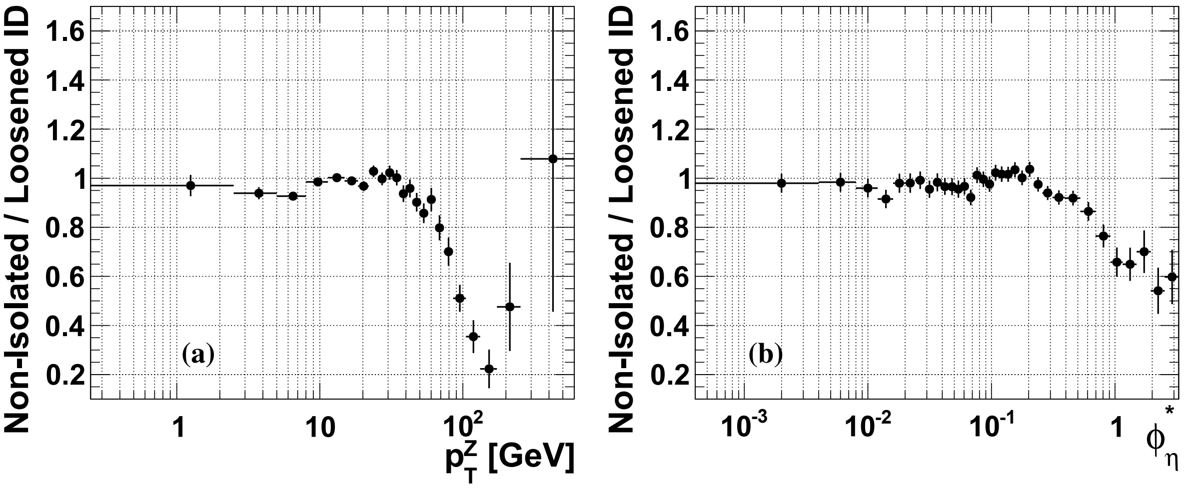

Figure 4.11: Ratio of two QCD background estimations as a function of p_T^Z (a) and as a function of ϕ_η^* (b). Only, the statistical uncertainty is shown.

The systematic uncertainty in the p_T^Z or ϕ_η^* shape is added in quadrature with the one from the template fit method. The total systematic uncertainty is $\sim 50\%$. The difference between the QCD background fractions estimated using two different shapes of the Z mass peak, as provided by non-reweighted PYTHIA and POWHEG simulations is 18%, well below the total systematic uncertainty of 50%.

Finally, the total systematic uncertainty of the QCD background estimation in different p_T^Z bins is shown in Table 4.5 and in different ϕ_η^* bins is shown in Table 4.6. The choice of bin widths for the p_T^Z spectrum and the ϕ_η^* spectrum will be discussed later in Chapter 5 and Chapter 6.

Bin	Range	Sys. unc. (%)	QCD fraction (%)
1	0.0 - 2.5	47	0.08
2	2.5 - 5.0	48	0.11
3	5.0 - 8.0	48	0.18
4	8.0 - 11.4	47	0.25
5	11.4 - 14.9	47	0.31
6	14.9 - 18.5	47	0.37
7	18.5 - 22.0	47	0.41
8	22.0 - 25.5	47	0.43
9	25.5 - 29.0	47	0.44
10	29.0 - 32.6	47	0.44
11	32.6 - 36.4	47	0.43
12	36.4 - 40.4	48	0.40
13	40.4 - 44.9	47	0.40
14	44.9 - 50.2	48	0.38
15	50.2 - 56.4	49	0.36
16	56.4 - 63.9	48	0.30
17	63.9 - 73.4	51	0.26
18	73.4 - 85.4	56	0.22
19	85.4 - 105.0	68	0.18
20	105.0 - 132.0	80	0.13
21	132.0 - 173.0	91	0.10
22	173.0 - 253.0	71	0.08
23	253.0 - 600.0	48	0.05

Table 4.5: The total systematic uncertainty of the QCD background estimation in different p_T^Z bins.

Bin	Range	Sys. unc. (%)	QCD fraction (%)
1	0.000 - 0.004	47	0.18
2	0.004 - 0.008	47	0.18
3	0.008 - 0.012	47	0.19
4	0.012 - 0.016	48	0.19
5	0.016 - 0.020	47	0.19
6	0.020 - 0.024	47	0.19
7	0.024 - 0.029	47	0.20
8	0.029 - 0.034	48	0.21
9	0.034 - 0.039	47	0.22
10	0.039 - 0.045	47	0.23
11	0.045 - 0.051	47	0.24
12	0.051 - 0.057	48	0.24
13	0.057 - 0.064	47	0.25
14	0.064 - 0.072	48	0.26
15	0.072 - 0.081	47	0.28
16	0.081 - 0.091	47	0.29
17	0.091 - 0.102	47	0.30
18	0.102 - 0.114	47	0.31
19	0.114 - 0.128	47	0.32
20	0.128 - 0.145	47	0.33
21	0.145 - 0.165	47	0.33
22	0.165 - 0.189	47	0.35
23	0.189 - 0.219	47	0.35
24	0.219 - 0.258	47	0.36
25	0.258 - 0.312	48	0.36
26	0.312 - 0.391	48	0.35
27	0.391 - 0.524	48	0.33
28	0.524 - 0.695	49	0.29
29	0.695 - 0.918	53	0.27
30	0.918 - 1.153	58	0.25
31	1.153 - 1.496	59	0.25
32	1.496 - 1.947	56	0.26
33	1.947 - 2.522	66	0.28
34	2.522 - 3.277	62	0.35

Table 4.6: The total systematic uncertainty of the QCD background estimation in different ϕ^*_η bins.

4.5 Selection results and control distributions

After applying all selection criteria, 1223711 $Z \to ee$ candidates are observed in data. The total number of predicted events is 1235240. The total number of observed $Z \to ee$ candidates therefore agrees at the level of 0.9% with the sum of predictions for the different contributing processes. The individual contributions of different background processes are detailed in Table 4.7. The signal MC $Z \to ee$ is from POWHEG. "Diboson" denotes the total result from WW, WZ, ZZ. The fraction of QCD background events amongst the selected $Z \to ee$ candidates is 0.27%, whilst the fraction of background events arising from all electroweak processes is 0.34%. Typical kinematic distributions of observed $Z \to ee$ candidates are compared to the prediction of the MC simulation in Figures 4.12, 4.13, 4.14 and 4.15.

Sample	Data	Prediction tot.	$Z \to ee$	QCD	$W \to e\nu$	$Z \to \tau\tau$	$t\bar{t}$	Diboson
# candidates	1223711	1235240	1227771	3256	222	643	1429	1919
Stat. Error	±1106	±573	±570	±6	±16	±54	±26	±7

Table 4.7: Number of $Z \to ee$ candidates after all selections in different samples. The total statistical error on the predicted number of Z candidates is indicated.

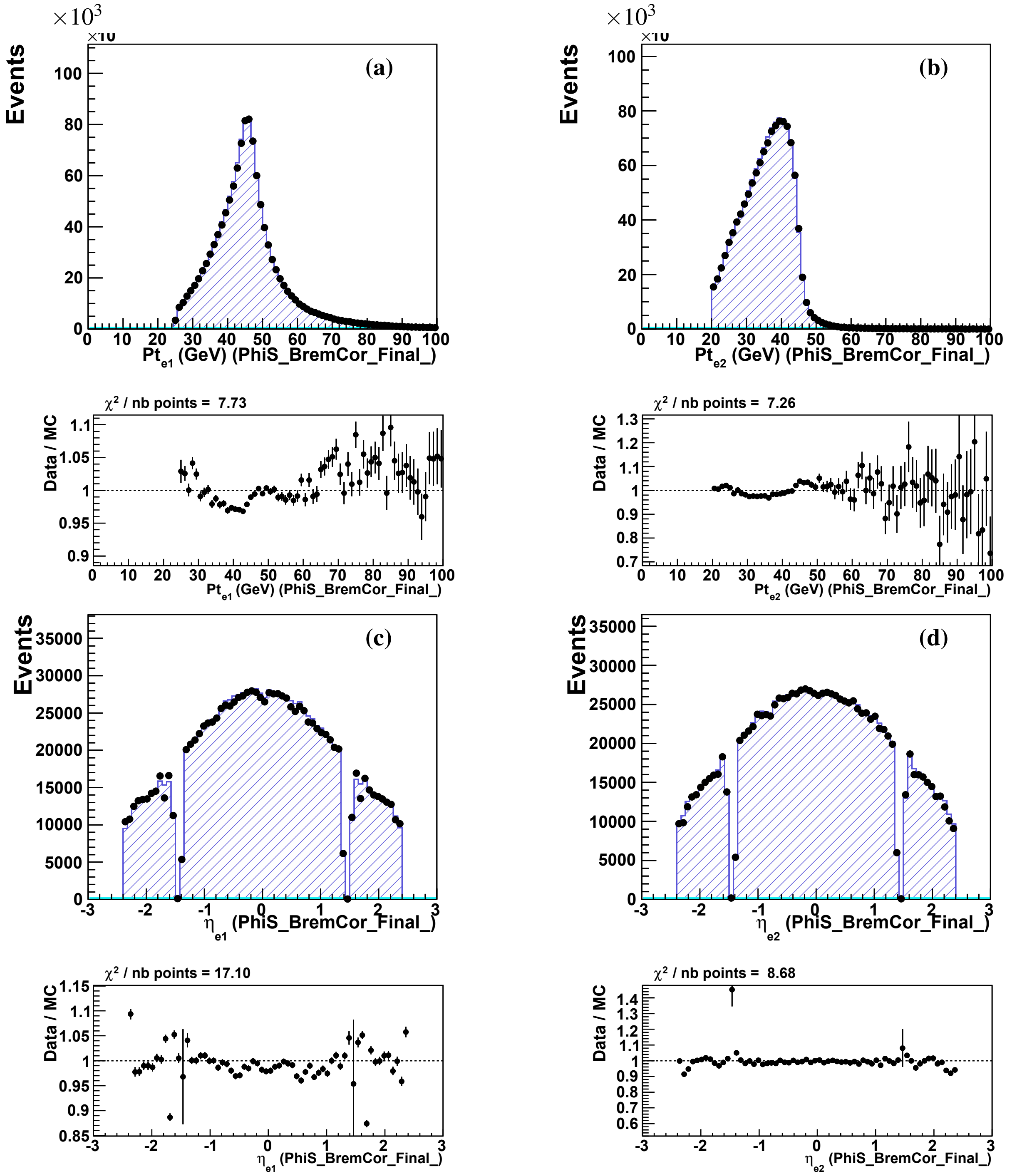

Figure 4.12: Control distributions of kinematic variables of the two electrons of the Z candidate. Data (black dots) are compared to the $Z \to ee$ POWHEG *MC simulation (hatched histograms). Only statistical errors, of both data and MC samples, are taken into account for the display of error bars in data/MC ratio plots. No errors are displayed for MC histograms [69].*

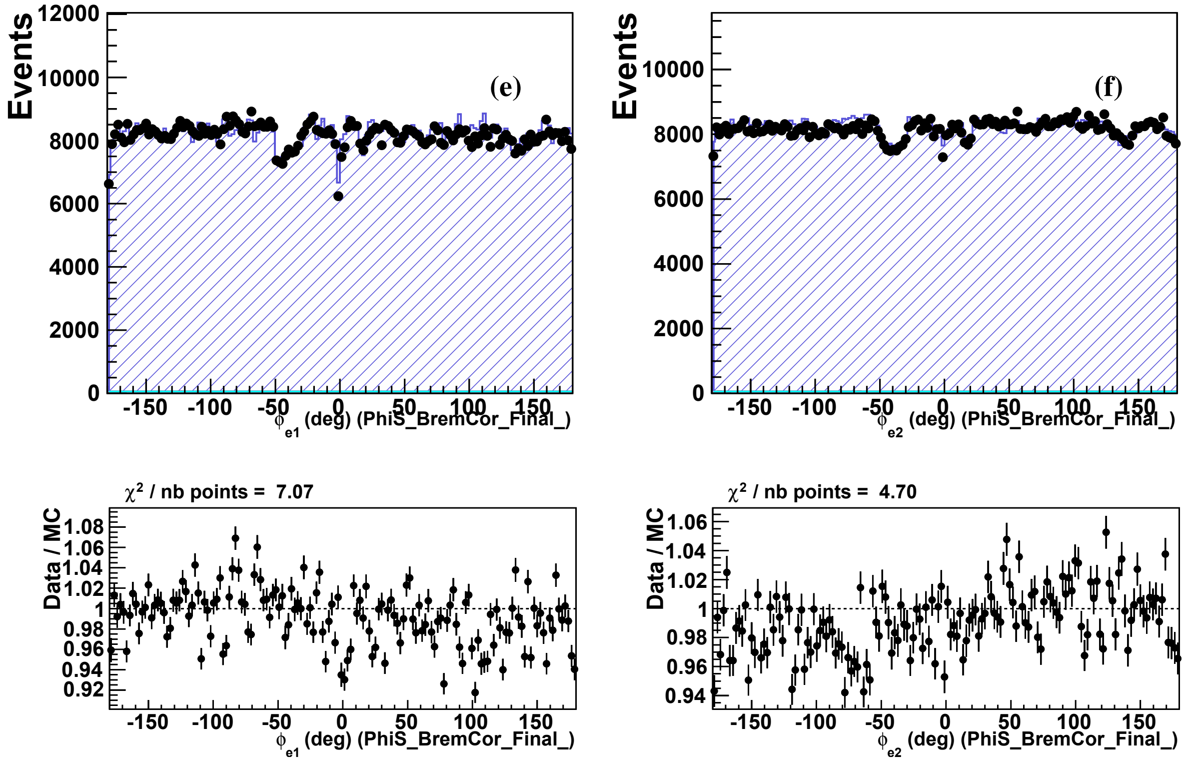

Figure 4.13: Control distributions of kinematic variables of the two electrons of the Z candidates. Data (black dots) are compared to the $Z \to ee$ POWHEG *MC simulation (hatched histograms). Only statistical errors, of both data and MC samples, are shown [69].*

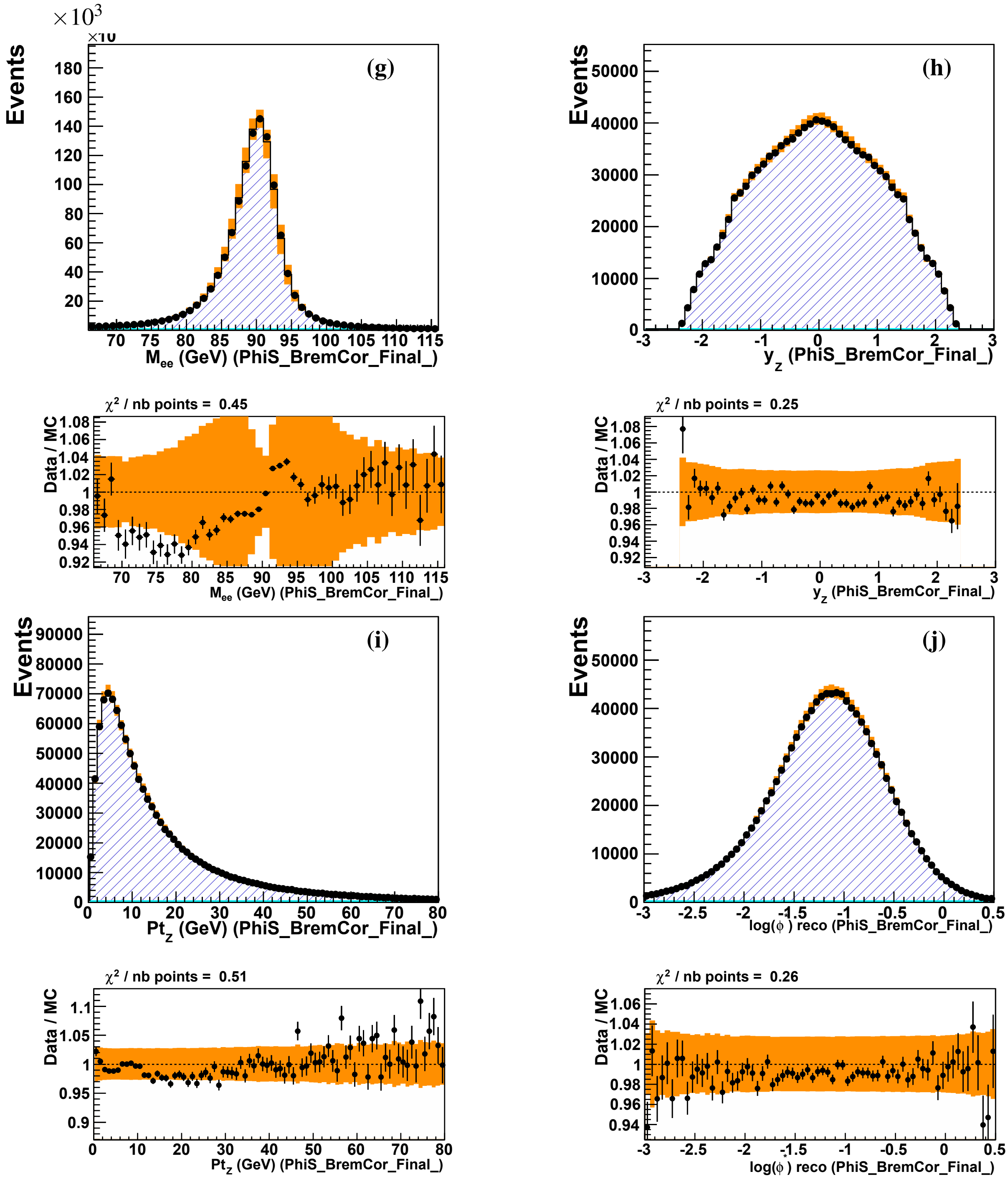

Figure 4.14: Control distributions of kinematic variables of the Z candidates. Data (black dots) are compared to the $Z \to ee$ POWHEG *MC simulation (hatched histograms). For these control distributions, the* POWHEG *MC simulation is reweighted as a function of ϕ^*_η to the measured differential cross section. Statistical errors of the data are represented by error bars on black dots. The total systematic errors are represented by the orange bands [69].*

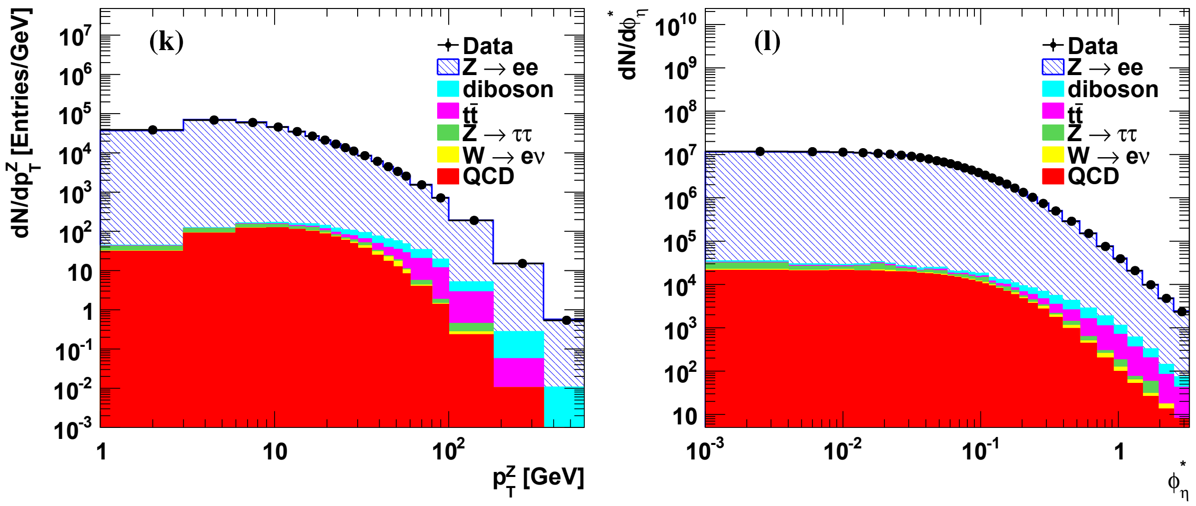

Figure 4.15: Control distributions of p_T^Z and ϕ_η^* of the Z candidates. Data (black dots) are compared to the stack of the signal and the EW background estimated from MC samples and the QCD background estimated using the data driven method. Only statistical errors of data are shown [69].

4.6 Summary

This chapter describes the event selection employed for the p_T^Z and ϕ_η^* measurements. All corrections due to remaining mis-calibrations in data or mis-modeling of the data by the MC were applied. Most of this chapter is dedicated to the QCD background estimation. Two independent data driven samples are used to extract the QCD background using a template fit method. Finally, the total number of observed $Z \to ee$ candidates in data agrees at the level of 0.9% with the sum of predictions for the different contributing processes. The agreement between data and MC in the p_T^Z and ϕ_η^* distributions is needed for the differential cross section measurements of $Z \to ee$ as a function of p_T^Z or as a function of ϕ_η^* in Chapter 5 and Chapter 6.

Chapter 5

The differential cross section of $Z \to ee$ as a funtion of p_T^Z

This chapter will describe the general steps towards the differential cross section measurements of $Z \to ee$ as a funtion of p_T^Z or as a function of ϕ_η^*. A short introduction of the unfolding procedure is presented in Section 5.1. Two unfolding methods are employed in this thesis work : Iterative bayesian unfolding for the p_T^Z measurement and bin-by-bin unfolding for the ϕ_η^* measurement. The measured distribution of p_T^Z or ϕ_η^* are unfolded to different truth levels which are defined in Section 5.2. The fiducial volume of the measurements are defined in Section 5.3. The extrapolation procedure of the fiducial measurements to the full phase space measurements is presented in Section 5.4.

The core of thesis work is the ϕ_η^* measurement. However the advantage of the ϕ_η^* measurement can be checked by comparing the quantified systematic uncertainties of the ϕ_η^* measurement with the ones of the p_T^Z measurement. Therefore the goal of this chapter is to estimate the main systematic uncertainties of the p_T^Z measurement which are presented in Section 5.6. In addition the result of the p_T^Z measurement is compared with theoretical predictions and with other p_T^Z measurements as will be shown in Section 5.7.

5.1 Unfolding methods

In experiments, the distribution of the measured observable is smeared and distorted from that of the corresponding true physical quantity due to detector effects, such as a limited acceptance, an imperfect efficiency, and a finite resolution. Mathematically, given a true variable x (to be determined in an experiment) distributed according to its probability density function (p.d.f.) $f(x)$, can not be measured perfectly due to both experimental and statistical uncertainties. As a result, instead of measuring x one typically measures a related variable y distributed according to a different p.d.f $g(y)$. The relation between $f(x)$ and $g(y)$ is given by the integral equation,

$$g(y) = \int A(y,x) f(x) dx, \tag{5.1}$$

called a Fredholm integral equation of the first kind. In practice often a known (measured or simulated) background contribution $b(y)$ has to be added to the right-hand side of equation 5.1. In this section with the purpose of presenting the methodology, this contribution is ignored. The resolution function $A(y,x)$ represents the effect of the detector. For a given value $x = x_0$ the function $A(y,x_0)$ describes the response of the detector in the variable y for that fixed value x_0. Determining the distribution $f(x)$ from the measured distribution $g(y)$ is called the inverse problem of unfolding. Unfolding of course requires the knowledge of the resolution function $A(y,x)$, i.e. all the effects of the limited acceptance, the imperfect efficiency, and the finite resolution.

In addition to the imperfections of the detector, there may be further effects between x and y, which are outside of the experimental control, even with an ideal detector. One example are radiative effects, which in experiments are often corrected afterwards (radiative corrections), but behave similarly as detector effects. If the true kinematical quantity is defined at the parton level, further effects from the fragmentation process of partons to the (observable) hadrons influence the measured quantity y.

For the numerical solution of equation 5.1, the distributions can be presented by histograms and the resolution function can be presented by a matrix in order to have a finite set of parameters. Equation 5.1 then becomes

$$\mathbf{y} = \mathbf{A}\mathbf{x}. \tag{5.2}$$

The vector $\mathbf{y}$ represents a histogram with n bins of the measured quantity while the vector $\mathbf{x}$ represents a histogram with m bins of the true quantity to be measured. The transformation from $\mathbf{x}$ to $\mathbf{y}$ is performed by $\mathbf{A}$ (now is called the response matrix) with a dimension of $n \times m$. The elements of the response matrix a_{ij} can be considered as the probability for a true value x_j to be measured as a value y_i.

In high energy physics experiments the problem is even more difficult than in other fields. Often the statistics of the measurement is not high and every $\mathbf{y}$-bin content (which is distributed due to the Poisson distribution around the expected value) has a large statistical fluctuation. Furthermore the resolution function $A(x,y)$ (or the response matrix $\mathbf{A}$) is not known analytically, but it is represented by a data set from Monte Carlo simulation of the process, based on some assumed distribution $f_{MC}(x)$,

$$g_{MC}(y) = \int A(y,x) f_{MC}(x) dx, \tag{5.3}$$

and is also statistically limited. Standard methods for the solution of integral equations or linear equations can not be used in this case.

A simple method like the so-called bin-by-bin correction may be meaningful if the measurement y is very close to the true value x. Advanced unfolding methods, for instance an iterative bayesian unfolding, take into account bin-by-bin migrations and reduce the dependence on the truth shape x in a Monte Carlo generator employed for the unfolding.

5.1.1 Bin-by-bin unfolding

The final goal is the measurement of the normalised differential cross section $(1/\sigma)(d\sigma/d\mathscr{R})$, where $\mathscr{R}$ is p_T^Z or ϕ_η^* in this analysis, σ is measured within the fiducial phase space, defined in Section 5.3. The measured $\mathscr{R}$ spectrum of the di-electron system can be corrected for detector and QED final state radiation (FSR) effects using an unfolding technique based on bin-by-bin correction factors. The unfolding procedure allows to go from the measured spectrum back to the underlying "true" spectrum (see Section 5.2). Using the bin-by-bin correction procedure the normalised fiducial cross section in the i-th $\mathscr{R}$ bin is given by:

$$\left(\frac{1}{\sigma}\right)_{fid} \left(\frac{\Delta\sigma_i}{\Delta\mathscr{R}_i}\right)_{fid} = \frac{C}{C^i} \cdot \frac{\left(N^i_{\text{data}} - N^i_{\text{bg}}\right)}{\Delta\mathscr{R}_i \cdot \left(N^{tot}_{\text{data}} - N^{tot}_{\text{bg}}\right)} \tag{5.4}$$

where σ is the inclusive cross section, $\Delta\sigma_i$ is the cross section for a given $\mathscr{R}$ bin i, $\Delta\mathscr{R}_i$ is its width, N^i_{data} is the number of observed candidates in bin i, N^i_{bg} is the number of expected background events in bin i, N^{tot}_{data} is the total number of candidate events and N^{tot}_{bg} is the total number of expected background events. There is no dependence on the luminosity, since both σ and $\Delta\sigma_i$ are proportional to it. The correction factors C^i are calculated per each bin from Monte Carlo. The factors C^i and of C are computed in the fiducial phase space at corresponding truth levels in 5.2 according to the following expressions:

$$C^i = \frac{N^i_{\text{MC,rec,cuts}}}{N^i_{\text{MC,gen,fid}}} \qquad C = \frac{N^{tot}_{\text{MC,rec,cuts}}}{N^{tot}_{\text{MC,gen,fid}}} \tag{5.5}$$

where $N^i_{\text{MC,rec,cuts}}$ is the number of reconstructed MC events in bin i after having applied all cuts, $N^i_{\text{MC,gen,fid}}$ is the number of generated MC events in bin i after having applied the fiducial cuts, $N^{tot}_{\text{MC,rec,cuts}}$

is the total number of reconstructed MC events after having applied all cuts and $N^{tot}_{\mathrm{MC,gen,fid}}$ is the total number of generated MC events after having applied the fiducial cuts. $C^i_{norm} = \frac{C^i}{C}$ is called the normalised correction factors in each bin of $\mathscr{R}$.

5.1.2 Iterative Bayesian unfolding

Iterative Bayesian unfolding allows to take into account the migration effect and correlations between adjacent bins which are neglected by the bin-by-bin correction technique.

The iterative unfolding technique proposed by D'Agostini [67, 68] and implemented in the RooUnfold package [25] relies on the construction of the unfolding matrix by means of Bayes' theorem. Starting with a prior assumption for the probability distribution $\mathbf{p} = (p_1, ..., p_N)$ for an event to originate from a given bin i of the true distribution, one infers the transition probability

$$p(t_i|o_j) \equiv p(\text{true value in bin } i|\text{observed value in bin } j)$$

by doing a probability inversion via Bayes' theorem:

$$p(t_i|o_j) = \frac{p(o_j|t_i)p_i}{\sum\limits_{i=1}^{N} p(o_j|t_i)p_i} \ . \tag{5.6}$$

The values of $p(o_j|t_i)$ can be inferred from Monte Carlo and constitute the so-called smearing matrix (or response matrix) representing the detector response. Taking into account the efficiency $\varepsilon = (\varepsilon_1, ..., \varepsilon_N)$, the number of events $\hat{\mu}_i$ in a given bin of the true distribution can now be estimated by the relation

$$\hat{\mu}_i = \frac{1}{\varepsilon_i} \sum_{j=1}^{m} p(t_i|o_j) n_j \ , \tag{5.7}$$

where n_j is the number of events observed in bin j. Since the shape of the true distribution is in general unknown, one often starts with a flat spectrum $\mathbf{p} = (\frac{1}{N}, ..., \frac{1}{N})$ as a prior, thus introducing a bias. This bias can be overcome by iterating the procedure, using the solution of the previous step as the new prior $\mathbf{p} = \frac{1}{\sum_{i=1}^{N} \mu_i}(\mu_1, ..., \mu_N)$. This algorithm is typically found to converge after several iterations. The estimation of uncertainties for the method described here is performed by full marginalisation. That means that the posterior distribution of bin contents after unfolding is obtained by integrating over the distributions associated with the measured bin contents and the unfolding matrices obtained from Monte Carlo. The integration is performed with Markov Chain Monte Carlo (MCMC), details can be found in [67]. All correlations are naturally taken into account in this approach.

The unfolded differential cross sections at different truth levels as discussed in Section 5.2 can be obtained using the iterative Bayesian unfolding method with corresponding response matrices inferred from MC at each level.

5.2 Definition of the truth levels

The unfolding procedure allows to go from the measured spectrum back to the underlying "true" spectrum, where the true spectrum can be defined at different reference points referring to the amount of QED radiative corrections considered at the generator level. Here, as in the published ATLAS paper on the measurement of the p_T^Z with 2010 data [16], the default reference point is the "Born" level corresponding to the $\mathscr{R}$ spectrum prior to QED FSR from the decay electrons. Nevertheless, as in previous ATLAS analyses, additional points of reference ("Bare" and "Dressed") have been considered. With respect to the "Born" level reference point, they have the advantage to be closer to the lepton measurements. The reference points considered in this analysis are:

- **Born:** the true $\mathscr{R}$ spectrum uses the electron momenta prior to QED FSR. This reference point is also referred to as "propagator Z".
- **Bare:** the true $\mathscr{R}$ spectrum uses the electron momenta after QED FSR.
- **Dressed:** the true $\mathscr{R}$ spectrum uses the electron momenta after QED FSR and includes the momenta of all photons which are radiated off the electron in a cone of $\Delta R < 0.1$ around the "bare" lepton direction. This reference point is supposed to be the closest to the measurement of $Z \to ee$. Given that the major part of the QED FSR photons is collinear and thus close to the electromagnetic cluster of the bare electron and that the ATLAS cluster reconstruction recombines the bare electron with 'close' photons, the amount of remaining QED FSR corrections is reduced if dressed electrons are used.

Details of the discussion on QED FSR will be presented in Section 5.6.3 and 6.2.3.

5.3 Definition of the fiducial phase space

The measurement is performed in the fiducial phase space defined by the acceptance cuts $p_{\mathrm{T}}^{el} > 20$ GeV and $|\eta^{el}| < 2.4$ on both electrons and by the di-electron mass cut $66 < M_{ee} < 116$ GeV. The use of a fiducial cross section has the advantage of reducing the dependence on the theory and/or on models. Events in which one of the two electrons passes the crack region between the barrel and the end-cap calorimeter ($1.37 < |\eta^{el}| < 1.52$) are discarded. Hence the measurement is corrected for this small acceptance hole.

5.4 Extrapolation procedure to the full phase space measurement

After corrections for detector and QED FSR effects using the bin-by-bin unfolding or the iterative Bayesian unfolding, the fiducial $\mathscr{R}$ spectrum is extrapolated to the full phase space (see Section 5.7.3 and 6.3.3) to allow further comparisons with theoretical calculations which can not describe final state lepton cuts and to facilitate the comparison with the results of other experiments. The extrapolation to the full phase space is done by introducing acceptance factors per each bin i defined as:

$$A^i = \frac{N^i_{\mathrm{MC,gen,ref,fid}}}{N^i_{\mathrm{MC,gen,ref}}} \quad \text{and} \quad A = \frac{N^{tot}_{\mathrm{MC,gen,ref,fid}}}{N^{tot}_{\mathrm{MC,gen,ref}}} \tag{5.8}$$

where “ref” can be ’Born’, ’Dressed’ or ’Bare’. The full phase space corresponds to all signal events within the region $66 < M_{ee} < 116$ GeV.

Therefore the normalised total cross section in the i-th ϕ^*_η bin is given by:

$$\left(\frac{1}{\sigma}\right)_{tot} \cdot \left(\frac{\Delta\sigma_i}{\Delta\mathscr{R}_i}\right)_{tot} = \left(\frac{A}{A^i}\right)\left(\frac{1}{\sigma}\right)_{fid}\left(\frac{\Delta\sigma_i}{\Delta\mathscr{R}_i}\right)_{fid} \tag{5.9}$$

$A^i_{norm} = \frac{A^i}{A}$ is called the normalised acceptance correction factors in each bin of $\mathscr{R}$.

5.5 The unfolding of the p_T^Z spectrum

From this section, we will discuss about the p_T^Z measurement. The unfolding procedure of the p_T^Z measurement is presented here while the evaluation of systematic uncertainties will be shown in Section 5.6.

5.5.1 Purity and binning optimization

The p_T^Z spectrum is measured in bins which have the size larger than the detector resolution at low p_T^Z and are adapted to the limited statistics at very high p_T^Z. The resolution of the p_T^Z measurement at Born level is shown in Figure 5.1. The highest p_T^Z reconstructed using 2011 ATLAS data is about 800 GeV but only few events with p_T^Z larger than 600 GeV are observed. The chosen p_T^Z range for this analysis is $p_T^Z < 600$ GeV.

An optimization procedure has been employed to select the bin widths of the p_T^Z spectrum. The binning optimization starts from the first bin with the size of 2.5 GeV which gives a purity (i.e. the fraction of simulated events reconstructed in a particular p_T^Z bin which have generator-level p_T^Z in the same bin) greater than 65%. In addition to this purity requirement the statistical uncertainty is required to be smaller than 1% up to $p_T^Z = 105$ GeV for each p_T^Z bin. The bin widths then have been smoothly increased up to 600 GeV. The optimization of the p_T^Z bin widths has been performed with these two requirements via an iterative scan of the p_T^Z spectrum using both data and signal MC events. The number of selected bins turns out to be 23 with the bin boundaries: 0, 2.5, 5, 8, 11.4, 14.9, 18.5, 22, 25.5, 29, 32.6, 36.4, 40.4, 44.9, 50.2, 56.4, 63.9, 73.4, 85.4, 105, 132, 173, 253, 600.

The purity of the p_T^Z reconstruction at the Born level is shown in Figure 5.2(a), the statistic uncertainty is calculated taking into account the bin-to-bin migrations [83]. Figure 5.2(b) shows the purity of p_T^Z measurement in 2010 (19 bins) [35].

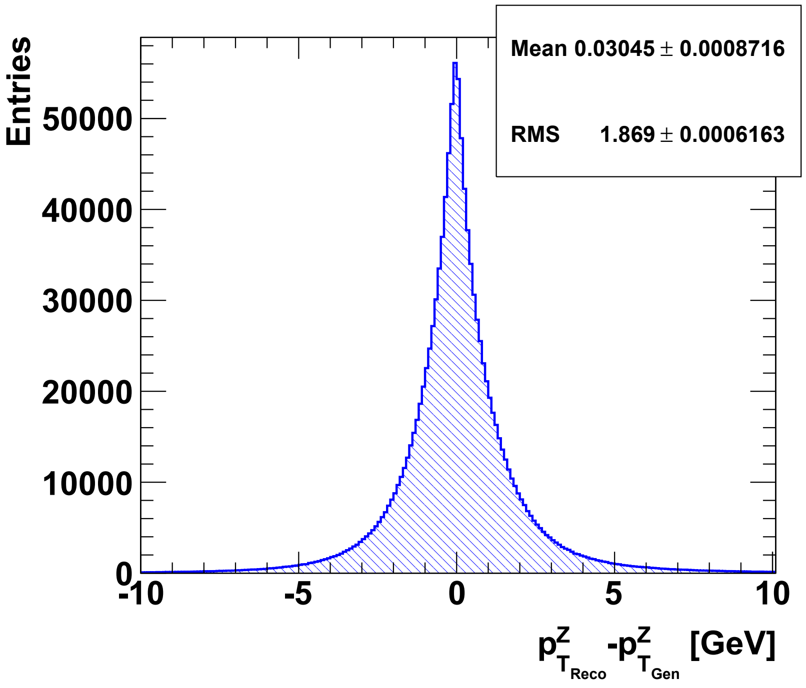

Figure 5.1: The resolution of p_T^Z reconstruction using GSF electron from MC $Z \rightarrow ee$ POWHEG *sample.*

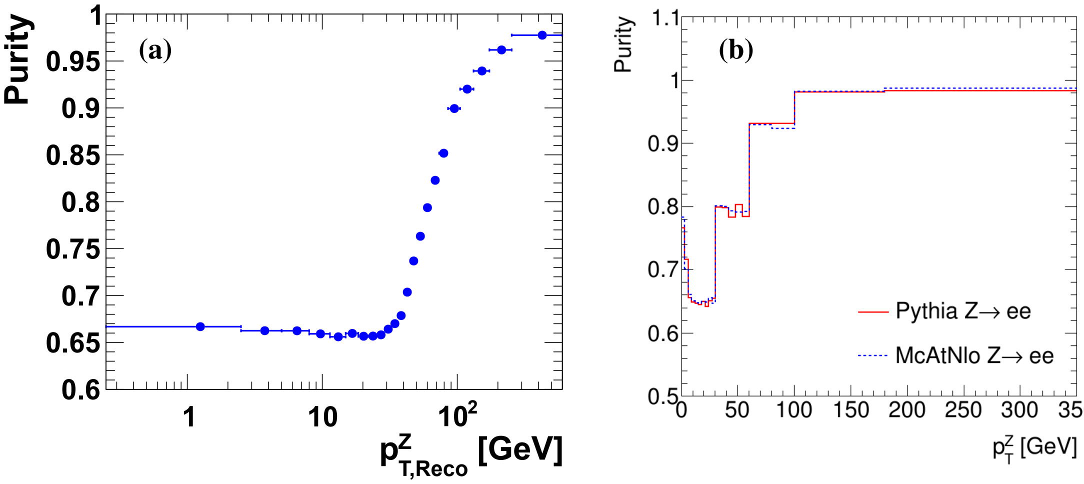

Figure 5.2: The purity of p_T^Z reconstruction using GSF electron from MC $Z \to ee$ Powheg *sample in this measurement (a), and in 2010 p_T^Z measurement (b).*

5.5.2 Bin-by-bin correction factors

Figure 5.3 shows the correction factors C^i_{norm} which correct the measured p_T^Z spectrum for detector and QED FSR effects and allow to get the underlying true spectrum defined at the "Born", "Dressed" and "Bare" levels. The values are shown in Tables 6.1.

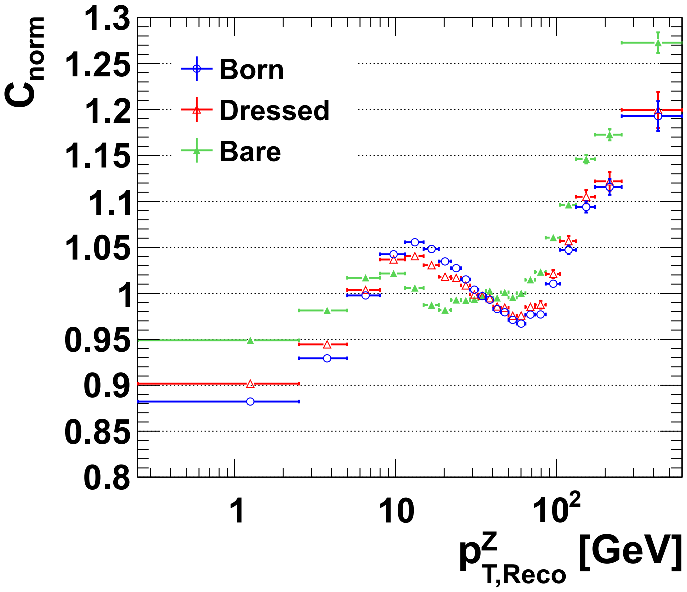

Figure 5.3: Normalised correction factor as function of p_T^Z obtained with MC $Z \to ee$ Powheg *sample. Statistical uncertainties calculated taking into account the bin-to-bin migrations [83] are shown.*

5.5.3 Iterative Bayesian unfolding and response matrix

The response matrix for the iterative Bayesian unfolding is obtained from the correlation histogram populated by the simulated events passing the event selections following p_T^Z bins in Monte Carlo. Figure 5.4 shows the response matrix obtained from MC $Z \to ee$ POWHEG sample. While the binning of the p_T^Z measurement is considered in the limit of 600 GeV as discussed in Section 5.5.1, the response matrix is performed up to 1000 GeV in order to check the migration from outside to the range of the p_T^Z measurement. The last bin 600 – 1000 GeV of the response matrix is diagonal. The migration from the bin 600 – 1000 GeV of the p_T^Z distribution to the bins below 600 GeV is negligible. So the p_T^Z measurement is conserved in the range 0 – 600 GeV.

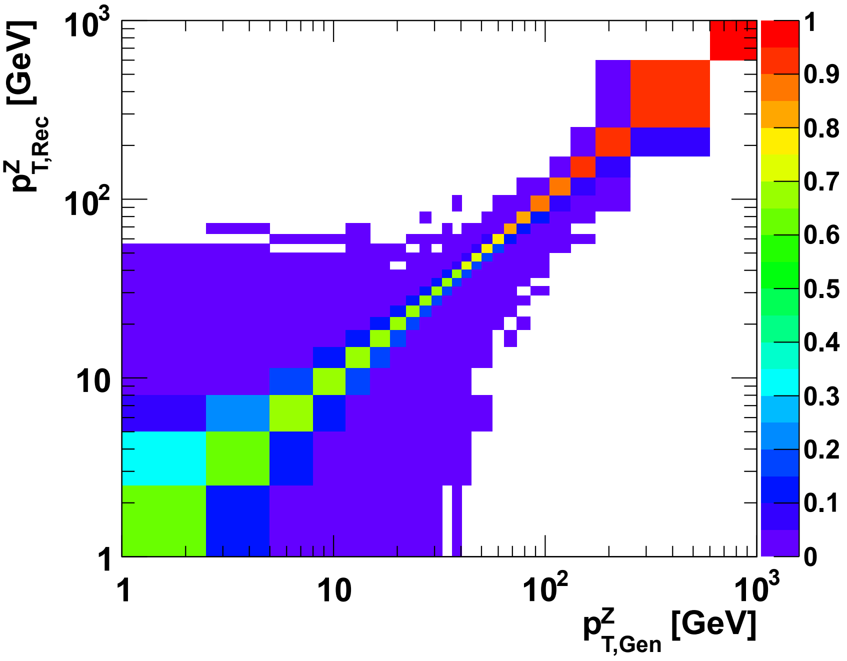

Figure 5.4: The response matrix obtained from from MC $Z \to ee$ POWHEG *sample.*

5.5.4 The choice of unfolding methods and the unfolded results

In this analysis, $Z \to ee$ POWHEG+PYTHIA is used as the reference MC (see Table 4.1). A disagreement between data and MC is observed in the low p_T^Z region as in Figure 5.5. Therefore, a reweighting procedure is applied on the p_T^Z spectrum of $Z \to ee$ POWHEG+PYTHIA sample to improve the description of data. Two p_T^Z truth spectra are used. One spectrum is provided by the RESBOS prediction and the

Bin	Range	Born		Dressed		Bare	
		C_{norm}	stat.(%)	C_{norm}	stat.(%)	C_{norm}	stat.(%)
1	0.0 - 2.5	0.882	0.179	0.902	0.198	0.949	0.155
2	2.5 - 5.0	0.929	0.117	0.944	0.130	0.981	0.100
3	5.0 - 8.0	0.998	0.103	1.004	0.115	1.017	0.087
4	8.0 - 11.4	1.042	0.109	1.037	0.122	1.022	0.091
5	11.4 - 14.9	1.056	0.127	1.040	0.143	1.006	0.107
6	14.9 - 18.5	1.048	0.147	1.031	0.166	0.987	0.125
7	18.5 - 22.0	1.035	0.174	1.018	0.196	0.982	0.148
8	22.0 - 25.5	1.027	0.199	1.017	0.224	0.993	0.169
9	25.5 - 29.0	1.015	0.225	1.009	0.253	0.992	0.191
10	29.0 - 32.6	1.004	0.249	0.999	0.279	0.993	0.211
11	32.6 - 36.4	0.997	0.270	0.997	0.302	0.997	0.227
12	36.4 - 40.4	0.993	0.291	0.995	0.326	1.002	0.245
13	40.4 - 44.9	0.983	0.304	0.986	0.341	0.995	0.254
14	44.9 - 50.2	0.979	0.309	0.984	0.348	1.001	0.255
15	50.2 - 56.4	0.971	0.323	0.976	0.365	0.995	0.264
16	56.4 - 63.9	0.967	0.335	0.976	0.380	1.000	0.270
17	63.9 - 73.4	0.977	0.348	0.985	0.397	1.015	0.275
18	73.4 - 85.4	0.977	0.378	0.988	0.432	1.023	0.296
19	85.4 - 105.0	1.010	0.376	1.021	0.435	1.061	0.283
20	105.0 - 132.0	1.047	0.451	1.057	0.526	1.096	0.334
21	132.0 - 173.0	1.094	0.554	1.105	0.653	1.146	0.399
22	173.0 - 253.0	1.116	0.762	1.122	0.908	1.173	0.530
23	253.0 - 600.0	1.193	1.364	1.200	1.641	1.273	0.878

Table 5.1: The normalized correction factors for the "Born", "Dressed" and "Bare" levels using MC $Z \to ee$ POWHEG *sample. Only statistical uncertainties are shown.*

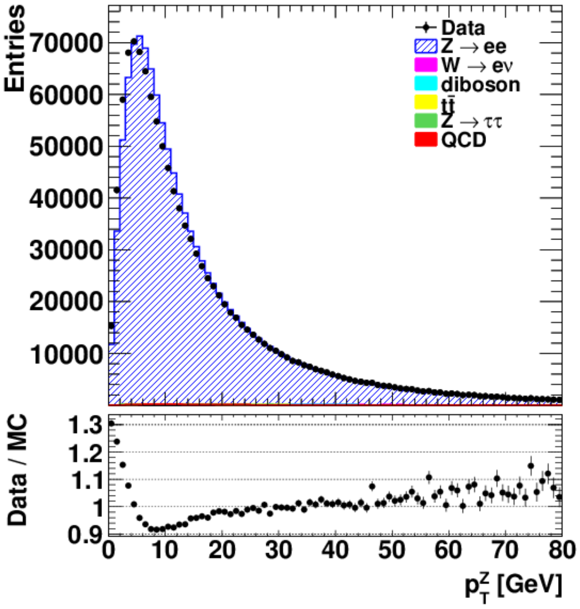

Figure 5.5: Control distribution in the p_T^Z *region* $(0-80$ *GeV) without any* p_T^Z *shape reweighting, the signal MC* $Z \to ee$ *from* POWHEG. *Only statistical errors are shown.*

other is the unfolded data spectrum obtained by employing the iterative Bayesian unfolding method with the response matrix from the default MC. The ratio of the reconstructed p_T^Z distribution in data to the one in $Z \to ee$ POWHEG+PYTHIA MC reweighted to different shapes mentioned above is presented in Figure 5.6. This figure shows that the MC sample reweighted to data has a better description of data. This MC sample will be used to obtain the central value of the final unfolded result.

In order to compare the iterative Bayesian unfolding and the bin-by-bin unfolding methods, the p_T^Z distribution in data is unfolded using both methods with the signal MC reweighted to the different shapes mentioned above. The unfolded data distributions are then compared, for the iterative Bayesian unfolding in Figure 5.7(a), for the bin-by-bin unfolding in Figure 5.7(b). It can be seen that the dependence on the shapes of the signal MC sample in the unfolding procedure of the p_T^Z measurement is smaller by using the iterative Bayesian unfolding than by using the bin-by-bin unfolding. Therefore the iterative Bayesian unfolding is chosen for this measurement.

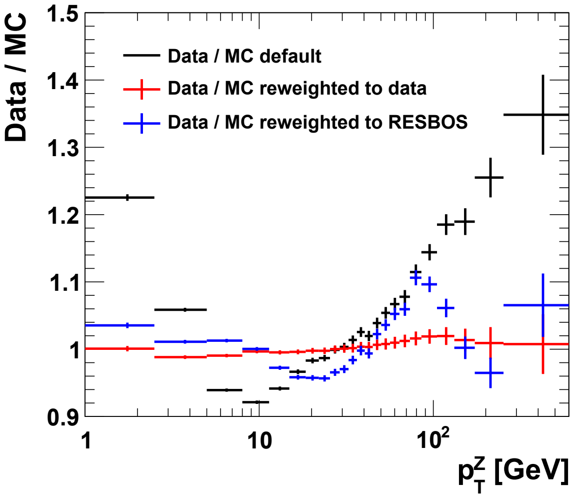

Figure 5.6: Ratio between the p_T^Z distributions reconstruced in data and in $Z \rightarrow ee$ MC reweighted to different shapes.

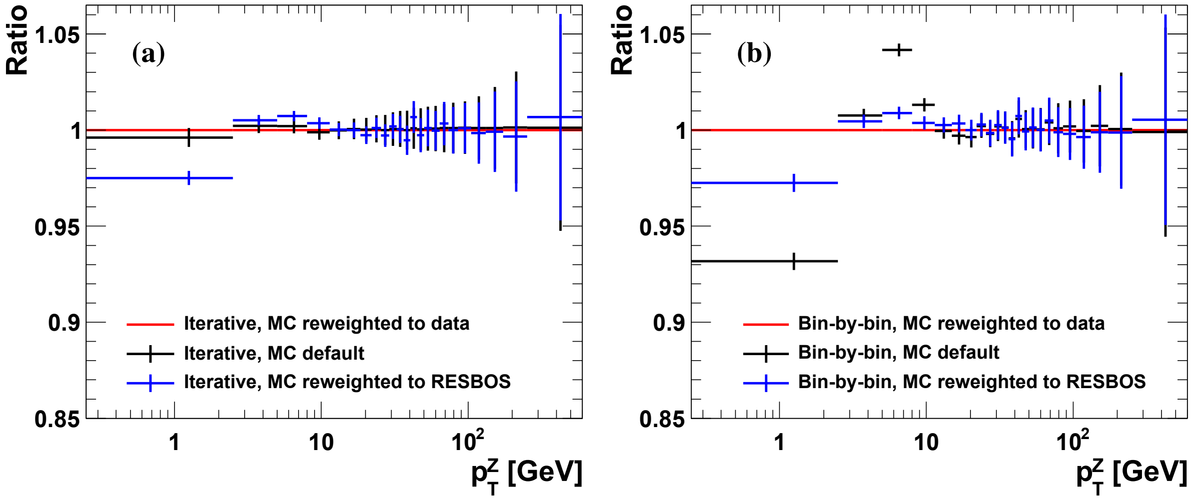

Figure 5.7: Comparison of unfolded results using difference MC shapes by the iterative unfolding (a), and by the bin-by-bin unfolding (b).

5.6 Evaluation of systematic uncertainties

To estimate the systematic uncertainties, the general idea is to compute the central unfolded spectrum using the correction factors $C_{central}$ or the unfolding matrix obtained from a high statistic Monte Carlo sample after applying all corrections and then subsequently varying all parameters in question to construct new correction factors $C_{systematic}$ or unfolding matrices. The new correction factors or unfolding matrices are then used to repeat the unfolding procedure and the relative deviation of the normalised differential cross sections is computed:

$$\mathrm{D} = \frac{[1/\sigma_{\text{fid}} \times d\sigma_{\text{fid}}/dp_T]_{\text{systematic}} - [1/\sigma_{\text{fid}} \times d\sigma_{\text{fid}}/dp_T]_{\text{central}}}{[1/\sigma_{\text{fid}} \times d\sigma_{\text{fid}}/dp_T]_{\text{central}}} \tag{5.10}$$

In the case of energy scale, energy resolution, electron efficiency and background systematic uncertainties, the relative deviation (up and down) is propagated by varying up and down one σ of each systematic uncertainty in the computation of the normalised differential cross section:

$$\mathrm{D}^{\text{up(down)}} = \frac{[1/\sigma_{\text{fid}} \times d\sigma_{\text{fid}}/dp_T]^{\text{up(down)}}_{\text{systematic}} - [1/\sigma_{\text{fid}} \times d\sigma_{\text{fid}}/dp_T]_{\text{central}}}{[1/\sigma_{\text{fid}} \times d\sigma_{\text{fid}}/dp_T]_{\text{central}}}. \tag{5.11}$$

The central systematic uncertainty value is then estimated as below:

$$D = \text{sign} \cdot \frac{1}{2} \cdot \left[|D^{\text{up}}| + |D^{\text{down}}|\right], \tag{5.12}$$

where $\text{sign} = 1$ if $D^{\text{up}} > 0$ and $\text{sign} = -1$ if $D^{\text{up}} < 0$.

All systematic uncertainties are considered as uncorrelated and added in quadrature, which gives the total systematic uncertainty of the measurement.

5.6.1 Pileup reweighting

As discussed in Section 4.1.3, MC samples are required to apply the pileup reweighting procedure in order to reproduce the average number of interactions per bunch-crossing, $< \mu >$, observed in data. Figures 5.8(a) and (b) show the good agreement between data and MC for $< \mu >$ distributions but not for the number of good vertices in the high region. In order to estimate the systematic uncertainty from the pileup reweighting, on top of all selection we apply the reweighting using the number of good vertices. The ratio between data and the signal $Z \to ee$ MC in the number of good vertices is used as the additional weight for the signal $Z \to ee$ MC. Figures 5.8(c, d) show the good agreement between data and MC for the number of good vertices while the $< \mu >$ distribution is varied due to the correlation between the two variables. The ratio between the response matrix including the vertex reweighting and the standard one is shown in Figure 5.9(a). The difference in the differential cross section with and without applying the vertex reweighting is considered as the systematic uncertainty due to the pileup reweighting which is shown in Figure 5.9(b).

5.6.2 Primary vertex position along z-axis

The impact of the reweighting of the z vertex shape of the signal MC (see section 4.1.3) on the correction factors C^i and on final cross sections has been estimated. Cross sections are calculated with and without applying this reweighting and the difference bewteen the two is taken as a systematic error. The ratio between the response matrix without the z vertex reweighting and the standard one is shown in Figure 5.10(a). The evolution of this uncertainty as a function of p_T^Z bins is represented in Figure 5.10(b).

5.6.3 QED final state radiation

QED final state radiation (FSR) can change the true level (or generated) fiducial cross section of $Z \to ee$ by about -5% [35]. However, the difference of the normalised true p_T^Z spectrum before and after final state QED radiation can be up to 8% [35]. Therefore an accurate simulation of the QED FSR including its kinematic dependencies is essential.

There are several programs implementing the QED FSR simulation. We will discuss here two programs: one is the Monte Carlo package PHOTOS [46,47,78] and one employs the YFS [101] formalism. PHOTOS works as an afterburner and can be interfaced to four-vectors produced by any host generator. This program is based on the collinear approximation for the radiation of photos together with corrections to reproduce the correct result in the soft limit [46, 47]. Recently, it has been improved to include the full next-to-leading order QED corrections for Z and W decays [78].

Despite the success of PHOTOS it is based on the collinear approximation for photon radiation. The production of radiation in these decays is normally simulated in the rest frame of the decaying particle. The kinematics of many of the decays, particularly of the unstable hadrons, is such that the energy of the decay products is not significantly larger than their mass, in which case we do not expect the collinear limit to be a good approximation. Hence, there is always a soft enhancement for the emission of QED radiation. This emission can be simulated basing on the YFS [101] formalism for the resummation of soft logarithms. This formalism has the major advantage that the exact higher order corrections can

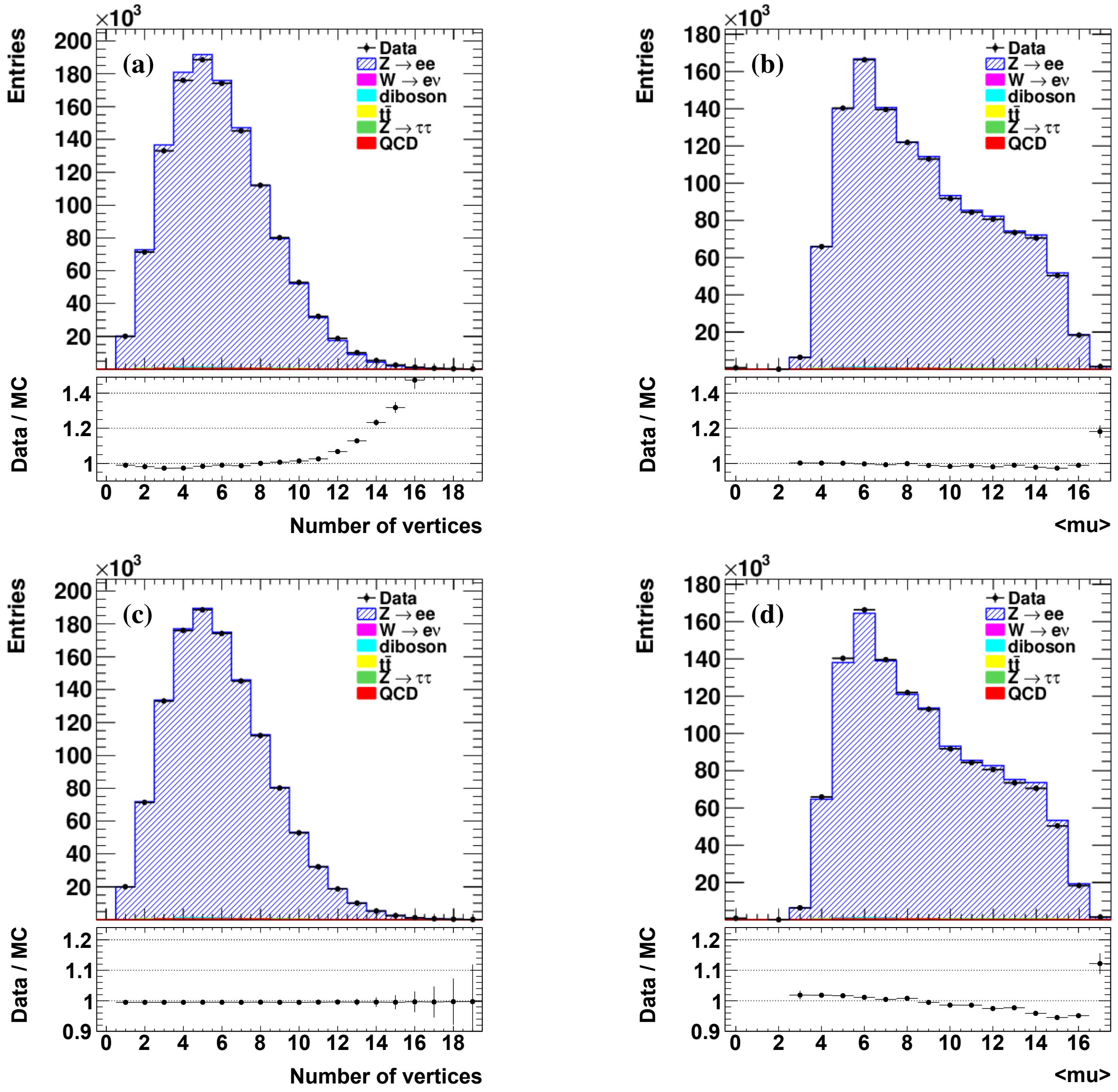

Figure 5.8: Distributions of $< \mu >$ and of the number of good vertices before the vertex reweighting (a, b) and after the vertex reweighting (c, d).

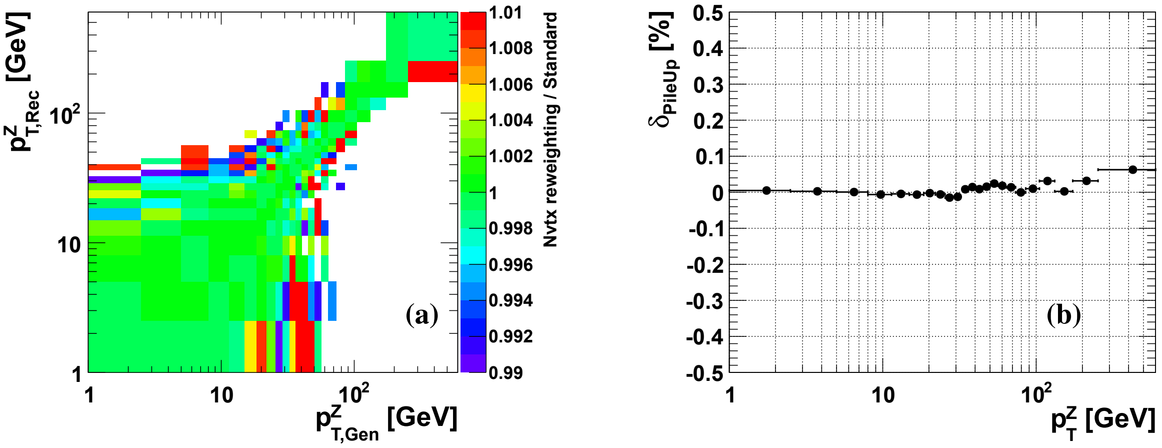

Figure 5.9: The difference of the response matrices due to the pileup reweighting (a) and the systematic uncertainty (δ_{PileUp}) associated to this effect as a function of p_T^Z (b). Uncertainties are given in per cent.

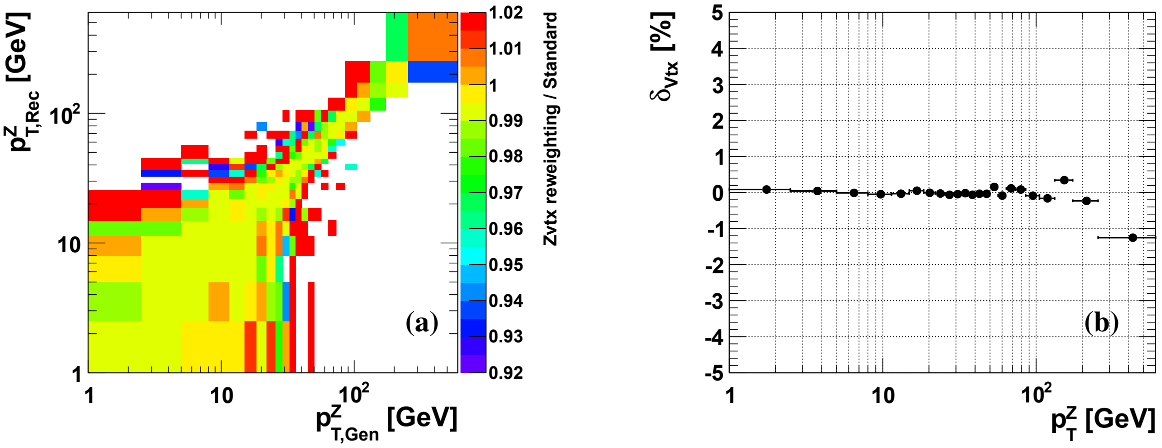

Figure 5.10: The difference of the response matrices due to the z vertex reweighting (a) and the evolution of the systematic uncertainty (δ_{Vtx}) associated to this effect as a function of p_T^Z (b). Uncertainties are given in per cent.

be systematically included, indeed the majority of the most accurate simulations including higher order QED corrections are based on this aprroach.

In order to understand the effect of the different QED FSR simulation programs on the p_T^Z measurement, we compared the QED FSR correction on the p_T^Z measurement simulated in $Z \to ee$ POWHEG+PYTHIA MC generator interfaced to the PHOTOS program and the one simulated in $Z \to ee$ SHERPA employing the YFS formalism. To reduce the effect of the statistic fluctuation on the result, high statistic MC samples are used for this study: 20 million events simulated in $Z \to ee$ POWHEG+PYTHIA and 30 million events simulated in $Z \to ee$ SHERPA.

Since the measured p_T^Z spectrum is unfolded to different truth levels: "Born", "Dressed", "Bare", the QED FSR correction on the p_T^Z measurement can be extracted by making the ratio between the p_T^Z truth distribution at the "Dressed" or "Bare" levels and the one at the "Born" level (named "Dressed→Born", "Bare→Born"). The ratio between the QED FSR correction found in $Z \to ee$ POWHEG+PYTHIA and the one found in $Z \to ee$ SHERPA yields the effect of the QED FSR correction on the p_T^Z measurement which is shown in Figure 5.11. The p_T^Z truth distribution at the "Born" level in $Z \to ee$ POWHEG+PYTHIA is reweighted to the one in $Z \to ee$ SHERPA to avoid the effect of the MC shape dependence on the QED FSR study.

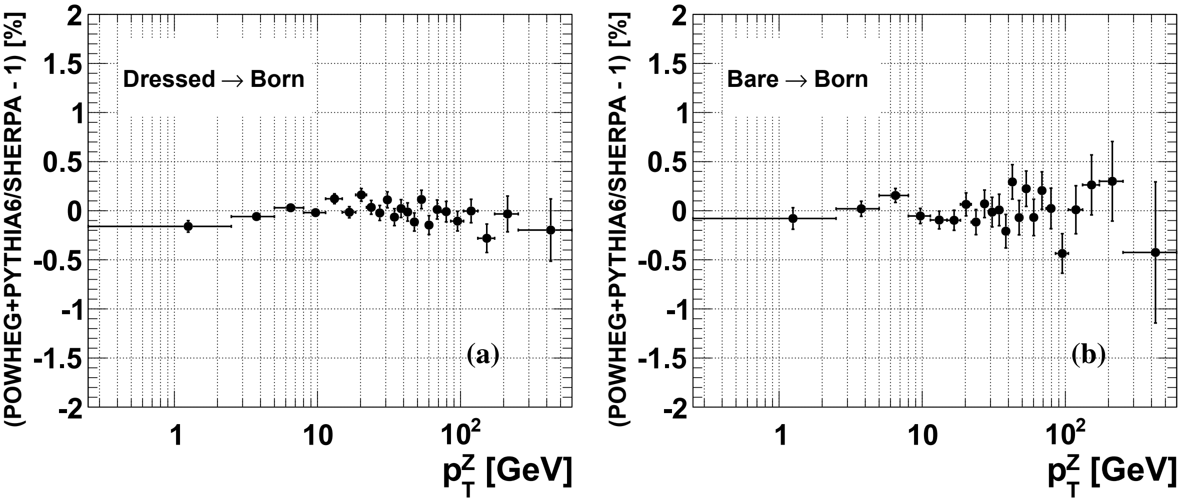

Figure 5.11: The difference of the QED FSR correction in $Z \to ee$ POWHEG+PYTHIA *and the one in $Z \to ee$* SHERPA *as a function of p_T^Z: from the "Dressed" level to the "Born" level (a) and from the "Bare" level to the "Born" level (b).*

A conservative systematic uncertainty of $\delta_{FSR} = 0.3\%$ is assigned to account for induced uncertainties due to the p_T^Z dependent modelling of QED FSR. This conclusion holds for p_T^Z distributions at the "Born", "Dressed" and "Bare" levels.

5.6.4 PDFs

The PDF uncertainty on the measurement can be estimated using the method explained in [95]. X is any one of the physical quantities of interest that depends on the PDFs. It is considered as a function of the parameters that define the PDFs at the initial scale $X(\vec{a})$, where $\vec{a}$ forms a vector with an N-dimensional PDF parameter space. In the Hessian formalism for the uncertainty analysis, this parton parameter space is spanned by a set of orthonormal eigenvectors obtained by a self-consistent iterative procedure. The uncertainty of the quantity $X(\vec{a})$ is characterized by $2N$ sets of published eigenvector PDF sets along with the central fit, 2 PDF sets for each of the N eigenvectors, along the ($\pm$) directions, it is defined as

$$\Delta X = |\vec{\bigtriangledown} X| = \frac{1}{2}\sqrt{\sum_{n=1}^{N}\left(X^{n(+)} - X^{n(-)}\right)^2}. \tag{5.13}$$

Two MC samples are used for this study: $Z \to ee$ POWHEG+PYTHIA and $Z \to ee$ PYTHIA. The PDF set used in $Z \to ee$ POWHEG+PYTHIA is CT10 (52 eigenvector PDF sets). The PDF set used in $Z \to ee$ PYTHIA is MRSTLO* which does not have any eigenvector PDF sets. In order to estimate the PDF uncertainty on the measurement using this sample, it is recommended to reweight to the PDF set MSTW08LO which has 40 eigenvector PDF sets. Each response matrix filled with the addition weight from the PDF reweighting is used to unfold the p_T^Z distribution. The PDF uncertainty on the normalized cross section in the i^{th} p_T^Z bin is estimated as:

$$\Delta\left(\frac{1}{\sigma}\frac{\Delta\sigma_i}{\Delta(\phi_\eta^*)_i}\right)_{PDF} = \frac{1}{2}\sqrt{\sum_{n=1}^{N}\left(\frac{\left(\frac{1}{\sigma}\frac{\Delta\sigma_i}{\Delta(\phi_\eta^*)_i}\right)_{rew}^{n(+)} - \left(\frac{1}{\sigma}\frac{\Delta\sigma_i}{\Delta(\phi_\eta^*)_i}\right)_{rew}^{n(-)}}{\left(\frac{1}{\sigma}\frac{\Delta\sigma_i}{\Delta(\phi_\eta^*)_i}\right)_{rew}^{0}}\right)^2}, \tag{5.14}$$

where $\left(\frac{1}{\sigma}\frac{\Delta\sigma_i}{\Delta(\phi_\eta^*)_i}\right)_{rew}^{n(+)}$ is the normalized differential cross section in the i^{th} p_T^Z bin reweighted from MRSTLO* to the eigenvector PDF set n of MSTW08LO and $\left(\frac{1}{\sigma}\frac{\Delta\sigma_i}{\Delta(\phi_\eta^*)_i}\right)_{rew}^{0}$ is the normalized correction factor reweighted from MRSTLO* to the central PDF set of MSTW08LO. The resulting PDF uncertainty as a function of p_T^Z cross section bins is shown in Figure 5.12. Similar results are observed by using $Z \to ee$ POWHEG+PYTHIA.

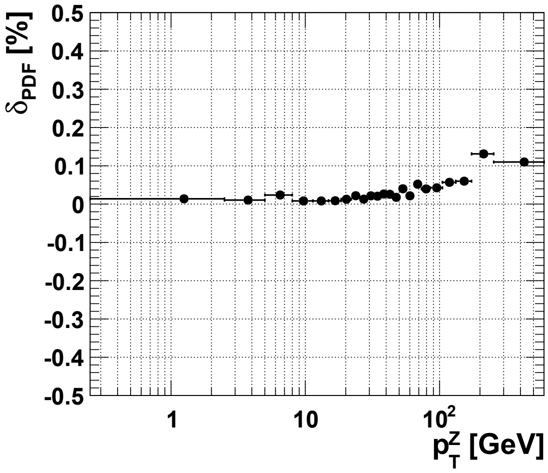

Figure 5.12: The PDF uncertainties (δ_{PDF}) as a function of p_T^Z cross section bins using $Z \to ee$ PYTHIA *MC sample. Uncertainties are given in per cent*

5.6.5 Unfolding

As discussed in Section 5.5.4, the unfolding procedure is affected by the p_T^Z spectrum in the signal MC $Z \to ee$ POWHEG+PYTHIA. The iterative Bayesian method was chosen for the p_T^Z measurement in order to reduce the systematic uncertainty due to this effect. The bias introduced by deviations from the MC shape dependence has to be taken into account. Since the central values of the p_T^Z distribution are obtained using MC reweighted to data, the maximum deviation of the p_T^Z distribution using the default MC and the p_T^Z distribution using MC reweighted to RESBOS from the central values will be quoted for the systematic uncertainty from the MC shape dependence which is shown in Figure 5.13

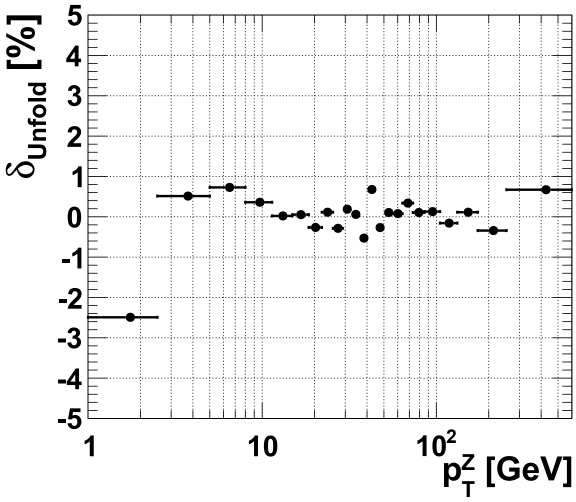

Figure 5.13: The systematic uncertainty (δ_{Unfold}) due to the MC shape dependence in the unfolding procedure as a function of p_T^Z. Uncertainties are given in per cent.

An another source of uncertainty in the unfolding process is the bias of the algorithm. This bias is tested using only the signal MC sample where the truth p_T^Z spectrum is well known. The signal MC sample is divided into two samples: a sample for buiding the response matrix and a sample for evaluating the bias. The reconstructed MC distribution of the second sample is then unfolded using a response matrix built from the first sample. The result is then compared with the truth distribution in the second sample and the difference in per cent is shown in Figure 5.14(a). As can be seen in this figure, the difference is mostly in the high p_T^Z region due to the statistic fluctuation in the recontructed p_T^Z distribution. This fluctuation is not considered as a systematic uncertainty. We also tested the bias due to a number of iterations in the iterative unfolding procedure. The above reconstructed p_T^Z spectrum is still used. The unfolded spectrum obtained after two or ten iterations is compared with the one obtained after one iteration. This difference is shown in Figure 5.14(b). It is not significant and is well covered by statistical errors. Therefore, we do not quote any systematic uncertainty due to the bias of the unfolding algorithm.

Finally, only MC shape dependence uncertainties are used to yield the total unfolding uncertainty. The effect of different PDF sets discussed in Section 5.6.4 is to change the p_T^Z shape of the MC used to unfold data, this difference is completely covered by the uncertainty from the MC shape dependence in the unfolding procedure, so we do not quote a separate uncertainty for PDFs. The total unfolding uncertainty can be found in Table 5.2.

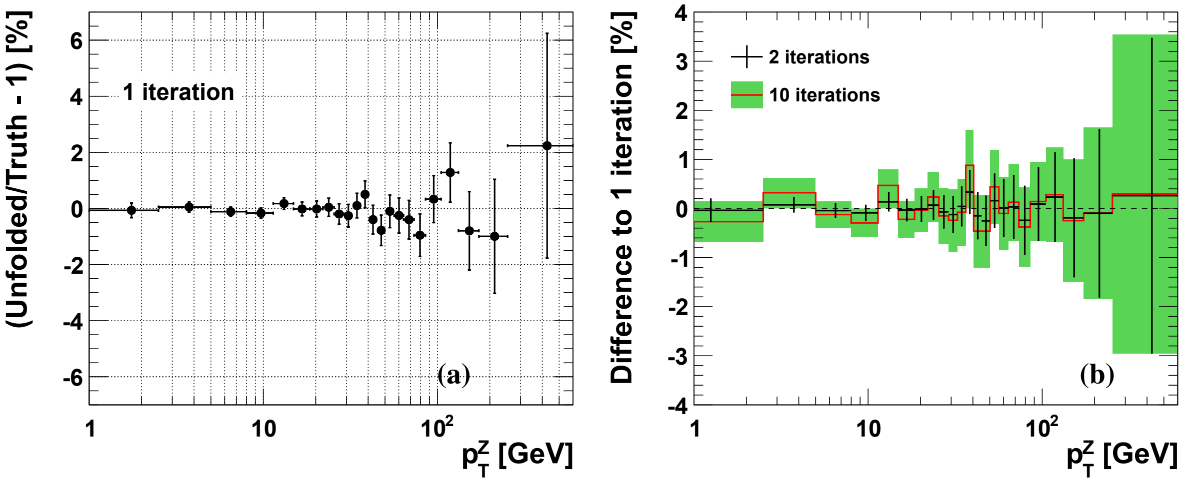

Figure 5.14: The difference between the unfolded p_T^Z spectrum reconstructed in the second MC sample using the response matrix from the first MC sample and the truth spectrum in the second MC sample(a). The difference between the unfolded p_T^Z spectrum with two or ten iterations and the one with one iteration in the iterative unfolding procedure(b). Statistical errors are shown.

5.6.6 Monte Carlo statistics

The response matrix obtained from MC is used to unfold the p_T^Z distribution in data. The limit of MC statistics can effect the unfolded results via the response matrix. The effect of MC statistics of the response matrix is studied by producing many copies of the response matrix randomly. The content of each bin of the response matrix is produced using the Gauss distribution with the mean is set by the nominal value and the sigma is set by the statistical error. Then the reconstructed p_T^Z distribution in data is unfolded using these response matrices. This process is repeated for 1000 trials. 1000 final cross sections are ploted for each p_T^Z bin. A Gauss function is used to fit these distributions. The fits for the first and the last p_T^Z bins are shown in Figure 5.15. The mean of the fit in each bin shows the normalised cross section. The difference between this differential normalised cross section and the one using the default response matrix is considered as the systematic uncertainty due to the limit of MC statistics. This systematic uncertainty is shown in Figure 5.16.

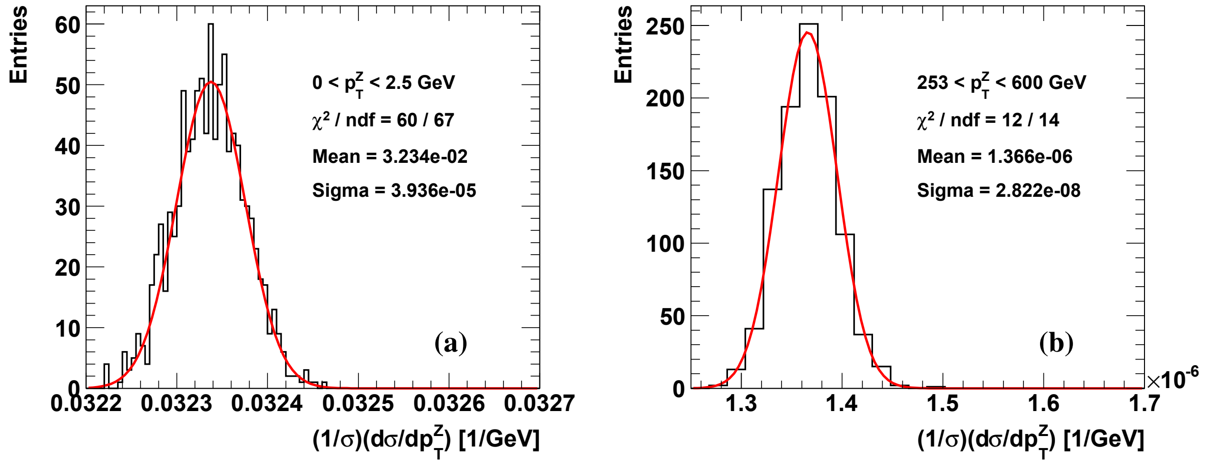

Figure 5.15: The fits of 1000 unfolded cross sections in data using the response matrices varied within their statistical errors for the first (a) and the last (b) p_T^Z bins.

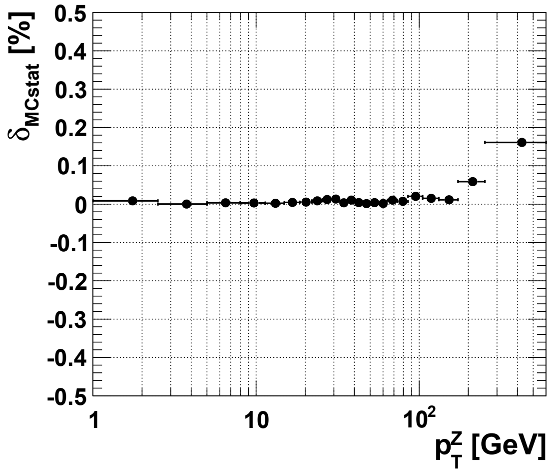

Figure 5.16: The systematic uncertainty due to the limit of MC statistics (δ_{MCstat}), uncertainties are given in per cent.

5.6.7 Energy scale and energy resolution

The uncertainty associated to our knowledge of the electron energy scale in data is estimated. Correlated variations of $\pm 1\sigma$ of the electron energy scale are applied on an event by event basis and propagated through the full analysis chain up to the normalised cross section using MC $Z \to ee$ events, as the generated luminosity of MC signal signal events is larger than the one available in data. The uncertainty associated to the description of the electron energy resolution by the MC is calculated in a similar way. The electron energy resolution in $Z \to ee$ MC events is varied and the effect is propagated to the normalised cross section. The resulting uncertainties on the normalised cross section are represented as a function of p_T^Z in Figures 5.17(a) and (b) for the electron energy scale and the electron energy resolution, respectively.

5.6.8 Electron reconstruction and identification efficiency

The systematic uncertainties on the electron reconstruction and identification efficiencies are calculated. Correlated variations of $\pm 1\sigma$ of the reconstruction and identification efficiencies for each electron of Z candidates are applied on an event by event basis and propagated through the full analysis chain up to the normalised cross section using MC $Z \to ee$ events. The resulting uncertainty on the normalised cross section is represented as a function of p_T^Z in Figure 5.17(c).

5.6.9 Electron trigger efficiency

The systematic uncertainty on the efficiency of single electron triggers used is calculated. Correlated variations of $\pm 1\sigma$ of the trigger efficiency are applied on an event by event basis and propagated through the full analysis chain up to the normalised cross section using MC $Z \to ee$ events. The resulting uncertainty on the normalised cross section is represented as a function of p_T^Z in Figure 5.17(d). This uncertainty is very small $< 0.008\%$.

5.6.10 Backgrounds

An uncertainty on the amount of QCD background events as defined in Table 4.5 is used. In each cross section bin, this uncertainty is combined with the statistical uncertainty on the estimated number of QCD events in the bin. This results in an uncertainty on the normalised cross section of $\sim 0.05\%$, which is considered as correlated between bins. The evolution of this uncertainty as a function p_T^Z cross section bins is represented in Figure 5.17(e).

Similarly, an uncertainty of 10% on the contribution of electroweak background processes as a function of p_T^Z is assumed. In each cross section bin, this uncertainty is combined with the statistical uncertainty on the estimated number of electroweak events in the bin, which may not be negligible in some cases due to the low MC statistics available for some of the processes. The evolution of this uncertainty as a function of p_T^Z cross section bins is represented in Figure 5.17(f).

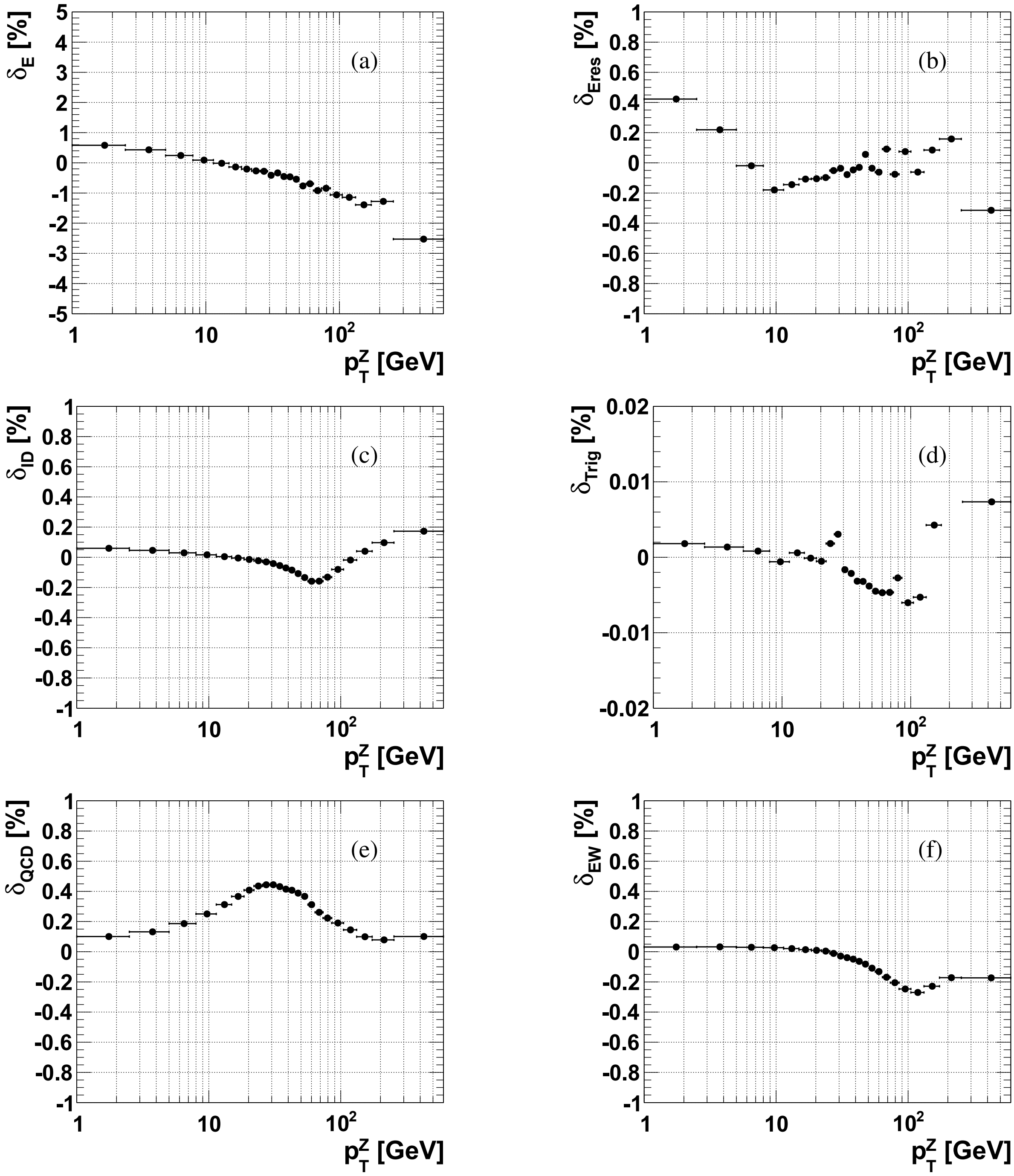

Figure 5.17: Evolution of absolute systematic uncertainties from different error sources as a function of p_T^Z: (a) δ_E uncertainty due to the electron energy scale correction, (b) δ_{Eres} uncertainty due to the electron energy resolution smearing, (c) δ_{ID} uncertainty due to the electron reconstruction and identification efficiency correction, (d) δ_{Trig} uncertainty due to the electron trigger efficiency correction, (e) δ_{QCD} uncertainty on the contribution of QCD background, (f) δ_{EW} uncertainty on the contribution of electroweak backgrounds. All uncertainties are given in per cent.

5.7 Results

5.7.1 The fiducial differential cross section as a function of p_T^Z

The normalised cross section $\frac{1}{\sigma}\frac{d\sigma}{dp_T^Z}$ as a function of p_T^Z and compared to the RESBOS prediction is presented in Figure 5.18(a), the ratio to the RESBOS prediction is shown in Figure 5.18(b). Numerical results are also provided in Table 5.2. Cross sections at “Born”, “Dressed” and “Bare” levels are also provided in Table 5.3.

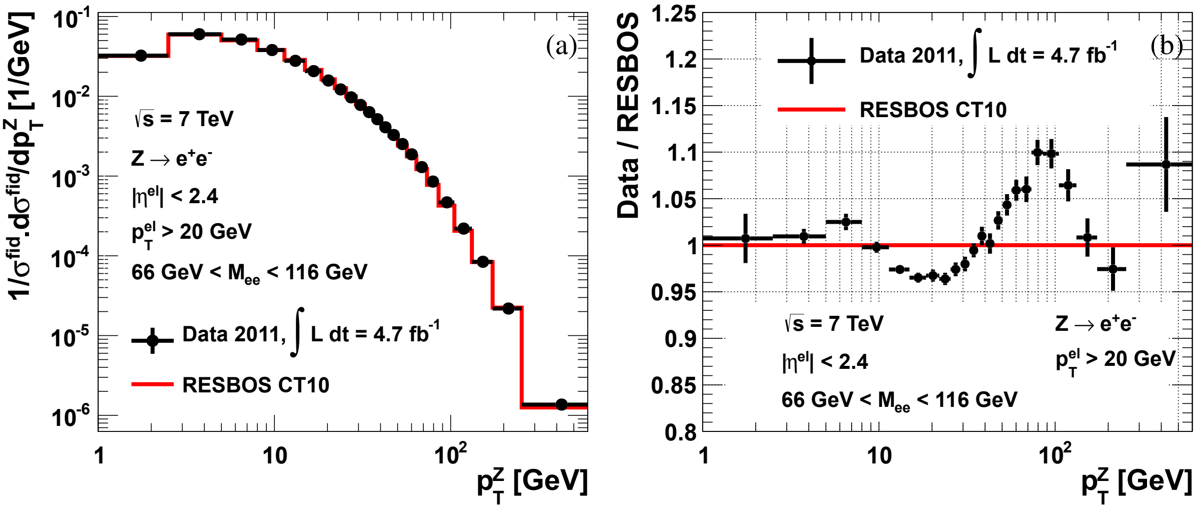

Figure 5.18: The normalised cross section $\frac{1}{\sigma}\frac{d\sigma}{dp_T^Z}$ as a function of p_T^Z compared to the RESBOS *prediction (a) and the ratio to the* RESBOS *prediction (b).*

p_T^Z bin [GeV]	$1/\sigma\, d\sigma/dp_T^Z$ [GeV^{-1}]	δ_{stat} [%]	δ_{sys} [%]	δ_{tot} [%]	δ_{FSR} [%]	δ_{MCstat} [%]	δ_{E} [%]	δ_{Eres} [%]	δ_{ID} [%]	δ_{Trig} [%]	δ_{QCD} [%]	δ_{EW} [%]	δ_{Unfold} [%]	δ_{PileUp} [%]	δ_{Vtx} [%]
0.0 - 2.5	0.0323	0.22	2.62	2.62	0.30	0.01	0.58	0.42	0.06	0.00	0.10	0.03	-2.49	0.00	0.08
2.5 - 5.0	0.0600	0.16	0.78	0.80	0.30	0.00	0.43	0.22	0.05	0.00	0.13	0.03	0.51	0.00	0.04
5.0 - 8.0	0.0515	0.16	0.85	0.86	0.30	0.00	0.24	-0.02	0.03	0.00	0.19	0.03	0.73	0.00	-0.01
8.0 - 11.4	0.0380	0.17	0.57	0.60	0.30	0.00	0.09	-0.18	0.02	-0.00	0.25	0.03	0.36	-0.01	-0.05
11.4 - 14.9	0.0278	0.20	0.46	0.50	0.30	0.00	-0.01	-0.14	0.00	0.00	0.31	0.02	0.02	-0.00	-0.03
14.9 - 18.5	0.0207	0.24	0.51	0.56	0.30	0.00	-0.14	-0.11	-0.01	-0.00	0.37	0.01	0.05	-0.01	0.05
18.5 - 22.0	0.0158	0.27	0.62	0.67	0.30	0.01	-0.21	-0.11	-0.01	-0.00	0.41	0.01	-0.26	-0.00	-0.01
22.0 - 25.5	0.0122	0.31	0.61	0.69	0.30	0.01	-0.27	-0.10	-0.02	0.00	0.44	0.00	0.11	-0.01	-0.03
25.5 - 29.0	0.0097	0.35	0.67	0.76	0.30	0.01	-0.28	-0.05	-0.03	0.00	0.44	-0.01	-0.29	-0.01	-0.06
29.0 - 32.6	0.0078	0.38	0.71	0.80	0.30	0.01	-0.41	-0.04	-0.04	-0.00	0.44	-0.03	0.19	-0.01	-0.05
32.6 - 36.4	0.0063	0.42	0.63	0.76	0.30	0.00	-0.33	-0.08	-0.05	-0.00	0.43	-0.04	0.06	0.01	-0.02
36.4 - 40.4	0.0052	0.46	0.87	0.98	0.30	0.01	-0.45	-0.05	-0.07	-0.00	0.41	-0.05	-0.53	0.01	-0.06
40.4 - 44.9	0.0041	0.49	0.97	1.09	0.30	0.00	-0.46	-0.03	-0.09	-0.00	0.41	-0.06	0.68	0.01	-0.03
44.9 - 50.2	0.0033	0.53	0.79	0.96	0.30	0.00	-0.54	0.06	-0.11	-0.00	0.39	-0.08	-0.27	0.02	-0.03
50.2 - 56.4	0.0025	0.58	0.94	1.10	0.30	0.00	-0.77	-0.04	-0.13	-0.00	0.37	-0.11	0.11	0.02	0.16
56.4 - 63.9	0.0019	0.62	0.85	1.06	0.30	0.00	-0.69	-0.06	-0.16	-0.00	0.31	-0.13	0.08	0.02	-0.09
63.9 - 73.4	0.0013	0.70	1.09	1.30	0.30	0.01	-0.92	0.09	-0.16	-0.00	0.26	-0.17	0.34	0.01	0.12
73.4 - 85.4	$8.5 \cdot 10^{-4}$	0.76	0.97	1.23	0.30	0.01	-0.84	-0.08	-0.13	-0.00	0.22	-0.21	0.11	-0.00	0.08
85.4 - 105.0	$4.7 \cdot 10^{-4}$	0.84	1.16	1.44	0.30	0.02	-1.06	0.07	-0.08	-0.01	0.19	-0.25	0.13	0.01	-0.09
105.0 - 132.0	$2.2 \cdot 10^{-4}$	1.04	1.24	1.62	0.30	0.02	-1.14	-0.06	-0.02	-0.01	0.14	-0.27	-0.16	0.03	-0.16
132.0 - 173.0	$8.4 \cdot 10^{-5}$	1.39	1.49	2.04	0.30	0.01	-1.39	0.08	0.04	0.00	0.10	-0.23	0.11	0.00	0.34
173.0 - 253.0	$2.2 \cdot 10^{-5}$	1.93	1.40	2.39	0.30	0.06	-1.28	0.16	0.10	0.02	0.08	-0.17	-0.34	0.03	-0.23
253.0 - 600.0	$1.4 \cdot 10^{-6}$	3.64	2.95	4.68	0.30	0.16	-2.53	-0.31	0.17	0.01	0.10	-0.17	0.67	0.06	-1.25

Table 5.2: The normalised cross section $\frac{1}{\sigma}\frac{d\sigma}{dp_T^Z}$ *corrected to the "Born" level in each* p_T^Z *bin.* POWHEG *$Z \to ee$ MC events are used to unfold the* p_T^Z *spectrum in data. All uncertainties are given in per cent.*

	Born			Dressed			Bare		
p_T^Z bin [GeV]	$1/\sigma\, d\sigma/dp_T^Z$ [GeV^{-1}]	δ_{stat} [%]	δ_{sys} [%]	$1/\sigma\, d\sigma/dp_T^Z$ [GeV^{-1}]	δ_{stat} [%]	δ_{sys} [%]	$1/\sigma\, d\sigma/dp_T^Z$ [GeV^{-1}]	δ_{stat} [%]	δ_{sys} [%]
0.0 - 2.5	0.0323	0.22	2.62	0.0315	0.23	2.62	0.0295	0.23	2.62
2.5 - 5.0	0.0600	0.16	0.78	0.0590	0.17	0.78	0.0567	0.17	0.78
5.0 - 8.0	0.0515	0.16	0.85	0.0514	0.16	0.85	0.0512	0.16	0.85
8.0 - 11.4	0.0380	0.17	0.57	0.0384	0.18	0.57	0.0393	0.17	0.57
11.4 - 14.9	0.0278	0.20	0.46	0.0283	0.21	0.46	0.0294	0.19	0.46
14.9 - 18.5	0.0207	0.24	0.51	0.0210	0.24	0.51	0.0220	0.22	0.51
18.5 - 22.0	0.0158	0.27	0.62	0.0160	0.28	0.62	0.0166	0.26	0.62
22.0 - 25.5	0.0122	0.31	0.61	0.0123	0.32	0.61	0.0126	0.30	0.61
25.5 - 29.0	0.0097	0.35	0.67	0.0098	0.35	0.67	0.0099	0.33	0.67
29.0 - 32.6	0.0078	0.38	0.71	0.0078	0.39	0.71	0.0079	0.37	0.71
32.6 - 36.4	0.0063	0.42	0.63	0.0063	0.43	0.63	0.0063	0.41	0.63
36.4 - 40.4	0.0052	0.46	0.87	0.0052	0.47	0.87	0.0051	0.45	0.87
40.4 - 44.9	0.0041	0.49	0.97	0.0041	0.50	0.97	0.0040	0.49	0.97
44.9 - 50.2	0.0033	0.53	0.79	0.0033	0.55	0.79	0.0032	0.53	0.79
50.2 - 56.4	0.0025	0.58	0.94	0.0025	0.59	0.94	0.0025	0.57	0.94
56.4 - 63.9	0.0019	0.62	0.85	0.0019	0.64	0.85	0.0018	0.62	0.85
63.9 - 73.4	0.0013	0.70	1.09	0.0013	0.71	1.09	0.0012	0.69	1.09
73.4 - 85.4	$8.5 \cdot 10^{-4}$	0.76	0.97	$8.4 \cdot 10^{-4}$	0.78	0.97	$8.2 \cdot 10^{-4}$	0.76	0.97
85.4 - 105.0	$4.7 \cdot 10^{-4}$	0.84	1.16	$4.6 \cdot 10^{-4}$	0.86	1.16	$4.5 \cdot 10^{-4}$	0.84	1.16
105.0 - 132.0	$2.2 \cdot 10^{-4}$	1.04	1.24	$2.2 \cdot 10^{-4}$	1.06	1.24	$2.1 \cdot 10^{-4}$	1.04	1.24
132.0 - 173.0	$8.4 \cdot 10^{-5}$	1.39	1.49	$8.3 \cdot 10^{-5}$	1.41	1.49	$8.1 \cdot 10^{-5}$	1.39	1.49
173.0 - 253.0	$2.2 \cdot 10^{-5}$	1.93	1.40	$2.2 \cdot 10^{-5}$	1.96	1.40	$2.1 \cdot 10^{-5}$	1.95	1.40
253.0 - 600.0	$1.4 \cdot 10^{-6}$	3.64	2.95	$1.4 \cdot 10^{-6}$	3.69	2.95	$1.3 \cdot 10^{-6}$	3.72	2.95

Table 5.3: Comparison of the normalised cross sections $\frac{1}{\sigma}\frac{d\sigma}{dp_T^Z}$ *corrected to the "Born", "Dressed" and "Bare" levels.* POWHEG $Z \rightarrow ee$ *MC events are used to unfold the* p_T^Z *spectrum in data. All uncertainties are given in per cent.*

5.7.2 Comparisons with theoretical predictions and other p_T^Z measurements

The fiducial normalised cross section is compared with theoretical predictions from RESBOS and FEWZ introduced in section 1.2.3 in Figure 5.19. The measured cross section agrees with RESBOS within 4% for the low p_T^Z region and 8% for the high p_T^Z region. For the larger p_T^Z values, the agreement of NNLO FEWZ with our measurement is within 10%. This was difficult to see in [16] due to the statistical fluctuation.

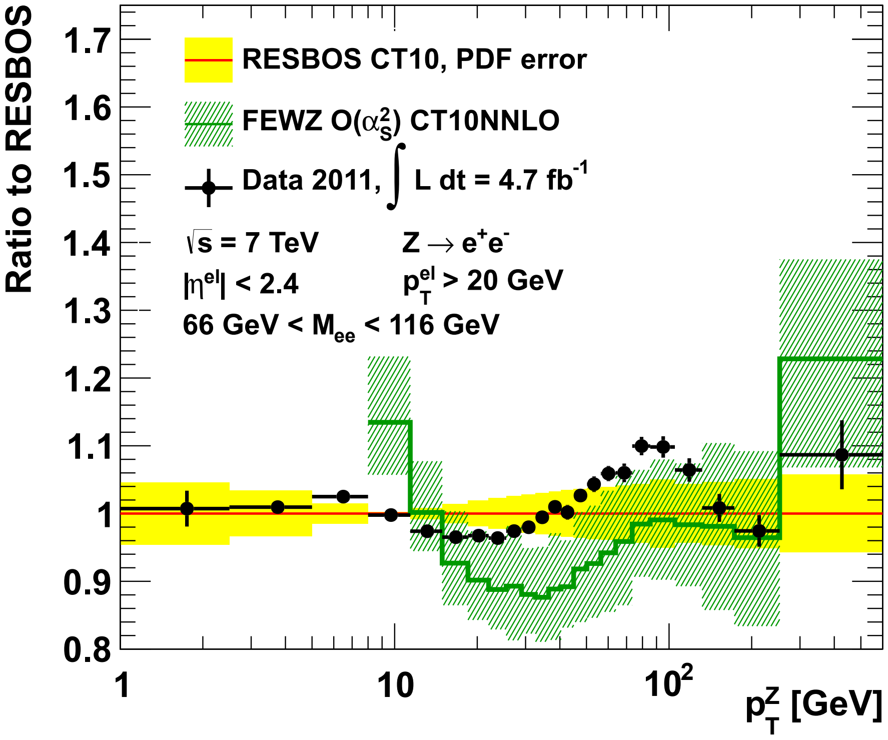

Figure 5.19: Ratio of the final normalised cross section $\frac{1}{\sigma}\frac{d\sigma}{dp_T^Z}$ *to* RESBOS *prediction as a function of* p_T^Z *and also compared to theoretical predictions from* FEWZ*.*

The effect of PDFs used in the RESBOS calculation is shown in Figure 5.20. The ratio of data or RESBOS calculation using CT10 PDF set to RESBOS calculation using CTEQ6.6 PDF set are presented. We observe that the agreement of data with CT10 predictions is better than with CTEQ6.6 in the low p_T^Z region $<$ 40 GeV.

In Figure 5.21, the final fiducial normalised cross section is also compared with predictions from different MC generators used so far by ATLAS. These predictions are presented in Section 1.2.4.2. The best descriptions of data are provided by the SHERPA, ALPGEN MC generators. The implementation

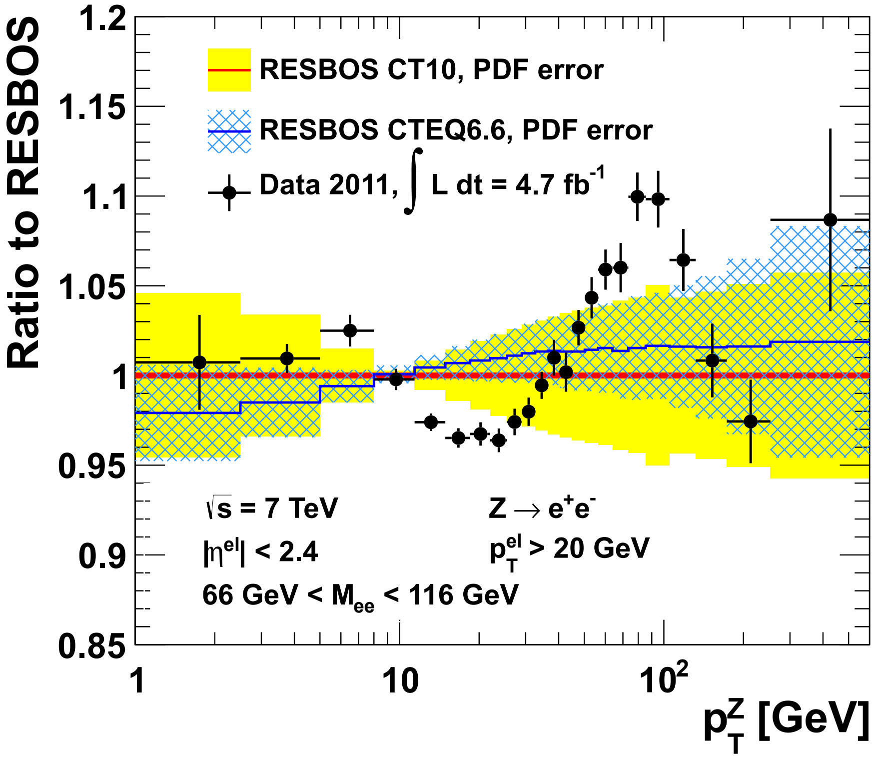

Figure 5.20: Comparisons of the fiducial normalised cross section $\frac{1}{\sigma}\frac{d\sigma}{dp_T^Z}$ *as a function of* p_T^Z *to the* RESBOS *prediction using CTEQ6.6 PDF set, the ratio between two* RESBOS *predictions using two different PDFs is shown.*

of multi-parton tree level matrix elements can help these two MC generators follow the shape of data in the high p_T^Z region. The new tuning of POWHEG+PYTHIA8 gives better agreement with data than POWHEG+PYTHIA6. The descriptions provided by MC@NLO or PYTHIA+HERWIG are the worst.

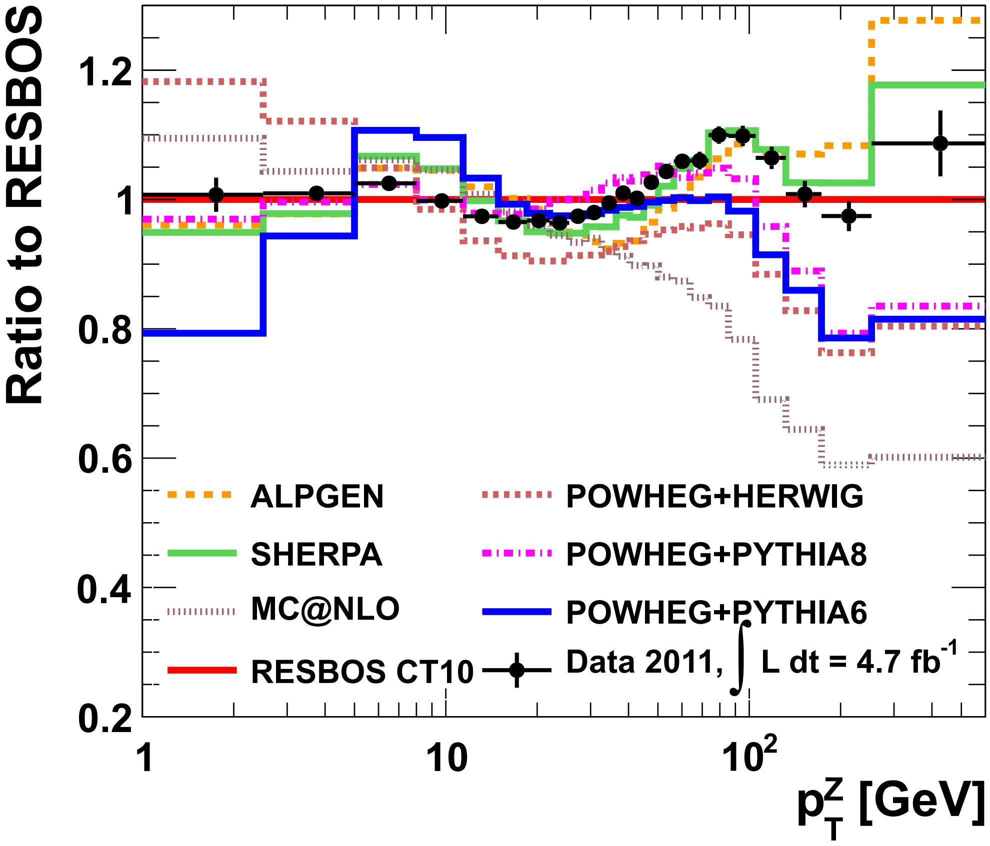

Figure 5.21: Comparison of the final normalised cross section $\frac{1}{\sigma}\frac{d\sigma}{dp_T^Z}$ *divided by the* RESBOS *prediction as a function of* p_T^Z *with predictions from different MC generators as used by ATLAS ("Born" level).*

In addition, this measurement using the high statistical data sample in 2011, 4.7 fb^{-1} of the total integrated luminosity is compared with the one measured in ATLAS using the early data in 2010, $35-40$ pb^{-1} of the total integrated luminosity . The high statistical sample allows to reduce the bin widths and increase the precision of the measurement. The detailed shape of p_T^Z can be studied. The range of the measurement is extended from 350 GeV to 600 GeV. As can be seen in Figure 5.22, the p_T^Z measurement published by ATLAS using $35-40$ pb^{-1} shows a good agreement with the result of this analysis obtained with 4.7 fb^{-1}.

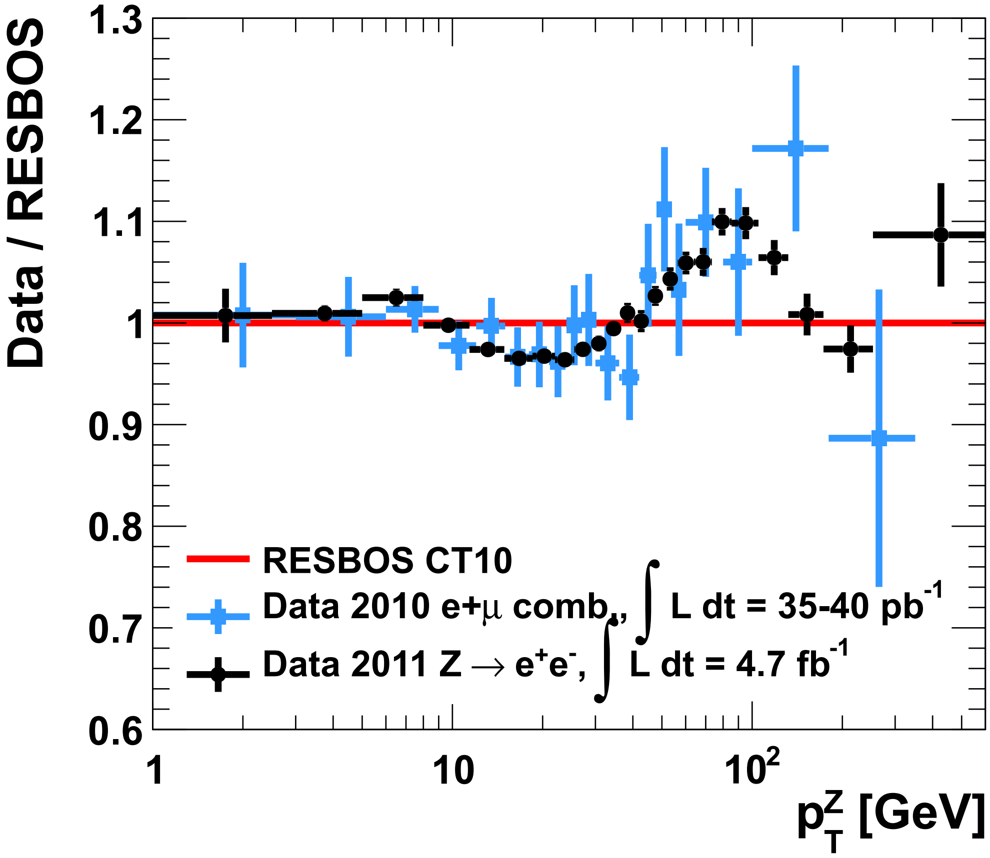

Figure 5.22: Comparison of the fiducial normalised cross section measurements $\frac{1}{\sigma}\frac{d\sigma}{dp_T^Z}$ *in electron channel using 2011 ATLAS dataset and in electron and muon combination using 2010 ATLAS dataset [16] with the* RESBOS *CT10 prediction as a function of* p_T^Z.

5.7.3 Acceptance correction to the full phase space measurement

As discussed in Section 5.1.1 the fiducial differential cross section as a function of p_T^Z of the Z boson can be extrapolated to the full phase space by applying the normalised acceptance correction factors A^i_{norm}. Factors determined at the "Born", "Dressed" and "Bare" levels are shown in Figure 5.23. As already observed in [16], the dominant uncertainty on these extrapolation factors results from the differences between the MC generators. The A^i_{norm} extrapolation factors determined at the "Born" level using different MC generators have therefore been compared. This comparison is presented in Figure 5.24. Differences are observed up to 8% , which will be used to define the systematic uncertainty on the determination of these A^i_{norm} factors. The values of A^i_{norm} correction factors are provided in Table 5.4.

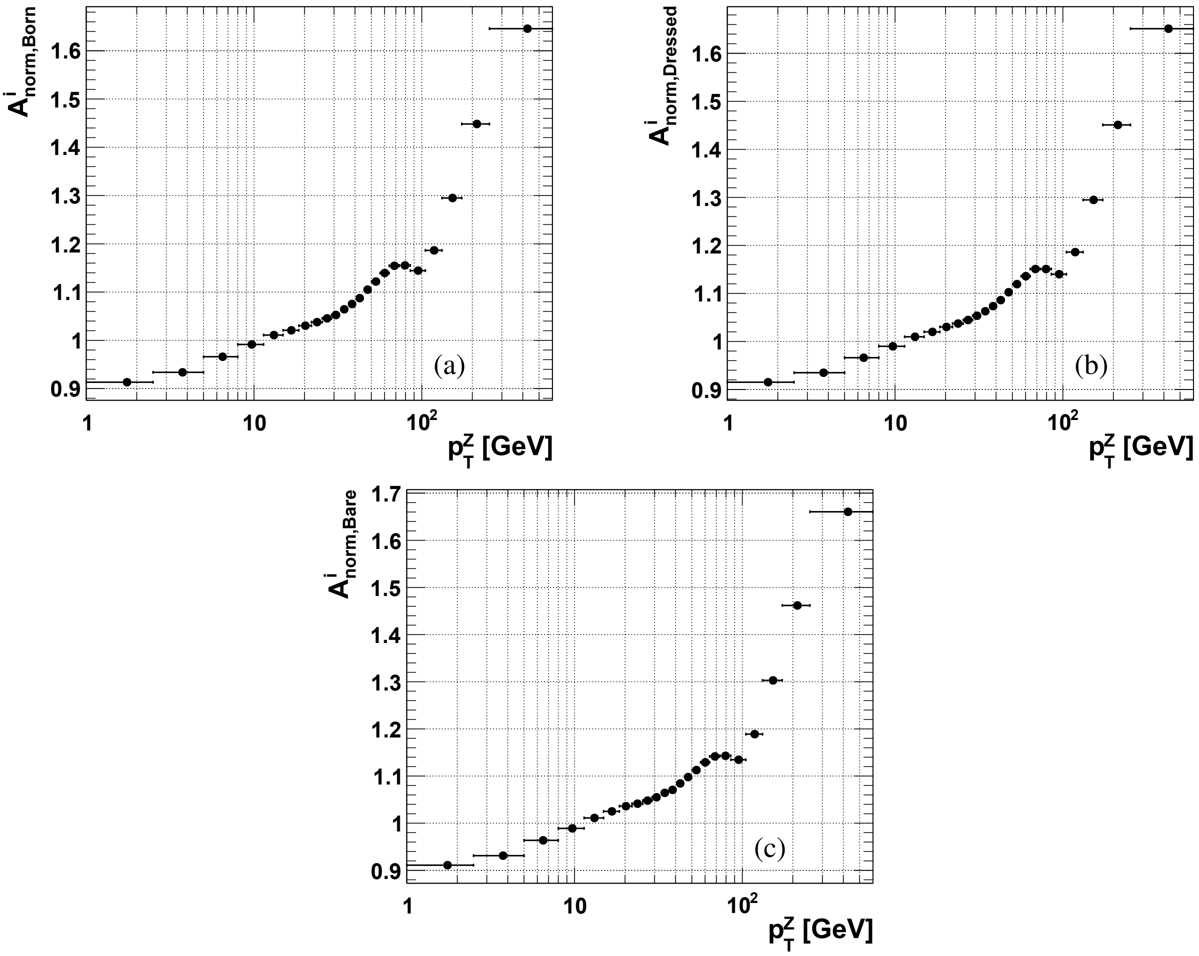

Figure 5.23: The normalised acceptance correction factors A^i_{norm} as function of p_T^Z obtained with POWHEG+PYTHIA. *The correction factors correct to the "Born" level (a), to the "Dressed" level (b) and to the "Bare" level (c). Only statistical uncertainties are shown.*

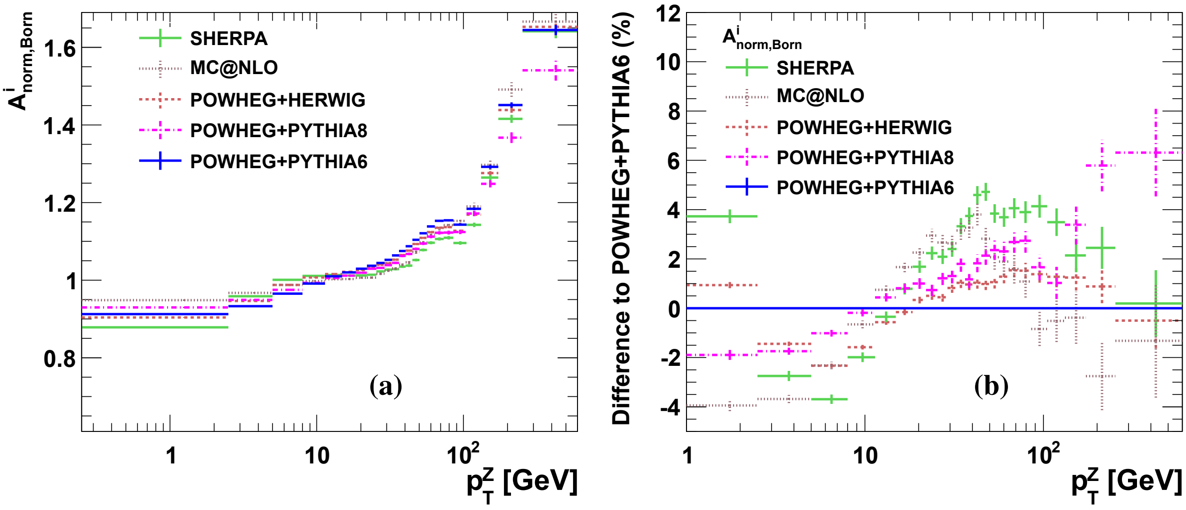

Figure 5.24: Comparison of A^i_{norm} *acceptance correction factors determined using different MC generators (a) and the ratio of* A^i_{norm} *factors obtained with different generators to the* A^i_{norm} *factor determined using* POWHEG+PYTHIA.

Bin i	p_T^Z [GeV]	A^i_{norm} (Born)	$1 - A_{Dressed}/A_{Born}$ [%]	$1 - A_{Bare}/A_{Born}$ [%]	δ_{model} [%]
1	0.0 - 2.5	0.913 ± 0.0498	-0.20	0.26	3.9
2	2.5 - 5.0	0.934 ± 0.0332	-0.11	0.29	3.7
3	5.0 - 8.0	0.966 ± 0.0300	0.00	0.26	3.7
4	8.0 - 11.4	0.991 ± 0.0322	0.16	0.25	2.0
5	11.4 - 14.9	1.011 ± 0.0374	0.12	-0.02	0.7
6	14.9 - 18.5	1.021 ± 0.0432	0.09	-0.41	1.7
7	18.5 - 22.0	1.030 ± 0.0504	0.02	-0.55	2.3
8	22.0 - 25.5	1.038 ± 0.0572	0.05	-0.36	2.9
9	25.5 - 29.0	1.046 ± 0.0641	0.09	-0.23	2.7
10	29.0 - 32.6	1.053 ± 0.0705	-0.09	-0.23	2.6
11	32.6 - 36.4	1.064 ± 0.0760	0.14	0.00	3.3
12	36.4 - 40.4	1.075 ± 0.0820	0.17	0.43	3.7
13	40.4 - 44.9	1.087 ± 0.0860	0.12	0.29	4.6
14	44.9 - 50.2	1.105 ± 0.0885	0.23	0.66	4.7
15	50.2 - 56.4	1.122 ± 0.0930	0.23	0.82	3.8
16	56.4 - 63.9	1.140 ± 0.0978	0.32	0.92	3.7
17	63.9 - 73.4	1.154 ± 0.1038	0.31	1.11	4.1
18	73.4 - 85.4	1.155 ± 0.1156	0.39	1.06	3.9
19	85.4 - 105.0	1.144 ± 0.1241	0.39	0.86	4.1
20	105.0 - 132.0	1.186 ± 0.1539	0.04	-0.21	3.5
21	132.0 - 173.0	1.295 ± 0.1894	0.02	-0.61	3.4
22	173.0 - 253.0	1.448 ± 0.2461	-0.18	-0.93	5.8
23	253.0 - 600.0	1.646 ± 0.4041	-0.33	-0.90	6.3

Table 5.4: The normalised acceptance correction factors A^i_{norm} at the “Born”, “Dressed” and “Bare” levels. Statistical uncertainties on A^i_{norm} at the “Born” level are shown, as well as the model uncertainty obtained by comparing different MC generators.

5.8 Summary

The differential cross section of $Z \to ee$ as a function of p_T^Z was studied. This measurement is improved mostly in the statistic uncertainty using 4.7 fb^{-1} in comparison with the same measurement in 2010 using $35-40$ pb^{-1} [16]. The main systematic uncertainties were estimated. The total systematic uncertainty is $\sim 1\%$ except the first bin with 2.6% and the last bin with 3%. Corresponding numbers in the 2010 measurement for the combined results of the electron and muon channels are $\sim 2\%$, 4.7% (the first bin), 5.4% (the last bin). Among all sources of systematic uncertainties of the p_T^Z measurement in this analysis, the dominant contributions come from the electron energy scale correction at high p_T^Z with the maximum is 2.5% and from the unfolding procedure at low p_T^Z with the maximum is 2.5%.

The precision of the p_T^Z measurement at LHC is limited by experimental systematic uncertainties rather than the available event statistics. Even most of statistics of this measurement is in the low p_T^Z region, the bin widths of the p_T^Z spectrum limited by the experimental resolution do not allow to access in detail the p_T^Z shape in this region which is important to understand the physics due to the soft and collinear gluon emission. New ideas are therefore needed in order to exploit fully the data for studying the physics of p_T^Z. As mentioned in Section 1.3, a new variable ϕ_η^* has number of advantages for this study. Details of the measurement using this optimized variable will be studied in Chapter 6.

Chapter 6

The differential cross section of $Z \rightarrow ee$ as a function of ϕ^*_η

As mentioned in Section 1.3, ϕ^*_η is less sensitive to the effects of experimental resolution while it can address the same physics issues as p^Z_T. This chapter will present the difference cross section measurement as a function of the ϕ^*_η of the Z boson. This work is reported in [69]. The unfolding procedure of the ϕ^*_η spectrum is presented in Section 6.1. The evaluation of systematic uncertainties is explained in Section 6.2. The result of the ϕ^*_η measurement will be compared with theoretical predictions in Section 6.3. Section 6.5 is dedicated to comparisons between the p^Z_T and ϕ^*_η measurements.

6.1 The unfolding of the ϕ^*_η spectrum

6.1.1 Purity and binning optimization

The ϕ^*_η bin widths have been optimized requiring a purity greater than 80% in each ϕ^*_η bin. In addition to this purity requirement the statistical uncertainty is required to be smaller than 0.5% up to $\phi^*_\eta = 0.5$ for each ϕ^*_η bin. The bin widths for $\phi^*_\eta > 0.5$ have been smoothly increased up to $\phi^*_{\eta,max} \sim 3$, this corresponds to $p^Z_T \sim 300$ GeV. The optimization of the ϕ^*_η bin widths has been performed with these two requirements via an iterative scan of the ϕ^*_η spectrum using both data and signal MC events following a similar procedure employed for p^Z_T. The number of selected bins turns out to be 34 and the final selected ϕ^*_η range is $[0 - 3.277]$. The purity of the ϕ^*_η reconstruction at the Born level using standard electrons and GSF electrons is shown in Figure 6.1. The greater purity achievable with the GSF electrons is the motivation for their use in the $Z \to ee$ analysis.

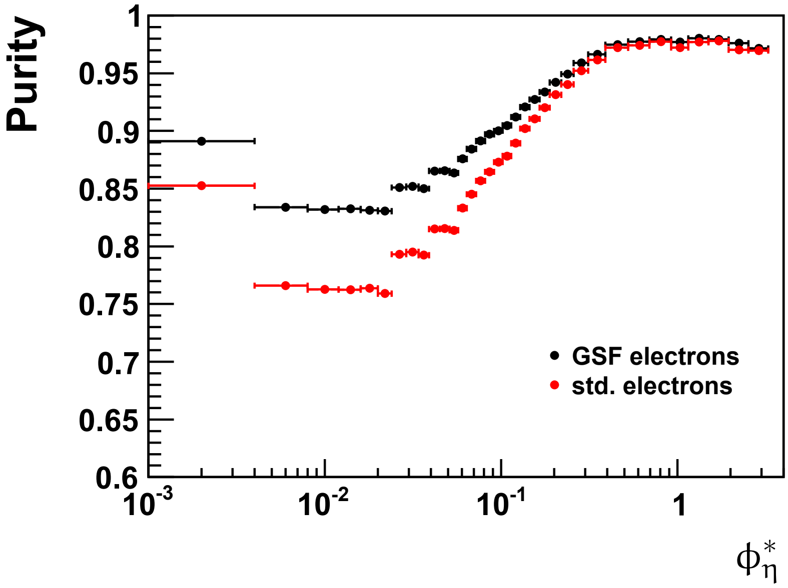

Figure 6.1: Purity as a function of the ϕ^*_η measurement. Purity factors obtained for GSF and standard electron reconstruction chains are compared [69].

6.1.2 Bin-by-bin correction factors

As discussed in Section 5.5.4, the p_T^Z spectrum provided by the POWHEG+PYTHIA MC can not describe the p_T^Z spectrum reconstructed in data. The same difference is observed in ϕ^*_η.

The unfolded p_T^Z spectrum using the default POWHEG+PYTHIA MC and the unfolded one using the POWHEG+PYTHIA MC reweighted to RESBOS are different up to $\sim 5\%$ in the low p_T^Z region by using the bin-by-bin unfolding. This difference is $\sim 3\%$ by using the iterative Bayesian unfolding. This led to the choice the iterative Bayesian unfolding method for the p_T^Z measurement. In the ϕ^*_η measurement the impact of the MC shape on the unfolding is very small. Even using bin-by-bin correction factors to unfold the ϕ^*_η spectrum, the difference observed by using the default POWHEG+PYTHIA MC and by using the POWHEG+PYTHIA MC reweighted to RESBOS is less than 0.2% [69]. Therefore, the bin-by-bin unfolding method is employed for this measurement.

Figure 6.2 shows the normalized bin-by-bin correction factors, C^i_{norm}, used to unfold the measured ϕ^*_η spectrum at the "Born", "Dressed" and "Bare" levels. The values are shown in Tables 6.1.

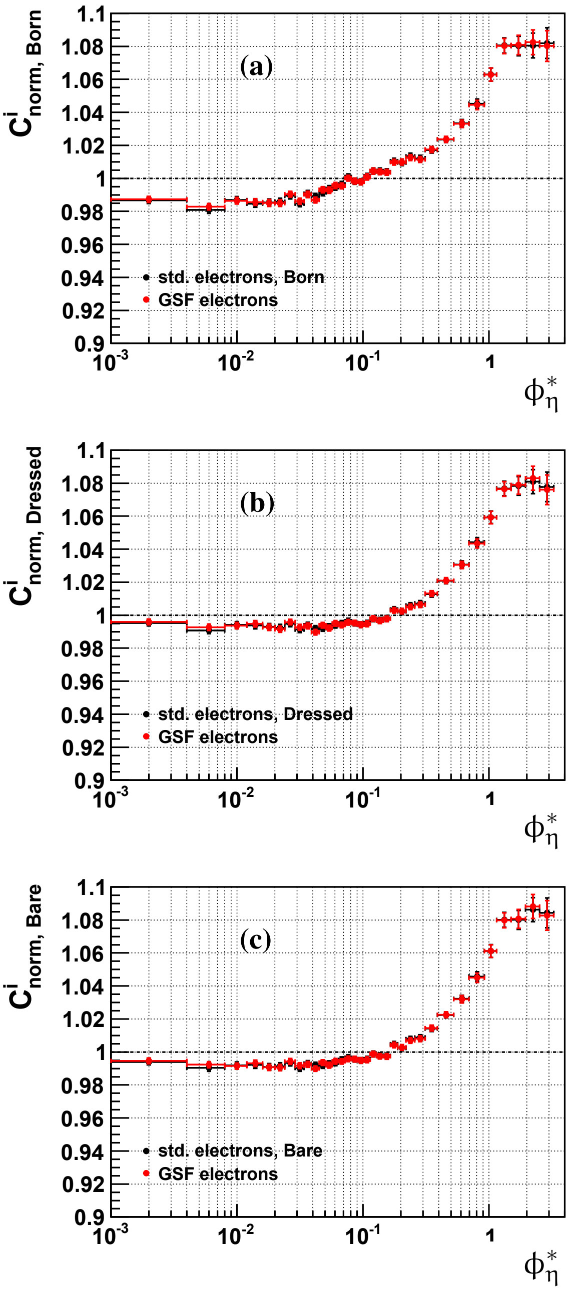

Figure 6.2: Normalised correction factor as function of ϕ^*_η *obtained with* POWHEG+PYTHIA. *The black dots indicate the correction factors for standard electrons while the red crosses indicate the correction factors for GSF electrons. The correction factors correct to the "Born" level* $C^i_{norm,Born}$ *(a), to the "Dressed" level* $C^i_{norm,Dressed}$ *(b), to the "Bare" level* $C^i_{norm,Bare}$ *(c). Only statistical uncertainties are shown [69].*

Bin i	Range	$C^i_{norm,Born}$	$C^i_{norm,Dressed}$	$C^i_{norm,Bare}$
0	0.000 – 0.004	0.987 ± 0.002	0.996 ± 0.002	0.995 ± 0.002
1	0.004 – 0.008	0.983 ± 0.002	0.993 ± 0.002	0.992 ± 0.002
2	0.008 – 0.012	0.986 ± 0.002	0.994 ± 0.002	0.991 ± 0.002
3	0.012 – 0.016	0.986 ± 0.002	0.995 ± 0.002	0.993 ± 0.002
4	0.016 – 0.020	0.985 ± 0.002	0.993 ± 0.002	0.991 ± 0.002
5	0.020 – 0.024	0.985 ± 0.002	0.992 ± 0.002	0.991 ± 0.002
6	0.024 – 0.029	0.990 ± 0.002	0.996 ± 0.002	0.994 ± 0.002
7	0.029 – 0.034	0.986 ± 0.002	0.993 ± 0.002	0.992 ± 0.002
8	0.034 – 0.039	0.990 ± 0.002	0.994 ± 0.002	0.993 ± 0.002
9	0.039 – 0.045	0.987 ± 0.002	0.990 ± 0.002	0.990 ± 0.002
10	0.045 – 0.051	0.993 ± 0.002	0.994 ± 0.002	0.994 ± 0.002
11	0.051 – 0.057	0.993 ± 0.002	0.992 ± 0.002	0.992 ± 0.002
12	0.057 – 0.064	0.996 ± 0.002	0.995 ± 0.002	0.994 ± 0.002
13	0.064 – 0.072	0.995 ± 0.002	0.994 ± 0.002	0.994 ± 0.002
14	0.072 – 0.081	1.000 ± 0.002	0.996 ± 0.002	0.996 ± 0.002
15	0.081 – 0.091	0.998 ± 0.002	0.995 ± 0.002	0.996 ± 0.002
16	0.091 – 0.102	0.998 ± 0.002	0.994 ± 0.002	0.995 ± 0.002
17	0.102 – 0.114	1.001 ± 0.002	0.995 ± 0.002	0.995 ± 0.002
18	0.114 – 0.128	1.004 ± 0.002	0.998 ± 0.002	0.999 ± 0.002
19	0.128 – 0.145	1.004 ± 0.002	0.997 ± 0.002	0.997 ± 0.002
20	0.145 – 0.165	1.004 ± 0.002	0.998 ± 0.002	0.997 ± 0.002
21	0.165 – 0.189	1.010 ± 0.002	1.003 ± 0.002	1.004 ± 0.002
22	0.189 – 0.219	1.010 ± 0.002	1.003 ± 0.002	1.003 ± 0.002
23	0.219 – 0.258	1.013 ± 0.002	1.005 ± 0.002	1.007 ± 0.002
24	0.258 – 0.312	1.011 ± 0.002	1.006 ± 0.002	1.008 ± 0.002
25	0.312 – 0.391	1.018 ± 0.002	1.013 ± 0.002	1.015 ± 0.002
26	0.391 – 0.524	1.024 ± 0.002	1.021 ± 0.002	1.023 ± 0.002
27	0.524 – 0.695	1.033 ± 0.002	1.030 ± 0.002	1.032 ± 0.002
28	0.695 – 0.918	1.044 ± 0.003	1.043 ± 0.003	1.045 ± 0.003
29	0.918 – 1.153	1.063 ± 0.004	1.059 ± 0.004	1.061 ± 0.004
30	1.153 – 1.496	1.080 ± 0.005	1.076 ± 0.004	1.080 ± 0.004
31	1.496 – 1.947	1.081 ± 0.006	1.079 ± 0.006	1.081 ± 0.006
32	1.947 – 2.522	1.082 ± 0.008	1.083 ± 0.007	1.088 ± 0.007
33	2.522 – 3.277	1.080 ± 0.009	1.076 ± 0.009	1.083 ± 0.009

*Table 6.1: The normalized correction factors for the "Born", "Dressed" and "Bare" levels in the $Z \to ee$ channel. Only statistical uncertainties are shown (*POWHEG+PYTHIA*).*

6.2 Evaluation of systematic uncertainties

The method to propagate the systematic uncertainties is explained in Section 5.6.

6.2.1 Pileup reweighting

The method to propagate the pileup reweighting uncertainty is explained in 5.6.1. The difference in the differential cross section with and without applying the additional vertex reweighting is considered as the systematic uncertainty due to the pileup reweighting which is shown in Figure 6.3.

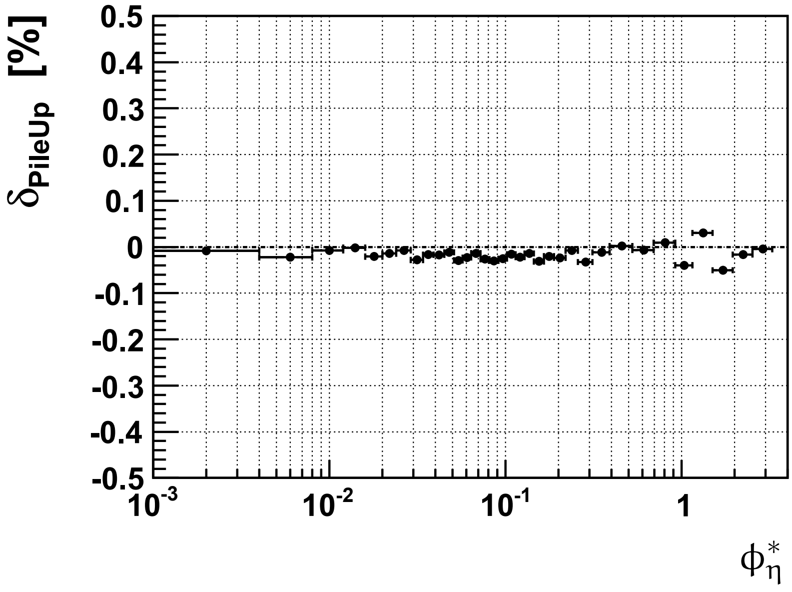

Figure 6.3: The systematic uncertainty due to the pileup reweighting (δ_{PileUp}) as a function of ϕ^*_η. Uncertainties are given in per cent [69].

6.2.2 Primary vertex position along z-axis

The impact of the reweighting of the z vertex shape of the signal MC (see section 4.1.3.3) on the correction factors C^i and on final cross sections has been estimated and found to be small. Cross sections are calculated with and without applying this reweighting and the difference between the two is taken as a systematic error. The evolution of this uncertainty as a function of ϕ^*_η bins is represented in Figure 6.4. As seen from the bin-by-bin fluctuation of this uncertainty, the precision of its determination is limited by the available statistics for the MC signal sample. This uncertainty is thus certainly smaller than the statistical precision of the MC statistics of $\sim 0.2\%$. As the shape of the z-vertex distribution in the MC is reweighted to the one measured in data, the impact of a possible mis-description of it in the MC simulation is expected to be much smaller than the effect shown in 6.4. This uncertainty can therefore be safely neglected.

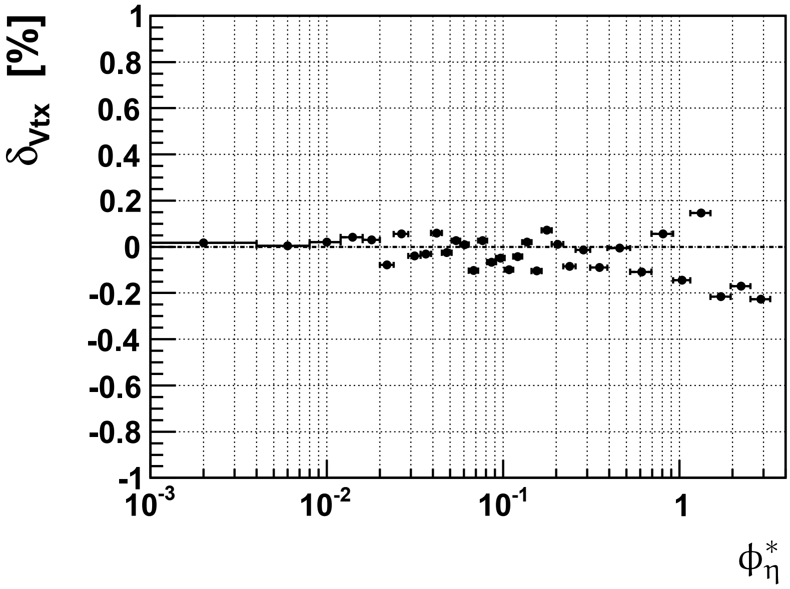

Figure 6.4: Evolution of the systematic uncertainty (δ_{Vtx}) associated to the reweight of the z vertex shape as a function of ϕ^*_η. Uncertainties are given in per cent [69].

6.2.3 QED final state radiation

The same study as in Section 5.6.3 is done for the ϕ^*_η measurement. The effect of the QED FSR correction on the ϕ^*_η measurement is shown in Figure 6.5. A conservative systematic uncertainty of $\delta_{FSR} = 0.3\%$ is assigned to account for uncertainties due to the ϕ^*_η dependent modelling of electroweak radiative corrections. This conclusion holds for ϕ^*_η distributions at the “Born”, “Dressed” and “Bare” levels.

6.2.4 PDFs

Details of the PDF uncertainty is explained in 5.6.4. The small difference between the p_T^Z measurement and the ϕ^*_η measurement is the unfolding method used to propagate the systematic uncertainties. Here, the PDF uncertainty propagation uses directly the bin-by-bin correction factors. The PDF uncertainty on

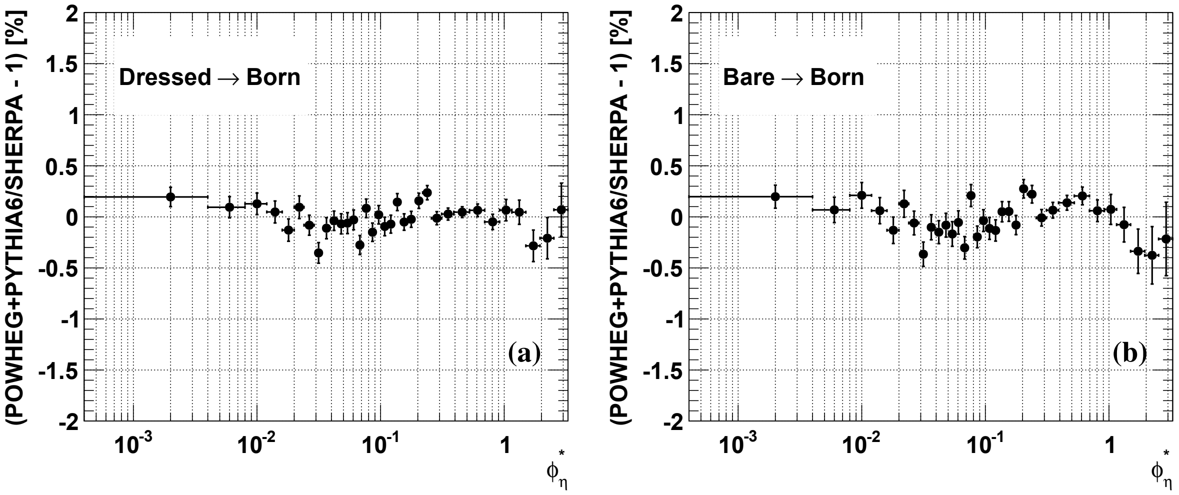

Figure 6.5: The difference of the QED FSR correction in $Z \to ee$ POWHEG+PYTHIA *and the one in $Z \to ee$* SHERPA *as a function of ϕ^*_η: from the "Dressed" level to the "Born" level (a) and from the "Bare" level to the "Born" level (b).*

the normalized cross section in the i^{th} ϕ^*_η bin is estimated as:

$$\Delta\Big(\frac{1}{\sigma}\frac{\Delta\sigma_i}{\Delta(\phi^*_\eta)_i}\Big)_{PDF} = \frac{1}{2}\sqrt{\sum_{n=1}^{N}\left(\frac{\Big(1/C^i_{norm}\Big)^{n(+)}_{rew} - \Big(1/C^i_{norm}\Big)^{n(-)}_{rew}}{\Big(1/C^i_{norm}\Big)^{0}_{rew}}\right)^2}, \tag{6.1}$$

where $(C^i_{norm})^{n(+)}_{rew}$ is the normalized correction factor in the i^{th} ϕ^*_η bin reweighted from MRSTLO* to the eigenvector PDF set n of MSTW08LO and $(C^i_{norm})^0_{rew}$ is the normalized correction factor reweighted from MRSTLO* to the central PDF set of MSTW08LO. The resulting PDF uncertainty as a function of ϕ^*_η cross section bins is shown in Figure 6.6. The uncertainty is increasing with ϕ^*_η up to $\sim 0.1\%$.

6.2.5 Unfolding

The effect of the MC shape dependence has been studied carefully for the ϕ^*_η measurement [69]. The reconstructed ϕ^*_η spectrum in POWHEG reweighted to RESBOS (i.e. the POWHEG ϕ^*_η spectrum is reweighted to the one provided by RESBOS) is unfolded using the C_Z factors computed with POWHEG reweighted to data. This distribution is compared with the true ϕ^*_η spectrum of POWHEG reweighted to RESBOS. We observe deviations smaller than 0.1% in the full ϕ^*_η range. Deviations of similar size are observed when the reconstructed ϕ^*_η spectrum provided by POWHEG reweighted to data is unfolded using the C_Z

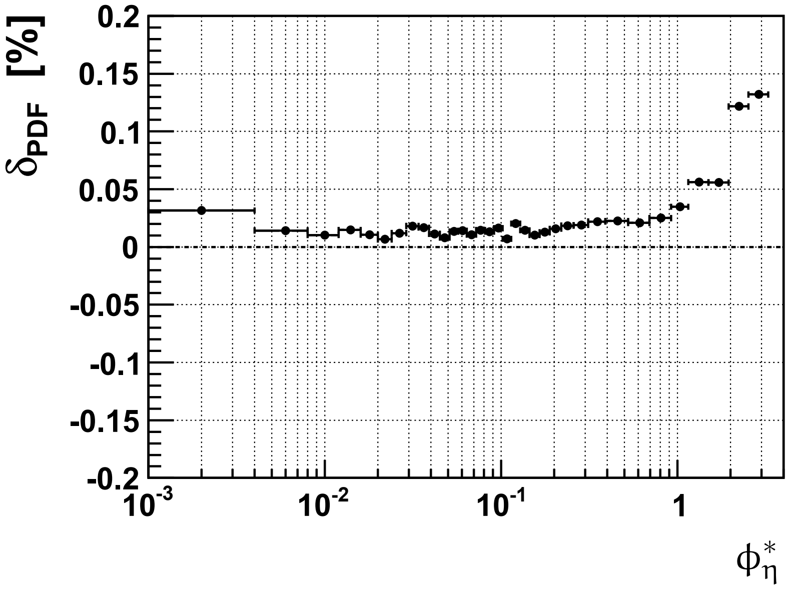

Figure 6.6: The PDF uncertainty (δ_{PDF}) for the Pythia *MC sample as a function of ϕ^*_η cross section bins. Uncertainties are given in per cent [69]*

factors calculated with Powheg reweighted to Resbos. The MC samples used for these tests are statistically correlated, the deviations observed are very small and due to different ϕ^*_η shapes in our MC. The statistical fluctuations due to the available MC statistics are taken into account as a separate systematic uncertainty. It is worth to say that if we used the default Powheg MC to unfold data, the variations we would observe would be anyway below 0.2%. In Figure 6.15 we show that data and Powheg differ up to 10% in some bins and this means that the unfolded ϕ^*_η spectrum is only slightly dependent on the ϕ^*_η shape provided by MC generators. In Figure 6.7 we plot the difference in per cent in each ϕ^*_η bin between the C_Z correction factors calculated using Powheg reweighted to Resbos and the C_Z correction factors calculated using Powheg reweighted to data. We quote these variations as systematic uncertainties.

The bin-by-bin unfolding is chosen for the ϕ^*_η measurement which has the high purity presented in Section 6.1.1. However, a small migration is still possible. It is well known that correlations between adjacent bins are neglected by the bin-by-bin correction technique. In order to understand the effect of the unfolding method on the systematic uncertainty found as in Figure 6.7, an iterative Bayesian unfolding technique has been employed. The results obtained by using these two unfolding technique are in good agreement. The effect of different PDF sets discussed in Section 6.2.4 is to change the ϕ^*_η shape of the MC used to unfold data, therefore we do not quote a separate uncertainty for PDFs.

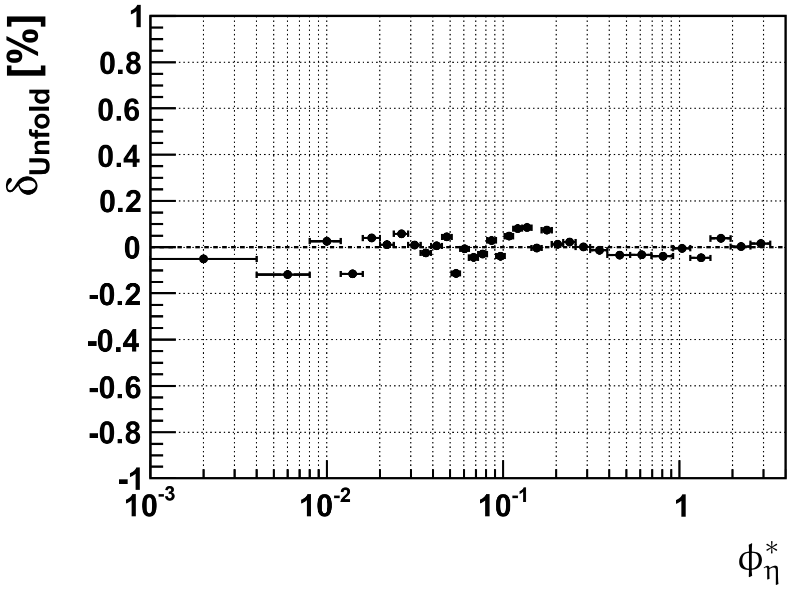

Figure 6.7: Difference in per cent in each ϕ^*_η bin between C_Z bin-by-bin correction factors calculated using POWHEG *signal MC reweighted to the ϕ^*_η spectrum produced by* RESBOS *predictions or measured using present data is quoted as the systematic uncertainty due to the unfolding procedure (δ_{Unfold}) [69].*

6.2.6 Monte Carlo statistics

Due to the limited statistics of the POWHEG signal MC sample, a sizable statistical uncertainty is present for the determination of the C^i correction factors. This leads to a systematic uncertainty on the cross section measurement which is uncorrelated between data points. Its evolution as a function of ϕ^*_η is shown in Figure 6.11(a). This uncertainty is of the order of 0.2%, increasing up to 0.8% for larger ϕ^*_η values.

6.2.7 Tracking

The tracking systematic uncertainty is studied carefully in the ϕ^*_η measurement [69]. Specific to the measurement of ϕ^*_η is the use of η and ϕ of the lepton track, measured at the interaction point. Therefore, a substantial part of the experimental systematic error is expected to come from the tracking. The ϕ^*_η variable is a function of the azimuthal opening angle in $[0,\pi]$, referred thereafter as $\Delta\phi$ and of $\Delta\eta$, the difference in η between the two leptons. This variable is directly sensitive to physics and therefore can not be compared to a simulated distribution to assess systematics.

The measurement of ϕ of electrons is dominantly affected by bremsstrahlung. Therefore, an angle $\theta = \pi$ - $\Delta\phi$ [1] was defined as shown in Figure 6.8(a): a sign is given depending on the relative position on the second track with respect to the reference one. The reference track can be either the positron track (θ_{Pos}) or the track associated to the highest energy cluster (θ_{Max}). A distribution of θ_{Pos} is shown in Figure 6.8(b). If bremsstrahlung was fully recovered by the tracking algorithm, the mean of θ_{Pos} would be 0, while the width of the distribution is not significant as it also reflects the physics.

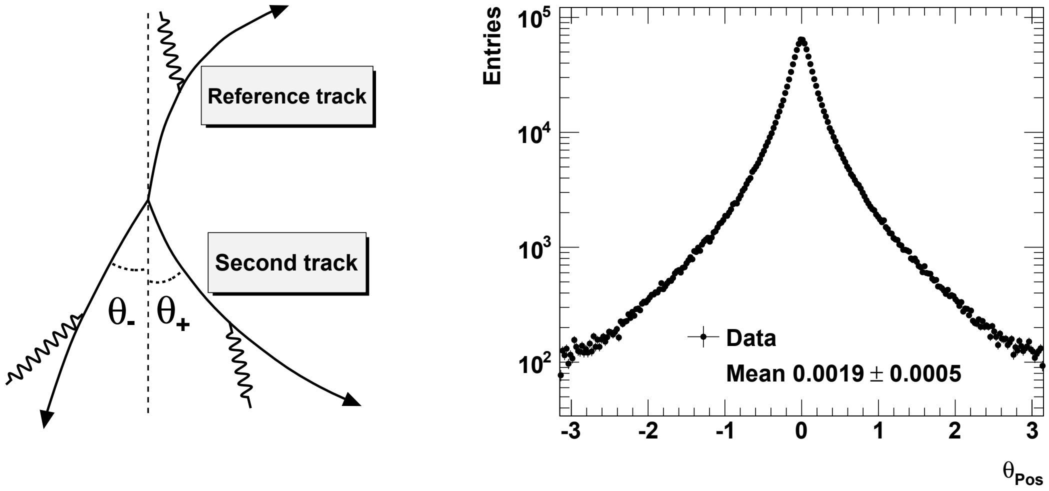

(a)

(b)

Figure 6.8: a) Definition of "signed" θ in the transverse plane. The reference track can be either the positron track or the track with the highest p_{T} . b) Example of a distribution of "signed" θ of the positron (θ_{Pos}) in the case of the GSF tracking [69].

The tracking systematic uncertainty can come from angular bias, angular resolution, the difference between data and MC in the ϕ_{el} of electrons as in Figure 4.12(f) and charge misidentification.

6.2.7.1 Angular bias

The distribution of the θ between electron and positron in $Z \rightarrow ee$ events is studied as a function of the ϕ and η of the positron. The mean value of this distribution in each bin of ϕ and η of the positron is determined using an iterative Lorentzian fit of the central part of the distribution. The evolutions of the mean values of the θ as a function of ϕ and η of the positron are studied.

---

[1] θ has the same definition as ϕ_{acop} mentioned in Section 1.3.1 but with the addition of a sign.

Values for data and MC are compared and the difference between data and MC values as a function of ϕ is presented in Figure 6.9(a). Differences between Data and MC values are within 1.5 mrad, given the statistical accuracy. A maximal bias of ±1.5 mrad on the $\Delta\phi$ angle between the two Z decay leptons will therefore be used as a systematic uncertainty. The resulting uncertainty on the measured ϕ^*_η cross section is presented in figure 6.9(b). It can be seen that bin-by-bin fluctuations of the uncertainty are about of the same order of magnitude as the statistical uncertainty on the calculated values. This means that given the available signal MC statistics it is difficult to precisely estimate the bin-by-bin correlations of this uncertainty. Therefore this uncertainty is treated as uncorrelated between ϕ^*_η bins and to use mean value of 0.1% in all ϕ^*_η bins.

Concerning a possible bias on η measurements of the leptons, the effect of a bias of 2 mrad on the measured ϕ^*_η cross section has been tested and it is negligible. No systematic uncertainty arising from a possible bias on η angles will therefore be considered.

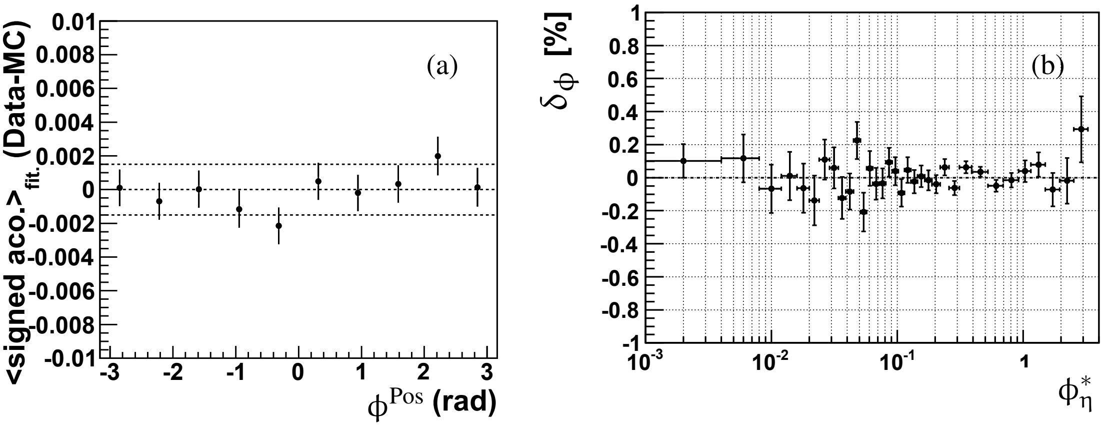

Figure 6.9: Evolution of the mean value of signed acoplanarity distribution as a function of ϕ of the positron, the difference between data and MC is presented (a). Evolution as a function of ϕ^*_η of the systematic uncertainty (δ_ϕ) associated to a possible bias of 1.5 mrad on ϕ (b). Uncertainties are given in per cent [69].

6.2.7.2 Angular resolution

The effect of a possible mis-description of the detector resolution on the measurements of ϕ and η angles has also been studied. The resolution in the MC on both angles was enlarged by 20% and the impact on the measured normalised cross section as a function of ϕ^*_η was calculated. We observe that a change of the resolution on η has no impact on the measured cross section. A change of the resolution on ϕ has a larger impact on the measured cross section, of maximally 0.2% as presented in figures 6.10. This will therefore be also considered as a systematic uncertainty on the final measurement.

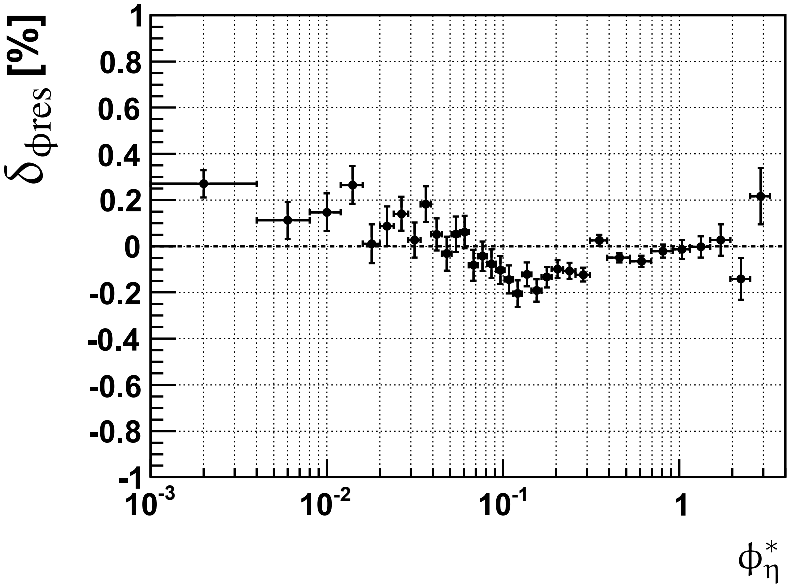

Figure 6.10: Evolution as a function of ϕ^*_η of the systematic uncertainty ($\delta_{\phi res}$) associated to a possible misdescription by 20% *in the MC of the resolution on ϕ angle. Uncertainties are given in per cent [69].*

6.2.7.3 Data/MC differences in ϕ_{el} distributions

In control distributions for the $Z \rightarrow ee$ decay channel, a small trend of ±1.5% is observed in the ratio between data and MC prediction for the distribution of the ϕ angle of the sub-leading electron, as seen in Figure 4.12(f). The impact of such a mis-description of an angular variable was studied by reweighting the MC to the data as a function of the ϕ_{el2} angle of the sub-leading electron and propagating this to the determination of the correction factors C^i_{norm}. The difference in per cent between nominal C^i_{norm} factors and those obtained after a reweighting of the signal MC is of the order of 0.02% and the impact on the final cross section measurement is therefore negligible.

6.2.7.4 Charge misidentification

The electron charge mis-identification has been measured in data and in MC in the 2011 data within the egamma group (see references in [69]). Charge mis-identification for electrons arise from a wrong track associated to the electron cluster. The rate of charge mis-identification measured in data and in MC simulations is the same in the central region, while increasing to maximally 3% at larger η_e values [69]. Possible effects of this small mis-description by the MC of the charge mis-identification rate observed in data have been tested. The resulting uncertainty on the measured normalised cross section is negligible.

6.2.8 Energy scale and energy resolution

The systematic uncertainties due to the electron energy scale and resolution corrections on the ϕ^*_η measurement are estimated in the same procedure as in Section 5.6.7. The resulting uncertainties on the normalised cross section are represented as a function of ϕ^*_η in Figures 6.11(b) and (c) for the electron energy scale and the electron energy resolution, respectively. The uncertainties are below 0.1% and only slightly dependent on ϕ^*_η.

6.2.9 Electron reconstruction and identification efficiency

The systematic uncertainties due to the electron reconstruction and identification efficiency correction on the ϕ^*_η measurement are estimated in the same procedure as in Section 5.6.8. The resulting uncertainty on the normalised cross section is represented as a function of ϕ^*_η in Figure 6.11(d).

6.2.10 Electron trigger efficiency

The systematic uncertainties due to the electron trigger efficiency correction on the ϕ^*_η measurement are estimated in the same procedure as in Section 5.6.9. The resulting uncertainty on the normalised cross section is negligible, maximally 0.004%.

6.2.11 Backgrounds

An uncertainty on the amount of QCD background events as defined in Table 4.6 is used. In each cross section bin, this uncertainty is combined with the statistical uncertainty on the estimated number of QCD events in the bin. This results in an uncertainty on the normalised cross section of $\sim 0.05\%$, which is considered as correlated between bins. The evolution of this uncertainty as a function ϕ^*_η cross section bins is represented in Figure 6.11(e).

Similarly, an uncertainty of 10% on the contribution of electroweak background processes as a function of ϕ^*_η is assumed. In each cross section bin, this uncertainty is combined with the statistical uncertainty on the estimated number of electroweak events in the bin, which may not be negligible in some cases due to the low MC statistics available for some of the processes. This results in an uncertainty on the normalised cross section of up to 0.35% at higher ϕ^*_η values, which is considered as correlated. The evolution of this uncertainty as a function of ϕ^*_η cross section bins is represented in Figure 6.11(f).

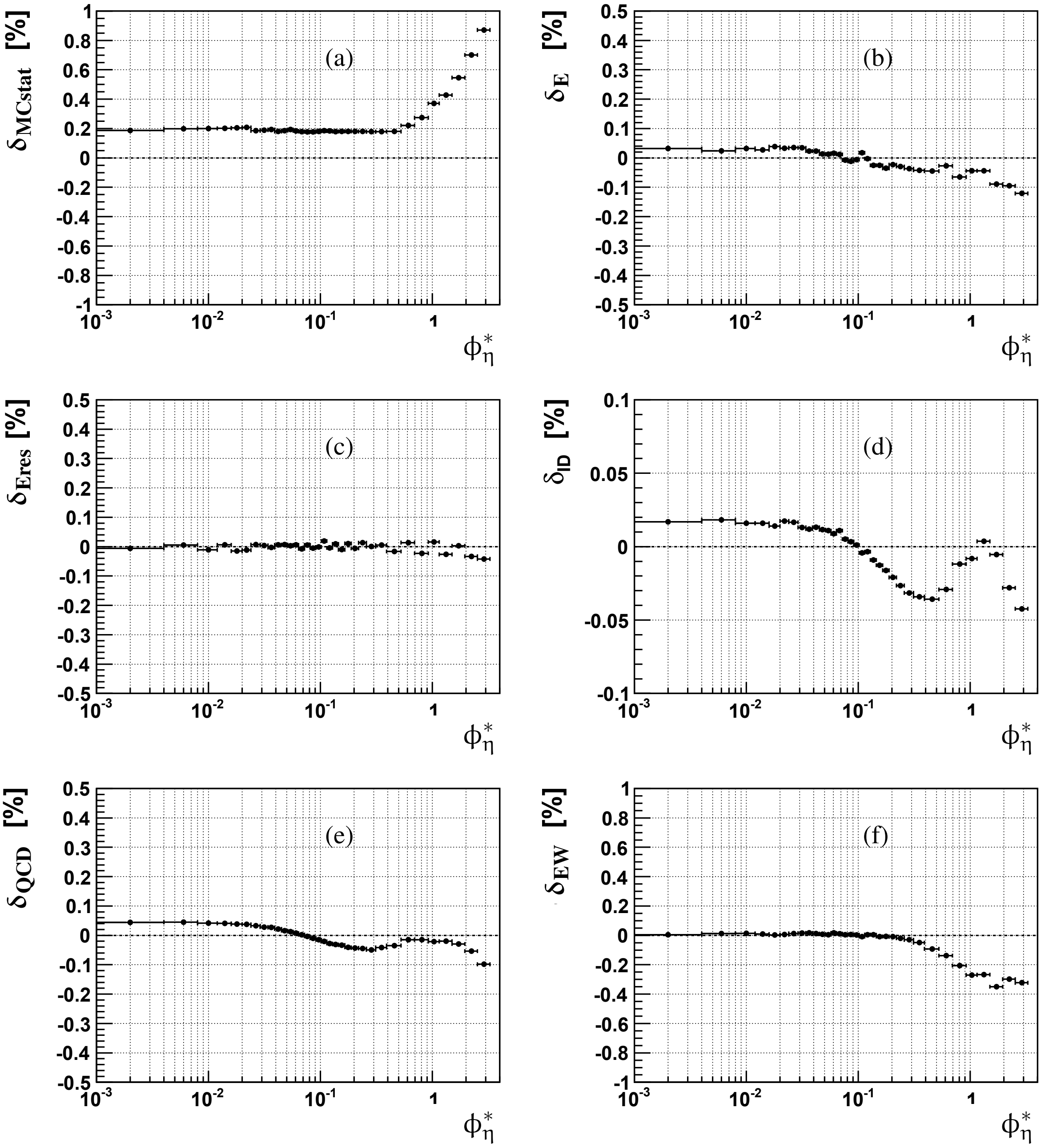

Figure 6.11: Evolution of absolute systematic uncertainties from different error sources as a function of ϕ^*_η: (a) δ_{MCstat} uncertainty due to the limit of MC statistics, (b) δ_E uncertainty due to the electron energy scale correction, (c) δ_{Eres} uncertainty due to the electron energy resolution smearing, (d) δ_{ID} uncertainty due to the electron reconstruction and identification efficiency correction, (e) δ_{QCD} uncertainty on the contribution of QCD background, (f) δ_{EW} uncertainty on the contribution of electroweak backgrounds. All uncertainties are given in per cent [69].

6.3 Results

6.3.1 The fiducial differential cross section as a function of ϕ^*_η

The normalised cross section $\frac{1}{\sigma}\frac{d\sigma}{d\phi^*_\eta}$ as a function of ϕ^*_η and compared to the RESBOS prediction is presented in Figure 6.12(a), the ratio to the RESBOS prediction is shown in Figure 6.12(b). Numerical results are also provided in Table 6.2. Cross sections at the “Born”, “Dressed” and “Bare” levels are also provided in Table 6.3. The typical systematic uncertainty of this measurement is well below 0.5% in most of the ϕ^*_η range.

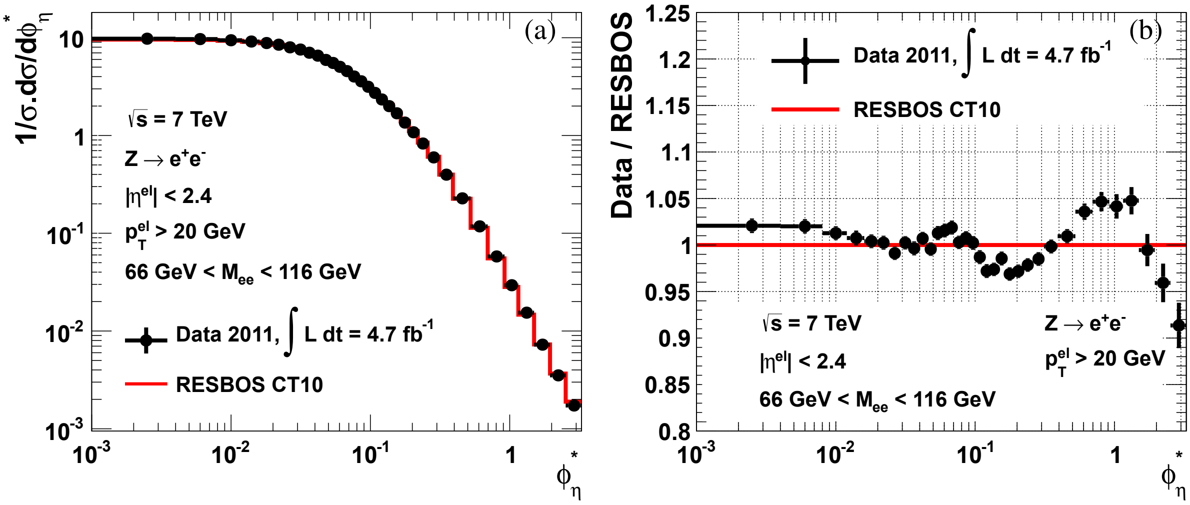

Figure 6.12: The normalised cross section $\frac{1}{\sigma}\frac{d\sigma}{d\phi^*_\eta}$ as a function of ϕ^*_η compared to the RESBOS prediction (a) and the ratio to the RESBOS prediction (b) [69].

ϕ^*_η bin	$1/\sigma\, d\sigma/d\phi^*_\eta$	δ_{stat} [%]	δ_{sys} [%]	δ_{tot} [%]	δ_{MCstat} [%]	δ_{FSR} [%]	δ_{ϕ} [%]	δ_{E} [%]	δ_{Eres} [%]	δ_{ID} [%]	δ_{Trig} [%]	$\delta_{\phi res}$ [%]	δ_{QCD} [%]	δ_{EW} [%]	δ_{Unfold} [%]	δ_{PileUp} [%]
0.000 – 0.004	9.771	0.46	0.46	0.65	0.19	0.30	0.10	0.03	-0.01	0.02	0.00	0.27	0.04	0.00	-0.02	-0.01
0.004 – 0.008	9.682	0.47	0.45	0.65	0.20	0.30	0.10	0.02	0.00	0.02	0.00	0.11	0.04	0.01	-0.21	-0.02
0.008 – 0.012	9.424	0.47	0.41	0.63	0.20	0.30	0.10	0.03	-0.01	0.02	0.00	0.15	0.04	0.01	0.06	-0.01
0.012 – 0.016	9.141	0.48	0.49	0.69	0.20	0.30	0.10	0.03	0.01	0.02	0.00	0.26	0.04	0.01	-0.17	-0.01
0.016 – 0.020	8.824	0.49	0.39	0.62	0.21	0.30	0.10	0.04	-0.01	0.02	0.00	0.01	0.04	0.00	0.08	-0.02
0.020 – 0.024	8.482	0.50	0.39	0.63	0.21	0.30	0.10	0.03	-0.01	0.02	0.00	0.09	0.04	0.01	-0.03	-0.02
0.024 – 0.029	7.974	0.46	0.40	0.61	0.19	0.30	0.10	0.03	0.01	0.02	0.00	0.14	0.03	0.01	0.05	-0.01
0.029 – 0.034	7.567	0.47	0.37	0.60	0.19	0.30	0.10	0.03	0.00	0.01	0.00	0.03	0.03	0.02	0.00	-0.03
0.034 – 0.039	7.021	0.49	0.42	0.64	0.19	0.30	0.10	0.02	0.00	0.01	0.00	0.18	0.03	0.02	-0.06	-0.02
0.039 – 0.045	6.553	0.46	0.37	0.59	0.18	0.30	0.10	0.02	0.01	0.01	0.00	0.05	0.02	0.01	0.01	-0.02
0.045 – 0.051	5.926	0.48	0.37	0.61	0.19	0.30	0.10	0.01	0.01	0.01	0.00	-0.03	0.02	0.01	0.02	-0.02
0.051 – 0.057	5.518	0.50	0.38	0.63	0.19	0.30	0.10	0.01	0.00	0.01	0.00	0.05	0.01	0.01	-0.07	-0.03
0.057 – 0.064	5.038	0.48	0.38	0.61	0.18	0.30	0.10	0.01	0.01	0.01	0.00	0.06	0.01	0.02	-0.06	-0.03
0.064 – 0.072	4.555	0.48	0.39	0.62	0.18	0.30	0.10	0.01	-0.01	0.01	0.00	-0.08	0.00	0.01	-0.12	-0.02
0.072 – 0.081	4.011	0.48	0.37	0.60	0.18	0.30	0.10	-0.01	0.01	0.00	0.00	-0.04	0.00	0.00	-0.03	-0.03
0.081 – 0.091	3.584	0.48	0.37	0.61	0.18	0.30	0.10	-0.01	0.01	0.00	0.00	-0.08	-0.01	0.01	0.03	-0.03
0.091 – 0.102	3.149	0.49	0.39	0.63	0.18	0.30	0.10	0.00	0.00	0.00	0.00	-0.10	-0.01	0.00	-0.09	-0.03
0.102 – 0.114	2.726	0.50	0.40	0.64	0.18	0.30	0.10	0.02	0.02	-0.01	0.00	-0.14	-0.02	-0.01	0.03	-0.02
0.114 – 0.128	2.336	0.50	0.42	0.66	0.18	0.30	0.10	0.00	0.00	-0.01	0.00	-0.20	-0.03	0.00	0.06	-0.03
0.128 – 0.145	1.996	0.49	0.39	0.63	0.18	0.30	0.10	-0.03	0.01	-0.01	0.00	-0.12	-0.03	0.00	0.03	-0.02
0.145 – 0.165	1.687	0.49	0.42	0.65	0.18	0.30	0.10	-0.02	-0.01	-0.01	0.00	-0.19	-0.03	-0.01	-0.02	-0.04
0.165 – 0.189	1.355	0.50	0.40	0.64	0.18	0.30	0.10	-0.03	0.01	-0.02	0.00	-0.13	-0.04	-0.01	0.05	-0.02
0.189 – 0.219	1.079	0.50	0.38	0.63	0.18	0.30	0.10	-0.02	-0.01	-0.02	0.00	-0.10	-0.04	-0.01	-0.02	-0.03
0.219 – 0.258	$8.274 \cdot 10^{-1}$	0.50	0.39	0.63	0.18	0.30	0.10	-0.03	0.01	-0.03	0.00	-0.11	-0.04	-0.02	-0.02	-0.01
0.258 – 0.312	$5.968 \cdot 10^{-1}$	0.50	0.39	0.64	0.18	0.30	0.10	-0.04	0.00	-0.03	0.00	-0.12	-0.05	-0.03	-0.01	-0.04
0.312 – 0.391	$3.973 \cdot 10^{-1}$	0.51	0.38	0.63	0.18	0.30	0.10	-0.04	0.00	-0.03	0.00	0.02	-0.04	-0.05	-0.04	-0.02
0.391 – 0.524	$2.275 \cdot 10^{-1}$	0.52	0.39	0.65	0.18	0.30	0.10	-0.05	-0.02	-0.04	0.00	-0.05	-0.03	-0.09	-0.06	0.00
0.524 – 0.695	$1.176 \cdot 10^{-1}$	0.64	0.42	0.76	0.22	0.30	0.10	-0.03	0.01	-0.03	0.00	-0.07	-0.01	-0.14	-0.06	-0.01
0.695 – 0.918	$5.790 \cdot 10^{-2}$	0.79	0.48	0.92	0.27	0.30	0.10	-0.07	-0.02	-0.01	0.00	-0.02	-0.01	-0.21	-0.06	0.00
0.918 – 1.153	$2.94 \cdot 10^{-2}$	1.07	0.56	1.21	0.37	0.30	0.10	-0.04	0.02	-0.01	0.00	-0.01	-0.02	-0.27	-0.02	-0.04
1.153 – 1.496	$1.54 \cdot 10^{-2}$	1.22	0.60	1.36	0.43	0.30	0.10	-0.03	-0.03	0.01	0.00	0.00	-0.02	-0.27	-0.07	0.03
1.496 – 1.947	$7.25 \cdot 10^{-3}$	1.55	0.73	1.71	0.54	0.30	0.10	-0.07	0.00	0.01	0.00	0.03	-0.03	-0.35	0.02	-0.05
1.947 – 2.522	$3.52 \cdot 10^{-3}$	1.97	0.84	2.14	0.69	0.30	0.10	-0.07	-0.03	-0.01	0.00	-0.13	-0.05	-0.30	-0.06	-0.02
2.522 – 3.277	$1.73 \cdot 10^{-3}$	2.46	1.00	2.65	0.86	0.30	0.10	-0.11	-0.04	-0.02	0.00	0.20	-0.10	-0.32	-0.01	-0.01

Table 6.2: The normalised cross section $\frac{1}{\sigma}\frac{d\sigma}{d\phi^*_\eta}$ *corrected to the "Born" level in each* ϕ^*_η *bin.* POWHEG *$Z \rightarrow ee$ MC events are used to calculate the C^i correction factors. All uncertainties are given in per cent.*

ϕ^*_η bin	$1/\sigma\, d\sigma/d\phi^*_\eta$ (Born)	δ_{stat} [%]	δ_{sys} [%]	$1/\sigma\, d\sigma/d\phi^*_\eta$ (Dressed)	δ_{stat} [%]	δ_{sys} [%]	$1/\sigma\, d\sigma/d\phi^*_\eta$ (Bare)	δ_{stat} [%]	δ_{sys} [%]
0.000 – 0.004	9.771	0.46	0.46	9.687	0.46	0.46	9.699	0.46	0.46
0.004 – 0.008	9.682	0.47	0.40	9.585	0.47	0.39	9.589	0.47	0.39
0.008 – 0.012	9.424	0.47	0.41	9.355	0.47	0.40	9.376	0.47	0.40
0.012 – 0.016	9.141	0.48	0.46	9.057	0.48	0.46	9.071	0.48	0.46
0.016 – 0.020	8.824	0.49	0.38	8.757	0.49	0.38	8.774	0.49	0.37
0.020 – 0.024	8.482	0.50	0.39	8.426	0.50	0.39	8.435	0.50	0.39
0.024 – 0.029	7.975	0.46	0.40	7.931	0.46	0.39	7.943	0.46	0.39
0.029 – 0.034	7.568	0.47	0.37	7.517	0.47	0.37	7.525	0.47	0.37
0.034 – 0.039	7.021	0.49	0.42	6.998	0.49	0.41	7.005	0.49	0.41
0.039 – 0.045	6.553	0.46	0.37	6.534	0.46	0.36	6.533	0.46	0.36
0.045 – 0.051	5.926	0.48	0.37	5.921	0.48	0.36	5.923	0.48	0.36
0.051 – 0.057	5.519	0.50	0.37	5.522	0.50	0.37	5.523	0.50	0.37
0.057 – 0.064	5.038	0.48	0.37	5.041	0.48	0.37	5.044	0.48	0.37
0.064 – 0.072	4.555	0.48	0.37	4.561	0.48	0.37	4.561	0.48	0.37
0.072 – 0.081	4.011	0.48	0.37	4.030	0.48	0.36	4.029	0.48	0.36
0.081 – 0.091	3.584	0.48	0.37	3.595	0.48	0.37	3.593	0.48	0.37
0.091 – 0.102	3.149	0.49	0.38	3.161	0.49	0.37	3.159	0.49	0.37
0.102 – 0.114	2.726	0.50	0.40	2.742	0.50	0.39	2.741	0.50	0.39
0.114 – 0.128	2.336	0.50	0.42	2.351	0.50	0.42	2.349	0.50	0.41
0.128 – 0.145	1.996	0.49	0.39	2.011	0.49	0.38	2.009	0.49	0.38
0.145 – 0.165	1.687	0.49	0.41	1.697	0.49	0.41	1.698	0.49	0.41
0.165 – 0.189	1.355	0.50	0.39	1.364	0.50	0.39	1.363	0.50	0.39
0.189 – 0.219	1.079	0.50	0.38	1.087	0.50	0.38	1.087	0.50	0.38
0.219 – 0.258	$8.274 \cdot 10^{-1}$	0.50	0.38	$8.336 \cdot 10^{-1}$	0.50	0.38	$8.320 \cdot 10^{-1}$	0.50	0.38
0.258 – 0.312	$5.968 \cdot 10^{-1}$	0.50	0.39	$5.998 \cdot 10^{-1}$	0.50	0.39	$5.988 \cdot 10^{-1}$	0.50	0.39
0.312 – 0.391	$3.973 \cdot 10^{-1}$	0.51	0.37	$3.991 \cdot 10^{-1}$	0.51	0.37	$3.985 \cdot 10^{-1}$	0.51	0.37
0.391 – 0.524	$2.275 \cdot 10^{-1}$	0.52	0.39	$2.282 \cdot 10^{-1}$	0.52	0.38	$2.278 \cdot 10^{-1}$	0.52	0.38
0.524 – 0.695	$1.176 \cdot 10^{-1}$	0.64	0.42	$1.179 \cdot 10^{-1}$	0.64	0.41	$1.177 \cdot 10^{-1}$	0.64	0.41
0.695 – 0.918	$5.790 \cdot 10^{-2}$	0.79	0.47	$5.796 \cdot 10^{-2}$	0.79	0.47	$5.787 \cdot 10^{-2}$	0.79	0.47
0.918 – 1.153	$2.94 \cdot 10^{-2}$	1.07	0.56	$2.95 \cdot 10^{-2}$	1.07	0.55	$2.95 \cdot 10^{-2}$	1.07	0.55
1.153 – 1.496	$1.54 \cdot 10^{-2}$	1.22	0.60	$1.55 \cdot 10^{-2}$	1.22	0.59	$1.54 \cdot 10^{-2}$	1.22	0.59
1.496 – 1.947	$7.25 \cdot 10^{-3}$	1.55	0.72	$7.26 \cdot 10^{-3}$	1.55	0.71	$7.25 \cdot 10^{-3}$	1.55	0.71
1.947 – 2.522	$3.52 \cdot 10^{-3}$	1.97	0.84	$3.51 \cdot 10^{-3}$	1.97	0.82	$3.50 \cdot 10^{-3}$	1.97	0.82
2.522 – 3.277	$1.73 \cdot 10^{-3}$	2.46	1.01	$1.73 \cdot 10^{-3}$	2.46	0.98	$1.72 \cdot 10^{-3}$	2.46	0.98

Table 6.3: Comparison of the normalised cross sections $\frac{1}{\sigma}\frac{d\sigma}{d\phi^*_\eta}$ *corrected to the "Born", "Dressed" and "Bare" levels.* POWHEG $Z \rightarrow ee$ *MC events are used to calculate the* C^i *correction factors. All uncertainties are given in per cent.*

6.3.2 Comparisons with theoretical predictions

The final normalised cross section is compared with theoretical predictions from RESBOS, FEWZ introduced in section 1.3.4 in Figure 6.13(a) and with the new theoretical prediction at NNLL+NNLO (a matching of a resummation algorithm with a fixed order $\mathscr{O}(\alpha_s^2)$ computed with the program MCFM [58]) from Ref. [41] as in Figure 6.13(b). The measured cross section agrees with RESBOS within 2% for low ϕ_η^* values below 0.1. For the larger ϕ_η^* values, the agreement of NNLO FEWZ and the new prediction from Ref. [41] with our measurement is poorer than of RESBOS. The new prediction from Ref. [41] quantifies the full theoretical uncertainty which is dominated by the resummation uncertainty at low ϕ_η^* and by the renormalization and factorization scale uncertainty at high ϕ_η^*.

The effect of PDFs used in the RESBOS calculation is shown in Figure 6.14. The ratio of data to RESBOS calculation using either CTEQ6.6 or CT10 PDFs are presented. We observe that the agreement of data with CT10 prediction is better than with CTEQ6.6 prediction in most of the ϕ_η^* range.

In Figure 6.15, the final normalised cross section is also compared with predictions from different MC generators used so far by ATLAS. These predictions are presented in Section 1.3.5. The agreement between the measured cross section and the prediction of each MC generator is quantified by calculating for each the global χ^2 between prediction and data. Only the statistical uncertaintes of the MC generation samples have been used to compute the χ^2/n_{dof}. The obtained values are listed in Table 6.4, where n_{dof} is the number of points. The best description of data is provided by the SHERPA MC generator. The POWHEG generator interfaced to PYTHIA8 is also able to describe the data. The effect of changing

Generator	χ^2/n_{dof}
RESBOS	6
ALPGEN	9
SHERPA	5
MC@NLO	65
POWHEG+HERWIG	66
POWHEG+PYTHIA8	8
POWHEG+PYTHIA6	47

Table 6.4: The global χ^2/n_{dof} between each MC prediction and data [69].

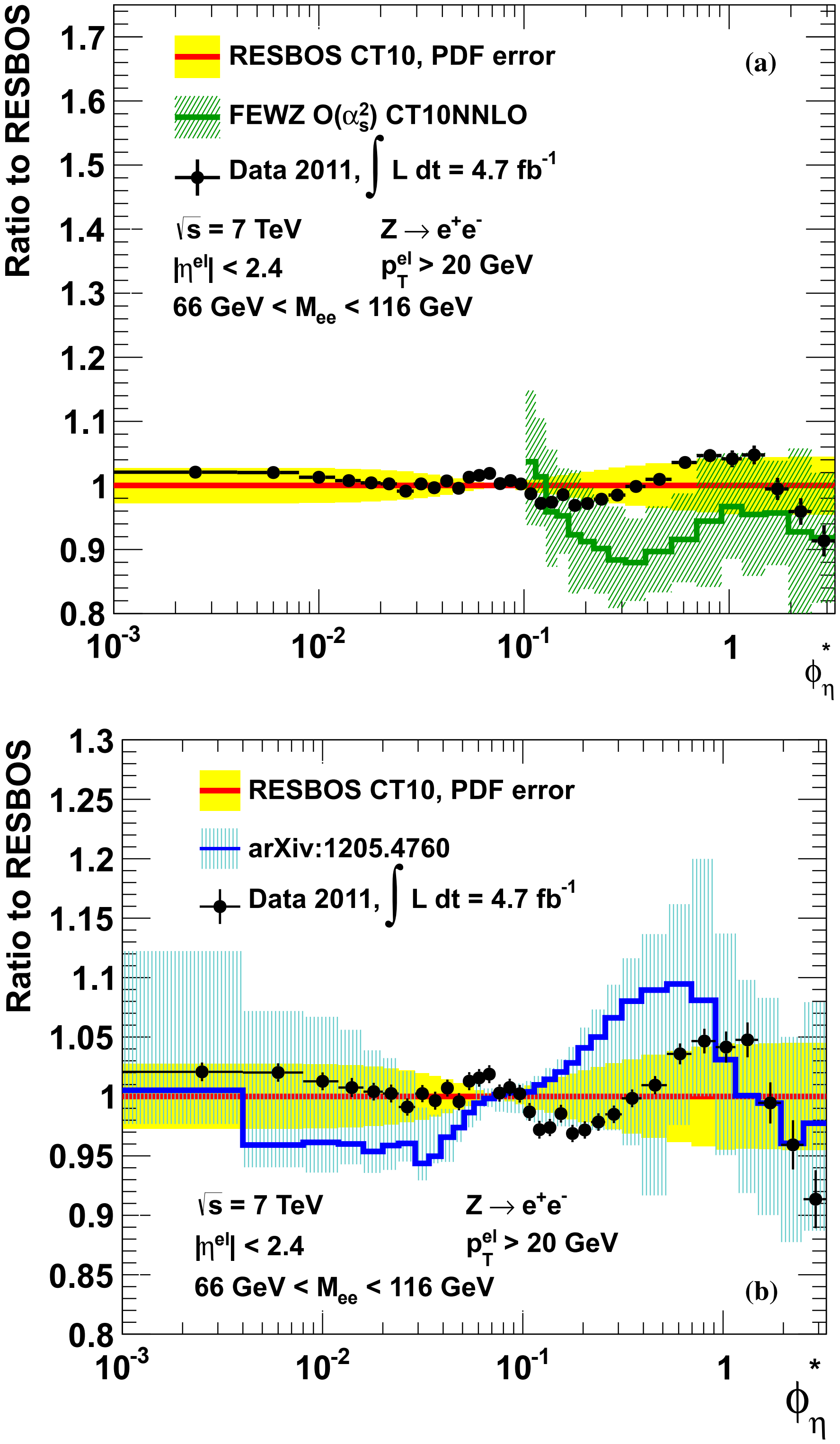

Figure 6.13: Ratio of the final normalised cross section $\frac{1}{\sigma}\frac{d\sigma}{d\phi^*_\eta}$ *to* RESBOS *prediction as a function of* ϕ^*_η *and compared to theoretical predictions from* FEWZ*(a), compared to the theoretical prediction from [41] (b) [69].*

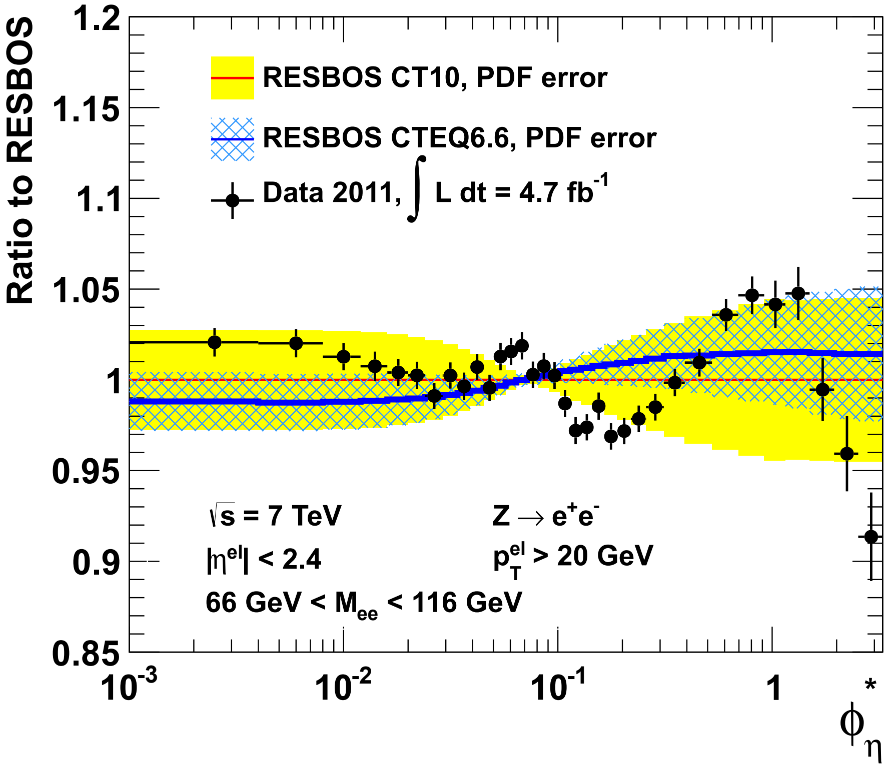

Figure 6.14: Comparisons of the normalised cross section $\frac{1}{\sigma}\frac{d\sigma}{d\phi^*_\eta}$ *as a function of* ϕ^*_η *to the* RESBOS *predictions using CT10 or CTEQ6.6 PDFs [69].*

the parton shower algorithms interfaced to POWHEG was investigated by using PYTHIA6 and HERWIG interfaced to the same POWHEG NLO calculation. These two variations give a worse description of data than PYTHIA8, and deviations from data of $\sim 10\%$ are observed. The description provided by MC@NLO interfaced to HERWIG does not properly describe the data for $\phi^*_\eta > 0.1$, and a deviation from data of the order of 7% are observed for $\phi^*_\eta < 0.1$.

The precision of this new measurement is by far better than the current uncertainties of theoretical predictions. It will therefore be valuable to constrain them further.

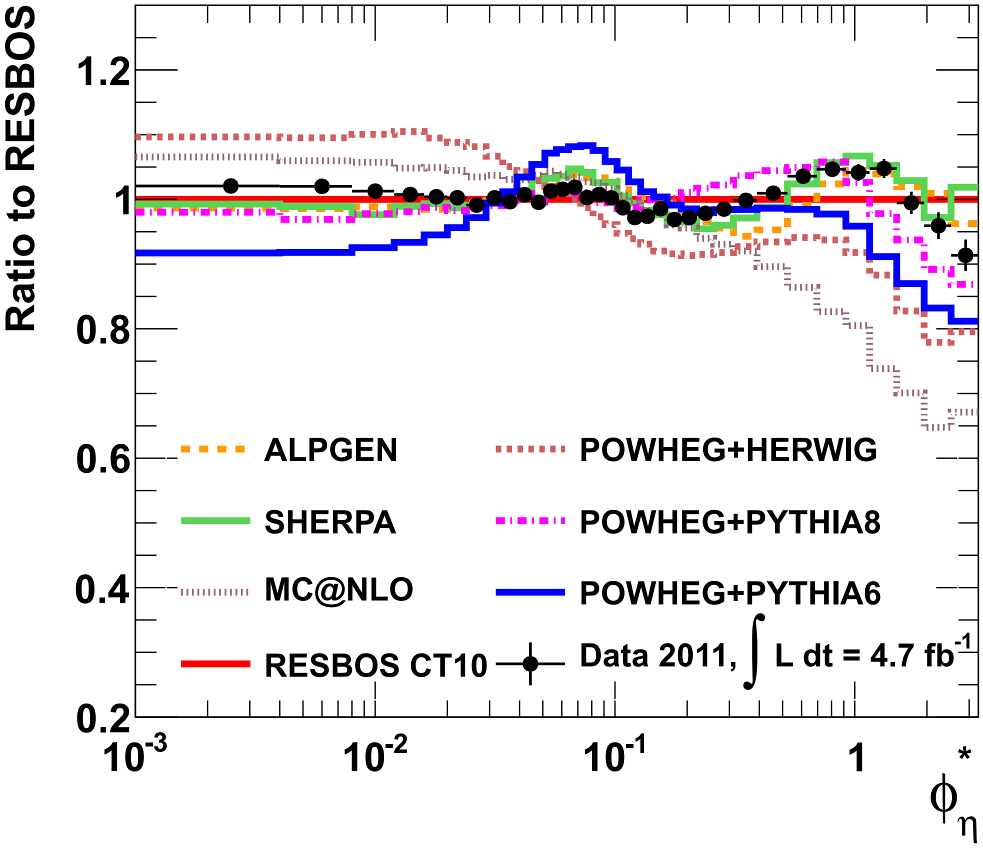

Figure 6.15: Comparison of the normalised cross section $\frac{1}{\sigma}\frac{d\sigma}{d\phi^*_\eta}$ *divided by the* RESBOS *prediction as a function of* ϕ^*_η *with predictions from different MC generators as used by ATLAS (at the "Born" level) [69].*

6.3.3 Acceptance correction to the full phase space measurement

As discussed in Section 5.1.1 the fiducial differential cross section as a function of ϕ^*_η of the Z boson can be extrapolated to the full phase space by applying the normalised acceptance correction factors A^i_{norm}. Factors determined at the "Born", "Dressed" and "Bare" levels are shown in Figure 6.16. As already observed in [16], the dominant uncertainty on these extrapolation factors results from the differences between the MC generators. The A^i_{norm} extrapolation factors determined at the "Born" level using different MC generators have therefore been compared. This comparison is presented in Figure 6.17. Differences of up to 10% are observed, which will be used to define the systematic uncertainty on the determination of these A^i_{norm} factors. The values of A^i_{norm} correction factors are provided in Table 6.5.

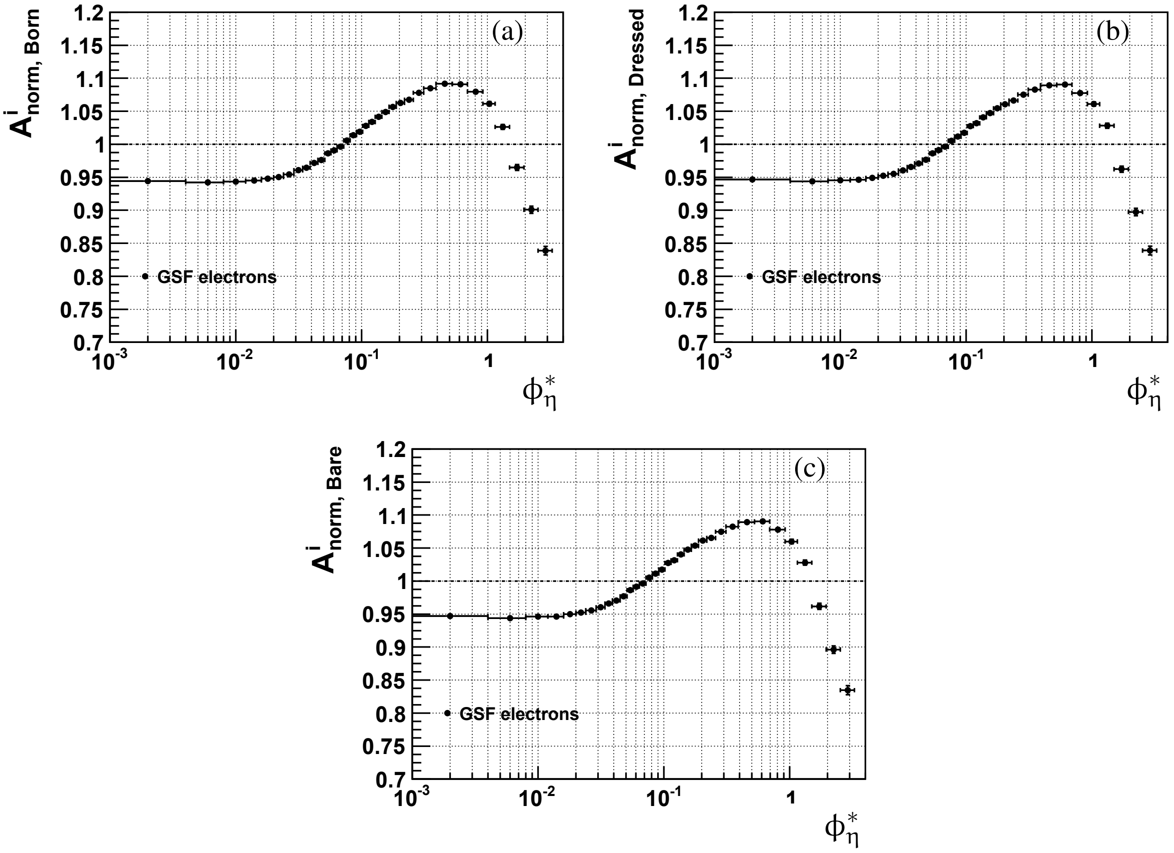

Figure 6.16: The normalised acceptance correction factors A^i_{norm} as function of ϕ^*_η obtained with POWHEG+PYTHIA. *The correction factors correct to the "Born" level (a), to the "Dressed" level (b) and to the "Bare" level (c). Only statistical uncertainties are shown [69].*

Bin i	ϕ^*_η	A^i_{norm} (Born)	$1 - A_{Dressed}/A_{Born}$ [%]	$1 - A_{Bare}/A_{Born}$ [%]	δ_{model} [%]
0	0.000 – 0.004	0.944 ± 0.0013	-0.24	-0.27	3.8
1	0.004 – 0.008	0.942 ± 0.0013	-0.15	-0.15	3.0
2	0.008 – 0.012	0.943 ± 0.0013	-0.20	-0.33	3.7
3	0.012 – 0.016	0.945 ± 0.0013	-0.13	-0.14	2.3
4	0.016 – 0.020	0.948 ± 0.0013	-0.12	-0.21	2.5
5	0.020 – 0.024	0.950 ± 0.0014	-0.19	-0.20	2.3
6	0.024 – 0.029	0.954 ± 0.0012	-0.10	-0.15	1.8
7	0.029 – 0.034	0.961 ± 0.0013	0.04	0.04	2.4
8	0.034 – 0.039	0.964 ± 0.0013	-0.10	-0.16	2.2
9	0.039 – 0.045	0.972 ± 0.0012	0.06	0.10	2.2
10	0.045 – 0.051	0.976 ± 0.0013	-0.04	-0.05	2.8
11	0.051 – 0.057	0.986 ± 0.0013	-0.01	-0.01	2.1
12	0.057 – 0.064	0.991 ± 0.0013	-0.03	-0.07	1.8
13	0.064 – 0.072	0.996 ± 0.0013	0.03	0.02	2.1
14	0.072 – 0.081	1.006 ± 0.0013	0.04	0.05	1.8
15	0.081 – 0.091	1.014 ± 0.0013	0.21	0.22	1.0
16	0.091 – 0.102	1.019 ± 0.0013	0.18	0.15	1.1
17	0.102 – 0.114	1.028 ± 0.0014	0.04	0.04	1.3
18	0.114 – 0.128	1.034 ± 0.0014	0.19	0.23	1.3
19	0.128 – 0.145	1.042 ± 0.0014	0.08	0.13	1.7
20	0.145 – 0.165	1.049 ± 0.0014	0.17	0.14	2.0
21	0.165 – 0.189	1.057 ± 0.0014	0.21	0.28	2.7
22	0.189 – 0.219	1.063 ± 0.0014	0.18	0.12	2.3
23	0.219 – 0.258	1.067 ± 0.0014	0.10	0.20	2.8
24	0.258 – 0.312	1.078 ± 0.0014	0.25	0.30	3.0
25	0.312 – 0.391	1.085 ± 0.0015	0.18	0.21	3.4
26	0.391 – 0.524	1.092 ± 0.0015	0.22	0.22	3.6
27	0.524 – 0.695	1.091 ± 0.0019	0.07	0.06	4.3
28	0.695 – 0.918	1.080 ± 0.0024	0.18	0.14	4.0
29	0.918 – 1.153	1.061 ± 0.0032	0.05	0.14	5.2
30	1.153 – 1.496	1.026 ± 0.0037	-0.18	-0.16	10.7
31	1.496 – 1.947	0.965 ± 0.0045	0.26	0.33	10.4
32	1.947 – 2.522	0.901 ± 0.0055	0.38	0.52	17.1
33	2.522 – 3.277	0.839 ± 0.0065	-0.03	0.47	16.4

Table 6.5: The normalised acceptance correction factors A^i_{norm} at the "Born", "Dressed" and "Bare" levels. Statistical uncertainties on A^i_{norm} at the "Born" level are shown, as well as the model uncertainty obtained by comparing different MC generators.

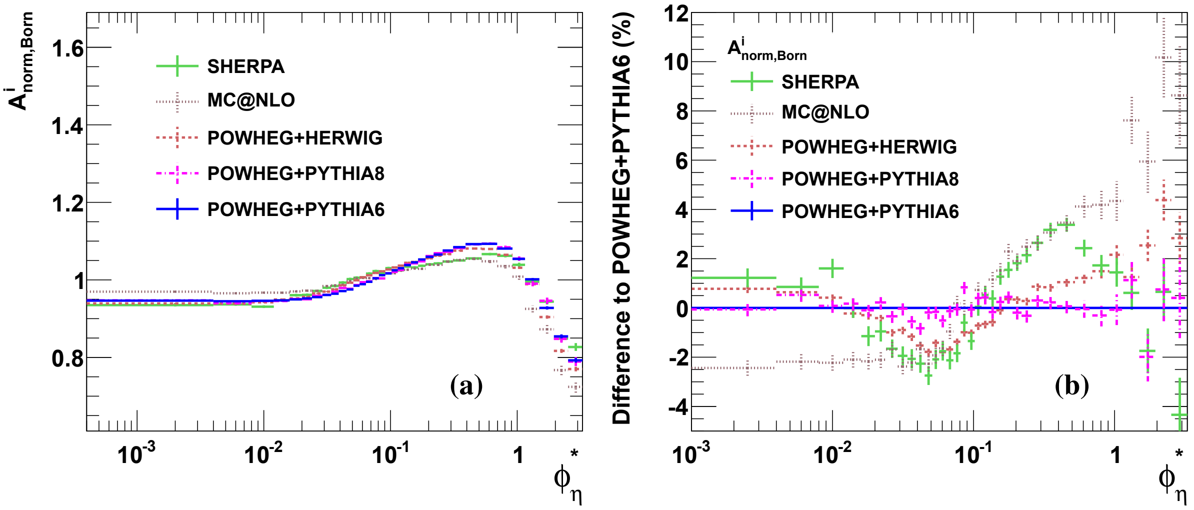

Figure 6.17: Comparison of $A^{i}_{norm,Born}$ acceptance correction factors determined using different MC generators (a) and the ratio of $A^{i}_{norm,Born}$ factors obtained with different generators to the $A^{i}_{norm,Born}$ factor determined using POWHEG+PYTHIA.

6.4 p_T^Z and ϕ^*_η correlation

In order to compare the results of the ϕ^*_η and p_T^Z measurements, a scaling factor need to be applied on the ϕ^*_η range. The relation between p_T^Z and ϕ^*_η was discussed in Section 1.3. The optimization of the ϕ^*_η variable was started from the p_T^Z and going through several variables: a_T, a_T/m_Z. For $Z \to ee$ events having equivalant transverse momenta of two leptons ($p_T^{(1)} \approx p_T^{(2)}$), it can be shown that $a_T \approx p_T^Z$. The ϕ^*_η variable is appoximated from the a_T/m_Z variable. Therefore a scaling factor of M_Z with $M_Z = 91.19$ GeV [52] will rise ϕ^*_η to the same scale as p_T^Z. This scaling factor can be also extracted using RESBOS program by plotting a ratio between p_T^Z and ϕ^*_η in each event of a high statistic generator sample. The ratio in each ϕ^*_η bin is shown in Figure 6.18(a) and the ratio for all sample is shown in Figure 6.18(b). A factor of M_Z is yielded from this study. The correlation between p_T^Z and ϕ^*_η scaled by a factor of M_Z is shown in Figure 6.19. A diagonal of this correlation shows that M_Z is a good approximation for the scaling factor of ϕ^*_η.

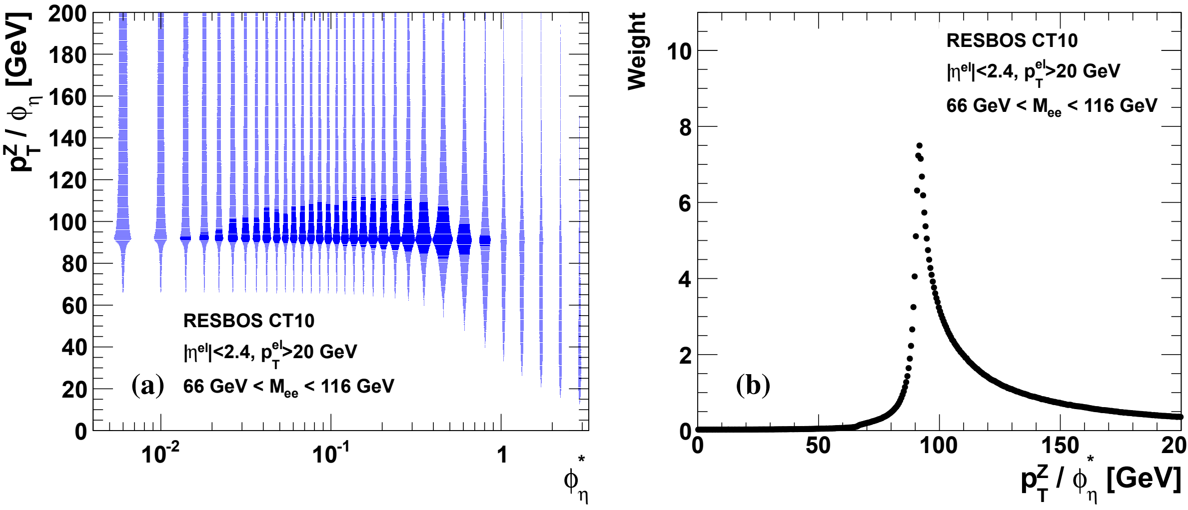

Figure 6.18: Ratio between p_T^Z and ϕ_η^* in each event: following ϕ_η^* bins (a) and for all sample (b).

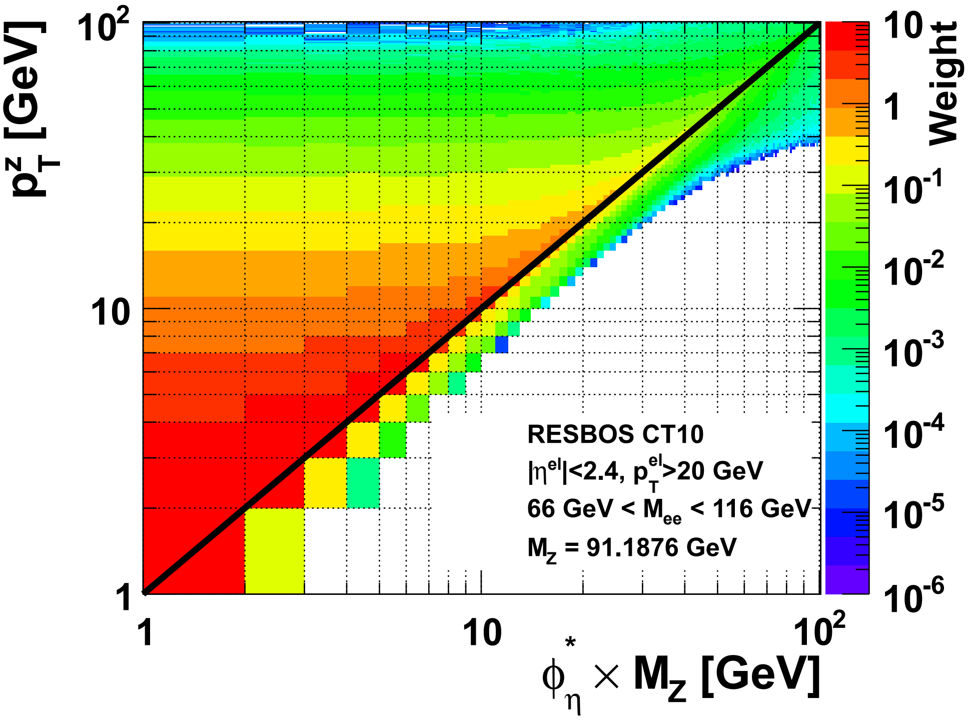

Figure 6.19: Correlation between p_T^Z and ϕ_η^* scaled by a factor of M_Z. The back line shows a diagonal of this correlation.

6.5 Discussion

The differential cross section of $Z \to ee$ as a function of ϕ^*_η was studied in this chapter. In this section, the comparison between the ϕ^*_η and the p_T^Z measurements will be presented. The ϕ^*_η range is multiplied by a scale factor of M_Z as studied in Section 6.4 in order to perform the same scale with p_T^Z.

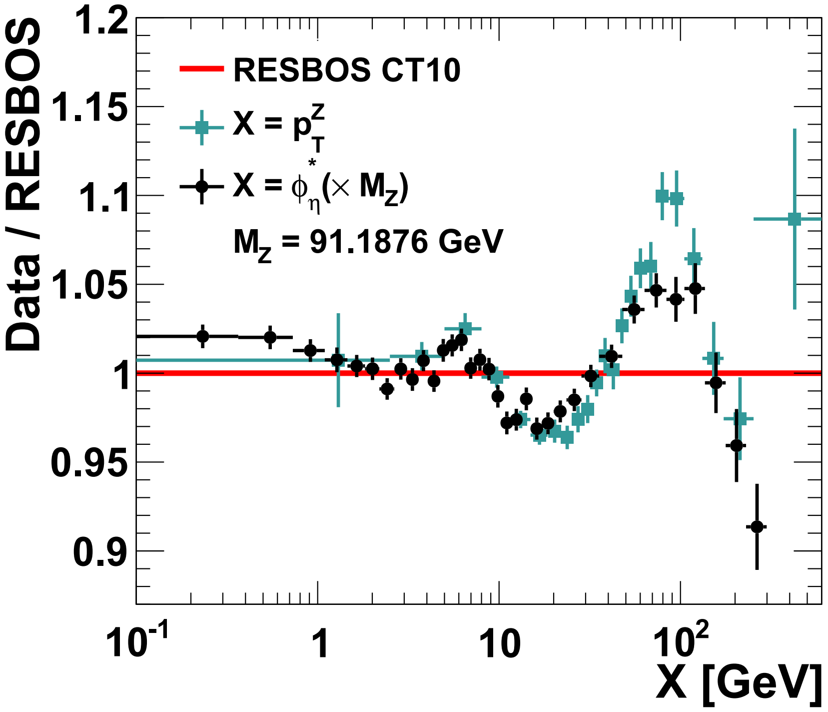

Figure 6.20: The differential cross section as a function of p_T^Z or as a function of ϕ^*_η measured in data are divided by corresponding RESBOS *predictions. The ϕ^*_η range is multiplied by a scale factor of M_Z as studied in Section 6.4 in order to perform the same scale with p_T^Z.*

Figure 6.20 shows together the p_T^Z and the ϕ^*_η measurements compared to the RESBOS predictions. At $p_T^Z \lesssim 10$ GeV, both measurements agree with the predictions within 3%. While the p_T^Z measurement is divided in three bins due to the limit of the p_T^Z resolution, the ϕ^*_η measurement can result the shape with more than ten bins. In the range 10 GeV $\lesssim p_T^Z \lesssim$ 50 GeV, the two measurements have the same level of the agreement with RESBOS predictions which is 5%. In the range 50 GeV $\lesssim p_T^Z \lesssim$ 200 GeV, the measured ϕ^*_η distribution matches the prediction within 5% while it is 10% for the measured p_T^Z distribution.

The maximum of the total systematic uncertainty of the ϕ^*_η measurement is 1.0% comparing with 3.0% of the p_T^Z measurement. At low p_T^Z, the ϕ^*_η measurement is even more precise with the total systematic uncertainty $< 0.5\%$. The evalutation of the total systematic uncertainty as a function of ϕ^*_η (p_T^Z) is shown in Figure 6.21. Since the two measurements do not have the same number of bins and bin widths. The distribution of the systematic uncertainty distribution is fitted by using an adapted function. The resulting fits are then used to compute the ratio of the total systematic uncertainties of the two measurements. The systematic uncertainty distribution of the p_T^Z is fitted by using an exponential function plus a parabolic function. The one of the ϕ^*_η measurement is fitted by using an exponential function. In most of the p_T^Z range the systematic uncertainty of the ϕ^*_η measurement is two times smaller than the one of the p_T^Z measurement. At very low p_T^Z the difference increases up to more than six times.

These comparisons prove the advantage of the new variable ϕ^*_η with respect to the p_T^Z variable.

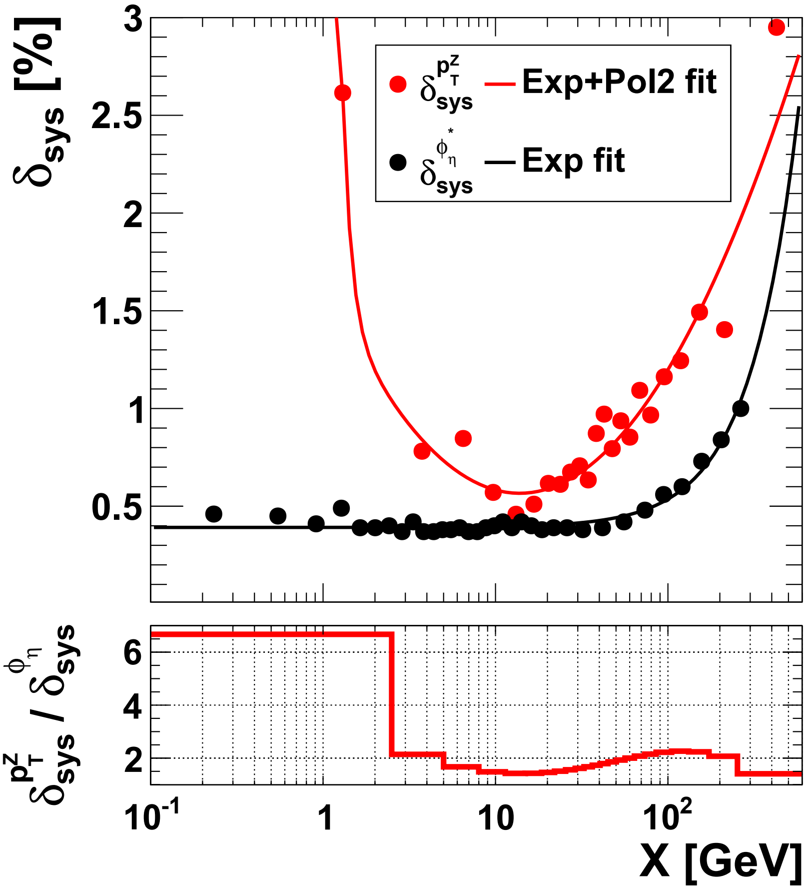

Figure 6.21: The total systematic uncertainty as a function of the ϕ^*_η, the total systematic uncertainty as a function of the p_T^Z and their ratio.

Both measurements were compared with the same predictions and they lead to the same conclusions. The effect of PDF sets used in the RESBOS calculation was presented by comparing the measured cross section with RESBOS predictions using different PDF sets. Both measurements showed a better agreement with CT10 predictions comparing to CTEQ6.6 predictions as shown in Figure 5.20 and Figure 6.14(a). In addition, the ϕ^*_η measurement was compared with the new theoretical prediction at NNLL+NLO from Ref. [41] which has the full theoretical uncertainty estimation as shown in Figure 6.14(b). This prediction gives an idea about the level of the theoretical uncertainty in different regions of p_T^Z.

The two measurements were also compared with the predictions from different MC generators as shown in Figure 5.21 and Figure 6.15. The same situations were observed in both measurements. The best description of data was provided by the SHERPA MC generator. The descriptions provided by MC@NLO and POWHEG+HERWIG are the worst.

The last bin in the p_T^Z measurement $253-600$ GeV is not performed in the ϕ^*_η measurement. It was expected that the correlation between two variables reduces in this region. From $p_T^Z >\sim 50$ GeV, it is visible that the p_T^Z shape is slightly going up in comparison with the theoretical prediction while the ϕ^*_η shape is slightly going down. Figure 6.22 shows the different trends of these two variables in the extrapolation to the full phase space measurement. However, the ϕ^*_η measurement would need to be extended to the higher region to understand the trend of the ϕ^*_η spectrum.

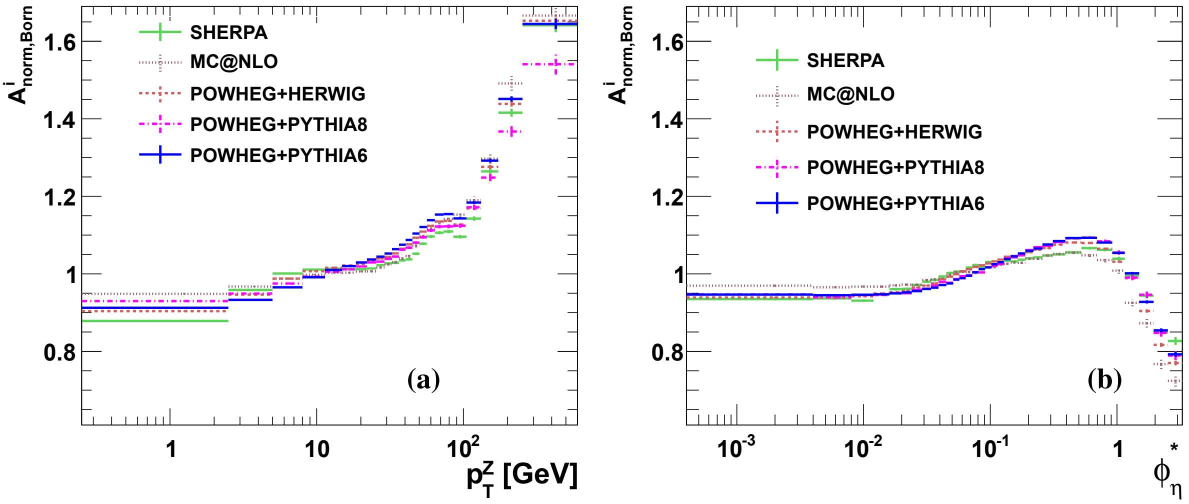

Figure 6.22: A^i_{norm} acceptance correction factors for the fiducial differential cross section as a function of p_T^Z (a) and as a function of ϕ^*_η (b) determined using different MC generators.

From the experimental point of view the ϕ^*_η measurement still has a better resolution than the p_T^Z measurement in the high p_T^Z region that was shown in Figure 1.12. The ϕ^*_η shapes in MC predictions in the high p_T^Z region is following the ϕ_η^* shape measured in data. The systematic uncertainty of the ϕ_η^* measurement is much smaller than the one of the p_T^Z measurement. Therefore the ϕ_η^* measurement is a good choice to constrain the theoretical predictions.

Conclusion

The first measurement of the ϕ_η^* spectrum of Z bosons at $\sqrt{s} = 7$ TeV of pp collisions has been studied in this thesis, which is an alternative way to probe the transverse momentum of Z bosons. The full data sample recorded by the ATLAS detector during 2011 run of the LHC was used, which corresponds with 4.7 fb^{-1} integrated luminosity. The results of this measurement were reported in Ref. [18] supported by the internal note in Ref. [69].

The transverse momentum spectrum of Z bosons produced via the Drell–Yan mechanism has been extensively studied by the Tevatron collaborations [19–21] and, recently, also by the LHC experiments [16, 62]. However, the precision of direct measurements of the Z/γ^* spectrum at low p_T^Z at the LHC and the Tevatron is limited by the experimental resolution rather than by the available event statistics. This limitation affects the choice of bin widths and the ultimate precision of the p_T^Z spectrum. In recent years, additional observables with better experimental resolution and smaller sensitivity to experimental systematic uncertainties have been investigated [43, 45, 54, 100]. The optimal experimental observable to probe the low-p_T^Z domain of Z/γ^* production was found to be ϕ_η^* which is defined [45] as: $\boldsymbol{\phi_\eta^* \equiv \tan(\phi_{\text{acop}}/2) \cdot \sin(\theta_\eta^*)}$, where $\phi_{\text{acop}} \equiv \pi - \Delta\phi$, $\Delta\phi$ is the azimuthal opening angle between the two leptons, and the angle θ_η^* is a measure of the scattering angle of the leptons with respect to the proton beam direction in the rest frame of the dilepton system. The angle θ_η^* is defined [45] by $\cos(\theta_\eta^*) \equiv \tanh[(\eta^- - \eta^+)/2]$ where η^- and η^+ are the pseudorapidities of the negatively and positively charged lepton, respectively. Therefore, ϕ_η^* depends exclusively on the directions of the two lepton tracks, which are better measured than their momenta. It is correlated to the quantity $p_{\text{T}}^Z/m_{\ell\ell}$, where $m_{\ell\ell}$ is the invariant mass of the lepton pair, and therefore probes the same physics as the transverse momentum p_T^Z [41]. Values of ϕ_η^* ranging from 0 to 1 probe the p_T^Z distribution mainly up to ~ 100 GeV.

In this thesis, the differential cross section of $Z \to ee$ as a function of ϕ_η^* has been measured and compared to fixed-order perturbative QCD calculations with/without a resummation for the low ϕ_η^* region. Calculations using RESBOS provide the best descriptions of the data. However, they are unable to reproduce the detailed shape of the measured cross section to better than 4%. The differential cross section was also compared to predictions from different Monte Carlo generators interfaced to a parton shower algorithm. The best descriptions of the measured ϕ^*_η spectrum are provided by SHERPA and POWHEG+PYTHIA8 Monte Carlo event generators. The precise measurement of the differential cross section as a function of ϕ^*_η provides valuable information for the tuning of MC generators. The typical experimental precision of this measurement ($\sim 0.5\%$) is ten times better than the typical theoretical precision and therefore is valuable to constrain the theoretical predictions further.

The p_T^Z measurement has been also studied to quantify the systematic uncertainty of this measurement using the high statistic data sample. This allows to compare two measurements which both address the physics issues of the Z transverse momentum. In most of the ϕ^*_η range, the systematic uncertainty of the p_T^Z measurement is two times larger than the one of the ϕ^*_η measurement. This comparison confirms the interest for the ϕ^*_η variable.

The measurements presented in this thesis has many implications for future studies. Tuning MC generators using the result of the precise measurement of the ϕ^*_η spectrum will minimize the uncertainty on the tuned parameters. A double differential cross section measurement as a function of p_T^Z and ϕ^*_η is interesting to understand the correlation between p_T^Z and ϕ^*_η variables. The precise measurement of the p_T^Z spectrum using the new variable ϕ^*_η can be applied to p_T^W. More precise measurement of p_T^W are important to obtain precise measurements of the W mass. In addition, a precise understanding of the p_T^Z spectrum is important to understand kinematic properties of Higgs boson production.

La première mesure du spectre en ϕ^*_η du boson Z à 7 TeV a été réalisée dans cette thèse. Cette variable permet de sonder la dynamique de production des Z de façon fine. L'échantillon complet des données enregistrées par ATLAS en 2011 a été utilisé ce qui correspond à 4.7 fb^{-1} de luminosité intégrée. Les résultats de cette mesure sont publiés dans la Ref. [18] fondé sur la note interne Ref. [69].

Le spectre en impulsion transverse du boson Z a été largement étudié par les collaborations du Tevatron [19–21] et, plus récemment, par les collaborations du LHC [16,62]. Cependant la précision des mesures directes du spectre en p_T^Z de Z/γ^* à faible impulsion transverse au LHC et au Tevatron est limitée par la résolution expérimentale plutôt que par la statistique. Cette limitation affecte le choix de la largeur des bins et la précision ultime du spectre en p_T^Z. Ces dernières années, des observables supplémentaires qui ont une meilleure résolution expérimentale et qui sont moins sensibles aux incertitudes systématiques ont été étudiées [43,45,54,100]. L'observable optimale pour sonder le domaine à petits p_T^Z du spectre de Z/γ^* est ϕ^*_η défini [45] par $\boldsymbol{\phi^*_\eta \equiv tan(\phi_{acop}/2) \cdot sin(\theta^*_\eta)}$, où $\phi_{\mathrm{acop}} \equiv \pi - \Delta\phi$ avec $\Delta\phi$ l'angle d'ouverture azimutale entre les deux leptons, et où l'angle θ^*_η est une mesure de l'angle de diffusion des leptons par rapport à la direction du faisceau de protons dans le repère au repos du système dilepton. L'angle θ^*_η est défini [45] par $\cos(\theta^*_\eta) \equiv \tanh[(\eta^- - \eta^+)/2]$ où η^- et η^+ sont respectivement la pseudorapidité du lepton de charge négative et de charge positive. Par conséquent θ^*_η dépend exclusivement de la direction des deux leptons qui est mieux mesurée que leur impulsion. Cette variable est corrélée à la quantité $p_T^Z/m_{\ell\ell}$, où $m_{\ell\ell}$ est la masse invariante de la paire de leptons et donc elle sonde la physique de la même façon que p_T^Z [41]. Les valeurs de ϕ^*_η allant de 0 à 1 correspondent à des valeurs de p_T^Z jusqu'à $\sim$ 100 GeV.

Dans cette thèse la section efficace différentielle de $Z \to ee$ en fonction ϕ^*_η a été mesurée et comparée aux calculs perturbatifs à ordre fixé, avec/sans resommation pour la région des petits ϕ^*_η. Le code RESBOS *fournit la meilleure description des données, cependant il est incapable de reproduire, à mieux de 4%, la forme détaillée de la section efficace mesurée. La section efficace différentielle a également été comparée aux prédictions de différents générateurs Monte Carlo interfacés avec un algorithme de parton shower. Les meilleures descriptions du spectre en ϕ^*_η mesuré sont données par les générateurs* SHERPA *et* POWHEG+PYTHIA8. *La mesure précise de la section efficace différentielle en ϕ^*_η fournit des informations précieuses pour l'ajustement des codes Monte Carlo. La précision expérimentale typique de cette mesure ($\sim$ 0.5%) est dix fois meilleure que la précision des calculs théoriques et elle est donc aussi précieuse pour contraindre la théorie.*

La mesure du spectre en p_T^Z *a également été faite pour quantifier l'incertitude systématique de cette mesure en utilisant la grande statistique de l'échantillon de données. Cela permet de comparer deux mesures qui traitent de l'impulsion transverse du boson Z. Dans la plupart du domaine en* ϕ_η^* *l'incertitude systématique de la mesure de* p_T^Z *est deux fois plus grande que celle de la mesure de* ϕ_η^*. *Cette comparaison confirme l'intérêt de la variable* ϕ_η^*.

Les résultats présentés dans cette thèse ont beaucoup d'implications pour les études futures. Ajustant les générateurs Monte Carlo en utilisant les résultats de la mesure précise du spectre en ϕ_η^* *minimisera l'incertitude sur leurs paramètres. Une mesure de la section efficace doublement différentielle en* p_T^Z *et* ϕ_η^* *est intéressante pour mieux comprendre la corrélation entre ces deux variables. La mesure précise du spectre en* p_T^Z *utilisant la variable* ϕ_η^* *peut être appliquée au spectre en* p_T^W *et on sait que des mesures plus fines du* p_T^W *sont importante pour une détermination précise de la masse du boson W. De plus, une compréhension précise du spectre en* p_T^Z *est importante pour comprendre les propriétés cinématiques de la production du boson de Higgs.*

List of Figures

List of Tables

Bibliography

[1] ATLAS Collaboration. Alignment of the ATLAS Inner Detector Tracking System with 2010 LHC proton-proton collisions at $\sqrt{s} = 7$ TeV. ATLAS-CONF-2011-012. Available from: `https://cds.cern.ch/record/1334582`.

[2] ATLAS Collaboration. ATLAS computing: Technical Design Report. CERN-LHCC-2005-022. Available from: `https://cds.cern.ch/record/837738`.

[3] ATLAS Collaboration. ATLAS: Detector and physics performance technical design report. Volume 1. CERN-LHCC-99-14. Available from: `https://cds.cern.ch/record/391176`.

[4] ATLAS Collaboration. ATLAS: Detector and physics performance technical design report. Volume 2. CERN-LHCC-99-15. Available from: `https://cds.cern.ch/record/391177`.

[5] ATLAS Collaboration. ATLAS EXPERIMENT - Public Results. `https://twiki.cern.ch/twiki/bin/view/AtlasPublic/`.

[6] ATLAS Collaboration. GRL. `http://atlasdqm.web.cern.ch/atlasdqm/grlgen/`.

[7] ATLAS Collaboration. Improved electron reconstruction in ATLAS using the Gaussian Sum Filter-based mode for bremsstrahlung. ATLAS-CONF-2012-047. Available from: `https://cds.cern.ch/record/1449796`.

[8] ATLAS Collaboration. J/ψ Performance of the ATLAS Inner Detector. ATLAS-CONF-2010-078. Available from: `https://cds.cern.ch/record/1281369`.

[9] ATLAS Collaboration. Kinematic Distributions of K_s^0 and Λ^0 decays in collision data at $\sqrt{s} = 7$ TeV. ATLAS-CONF-2010-033. Available from: `https://cds.cern.ch/record/1277668`.

[10] ATLAS Collaboration. Luminosity Determination Using the ATLAS Detector. ATLAS-CONF-2010-060. Available from: https://cds.cern.ch/record/1281333.

[11] ATLAS Collaboration. Performance of the ATLAS Electron and Photon Trigger in $p-p$ Collisions at $\sqrt{s}=7$ TeV in 2011. ATLAS-CONF-2012-048. Available from: https://cds.cern.ch/record/1450089.

[12] ATLAS Photos. http://www.atlas.ch/photos/index.html.

[13] LHC Webmaster. LHC Commissioning with Beam. http://lhc-commissioning.web.cern.ch/lhc-commissioning/.

[14] G. Aad et al. ATLAS Collaboration. Expected Performance of the ATLAS Experiment - Detector, Trigger and Physics. CERN-OPEN-2008-020. arXiv:0901.0512.

[15] G. Aad et al. ATLAS Collaboration. The ATLAS Experiment at the CERN Large Hadron Collider. *J. Instrum. 3*, S08003:437, 2008. doi:10.1088/1748-0221/3/08/S08003.

[16] G. Aad et al. ATLAS Collaboration. Measurement of the transverse momentum distribution of Z/γ^* bosons in proton-proton collisions at $\sqrt{s}=7$ TeV with the ATLAS detector. *Phys. Lett. B*, 705:415–434, 2011. arXiv:1107.2381.

[17] G. Aad et al. ATLAS Collaboration. Electron performance measurements with the ATLAS detector using the 2010 LHC proton-proton collision data. *Eur. Phys. J. C*, 72:1909, 2012. arXiv:1110.3174.

[18] G. Aad et al. ATLAS Collaboration. Measurement of angular correlations in Drell-Yan lepton pairs to probe Z/γ^* boson transverse momentum at $\sqrt{s}=7$ TeV with the ATLAS detector. *submitted to Phys. Lett. B*, 2012. arXiv:1211.6899.

[19] T. Aaltonen et al. CDF Collaboration. Transverse momentum cross section of e^+e^- pairs in the Z-boson region from $p\bar{p}$ collisions at $\sqrt{s}=1.96$ TeV. *Phys. Rev. D*, 86:052010, 2012. arXiv:1207.7138.

[20] V. M. Abazov et al. D0 Collaboration. Measurement of the shape of the boson transverse momentum distribution in $p\bar{p}\ Z/\gamma^* \rightarrow e^+e^- +$ X events produced at $\sqrt{s}=1.96$ TeV. *Phys. Rev. Lett.*, 100:102002, 2008. arXiv:0712.0803.

[21] V. M. Abazov et al. D0 Collaboration. Measurement of the normalized $Z/\gamma^* \to \mu^+\mu^-$ transverse momentum distribution in $p\bar{p}$ collisions at $\sqrt{s} = 1.96$ TeV. *Phys. Lett. B*, 693:522, 2010. arXiv:1006.0618.

[22] V. M. Abazov et al. D0 Collaboration. Precise study of the Z/γ^* boson transverse momentum distribution in $p\bar{p}$ collisions using a novel technique. *Phys. Rev. Lett.*, 106:122001, 2011. arXiv:1010.0262.

[23] H. Abreu et al. Performance of the electronic readout of the ATLAS liquid argon calorimeters. *JINST*, 5:P09003, 2010. doi:10.1088/1748-0221/5/09/P09003.

[24] C. Adloff et al. H1 Collaboration. Measurements of transverse energy flow in deep inelastic-scattering at HERA. *Eur. Phys. J.*, C12:595, 2000. arXiv:hep-ex/9907027.

[25] T. Adye et al. RooUnfold: ROOT Unfolding Framework. http://hepunx.rl.ac.uk/~adye/software/unfold/RooUnfold.html.

[26] S. Agostinelli et al. GEANT4 Collaboration. GEANT4: A simulation toolkit. *Nucl. Instrum. Meth. A*, 506:250, 2003. doi:10.1016/S0168-9002(03)01368-8.

[27] M. Agustoni et al. Electromagnetic energy scale in-situ calibration and performance : Supporting document for the egamma performance paper. ATL-COM-PHYS-2011-263.

[28] M. Aharrouche et al. Energy linearity and resolution of the ATLAS electromagnetic barrel calorimeter in an electron test-beam. *Nucl. Instrum. Methods A*, 568:601, 2006. arXiv:physics/0608012.

[29] M. Aharrouche et al. Response uniformity of the ATLAS liquid argon electromagnetic calorimeter. *Nucl. Instrum. Methods A*, 582:429, 2007. arXiv:0709.1094.

[30] M. Aharrouche et al. Measurement of the response of the ATLAS liquid argon barrel calorimeter to electrons at the 2004 combined test-beam. *Nucl. Instrum. Methods A*, 614:400, 2010. doi:10.1016/j.nima.2009.12.055.

[31] A. Ahmad and M. Boonekamp. Calibrated $Z \to e^+e^-$ mass with 2011 data . ATL-COM-PHYS-2011-1637.

[32] S. Aid et al. H1 Collaboration. Transverse energy and forward jet production in the low x regime at HERA. *Phys. Lett. B*, 356:118, 1995. `arXiv:hep-ex/9506012`.

[33] M. Aleksa et al. 2004 ATLAS Combined Testbeam : Computation and Validation of the Electronic Calibration Constants for the Electromagnetic Calorimeter. ATL-LARG-PUB-2006-003. Available from: `http://hal.in2p3.fr/in2p3-00125867`.

[34] G. Altarelli and G. Parisi. Asymptotic freedom in parton language. *Nucl. Phys. B*, 126:298, 1977. `doi:10.1016/0550-3213(77)90384-4`.

[35] O. Arnaez et al. A first measurement of the transverse momentum distribution of Drell-Yan lepton pairs at $\sqrt{s} = 7$ TeV with ATLAS. ATL-COM-PHYS-2011-233.

[36] O. Arnaez et al. Electron efficiency measurements using ATLAS 2010 data at $\sqrt{s} = 7$ TeV : Supporting note for the 2010 egamma paper. ATL-COM-PHYS-2011-322.

[37] P. B. Arnold and M. Hall Reno. The complete computation of high-p_T W and Z production in second-order QCD. *Nucl. Phys. B*, 319:37, 1989. `doi:10.1016/0550-3213(89)90600-7`.

[38] P. B. Arnold and R. P. Kauffman. W and Z production at next-to-leading order from large q_T to small. *Nucl. Phys. B*, 349:381, 1991. `doi:10.1016/0550-3213(91)90330-Z`.

[39] C. Balazs, P. Nadolsky, and C.-P. Yuan. Resbos input grid files in general purpose. `http://hep.pa.msu.edu/resum/`.

[40] C. Balazs and C.-P. Yuan. Soft gluon effects on lepton pairs at hadron colliders. *Phys. Rev. D*, 56:5558, 1997. `doi:10.1103/PhysRevD.56.5558`.

[41] A. Banfi, A. Dasgupta, S. Marzani, and L. Tomlinson. Predictions for Drell-Yan ϕ^*_η and Q_T observables at the LHC. *Phys.Lett. B*, 715, 2012. `arXiv:1205.4760`.

[42] A. Banfi, M. Dasgupta, and R. Delgado. The a_T distribution of the Z boson at hadron colliders. *JHEP*, 0912:022, 2009. `arXiv:0909.5327`.

[43] A. Banfi, M. Dasgupta, and S. Marzani. QCD predictions for new variables to study dilepton transverse momenta at hadron colliders. *Phys. Lett. B*, 701:75, 2011. `arXiv:1102.3594`.

[44] A. Banfi, M. Dasgupta, S. Marzani, and L. Tomlinson. Probing the low transverse momentum domain of Z production with novel variables. *JHEP*, 01:044, 2012. arXiv:1110.4009.

[45] A. Banfi, S. Redford, M. Vesterinen, P. Waller, and T. R. Wyatt. Optimisation of variables for studying dilepton transverse momentum distributions at hadron colliders. *Eur. Phys J. C*, 71:1600, 2011. arXiv:1009.1580.

[46] E. Barberio, B. van Eijk, and Z. Was. PHOTOS: A Universal Monte Carlo for QED Radiative Corrections in Decays. *Comput. Phys. Commun.*, 66:115, 1991. doi:10.1016/0010-4655(91)90012-A.

[47] E. Barberio and Z. Was. PHOTOS: A Universal Monte Carlo for QED Radiative Corrections. Version 2.0. *Comput. Phys. Commun.*, 79:291, 1994. doi:10.1016/0010-4655(94)90074-4.

[48] M. Benedikt et al. LHC Design Report v.3: the LHC Injector Chain. CERN-2004-003-V-3. Available from: https://cds.cern.ch/record/823808.

[49] S. Berge and P. Nadolsky. Resbos input grid files in the small-x broadening. http://hep.pa.msu.edu/resum/.

[50] S. Berge, Pavel M. Nadolsky, Fredrick I. Olness, and C.-P. Yuan. Transverse momentum resummation at small x for the Tevatron and LHC. *Phys. Rev. D*, 72:033015, 2005. arXiv:hep-ph/0410375.

[51] E. Berglund. Cross section of W and Z inclusive production and the W/Z cross section ratio in association with one jet for the boson decaying into electron(s) with ATLAS 7 TeV data. CERN-THESIS-2011-148. Available from: https://cds.cern.ch/record/1394607.

[52] J. Beringer et al. Particle Data Group. Review of Particle Physics. *Phys. Rev. D*, 86:010001, 2012. doi:10.1103/PhysRevD.86.010001.

[53] A. Bocci et al. Electron identification efficiency dependence on pileup. ATL-COM-PHYS-2011-1636.

[54] M. Boonekamp and M. Schott. Z boson transverse momentum spectrum from the lepton angular distributions. *JHEP*, 1011:153, 2010. arXiv:1002.1850.

[55] G. Bozzi, S. Catani, G. Ferrera, D. de Florian, and M. Grazzini. Production of Drell–Yan lepton pairs in hadron collisions: transverse-momentum resummation at next-to-next-to-leading logarithmic accuracy. *Phys. Lett. B*, 696:207, 2011. arXiv:1007.2351.

[56] 0. S. Bruning et al. LHC Design Report v.1: the LHC Main Ring. CERN-2004-003-V-1. Available from: https://cds.cern.ch/record/782076.

[57] J.M. Butterworth et al. ATLAS Collaboration. Single Boson and Diboson Production Cross Sections in pp Collisions at $\sqrt{s} = 7$ TeV. ATL-COM-PHYS-2010-695.

[58] J. Campbell, R. K. Ellis, and D. Rainwater. Next-to-leading order QCD predictions for W + 2jet and Z + 2jet production at the CERN LHC. *Phys. Rev. D*, 68:094021, 2003. arXiv:hep-ph/0308195.

[59] J. M. Campbell, J. W. Huston, and W. J. Stirling. Hard Interactions of Quarks and Gluons: a Primer for LHC Physics. *Rept. Prog. Phys.*, 70:89, 2007. arXiv:hep-ph/0611148.

[60] S. Catani, L. Cieri, G. Ferrera, D. de Florian, and M. Grazzini. Vector boson production at hadron colliders: a fully exclusive QCD calculation at NNLO. *Phys. Rev. Lett.*, 103:082001, 2009. arXiv:0903.2120.

[61] S. Catani, F. Krauss, R. Kuhn, and B. R. Webber. QCD Matrix Elements + Parton Showers. *JHEP*, 0111:063, 2001. arXiv:hep-ph/0109231.

[62] S. Chatrchyan et al. CMS Collaboration. Measurement of the rapidity and transverse momentum distribution of Z bosons in p-p collisions at $\sqrt{s} = 7$ TeV. *Phys. Rev. D*, 85:032002, 2012. arXiv:1110.4973.

[63] J. C. Collins and D. E. Soper. Angular distribution of dileptons in high-energy hadron collisions. *Phys. Rev. D*, 16:2219, 1977. doi:10.1103/PhysRevD.16.2219.

[64] J. C. Collins, D. E. Soper, and G. Sterman. Transverse momentum distribution in Drell-Yan pair and W and Z boson production. *Nucl. Phys. B*, 250:199, 1985. doi:10.1016/0550-3213(85)90479-1.

[65] P. D. B. Collins and A. D. Martin. *Hadron Interactions*. Adam Hilger Ltd, Bristol (published in association with the University of Sussex Press), 1984.

[66] G. Corcella et al. HERWIG 6.5: an event generator for Hadron Emission Reactions With Interfering Gluons. *JHEP*, 0101:010, 2001. `arXiv:hep-ph/0011363`.

[67] G. D'Agostini. Improved iterative Bayesian unfolding. `arXiv:1010.0632`.

[68] G. D'Agostini. A multidimensional unfolding method based on Bayes' theorem. *Nucl. Instrum. Meth.*, A362:487, 1995. `doi:10.1016/0168-9002(95)00274-X`.

[69] L. Di Ciaccio, T. K. O. Doan, C. Goy, H. Keoshkerian, M. Lefebvre, V. Lombardo, and E. Sauvan. A measurement of the transverse momentum distribution of Drell-Yan lepton pairs at $\sqrt{s} = 7$ TeV using the ϕ^*_η variable with ATLAS. ATL-COM-PHYS-2012-472.

[70] Y. L. Dokshitzer. Calculation of the Structure Functions for Deep Inelastic Scattering and $e^+ e^-$ Annihilation by Perturbation Theory in Quantum Chromodynamics. *Sov. Phys. JETP*, 46:641, 1977. Available from: `http://inspirehep.net/record/126153`.

[71] S. D. Drell and T. M. Yan. Massive Lepton-Pair Production in Hadron-Hadron Collisions at High Energies. *Phys. Rev. Lett.*, 25:316, 1970. `doi:10.1103/PhysRevLett.25.316`.

[72] R. K. Ellis, W. J. Stirling, and B. R. Webber. *QCD and Collider Physics*. Cambridge monographs on particle physics, nuclear physics and cosmology, 1996.

[73] S. Frixione, P. Nason, and C. Oleari. Matching NLO QCD computations with Parton Shower simulations: the POWHEG method. *JHEP*, 11:070, 2007. `arXiv:0709.2092`.

[74] S. Frixione and B. R. Webber. Matching NLO QCD computations and parton shower simulations. *JHEP*, 0206:029, 2002. `arXiv:hep-ph/0204244`.

[75] R. Gavin, Y. Li, F. Petriello, and S. Quackenbush. FEWZ 2.0: A code for hadronic Z production at next-to- next-to-leading order. *Computer Physics Communications*, 182:2388, 2011. `arXiv:1011.3540`.

[76] R. Gavin, Y. Li, F. Petriello, and S. Quackenbush. W physics at the LHC with FEWZ 2.1. *Computer Physics Communications*, 184:209, 2013. `arXiv:1201.5896`.

[77] T. Gleisberg, S. Hoeche, F. Krauss, M. Schoenherr, S. Schumann, F. Siegert, and J. Winter. Event generation with SHERPA 1.1. *JHEP*, 0902:007, 2009. `arXiv:0811.4622`.

[78] P. Golonka and Z. Was. PHOTOS Monte Carlo: A Precision tool for QED corrections in Z and W decays. *Eur. Phys. J. C*, 45:97, 2006. arXiv:hep-ph/0506026.

[79] R. J. Gonsalves, J. Pawlowski, and C.-F. Wai. QCD radiative corrections to electroweak-boson production at large transverse momentum in hadron collisions. *Phys. Rev. D*, 40:2245, 1989. doi:10.1103/PhysRevD.40.2245.

[80] V. N. Gribov and L. N. Lipatov. Deep inelastic $e\ p$ scattering in perturbation theory. *Sov. J. Nucl. Phys.*, 15:438, 1972. Available from: http://inspirehep.net/record/73449.

[81] L. Iconomidou-Fayard et al. Electron efficiency measurements in early 2012. ATL-COM-PHYS-2012-783.

[82] U. Klein and V. Radescu. ATLAS Collaboration. Guidance for scale choices and an estimate of their uncertainties. ATL-COM-PHYS-2012-419.

[83] B. Laforge and L. Schoeffel. Elements of statistical methods in high-energy physics analyses. *Nucl. Instrum. Methods Phys. Res. A*, 394:115, 1997. doi:10.1016/S0168-9002(97)00649-9.

[84] H.-L. Lai, M. Guzzi, J. Huston, Z. Li, P. M. Nadolsky, J. Pumplin, and C.-P. Yuan. New parton distributions for collider physics. *Phys.Rev. D*, 82:074024, 2010. arXiv:1007.2241.

[85] F. Landry, R. Brock, G. Ladinsky, and C.-P. Yuan. New fits for the nonperturbative parameters in the CSS resummation formalism. *Phys. Rev. D*, 63:013004, 2001. arXiv:hep-ph/9905391.

[86] F. Landry, R. Brock, P. M. Nadolsky, and C.-P. Yuan. Tevatron Run-1 Z boson data and Collins-Soper-Sterman resummation formalism. *Phys. Rev. D*, 67:073016, 2003. arXiv:hep-ph/0212159.

[87] U. Langenfeld, S. Moch, and P. Uwer. Measuring the running top-quark mass. *Phys. Rev. D*, 80:054009, 2009. arXiv:0906.5273.

[88] A. Limosani et al. Commissioning and Performance of the ATLAS Inner Detector with proton-proton Collisions at the LHC. ATL-INDET-PROC-2010-046. Available from: https://cds.cern.ch/record/1311560/.

[89] L. N. Lipatov. The parton model and perturbation theory. *Sov. J. Nucl. Phys.*, 20:94, 1975. Available from: http://inspirehep.net/record/91556.

[90] M. L. Mangano, M. Moretti, F. Piccinini, R. Pittau, and A. D. Polosa. ALPGEN, a generator for hard multiparton processes in hadronic collisions. *JHEP*, 0307:001, 2003. `arXiv:hep-ph/0206293`.

[91] K. Melnikov and F. Petriello. Electroweak gauge boson production at hadron colliders through $\mathcal{O}(\alpha_s^2)$. *Phys. Rev. D*, 74:114017, 2006. `arXiv:hep-ph/0609070`.

[92] A. Morley. Electron track fitters. Egamma Workshop 2010.

[93] P. Nadolsky et al. CT10 NLO and NNLO parton distribution functions. `http://hep.pa.msu.edu/cteq/public/index.html`.

[94] P. Nadolsky, D. R. Stump, and C.-P. Yuan. Semiinclusive hadron production at HERA: The Effect of QCD gluon resummation. *Phys. Rev. D*, 61:014003, 2000. `arXiv:hep-ph/9906280`.

[95] P. M. Nadolsky, H.-L. Lai, Q.-H. Cao, J. Huston, J. Pumplin, D. Stump, W.-K. Tung, and C.-P. Yuan. Implications of CTEQ global analysis for collider observables. *Phys. Rev. D*, 78:013004, 2008. `arXiv:0802.0007v3`.

[96] P. M. Nadolsky, D. R. Stump, and C.-P. Yuan. Phenomenology of multiple parton radiation in semiinclusive deep-inelastic scattering. *Phys. Rev. D*, 64:114011, 2001. `arXiv:hep-ph/0012261`.

[97] M. E. Peskin and D. V. Schroeder. *An Introduction to Quantum Field Theory*. Westview Press, 1995.

[98] T. Sjostrand, S. Mrenna, and P. Skands. PYTHIA 6.4 Physics and Manual. *JHEP*, 0605:026, 2006. `arXiv:hep-ph/0603175`.

[99] L. Skinnari and M. Shapiro. Tracking Performance Plots for LHCC. ATL-COM-PHYS-2011-1247.

[100] M. Vesterinen and T. R. Wyatt. A Novel Technique for Studying the Z Boson Transverse Momentum Distribution at Hadron Colliders. *Nucl. Instrum. Meth. A*, 602:432, 2009. `arXiv:0807.4956`.

[101] D. R. Yennie, S. C. Frautschi, and H. Suura. The infrared divergence phenomena and high-energy process. *Annals of Physics*, 13:379, 1961. `doi:10.1016/0003-4916(61)90151-8`.

[102] C.-P. Yuan. ResBos CP. http://hep.pa.msu.edu/resum/code/resbos_cp.

[103] C.-P. Yuan et al. Q_T resummation portal. http://hep.pa.msu.edu/resum.